

A Search in the Two-Photon Final State for Evidence of New Particle Production in  
pp Collisions at  $\sqrt{s} = 7$  TeV

Rachel Paula Yohay  
Merrick, NY

B.S., California Institute of Technology, 2006

A Dissertation presented to the Graduate Faculty  
of the University of Virginia in Candidacy for the Degree of  
Doctor of Philosophy

Department of Physics

University of Virginia  
August, 2012

---

---

---

---

## Abstract

This thesis presents a search for evidence of new particle production in the two-photon + jets + missing transverse energy final state using the 2011 Large Hadron Collider proton-proton data, at a center-of-mass energy of 7 TeV, collected by the Compact Muon Solenoid experiment. The distinctive signature of two photons, jets, and a momentum imbalance in the plane transverse to the proton beam direction is chiefly motivated by the theory of supersymmetry, which may provide a solution to the hierarchy problem in particle physics. The instrumental background from ordinary quantum chromodynamics and  $W \rightarrow e\nu$  production dominates the total background estimate, and is measured from the data. This background estimate, as well as the high efficiency ( $\sim 80\%$ ) to select and identify two high-energy photons in the data, relies on the superior energy resolution of the lead tungstate crystal electromagnetic calorimeter of the Compact Muon Solenoid as compared to the hadronic energy resolution. Signal efficiencies for gauge-mediated supersymmetric models, ranging from a few percent to approximately 25%, are taken from Monte Carlo simulation. No evidence of new particles is found in a dataset of  $4.7 \text{ fb}^{-1}$  of integrated luminosity. Upper limits between 5 and 15 fb on the cross sections of various new physics models are set at the 95% confidence level. The upper limits measured in this search are the most stringent to date for gauge-mediated models of supersymmetry.

# Contents

<b>List of Figures</b>	<b>v</b>
<b>List of Tables</b>	<b>xix</b>
<b>Acknowledgements</b>	<b>xxii</b>
<b>1 Introduction</b>	<b>1</b>
<b>2 Motivation for Physics Beyond the Standard Model</b>	<b>4</b>
2.1 The Standard Model and Electroweak Symmetry Breaking . . . . .	7
2.2 Implications of the Higgs Mechanism . . . . .	10
2.3 Addressing Problems of the Standard Model with Supersymmetry . .	12
<b>3 The Supersymmetric Extension to the Standard Model</b>	<b>16</b>
3.1 Supermultiplet Representation . . . . .	16
3.2 The Unbroken SUSY Lagrangian . . . . .	17
3.3 Soft SUSY Breaking . . . . .	23
3.4 Gauge-Mediated SUSY Breaking . . . . .	26
3.5 Phenomenology of General Gauge Mediation . . . . .	29
3.6 Experimental Status of SUSY . . . . .	32
<b>4 The Large Hadron Collider</b>	<b>38</b>
4.1 Design Considerations and Performance Limitations . . . . .	39

4.2	Beam Injection . . . . .	42
4.3	Magnets and Cryogenics . . . . .	46
4.4	Radiofrequency Cavities . . . . .	48
<b>5</b>	<b>The Compact Muon Solenoid Experiment</b>	<b>50</b>
5.1	The Detectors and Their Operating Principles . . . . .	54
5.1.1	Tracking System . . . . .	54
5.1.2	Electromagnetic Calorimeter . . . . .	63
5.1.3	Hadronic Calorimeter . . . . .	76
5.1.4	Muon System . . . . .	79
5.2	Triggering, Data Acquisition, and Data Transfer . . . . .	83
5.2.1	Level 1 and High Level Trigger Systems . . . . .	83
5.2.2	Data Acquisition System . . . . .	87
5.2.3	Data Processing and Transfer to Computing Centers . . . . .	90
<b>6</b>	<b>Event Selection</b>	<b>93</b>
6.1	Object Reconstruction . . . . .	94
6.1.1	Photons . . . . .	94
6.1.2	Electrons . . . . .	107
6.1.3	Jets and Missing Transverse Energy . . . . .	107
6.2	HLT . . . . .	114
6.3	Event Quality . . . . .	117
6.4	Photon Identification Efficiency . . . . .	119
6.4.1	Tag and Probe Method . . . . .	120
6.4.2	Photon Efficiency Scale Factor $\epsilon_e^{\text{data}}/\epsilon_e^{\text{MC}}$ . . . . .	127
<b>7</b>	<b>Data Analysis</b>	<b>130</b>
7.1	Control Samples . . . . .	131
7.2	Modeling the QCD Background . . . . .	134

7.2.1	Outline of the Procedure . . . . .	134
7.2.2	Reweighting . . . . .	135
7.2.3	Normalization . . . . .	151
7.3	Modeling the Electroweak Background . . . . .	154
7.4	Errors on the Background Prediction . . . . .	158
7.5	Results . . . . .	166
<b>8</b>	<b>Interpretation of Results in Terms of GMSB Models</b>	<b>172</b>
8.1	Simplified Models . . . . .	172
8.2	Upper Limit Calculation and Model Exclusion . . . . .	174
8.2.1	Signal Acceptance $\times$ Efficiency . . . . .	174
8.2.2	$CL_s$ and the Profile Likelihood Test Statistic . . . . .	178
8.3	Cross Section Upper Limits . . . . .	186
8.4	Exclusion Contours . . . . .	186
<b>9</b>	<b>Conclusion</b>	<b>192</b>
<b>A</b>	<b>Monte Carlo Samples</b>	<b>194</b>
A.1	List of Samples . . . . .	194
A.2	Explanation of Naming Conventions . . . . .	195
	<b>Bibliography</b>	<b>197</b>

## List of Figures

2.1	Selected LEP measurements demonstrating its contribution to the precise understanding of the Standard Model. Reprinted from ref. [9]. . .	6
2.2	Higgs potential (the sombrero) as a function of the real and imaginary parts of the complex scalar field. The movement of the balls shows that the symmetry $\phi = 0$ is spontaneously broken, the stable vacuum state of nature being somewhere along the circle of minimum potential. Reprinted from Fig. 1 of ref. [15]. . . . .	10
2.3	Predicted evolution of the free parameters of supersymmetry as a function of renormalization scale for a representative set of SUSY parameters. Note the dash-dotted line marked “ $H_u$ ” that goes negative at $\sim 1$ TeV; this indicates $\mu^2$ running negative. Reprinted from Fig. 7.4 of ref. [20]. . . . .	13
2.4	Inverse gauge couplings as a function of renormalization scale for the Standard Model assumption (dotted lines) and the SUSY assumption (solid lines; the double lines represent variations in SUSY parameters and in $\alpha_S(m_Z)$ ). Reprinted from Fig. 5.8 of ref. [20]. . . . .	15
3.1	Interactions in the unbroken SUSY Lagrangian. . . . .	24
3.2	Contributions to sfermion and gaugino masses from loop interactions with messenger particles in the GMSB framework. . . . .	27

3.3 Possible contribution to $\mu \rightarrow e\gamma$ from $m_{\tilde{e}ij}$ soft term. Reprinted from Fig. 5.6(a) of ref. [20]. . . . .	28
3.4 Typical LHC signatures of the bino and wino NLSP scenarios. . . . .	33
3.5 CMS limits on mSUGRA with $\tan \beta = 10$ , corresponding to a model with third- generation squarks and sfermions somewhat lighter than their first- and second-generation counterparts. The limits set by individual searches are shown as separate colored lines. Solid lines refer to 2011 searches (i.e. using an integrated luminosity of $\sim 1 \text{ fb}^{-1}$ ), while dashed lines refer to 2010 searches ( $\sim 36 \text{ pb}^{-1}$ ). Reprinted from ref. [52].	34
3.6 ATLAS cross section upper limit on the SPS8 [53] model of mGMSB as a function of SUSY breaking scale $\Lambda$ , lightest neutralino mass $m_{\tilde{\chi}_1^0}$ , or lightest chargino mass $m_{\tilde{\chi}_1^\pm}$ . Values of $\Lambda$ , $m_{\tilde{\chi}_1^0}$ , or $m_{\tilde{\chi}_1^\pm}$ below the intersection point between the blue (predicted SPS8 cross section) and black (observed cross section upper limit) curves are excluded. The model parameters listed above the plot are defined in Secs. 3.4 and 3.5, except for $\tau_{\text{NLSP}}$ , which is the neutralino lifetime. Reprinted from ref. [38]. . . . .	35
3.7 CDF exclusion contour in the $\tau_{\tilde{\chi}_1^0}$ - $m_{\tilde{\chi}_1^0}$ plane, where $\tau_{\tilde{\chi}_1^0}$ is the lifetime of the neutralino. Reprinted from ref. [39]. . . . .	36
4.1 Bird's-eye view of the LHC ring, showing the locations of the experiments and local landmarks. Arrows show the beam direction. ATLAS is located at Point 1, ALICE at Point 2, CMS at Point 5, and LHCb at Point 8. The ring figure is reprinted from Fig. 2.1 of ref. [60]. The CERN Globe of Innovation photo comes from ref. [63] and the airplane cartoon comes from ref. [64]. . . . .	40
4.2 Overview of the LHC injector complex at CERN [68]. . . . .	43
4.3 LHC injection scheme. Reprinted from Fig. 12.2 of ref. [60]. . . . .	44

4.4	Cross-sectional view of septum magnet (beam direction is into or out of the page) showing the holes for the circulating beams and the separate gap for injected particles. Reprinted from Fig. 11.2 of ref. [60]. . . . .	45
4.5	LHC injection kicker pulse shape. The $y$ -axis measures percentage of maximum current. Reprinted from Fig. 11.7 of ref. [60]. . . . .	45
4.6	Cross-sectional view of LHC dipole + cryostat. Reprinted from Fig. 3.3 of ref. [60]. . . . .	46
4.7	Magnetic field lines of the dipole field. The beam direction is into the page. Reprinted from Fig. 4 of ref. [69]. . . . .	47
4.8	Superconducting coils in a twin-bore dipole [70]. . . . .	48
4.9	Cross section of the LHC tunnel, showing the cryogen delivery apparatus for a dipole. Reprinted from Fig. 7.1 of ref. [60]. . . . .	49
5.1	CMS coordinate system. . . . .	51
5.2	Cutaway view of CMS. Reprinted from Fig. 1.1 of ref. [71]. . . . .	52
5.3	Longitudinal quarter cross-sectional view of CMS. The nominal interaction point is at the lower right-hand corner of the drawing. The tracker is shown in purple diagonal hashing, the electromagnetic calorimeter in green, the hadronic calorimeter in blue, and the muon stations in red. The solenoid is shown in black and white and labeled COIL, and the magnet return yoke is shown in yellow. Radial and longitudinal distances are measured in millimeters. Reprinted from Fig. CP 1 of ref. [72]. . . . .	54
5.4	Longitudinal quarter view of the pixel detector. Reprinted from Fig. 3.6 of ref. [71]. . . . .	56
5.5	BPix and FPix mechanical structures. . . . .	56
5.6	Pixel control and readout system. Reprinted from Fig. 3.9 of ref. [71]. . . . .	58
5.7	Pixel detector performance highlights. . . . .	59

5.8 Longitudinal cross section of the silicon strip detector. Reprinted from Fig. 3.1 of ref. [71]. . . . .	60
5.9 View of one tracker endcap, with the outline of a petal shown in blue. There are nine petals per wedge-shaped sector (one per TEC disk). Reprinted from Fig. 3.30 of ref. [71]. . . . .	61
5.10 Exploded view of a strip module with two sensors. Reprinted from Fig. 3.22 of ref. [71]. . . . .	62
5.11 Block diagram of the strip readout architecture. Reprinted from Fig. 3.20 of ref. [71]. . . . .	62
5.12 Strip detector performance highlights. . . . .	64
5.13 Layout of the ECAL detector. Reprinted from Fig. 4.5 of ref. [71]. . .	65
5.14 Left: EB crystal with attached APD. Right: EE crystal with attached VPT. Reprinted from Fig. 4.2 of ref. [71]. . . . .	66
5.15 Flow chart of the crystal readout, showing the 10-sample pulse shape. Reprinted from Fig. 4.9 of ref. [71]. . . . .	66
5.16 Relative response of the crystals to blue laser pulses from February 1, 2011 to January 1, 2012 [80]. Technical stops, during which the LHC is turned off for maintenance and development, are shown in gray. These periods of inactivity correspond to growth in the crystal response, as radiation damage recovery occurs. . . . .	68
5.17 Architecture of the laser monitoring system. Reprinted from Fig. 4.16 of ref. [71]. . . . .	69

5.18 Change in response of nine different VPTs in zero magnetic field vs. time. The response of each VPT is normalized to its response for the earliest data point taken. For times less than 0, no light pulsing is applied to the VPTs. For times between 0 and 20 minutes, pulsed LED light was applied to the VPTs. For times later than 20 minutes, the pulsing source was again removed. . . . .	69
5.19 VPT response in a 3.8 T laboratory magnetic field to blue LED light vs. integrated charge at photocathode [82]. The response is corrected for changes in the LED light output by PIN diode normalization. For integrated charge less than $\sim 0.003$ C, the average current draw at the photocathode is $\sim 1$ nA, delivered by blue LED triggered at 2 kHz. For integrated charge greater than $\sim 0.003$ C, the average current draw is $\sim 10$ nA from a 20 kHz trigger rate. . . . .	70
5.20 Diagram of the LED inputs to a diffusing sphere and the fanout to the crystals. Adapted from Fig. 4.8 of ref. [71]. . . . .	71
5.21 Hardware setup of the LED system. . . . .	72
5.22 Software control flow of the LED system. . . . .	74
5.23 Energy resolution vs. $ \eta $ for $Z$ decay electrons for data (filled blue circles) and MC (empty red squares). The dotted lines show the locations of module gaps (three per SM). . . . .	75
5.24 Distribution of reconstructed times of $Z$ decay electrons in EE [87]. .	75
5.25 Quarter longitudinal cross-sectional view of HCAL (and muon stations in purple). Reprinted from Fig. 5.1 of ref. [71]. . . . .	77
5.26 Diagram of the optical readout of HB. Reprinted from Fig. 5.7 of ref. [71]. . . . .	78
5.27 Cross-sectional view of one side of HF. The $z$ -axis is horizontal. Reprinted from Fig. 5.28 of ref. [71]. . . . .	78

5.28 Selected HCAL performance results. . . . .	80
5.29 View of the MB and ME layout in CMS. . . . .	81
5.30 Electric field lines within a drift tube as well as the contours of equal drift time. Reprinted from Fig. 7.5 of ref. [71]. . . . .	82
5.31 CSC wedge, showing the cathode and wire planes. Reprinted from Fig. 7.49 of ref. [71]. . . . .	83
5.32 Muon $p_T$ resolution as a function of muon $p_T$ for tracker information only (blue), muon information only (black), and both tracker and muon information combined (red). Reprinted from Fig. 1.2 of ref. [71]. . . . .	84
5.33 Di-muon invariant mass spectrum broken down by trigger path [91]. The light(dark) gray regions show the contribution from high- $p_T$ (low- $p_T$ ) di-muon triggers. Note that no $B_s \rightarrow \mu^+\mu^-$ decays have been observed [92]; the light blue region just shows the amount of triggers dedicated to the $B_s \rightarrow \mu^+\mu^-$ search. . . . .	84
5.34 Block diagram of the L1 trigger. Reprinted from Fig. 8.1 of ref. [71]. . . . .	86
5.35 Geometry of an EM RCT candidate. Reprinted from Fig. 8.2 of ref. [71]. . . . .	87
5.36 Diagram of the DAQ system. The identical event builder systems, shown as inputs and outputs to the boxes labeled “Readout Builder 1”, “Readout Builder 2”, etc., represent the eight slices. Within one slice, data can flow from the detector front ends to the readout systems to the builder network (which assembles the event fragments) to the filter systems (HLT) independently of the other slices. Reprinted from Fig. 9.8 of ref. [71]. . . . .	88
5.37 Diagram of the WLCG tier system showing data archival and reconstruction at each tier along with data transfer between tiers. Reprinted from Fig. 11.2 of ref. [71]. . . . .	92
6.1 Two gluinos each decay via $\tilde{\chi}_1^0 \rightarrow \gamma \tilde{G}$ . . . . .	94

6.2 Typical ECAL channel pulse shape. $\hat{P}$ is the pedestal value, $\hat{A}$ is the pulse amplitude, and $\hat{T}_{\max}$ is the hit time. The red line is the assumed pulse shape from which the weights are derived. Reprinted from ref. [100]. . . . .	95
6.3 $Z$ peak reconstructed using pre-LHC calibration constants (red) or September 2011 $\pi^0/\eta$ -derived intercalibration constants (blue). Reprinted from ref. [109]. . . . .	98
6.4 Hybrid algorithm in EB. The shower extent is constant in $\eta$ (five crystals), but spreads out in $\phi$ as the two sub-clusters (or basic clusters) are grouped into the same supercluster. The maximum extent in $\phi$ is 17 crystals. Reprinted from ref. [110]. . . . .	100
6.5 $Z$ peak reconstructed in the dielectron channel for different kinds of clustering. The constituent hits were calibrated with the best available intercalibrations and laser calibrations as of December 2011. The light blue histogram shows the reconstruction using a $5 \times 5$ energy sum, the red histogram shows the reconstruction using the SC energy for crystals only (the dark blue histogram in the EE plot adds in the energy from ES), and the black histogram shows the reconstruction after the SCs are corrected using a multivariate method [111]. Reprinted from Fig. 30 of ref. [111]. . . . .	101
6.6 ECAL, HCAL, and track isolation cones. . . . .	103
6.7 $\rho$ distribution for a sample of two-photon events, with at least one 40 GeV and one 25 GeV photon, passing the selection requirements in Table 6.1 and the trigger requirements in Table 6.3. This sample covers the full 2011 dataset of $4.7 \text{ fb}^{-1}$ . . . . .	104

6.8 $S/\sqrt{B}$ ( $S$ and $B$ defined in the text) vs. $I_{\text{comb}}$ . “DR03” in the legend indicates that this combined isolation was calculated in $\Delta R = 0.3$ cones, as used throughout this analysis. Reprinted from Fig. 7 of ref. [116]. . . . .	105
6.9 Neyman’s $\chi^2$ between the $ff$ and $\gamma\gamma$ $E_T$ distributions, truncated at either 25 (red) or 50 (blue) GeV, vs. upper bound on fake combined isolation. A jet is defined as in Table 6.2, but with the $\Delta R$ cleaning criteria of Table 6.2 applied to the two primary EM objects and all additional electrons, photons, and fake photons. The full reweighting and normalization procedure is employed in the $E_T$ calculation (see Sec. 7.2). Reprinted from Fig. 9 of ref. [116]. . . . .	106
6.10 Example event display showing jets clustered via the anti- $k_T$ algorithm. $y$ is pseudorapidity. Reprinted from slide 85 of ref. [122]. . . . .	110
6.11 Total jet energy correction factor $C_{\text{offset}}C_{\text{MC}}C_{\text{rel}}C_{\text{abs}}$ vs. $\eta$ , including uncertainty band, for jets reconstructed with the anti- $k_T$ algorithm, $R = 0.5$ . Reprinted from Fig. 26 of ref. [120]. . . . .	111
6.12 $\sigma$ of a Gaussian fit to the x- and y-components of calibrated $E_T$ vs. the calibrated PF $E_T$ sum in a sample of events containing at least two jets with $p_T > 25$ GeV. $\sigma$ is calibrated such that the $E_T$ scale is equal for all three algorithms. PF $\sum E_T$ is corrected, on average, to the particle level using a Pythia v8 simulation [129]. The blue markers (data) and line (MC) refer to PF jets. Reprinted from Fig. 13 of ref. [125]. . . . .	113
6.13 Efficiency of <code>HLT_Photon36_CaloIdL_IsoVL_Photon22_CaloIdL_IsoVL</code> for offline selected leading photon (left) and trailing photon (right) vs. photon $p_T$ . Reprinted from Fig. 2 of ref. [116]. . . . .	116

6.14 $(TS4 - TS5)/(TS4 + TS5)$ vs. $TS4 + TS5$ for a minimum bias sample. HB/HE hits are considered noisy if they lie in the sparsely populated gray region labeled "NOISE" defined by the curved red lines. Adapted from ref. [133]. . . . .	119
6.15 Tag and probe invariant mass fits for $15 \text{ GeV} \leq \text{probe } E_T < 20 \text{ GeV}$ . Errors are statistical only. The tag-pass fit is shown in green in the upper-left-hand plot, the tag-fail fit in red in the upper-right-hand plot, and a fit to both samples in blue in the lower-left-hand plot. Dotted lines are the background components of the fits; solid lines are signal plus background. . . . .	125
6.16 Tag and probe invariant mass fits for $-0.25 \leq \text{probe } \eta < -0.5$ . Errors are statistical only. The tag-pass fit is shown in green in the upper- left-hand plot, the tag-fail fit in red in the upper-right-hand plot, and a fit to both samples in blue in the lower-left-hand plot. Dotted lines are the background components of the fits; solid lines are signal plus background. . . . .	126
6.17 Dependence of the photon ID efficiency scale factor on some kinematic variables. Errors are statistical only. . . . .	127
6.18 Dependence of the photon ID efficiency scale factor on the number of primary vertices per event. Errors are statistical only. . . . .	128
7.1 Representative Feynman diagrams of some QCD backgrounds to the GGM SUSY search. . . . .	132
7.2 Representative Feynman diagrams of some electroweak backgrounds to the GGM SUSY search. . . . .	133

7.3	$H_T$ , defined as the scalar sum of corrected jet $E_T$ for jets defined as in Table 7.2. $\gamma\gamma$ is in black, $ee$ ( $81 \text{ GeV} \leq m_{ee} < 101 \text{ GeV}$ ) is in red, and $ff$ is in blue. The $ee$ and $ff$ distributions are normalized to the number of events in the $\gamma\gamma$ distribution. Errors are statistical only. . . . .	136
7.4	Number of jets per event for jets defined as in Table 7.2. $\gamma\gamma$ is in black, $ee$ ( $81 \text{ GeV} \leq m_{ee} < 101 \text{ GeV}$ ) is in red, and $ff$ is in blue. The $ee$ and $ff$ distributions are normalized to the number of events in the $\gamma\gamma$ distribution. Errors are statistical only. . . . .	137
7.5	$\mathcal{H}_T$ , defined as the magnitude of the negative vectorial sum of corrected jet $E_T$ for jets defined as in Table 7.2. $\gamma\gamma$ is in black, $ee$ ( $81 \text{ GeV} \leq m_{ee} < 101 \text{ GeV}$ ) is in red, and $ff$ is in blue. The $ee$ and $ff$ distributions are normalized to the number of events in the $\gamma\gamma$ distribution. Errors are statistical only. . . . .	138
7.6	Corrected $E_T$ for the jet with the largest corrected $E_T$ per event, for jets defined as in Table 7.2 (excluding the $p_T$ requirement). $\gamma\gamma$ is in black, $ee$ ( $81 \text{ GeV} \leq m_{ee} < 101 \text{ GeV}$ ) is in red, and $ff$ is in blue. The $ee$ and $ff$ distributions are normalized to the number of events in the $\gamma\gamma$ distribution. Errors are statistical only. . . . .	139
7.7	$\rho$ (average pileup energy density in the calorimeters per unit $\eta \cdot \phi$ , cf. Sec. 6.1.1). $\gamma\gamma$ is in black, $ee$ ( $81 \text{ GeV} \leq m_{ee} < 101 \text{ GeV}$ ) is in red, and $ff$ is in blue. The $ee$ and $ff$ distributions are normalized to the number of events in the $\gamma\gamma$ distribution. Errors are statistical only. . . . .	140
7.8	Number of good reconstructed primary vertices per event according to the criteria of Sec. 6.3. $\gamma\gamma$ is in black, $ee$ ( $81 \text{ GeV} \leq m_{ee} < 101 \text{ GeV}$ ) is in red, and $ff$ is in blue. The $ee$ and $ff$ distributions are normalized to the number of events in the $\gamma\gamma$ distribution. Errors are statistical only. . . . .	141

7.9 Cartoon showing the di-EM system in blue and the hadronic recoil in black. The di-EM $p_T$ (dashed blue line) is used to reweight the control sample kinematic properties to match those of the candidate $\gamma\gamma$ sample.	143
7.10 $E_T$ vs. di-EM $p_T$ . . . . .	144
7.11 $E_T$ spectra of the reweighted $ee$ ( $81 \text{ GeV} \leq m_{ee} < 101 \text{ GeV}$ ) and $ff$ control samples. Blue squares indicate di-EM $p_T$ reweighting only; red triangles indicate di-EM $p_T +$ number of jets reweighting. PF $p_T$ (cf. p. 144) is used to calculate the di-EM $p_T$ . The full normalization procedure is employed, along with $ee$ sideband subtraction (discussed at the end of this section). Error bars are statistical only. . . . .	145
7.12 Relative difference between the ECAL-only $E_T$ measurement and the PF $E_T$ measurement vs. EMF. PF $E_T$ is defined in the text. . . . .	147
7.13 Average relative difference between the ECAL-only $E_T$ measurement and the PF $E_T$ measurement vs. EMF for the leading (filled marker) and trailing (open marker) electrons in $ee$ events (red triangles), fakes in $ff$ events (blue squares), and photons in $\gamma\gamma$ events (black circles). These are nothing more than profile histograms of Fig. 7.12. PF $E_T$ is defined in the text. Error bars are statistical only. . . . .	148
7.14 $E_T$ spectra of the reweighted $ee$ ( $81 \text{ GeV} \leq m_{ee} < 101 \text{ GeV}$ ) and $ff$ control samples. Blue squares indicate reweighting using the ECAL-only $p_T$ estimate; red triangles indicate reweighting using the PF $p_T$ estimate. The full reweighting and normalization procedure is employed, along with $ee$ sideband subtraction (discussed at the end of this section). Error bars are statistical only. . . . .	149

7.15 $\cancel{E}_T$ spectra of the $ee$ ( $81 \text{ GeV} \leq m_{ee} < 101 \text{ GeV}$ ) and $ff$ control samples. Red triangles indicate full di-EM $p_T$ + number of jets reweighting; blue squares indicate no reweighting. PF $p_T$ (cf. p. 147) is used to calculate the di-EM $p_T$ . The full normalization procedure is employed, along with $ee$ sideband subtraction (discussed at the end of this section). Error bars are statistical only. . . . .	150
7.16 $ee$ sideband di-EM $p_T$ weights for events with 0, 1, or $\geq 2$ jets (as in Table 6.2). Errors are statistical only. . . . .	152
7.17 $\cancel{E}_T$ spectra of the $ee$ sample for $71 \text{ GeV} \leq m_{ee} < 81 \text{ GeV}$ (red triangles), $81 \text{ GeV} \leq m_{ee} < 101 \text{ GeV}$ (black circles), and $101 \text{ GeV} \leq m_{ee} < 111 \text{ GeV}$ (blue squares). The two sideband distributions (red and blue) and the $Z$ signal distribution (black) are normalized to the total number of $\gamma\gamma$ events. Errors are statistical only. . . . .	152
7.18 $ee$ ( $81 \text{ GeV} \leq m_{ee} < 101 \text{ GeV}$ ) (red triangles), $ff$ (blue squares), and $\gamma\gamma$ (black circles) di-EM $p_T$ spectra for events with 0, 1, or $\geq 2$ jets (as in Table 6.2). Errors are statistical only. . . . .	153
7.19 $ee$ ( $81 \text{ GeV} \leq m_{ee} < 101 \text{ GeV}$ ) and $ff$ di-EM $p_T$ weights for events with 0, 1, or $\geq 2$ jets (as in Table 6.2). Errors are statistical only. . .	154
7.20 Fits to the $ee$ and $e\gamma$ invariant mass spectra using the Crystal Ball <code>RooCMSShape</code> function described in the text and in Table 7.3. The total fit is shown in blue, while the background component is shown in red. . .	157
7.21 $f_{e\rightarrow\gamma}$ vs. electron $p_T$ and $\eta$ . . . . .	157
7.22 $\cancel{E}_T$ spectrum of the $e\gamma$ sample after scaling by $f_{e\rightarrow\gamma}$ . The total error on $f_{e\rightarrow\gamma}$ is propagated to the total error on the electroweak background estimate. . . . .	158

7.23 $E_T$ spectrum of the $e\gamma$ sample in $35 \text{ pb}^{-1}$ of 2010 LHC data scaled by the 2010 measured $f_{e \rightarrow \gamma}$ (black dots), QCD and real $Z$ predicted background from the 2010 $ee$ sample (solid orange line), MC $W + \text{jet}$ estimate (dash-dotted purple line), and MC $W\gamma$ estimate (dashed blue line). The total $e\gamma$ prediction (red band) is the sum of the $ee$ , $W + \text{jet}$ , and $W\gamma$ predictions. Reprinted from Fig. 2 of ref. [141]. . . . .	159
7.24 Average $\cancel{E}_T$ vs. di-EM $p_T$ for the $ff$ (blue squares), $ee$ (red triangles), and $\gamma\gamma$ (black circles) samples. . . . .	162
7.25 $ee$ $\cancel{E}_T$ distributions using the nominal sideband subtraction (black circles), low sideband only (red squares), and high sideband only (blue triangles). The bottom plot shows the ratio of the low sideband distribution to the nominal (red squares) and the ratio of the high sideband distribution to the nominal (blue triangles). . . . .	163
7.26 Comparison of $\cancel{E}_T$ distributions for five different di-EM $p_T$ bin definitions: uniform bins of width 10 GeV (red diamonds); uniform bins of width 50 GeV (blue downward-pointing triangles); bins with lower edges $\{0.0, 5.0, 10.0, 15.0, 20.0, 30.0, 40.0, 50.0, 60.0, 70.0, 80.0, 100.0, 750.0\}$ GeV for 0-jet events and $\{0.0, 5.0, 10.0, 15.0, 20.0, 30.0, 40.0, 50.0, 60.0, 70.0, 80.0, 100.0, 120.0, 150.0, 200.0, 700.0\}$ GeV for $\geq 1$ -jet events (magenta upward-pointing triangles), i.e. a single wide bin at high di-EM $p_T$ ; bins with lower edges $\{0.0, 5.0, 10.0, 15.0, 20.0, 30.0, 40.0, 50.0, 60.0, 70.0, 80.0, 100.0, 120.0, 150.0, 200.0\}$ GeV for 0-jet events and $\{0.0, 5.0, 10.0, 15.0, 20.0, 30.0, 40.0, 50.0, 60.0, 70.0, 80.0, 100.0, 120.0, 150.0, 200.0\}$ GeV for $\geq 1$ -jet events (green squares), i.e. the bins used in ref. [59]; and the nominal bin definitions shown in Fig. 7.19 (black circles). . . . .	164
7.27 Agreement between $\gamma\gamma$ , $ee$ , and $ff$ samples for uncorrected (red triangles) and corrected (blue squares) $\cancel{E}_T$ . . . . .	165

7.28 $\cancel{E}_T$ distribution of the $\gamma\gamma$ search sample (black circles) along with the predicted $\cancel{E}_T$ distributions of the QCD and electroweak backgrounds (blue band for $ee$ QCD prediction + electroweak prediction, purple band for $ff$ QCD prediction + electroweak prediction). The electroweak background prediction is shown in green. The bottom plots show the ratio of the $\gamma\gamma \cancel{E}_T$ distribution to the $ee + e\gamma$ background distribution (blue) and $ff + e\gamma$ background distribution (purple). . . . .	169
7.29 $\cancel{E}_T$ distribution of the $\gamma\gamma + \geq 1$ jet search sample (black circles) along with the predicted $\cancel{E}_T$ distributions of the QCD and electroweak backgrounds (blue band for $ee$ QCD prediction + electroweak prediction, purple band for $ff$ QCD prediction + electroweak prediction). The electroweak background prediction is shown in green. The bottom plots show the ratio of the $\gamma\gamma \cancel{E}_T$ distribution to the $ee + e\gamma$ background distribution (blue) and $ff + e\gamma$ background distribution (purple). . . . .	170
8.1 Next to leading order cross sections for the three different MC scenarios described in the text. . . . .	175
8.2 Signal acceptance $\times$ efficiency (defined in the text) for the three different scenarios described in Sec. 8.1. . . . .	177
8.3 Cross section upper limits for the three different scenarios described in Sec. 8.1. . . . .	187
8.4 Diagram of the points (red squares) used in the estimation of an upper limit when a computational failure occurs (middle white square). . . . .	188
8.5 Exclusion contours for the three different scenarios described in Sec. 8.1.189	

## List of Tables

3.2 Gauge supermultiplets of the supersymmetric Standard Model. Adapted from Table 1.2 of ref. [20]. . . . .	19
6.1 Selection criteria for photons and fakes. “Pixel seed,” $I_{\text{comb}}$ , and $\sigma_{i\eta i\eta}$ are defined in the text. . . . .	102
6.2 Definition of HB/HE hadronic jets. . . . .	112
6.3 HLT paths triggered by the $\gamma\gamma$ , $e\gamma$ , $ee$ , and $ff$ samples, by run range. No triggers are prescaled. . . . .	115
6.4 Candidate photon ID requirements. . . . .	121
6.5 Tag and probe criteria. The superscript 0.4 indicates that the isolation variable was calculated in a cone of $\Delta R = 0.4$ around the photon candidate. The isolations without superscripts use the standard $\Delta R = 0.3$ cones. . . . .	122
6.6 Parameter values (parameter definitions are in the text) for the signal and background PDFs for the different samples. The background PDF applies to all efficiency bins except the four lowest $E_T$ bins, which use a floating <code>RooCMSShape</code> background. When a bracketed range is given, the parameter is allowed to float within that range. When a constant is given, the parameter is fixed to that constant. . . . .	124
7.1 Selection criteria for $\gamma\gamma$ , $e\gamma$ , $ee$ , and $ff$ events. . . . .	130
7.2 Definition of HB/HE/HF hadronic jets. . . . .	142
7.3 Parameter values for the signal and background PDFs for the $ee$ and $e\gamma$ samples. When a bracketed range is given, the parameter is allowed to float within that range. When a constant is given, the parameter is fixed to that constant. . . . .	156
7.4 Errors on the $ee$ QCD background prediction as a fraction of the $ee$ prediction. . . . .	166

7.5 Errors on the $ff$ QCD background prediction as a fraction of the $ff$ prediction. . . . .	167
7.6 Errors on the $e\gamma$ electroweak background prediction as a fraction of the $e\gamma$ prediction. . . . .	167
7.7 Errors on the total QCD + electroweak background prediction as a fraction of the total prediction. . . . .	168
7.8 Observed numbers of two-photon events, $ee$ and $ff$ background estimates and their errors, and expected numbers of two-photon events from two representative GGM SUSY models (details of MC simulation given in Chapter 8) for the $\cancel{E}_T$ bins used in the search. The $ee$ estimate is shown for comparison; the $ff$ estimate is the official result used in the interpretation. Errors on the background estimates are detailed in Tables 7.4, 7.5, 7.6, and 7.7. Errors on the expected numbers of GGM events are purely statistical. . . . .	168
7.9 Observed numbers of two-photon + $\geq 1$ -jet events, $ee$ and $ff$ background estimates and their errors, and expected numbers of two-photon + $\geq 1$ -jet events from two representative GGM SUSY models (details of MC simulation given in Chapter 8) for the $\cancel{E}_T$ bins used in the search. The $ee$ estimate is shown for comparison; the $ff$ estimate is the official result used in the interpretation. Errors on the background estimates are detailed in Tables 7.4, 7.5, 7.6, and 7.7. Errors on the expected numbers of GGM events are purely statistical. . . . .	171

## Acknowledgements

This thesis would have been simply impossible without the dedicated efforts of the Large Hadron Collider accelerator team. I would like to acknowledge the excellent performance of the machine and thank the men and women who worked so hard to build and run it. Along the same lines, I would also like to thank all the members of the Compact Muon Solenoid collaboration who put in the sweat required to realize the full potential of this amazing detector. The result arrived at in this thesis is just the last step in a chain of collaborative efforts.

A critical part of my graduate physics education came from working on the installation and commissioning of the electromagnetic calorimeter endcaps. Special thanks go out to Dave Cockerill, Ken Bell, and Nicolo' Cartiglia for their extraordinary leadership and mentorship. While working on the LED system software, I frequently sought the advice of Philippe Gras, who was always patient and helpful.

The RA3 analysis group has served simultaneously as a source of new ideas, a sounding board for my own conclusions, and a motivator. Manfred Paulini, Dave Mason, and Mike Hildreth provided the organizational leadership needed to bring our results to a wider audience, for which I thank them enormously. I would not have a completed analysis today if it weren't for countless discussions with my fellow RA3 graduate students: Bernadette Heyburn, Robert Stringer, Michael Balazs, Yueh-Feng Liu, and especially Dave Morse and Brian Francis. Thanks for the insights, the availability, and the lines of code.

The University of Virginia high energy physics group has been an intellectually stimulating home for me these last six years. First and foremost, I have to thank my advisor Brad Cox for his direction and motivation. He has given me many golden opportunities to participate in the building of the detector, and encouraged me in an analysis effort that has proved to be extremely academically rewarding. Of course, I might have blown all of these opportunities without the mentorship and exceptional

patience of Sasha Ledovskoy. I would like to thank Sasha for guiding me through the LED and endcaps work, for introducing me to the analysis software, and for always finding time to answer my questions. As for the LED work, I must thank Mike Arenton for his technical ability.

One of the most fun and unusual projects I got to work on at UVa was the 4 T magnet. For his enduring work ethic and attention to detail, I thank Al Tobias. Without his expertise we were doomed. My other partner in crime at Maggie's Farm was Dave Phillips, who was also my first HEP lab guru and a good friend. Thanks also to Chris Neu and Bob Hirosky, who, as well as being expert physicists and wonderful teachers, were great fun to be around.

My life in Charlottesville and at CERN has been enriched indescribably by the friends that I made. They are no small part of the reason I'm in this field. Thanks to Sean Lynch, Jamie Antonelli, Jeff Kolb, Doug Berry, Sarah Boutle, Anna Woodard, Tessa Pearson, Jason Slaunwhite, and honorary member Kat Morse of Bldg. 512; Florian Hirsch, Max Scherzer, Heather Gray, Emma Fauss, and Me Linh Jones, my roommates at one time or another; Jirakan Nunkaew and Nick Kvaltine for the fun times in Charlottesville; Justin Griffiths, who might as well be a roommate; Orin Harris for tennis, tuna, and much more; and Toyoko Orimoto, who throws the best parties in Geneva.

None of this would have been possible without the love and support of my family. Their enthusiasm for my enthusiasm about the Large Hadron Collider has never wavered. Finally, my deepest thanks go to Ted Kolberg, who has always been on my side.

# Chapter 1

## Introduction

Although the Standard Model of particle physics has passed every experimental test to date, it leaves some very fundamental questions unanswered. Why do particles have mass? Why are their masses so different? Up to what energy scale is the Standard Model a valid description of nature? Many competing theories have been proposed to answer these questions. Establishing the existence of any one of them requires careful searches for deviations from Standard Model predictions of particle production or decay rates. The stellar performance of the Large Hadron Collider, the 7 TeV center-of-mass energy proton collider located at the European Organization for Nuclear Research (CERN) in Geneva, Switzerland, presents a golden opportunity to do such a search for evidence of new physical phenomena.

One nearly universal prediction of theories of physics beyond the Standard Model is that at a high enough collision energy, heavy particles introduced by the new theory will be produced. The heavy particles will then decay, leading to distinctive signatures in the hermetic detectors that completely surround the collision points. By comparing the observed rate of processes with a particular signature to the expected rate from the Standard Model alone, the existence of a particular theory of new physics can be confirmed or ruled out.

This thesis presents a search for evidence of new heavy particles decaying to a final state with two photons, jets, and a striking momentum imbalance that implies the existence of a new kind of particle that can easily pass through matter without leaving a trace. The signature is motivated by theories that incorporate supersymmetry, a new symmetry of nature that predicts supersymmetric antiparticles to the known particles, just as charge symmetry predicts a positively charged antiparticle for every negatively charged particle and vice versa. Supersymmetry can provide answers to some of the questions posed in the first paragraph: it predicts unification of all fundamental forces at a specific energy scale and explains the Standard Model mechanism for endowing particles with mass. Furthermore, it may also predict a source of astrophysical dark matter. Besides its theoretical motivation, the choice of signature is also driven by the low rate of expected Standard Model background.

The search is performed at the Compact Muon Solenoid experiment, a detector capable of identifying photons, electrons, muons, quark jets,  $\tau$  leptons, and momentum imbalances with high efficiency. The central feature of the experiment is a superconducting solenoid, which, at a length of 13 m and a diameter of 7 m [1], is one of the largest superconducting magnets ever built. By bending the paths of charged particles in the final state under the Lorentz force, the magnetic field produced by the solenoid allows charged particle momenta to be accurately measured. Highly granular calorimeters sit inside the solenoid for the purpose of measuring the energy of neutral final state particles.

This thesis is organized as follows. Chapters 2 and 3 motivate the search for physics beyond the Standard Model and the specific signature of two photons, as well as give an overview of the Standard Model and supersymmetric theoretical frameworks. A description is given of the Large Hadron Collider in Chapter 4 and the Compact Muon Solenoid detector in Chapter 5. Chapters 6 and 7 explain in detail the experimental techniques used in the search. Chapter 6 shows how collisions that are likely to have

produced a new particle are selected from the enormous amount of data collected, then Chapter 7 shows the data analysis in detail and presents the results. An interpretation of the results in terms of new physics models is given in Chapter 8. Finally, the thesis is concluded in Chapter 9.

## Chapter 2

# Motivation for Physics Beyond the Standard Model

In the 1960s, Sheldon Glashow, Steven Weinberg, and Abdus Salam proposed a mathematical framework that unified the electromagnetic and weak forces at an energy scale in the hundreds of GeV/c, as well as a mechanism for breaking the electroweak symmetry at low energies [2–6]. At the same time, Murray Gell-Mann introduced the concept of quarks to describe hadron spectroscopy, a concept that would later grow into quantum chromodynamics (QCD), the full theory of the strong force [7, 8]. These two key developments motivated the unified representation of particle physics as a set of fields whose dynamics are invariant under the Standard Model (SM) gauge group

$$SU(3)_C \otimes SU(2)_L \otimes U(1)_Y \quad (2.1)$$

where  $SU(3)_C$  describes the quark QCD interactions,  $SU(2)_L$  describes the weak interactions among quarks and leptons, and  $U(1)_Y$  describes the electromagnetic interaction.

The Standard Model has been an extremely successful predictor of particle production mechanisms and the relationships between interaction cross-sections and de-

decay rates, as well as of the exact relationship between the masses of the electroweak force carriers and the electroweak couplings. The case for the validity of the Standard Model was bolstered by the many precision QCD and electroweak measurements carried out at the Large Electron-Positron (LEP) collider, which ran from 1989-2000 at center-of-mass energies between 65 and 104 GeV/ $c$  [9]. Figure 2.1 shows some of the highlights of the LEP program. Figure 2.1(a) shows the decay width of the  $Z$  boson, which established with high precision the existence of only three families of quarks and leptons. Figure 2.1(b) shows the measured and predicted cross sections of  $e^+e^- \rightarrow q\bar{q}$ ,  $e^+e^- \rightarrow \mu^+\mu^-$ , and  $e^+e^- \rightarrow \tau^+\tau^-$ . The data agree very well with the Standard Model prediction. This result confirms lepton universality (the  $\mu^+\mu^-$  and  $\tau^+\tau^-$  cross sections are the same) and the expected amplitude of hadron production with respect to lepton production. Figure 2.1(c) shows the measured and predicted  $W^+W^-$  cross section. The fact that the data prefer the prediction that includes the  $ZW^+W^-$  vertex lends further support to the correctness of the Standard Model. Finally, the running of the strong coupling constant with energy is shown in Figure 2.1(d), corroborating the predictions of SM renormalization.

However, there are still deep problems with the Standard Model, stemming from the introduction of the Higgs scalar into the theory to break electroweak symmetry [10–12]. Since the Higgs self-energy diagram diverges as the square of the ultraviolet cutoff scale, and assuming that there are no new important energy scales of physics between the weak scale ( $\mathcal{O}(10^2 \text{ GeV}/c)$ ) and the Planck scale ( $\mathcal{O}(10^{19} \text{ GeV}/c)$ ), in order to be consistent with experimental measurements, this diagram must include a remarkable 17-orders-of-magnitude cancellation that is otherwise poorly motivated [13]. The quest to find new physics at an intermediate energy scale between the weak and Planck scales, and thus extend the Standard Model, was the driving force behind the construction of the Large Hadron Collider (LHC) in 2009, the world’s highest energy particle accelerator to date.

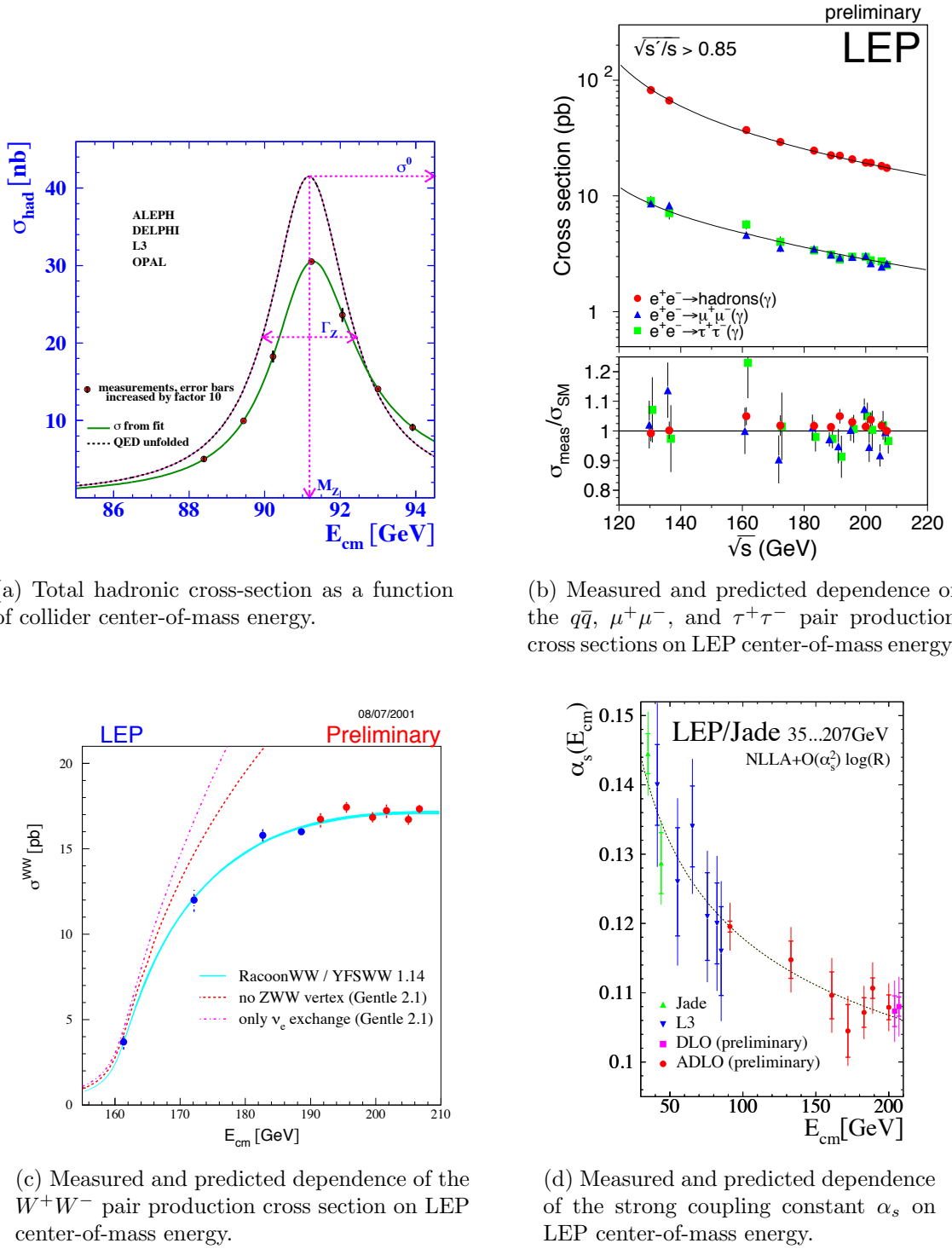


Figure 2.1: Selected LEP measurements demonstrating its contribution to the precise understanding of the Standard Model. Reprinted from ref. [9].

Section 2.1 of this chapter gives a brief overview of the Standard Model and electroweak symmetry breaking. Sections 2.2 and 2.3 examine the issues raised by electroweak symmetry breaking that the Standard Model is as yet ill-prepared to address.

## 2.1 The Standard Model and Electroweak Symmetry Breaking

All of the elementary matter particles (fermions)—quarks, charged leptons, and neutrinos—can be put in fundamental representations of the SM gauge groups. The fermion content of the Standard Model is summarized in Table 2.1. The left-handed doublets are analogous to the spinors of non-relativistic quantum mechanics, with the  $z$  component of “weak isospin”  $I_3$  equal to  $+1/2(-1/2)$  for the upper(lower) component of the doublet.

There are two types of weak interactions: flavor-changing charged currents, in which an up-type and down-type quark or charged lepton and neutrino couple to a charged  $W$ , and neutral currents, in which a fermion couples to another of the same flavor and to a neutral  $Z$ . The charged current interaction is maximally parity violating—it only couples left-handed fermion doublets. The neutral current interaction has a term coupling left-handed doublets and a term coupling right-handed singlets. There are no mass terms of the form  $m_f^2(f_L\bar{f}_R + f_R\bar{f}_L)$  in the electroweak part of the Lagrangian, as these would violate gauge invariance [14]. The simplest way to link the left-handed and right-handed fermions is via a Yukawa interaction  $-\xi [\bar{f}_R(\phi^\dagger f_L) + (\bar{f}_L\phi)f_R]$  where  $\phi$  is a doublet of complex scalar fields [14].

The fermion interaction part of the Lagrangian is [14]

Table 2.1: Fermion content of the Standard Model. In the third column, the first number refers to the supermultiplet representation under  $SU(3)_C$  (e.g. **3** means it has color charge and feels QCD), the second number refers to the representation under  $SU(2)_L$  (e.g. **2** means it has weak isospin and feels the weak interaction), and the third number is the value of the hypercharge. A bar over a number refers to the adjoint representation. **1** means that the supermultiplet is not charged under that group, and thus does not feel the associated force (for example, the right-handed fermion singlets do not feel the weak interaction).

Type	Notation	Representation under $SU(3)_C \otimes SU(2)_L \otimes U(1)_Y$	Couples to
Left-handed quark doublet	$\begin{pmatrix} u_L \\ d_L \\ c_L \\ s_L \\ b_L \\ t_L \end{pmatrix}$	( <b>3</b> , <b>2</b> , $\frac{1}{6}$ )	$g, W, Z, \gamma$
Right-handed up-type quark singlet	$\begin{pmatrix} u_R^\dagger \\ c_R^\dagger \\ b_R^\dagger \end{pmatrix}$	( $\bar{\mathbf{3}}$ , <b>1</b> , $-\frac{2}{3}$ )	$g, \gamma$
Right-handed down-type quark singlet	$\begin{pmatrix} d_R^\dagger \\ s_R^\dagger \\ t_R^\dagger \end{pmatrix}$	( $\bar{\mathbf{3}}$ , <b>1</b> , $\frac{1}{3}$ )	$g, \gamma$
Left-handed lepton doublet	$\begin{pmatrix} \bar{\nu}_{eL} \\ e_L \\ \bar{\nu}_{\mu L} \\ \mu_L \\ \bar{\nu}_{\tau L} \\ \tau_L \end{pmatrix}$	( <b>1</b> , <b>2</b> , $-\frac{1}{2}$ )	$W, Z, \gamma^a$
Right-handed charged lepton singlet	$\begin{pmatrix} e_R^\dagger \\ \mu_R^\dagger \\ \tau_R^\dagger \end{pmatrix}$	( $\bar{\mathbf{1}}$ , <b>1</b> , 1)	$\gamma$

<sup>a</sup>Except for neutrinos, which have zero electric charge.

$$\begin{aligned}\mathcal{L}_{\text{int}} &= \bar{f}_R i\gamma^\mu (\partial_\mu + i\frac{g_Y}{2} A_\mu Y) f_R \\ &\quad + \bar{f}_L i\gamma^\mu (\partial_\mu + i\frac{g_Y}{2} A_\mu Y + i\frac{g_L}{2} \vec{\tau} \cdot \vec{b}_\mu) f_L\end{aligned}\quad (2.2)$$

where  $g_Y$  and  $g_L$  are the electromagnetic and weak coupling constants, respectively;  $Y$  is the weak hypercharge;  $A_\mu$  is the EM gauge field;  $\vec{b}_\mu$  is a three-component vector of weak gauge fields; and  $\vec{\tau}$  is a three-component vector of the three Pauli matrices. Before electroweak symmetry breaking, the three weak gauge fields and the one EM gauge field are massless. The three weak gauge fields correspond to the three generators (the Pauli matrices) of  $SU(2)_L$ . The one EM gauge field corresponds to the one generator (the real scalar  $Y$ ) of  $U(1)_Y$ , where  $Y = 2(Q - I_3)$  ( $Q$  is electric charge). For the  $SU(3)_C$  part of the Lagrangian, there are eight massless gauge fields (the gluons) corresponding to the eight generators of  $SU(3)_C$  (the Gell-Mann matrices).

To break the electroweak symmetry implicit in the massless gauge bosons, a doublet of complex scalar fields (the Higgs) is introduced. It has a potential [14]

$$V(\phi^\dagger \phi) = \mu^2 \phi^\dagger \phi + |\lambda| (\phi^\dagger \phi)^2. \quad (2.3)$$

Since  $\mu^2 < 0$ , the potential has the shape of a sombrero, as shown in Figure 2.2. At the minimum of the potential, the scalar fields are not zero, but have some positive vacuum expectation value (VEV) (it can be chosen such that one component is zero and the other is  $\sqrt{-\mu^2/2|\lambda|}$ ). Nature spontaneously chooses one of the infinitely many vacua along the circle of minimum  $V$  in  $(\Re[\phi], \Im[\phi])$  space.

Expanding  $\phi$  about its VEV  $v$  in the Lagrangian introduces one massive scalar, the Higgs, and new mass terms for the gauge bosons. However, the terms with positive mass are not the original  $b_1$ ,  $b_2$ ,  $b_3$ , and  $A$  (spacetime indices dropped), but the

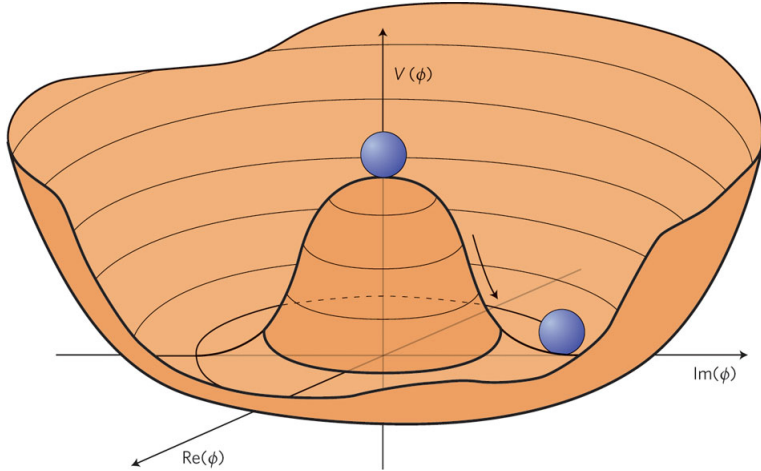


Figure 2.2: Higgs potential (the sombrero) as a function of the real and imaginary parts of the complex scalar field. The movement of the balls shows that the symmetry  $\phi = 0$  is spontaneously broken, the stable vacuum state of nature being somewhere along the circle of minimum potential. Reprinted from Fig. 1 of ref. [15].

observable  $W^\pm$  and  $Z^0$ . The  $W^\pm$  are linear combinations of  $b_1$  and  $b_2$ . The  $Z^0$  is one of the linear combinations of  $b_3$  and  $A$ , the other being the massless photon  $\gamma$ . After electroweak symmetry breaking (EWSB), the only remaining symmetry of the vacuum is electric charge, because the value of the electric charge operator acting on the Higgs VEV is zero. As expected, there is one massless photon in the SM to reflect this symmetry. The SM fermions can also acquire masses as a by-product of the Higgs mechanism via Yukawa terms.

## 2.2 Implications of the Higgs Mechanism

Before the formulation of the Higgs mechanism, physicists suspected that a heavy boson mediated the weak force from observations of  $\beta$  decay, but had no way of putting a mass term into the Lagrangian without breaking gauge symmetry. The Higgs mechanism of EWSB provided a way to generate masses for the  $SU(2)_L$  gauge bosons. Furthermore, it predicted the  $W$  and  $Z$  masses in terms of  $g_L$ ,  $g_Y$ , and  $v$ .  $g_L$  and  $g_Y$  could be measured in scattering experiments, and in 1983 the  $W$  and  $Z$  were

first observed at the Super Proton-Antiproton Synchrotron (Sp $\bar{p}$ S) at the European Organization for Nuclear Research (CERN) in Geneva, Switzerland [16, 17]. Crucially, the values of the coupling constants and the gauge boson masses predict that the Higgs VEV should be 246 GeV, so the Higgs mass should not be too much different than that if  $\lambda$  is to remain small enough to do perturbation theory [18].

The Higgs mechanism raises some interesting questions that cannot be immediately answered by SM physics. First of all, why should  $\mu^2$  be negative? The form of the Higgs potential given in Eq. 2.3 is about the simplest renormalizable form that can be written for a scalar field, but the choice of  $\mu^2 < 0$  is completely arbitrary. Second, how can the hierarchy problem be avoided?

The Higgs mass squared receives one-loop corrections from all the particles it couples to; namely, all particles with mass. Because the Higgs is a scalar particle, one-loop corrections are proportional to  $\Lambda_{\text{UV}}^2$ , where  $\Lambda_{\text{UV}}$  is the ultraviolet cutoff energy of the loop integral.  $\Lambda_{\text{UV}}$  can be interpreted as the energy at which the SM can no longer describe particle physics and non-SM physics takes over. Ideally,  $\Lambda_{\text{UV}}$  is something like the Planck scale. However, taking  $\Lambda_{\text{UV}} = M_{\text{Planck}}$  implies that in order to keep the Higgs mass of order a few hundred GeV, as required by experimental tests of EWSB, a very large and precise counterterm must be applied at all orders in perturbation theory to the bare  $m_H^2$ . The quadratic sensitivity of the Higgs mass to the cutoff scale and the extremely fine-tuned counterterms it necessitates is called the hierarchy problem. SM fermions do not experience this problem because chiral symmetry prevents explicit fermion mass terms at any order, so by dimensional analysis, fermion masses can only be sensitive to  $\ln \frac{\Lambda_{\text{UV}}}{\Lambda_{\text{other}}}$ .

One of the most elegant ways to address these problems is to incorporate *supersymmetry* (SUSY) into the SM. Supersymmetry is new fundamental symmetry of nature between bosons and fermions, and will be discussed more thoroughly in Chapter 3. The next section just briefly describes how supersymmetry can mitigate some

of the problems of the Higgs mechanism.

## 2.3 Addressing Problems of the Standard Model with Supersymmetry

As in the ordinary Standard Model, the couplings and masses in supersymmetric theory can be imposed at the supersymmetric scale and evolved down to the weak scale by use of renormalization group equations. For many typical supersymmetric scenarios (like the one shown in Figure 2.3),  $\mu^2$  is positive at the supersymmetric scale but runs negative at the weak scale, leading to precisely the conditions needed for EWSB. This is a consequence of the fact that the evolution of  $m_H^2$  depends on the top quark Yukawa coupling, which, since the top is very heavy compared to the other quarks ( $m_t \sim 42m_b$ ,  $m_t \sim 136m_c$  [19]), is large. In some sense, then, supersymmetry not only provides the conditions for EWSB, but also explains why the top quark must be so much heavier than the other quarks.

SUSY's greatest strength, however, comes from the way it elegantly solves the hierarchy problem. The Higgs squared mass corrections from fermion loops take the form [20]

$$\Delta m_H^2 = -\frac{|\lambda_F|^2}{8\pi^2} \Lambda_{\text{UV}}^2 + \dots \quad (2.4)$$

while the corrections from scalar loops would take the form [20]

$$\Delta m_H^2 = \frac{|\lambda_S|^2}{16\pi^2} \Lambda_{\text{UV}}^2 + \dots \quad (2.5)$$

where the ellipsis indicates terms proportional to  $\ln \Lambda_{\text{UV}}$  that do not pose a prob-

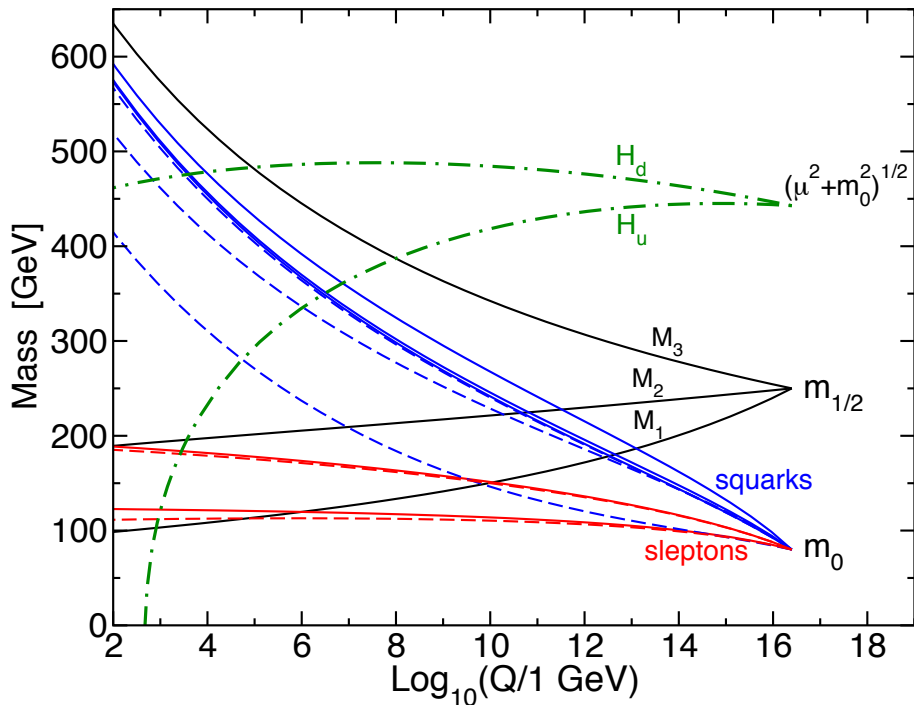


Figure 2.3: Predicted evolution of the free parameters of supersymmetry as a function of renormalization scale for a representative set of SUSY parameters. Note the dash-dotted line marked “ $H_u$ ” that goes negative at  $\sim 1$  TeV; this indicates  $\mu^2$  running negative. Reprinted from Fig. 7.4 of ref. [20].

lem for the validity of the SM up to the Planck scale. Since the fermion and scalar contributions have opposite signs, if each SM fermion were accompanied by two as-yet-undiscovered real scalar fields with  $\lambda_S = |\lambda_F|^2$ , then the problematic quadratic terms in Eqs. 2.4 and 2.5 would exactly cancel. This is precisely the foundation of supersymmetry: for each fermion, there is a supersymmetric partner complex scalar boson.<sup>1</sup> This would remove the hierarchy problem altogether, and is the main reason physicists are eager to find evidence for the existence of supersymmetry at the LHC.

In addition to providing some rationale for the Higgs mechanism, SUSY makes two other very desirable predictions. The first is that the strong, weak, and electromagnetic coupling constants will exactly unify at an energy scale of  $10^{16}$  GeV/ $c$ , as shown in Figure 2.4. Unification of forces is not required by any experimental consideration, but is an elegant result nonetheless. The second prediction of SUSY, explained in more detail in Sec. 3.5, is the existence of a new stable and electrically neutral particle, undiscovered as of yet because of its extremely feeble (i.e. weak or gravitational) interactions with ordinary matter. This particle might be what astronomers have observed as dark matter. In fact, regardless of any theory, searches for evidence of dark matter at colliders are well motivated by suggestions from astronomy that some or all of the dark matter should have a mass at the weak scale [21].

Everything discussed in this chapter assumes that the Higgs mechanism is indeed the origin of EWSB. It is important to remember that no experimental observation to date unequivocally establishes the existence of the Higgs scalar, although some activity recently unearthed in the LHC data [22, 23] tentatively suggest a Higgs mass of  $\sim 125$  GeV. The discovery of the Higgs scalar would place an important restriction on the types of SUSY theories that might be consistent with experiment. Operating at a 7 TeV center-of-mass energy, the LHC can thoroughly probe the scale of EWSB and the expected mass range of the Higgs, as well as the mass range of

---

<sup>1</sup>The two real scalar fields combine to form one complex scalar field.

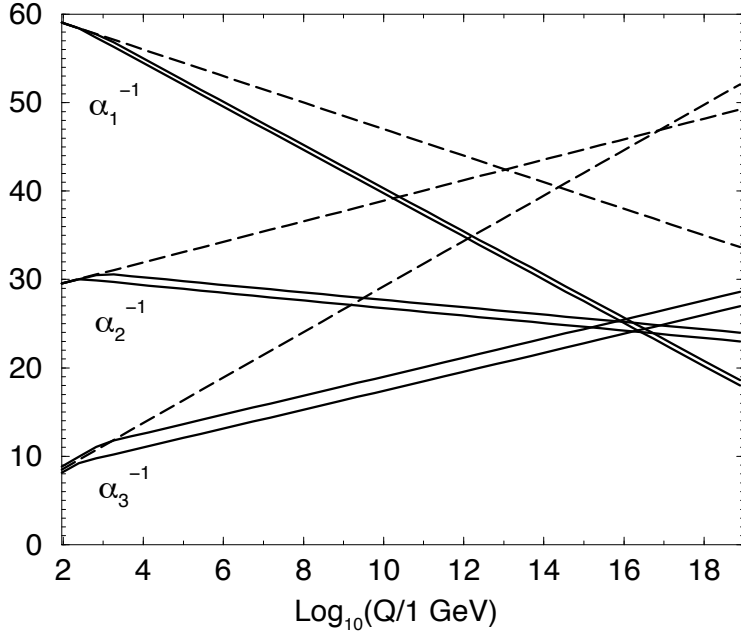


Figure 2.4: Inverse gauge couplings as a function of renormalization scale for the Standard Model assumption (dotted lines) and the SUSY assumption (solid lines; the double lines represent variations in SUSY parameters and in  $\alpha_S(m_Z)$ ). Reprinted from Fig. 5.8 of ref. [20].

supersymmetric particles if SUSY is indeed the solution to the hierarchy problem and the light Higgs is found. Therefore, discovering or excluding SUSY is a key goal of the LHC physics program. The next chapter discusses SUSY more formally and shows what phenomenological consequences it entails.

# Chapter 3

## The Supersymmetric Extension to the Standard Model

The following introduction to SUSY focuses primarily on the aspects of the formalism that are relevant to phenomenology. In particular, most of the details of SUSY breaking (about which there is little theoretical consensus) are omitted, except where they are relevant to experiment. The notation is similar to that used in refs. [13] and [20], and much of the information presented is culled from those references.

### 3.1 Supermultiplet Representation

The Standard Model is extended to include supersymmetry by the introduction of a supersymmetry transformation that takes fermionic states to bosonic states and vice versa. The resulting model is called the *supersymmetric Standard Model*. In analogy with the known symmetries of the Standard Model, the SUSY transformation has associated generators that obey defining commutation and anticommutation relations, and a fundamental representation. All SM particles and their *superpartners* fall into one of two *supermultiplet* representations. Using the property of SUSY that

$$n_F = n_B, \quad (3.1)$$

where  $n_F$  is the number of fermionic degrees of freedom per supermultiplet and  $n_B$  is the number of bosonic degrees of freedom, the two types of supermultiplets are

1. *Chiral supermultiplets*: Weyl fermions (two helicity states  $\Rightarrow n_F = 2$ ) associated with complex scalar fields (with two real components  $\Rightarrow n_B = 2$ )
2. *Gauge supermultiplets*: Spin-1 vector bosons (two helicity states  $\Rightarrow n_B = 2$ ) associated with Weyl fermions (two helicity states  $\Rightarrow n_F = 2$ )

In the gauge supermultiplet, the vector boson is assumed massless (i.e. before EWSB generates a mass for it). Since the superpartners to the SM particles have not yet been discovered, they must be significantly heavier than their SM counterparts. Unbroken SUSY predicts that the SM particles and their superpartners must have exactly the same mass, so ultimately a mechanism for SUSY breaking, in addition to EWSB, must be introduced to generate masses for the superpartners (see Sec. 3.3). Tables 3.1 and 3.2 show the chiral and gauge supermultiplets of the supersymmetric Standard Model, respectively. Note that the scalar partners to the SM fermions are denoted by placing an “s” in front of their names, while the chiral fermion partners to the SM gauge bosons are denoted by appending “ino” to their names.

## 3.2 The Unbroken SUSY Lagrangian

The first piece of the full unbroken SUSY Lagrangian density consists of the kinetic and interacting terms related to the chiral supermultiplets. As explained in Sec. 3.1, a chiral supermultiplet consists of Weyl fermions  $\psi$  (the ordinary fermion) and complex scalars  $\phi$  (the sfermion). For a collection of such chiral supermultiplets, the Lagrangian is

Table 3.1: Chiral supermultiplets of the supersymmetric Standard Model. In the last column, the first number refers to the supermultiplet representation under  $SU(3)_C$  (e.g. **3** means it has color charge and feels QCD), the second number refers to the representation under  $SU(2)_L$  (e.g. **2** means it has weak isospin and feels the weak interaction), and the third number is the value of the hypercharge. A bar over a number refers to the adjoint representation. **1** means that the supermultiplet is not charged under that group, and thus does not feel the associated force (for example, the right-handed fermion singlets do not feel the weak interaction). Adapted from Table 1.1 of ref. [20].

Type of supermultiplet	Notation	Spin-0 component	Spin-1/2 component	Representation under $SU(3)_C \otimes SU(2)_L \otimes U(1)_Y$
Left-handed quark/squark doublet ( $\times 3$ families)	$Q$	$(\tilde{u}_L \tilde{d}_L)$	$(u_L d_L)$	$(\mathbf{3}, \mathbf{2}, \frac{1}{6})$
Right-handed up-type quark/squark singlet ( $\times 3$ families)	$\bar{u}$	$\tilde{u}_R^*$	$u_R^\dagger$	$(\overline{\mathbf{3}}, \mathbf{1}, -\frac{2}{3})$
Right-handed down-type quark/squark singlet ( $\times 3$ families)	$\bar{d}$	$\tilde{d}_R^*$	$d_R^\dagger$	$(\overline{\mathbf{3}}, \mathbf{1}, \frac{1}{3})$
Left-handed lepton/slepton doublet ( $\times 3$ families)	$L$	$(\tilde{\nu}_{eL} \tilde{e}_L)$	$(\bar{\nu}_{eL} e_L)$	$(\mathbf{1}, \mathbf{2}, -\frac{1}{2})$
Right-handed lepton/slepton singlet ( $\times 3$ families)	$\bar{e}$	$\tilde{e}_R^*$	$e_R^\dagger$	$(\overline{\mathbf{1}}, \mathbf{1}, 1)$
Up-type Higgs/Higgsino doublet	$H_u$	$(H_u^+ H_u^0)$	$(\tilde{H}_u^+ \tilde{H}_u^0)$	$(\mathbf{1}, \mathbf{2}, \frac{1}{2})$
Down-type Higgs/Higgsino doublet	$H_d$	$(H_d^0 H_d^-)$	$(\tilde{H}_d^0 \tilde{H}_d^-)$	$(\mathbf{1}, \mathbf{2}, -\frac{1}{2})$

Table 3.2: Gauge supermultiplets of the supersymmetric Standard Model. Adapted from Table 1.2 of ref. [20].

Type of supermultiplet	Spin-1/2 component	Spin-1 component	Representation under $SU(3)_C \otimes SU(2)_L \otimes U(1)_Y$
Gluon/gluino	$\tilde{g}$	$g$	(8, 1, 0)
W/wino	$\widetilde{W}^\pm \widetilde{W}^0$	$W^\pm W^0$	(1, 3, 0)
B/bino	$\tilde{B}^0$	$B^0$	(1, 1, 0)

$$\begin{aligned} \mathcal{L}_{\text{chiral}} = & -\partial^\mu \phi^{*i} \partial_\mu \phi_i - V_{\text{chiral}}(\phi, \phi^*) - i\psi^{\dagger i} \bar{\sigma}^\mu \partial_\mu \psi_i - \frac{1}{2} M^{ij} \psi_i \psi_j \\ & - \frac{1}{2} M_{ij}^* \psi^{\dagger i} \psi^{\dagger j} - \frac{1}{2} y^{ijk} \phi_i \psi_j \psi_k - \frac{1}{2} y_{ijk}^* \phi^{*i} \psi^{\dagger j} \psi^{\dagger k} \end{aligned} \quad (3.2)$$

where  $i$  runs over all supermultiplets in Table 3.1,  $\bar{\sigma}^\mu$  are the negative of the Pauli matrices (except for  $\sigma^0 = \bar{\sigma}^0$ ),  $M^{ij}$  is a mass matrix for the fermions,  $y^{ijk}$  are the Yukawa couplings between one scalar and two spinor fields, and  $V_{\text{chiral}}(\phi, \phi^*)$  is the scalar potential

$$\begin{aligned} V_{\text{chiral}}(\phi, \phi^*) = & M_{ik}^* M^{kj} \phi^{*i} \phi_j + \frac{1}{2} M^{in} y_{jkn}^* \phi_i \phi^{*j} \phi^{*k} \\ & + \frac{1}{2} M_{in}^* y^{jkn} \phi^{*i} \phi_j \phi_k + \frac{1}{4} y^{ijn} y_{klm}^* \phi_i \phi_j \phi^{*k} \phi^{*l}. \end{aligned} \quad (3.3)$$

The Lagrangian can also be written as the kinetic terms plus derivatives of the *superpotential*  $W$ :

$$\begin{aligned} \mathcal{L}_{\text{chiral}} = & -\partial^\mu \phi^{*i} \partial_\mu \phi_i - i\psi^{\dagger i} \bar{\sigma}^\mu \partial_\mu \psi_i \\ & - \frac{1}{2} \left( \frac{\delta^2 W}{\delta \phi^i \delta \phi^j} \psi_i \psi_j + \frac{\delta^2 W^*}{\delta \phi_i \delta \phi_j} \psi^{\dagger i} \psi^{\dagger j} \right) - \frac{\delta W}{\delta \phi^i} \frac{\delta W^*}{\delta \phi_i} \end{aligned} \quad (3.4)$$

where

$$W = M^{ij} \phi_i \phi_j + \frac{1}{6} y^{ijk} \phi_i \phi_j \phi_k. \quad (3.5)$$

The second part of the Lagrangian involves the gauge supermultiplets. In terms of the spin-1 ordinary gauge boson  $A_\mu^a$  and the spin-1/2 Weyl spinor gaugino  $\lambda^a$  of the gauge supermultiplet, where  $a$  runs over the number of generators for the SM subgroup (i.e. 1-8 for  $SU(3)_C$ , 1-3 for  $SU(2)_L$ , and 1 for  $U(1)_Y$ ), this part of the Lagrangian is

$$\mathcal{L}_{\text{gauge}} = -\frac{1}{4} F_{\mu\nu}^a F^{\mu\nu a} - i \lambda^a \bar{\sigma}^\mu D_\mu \lambda^a + \frac{1}{2} D^a D^a \quad (3.6)$$

where

$$F_{\mu\nu}^a = \partial_\mu A_\nu^a - \partial_\nu A_\mu^a + g f^{abc} A_\mu^b A_\nu^c \quad (3.7)$$

( $g$  is the coupling constant and  $f^{abc}$  are the structure constants for the particular SM gauge group),

$$D_\mu \lambda^a = \partial_\mu \lambda^a + g f^{abc} A_\mu^b \lambda^c, \quad (3.8)$$

and  $D^a$  is an auxiliary field that is introduced as a bookkeeping tool to keep the fermionic and bosonic degrees of freedom equal both on- and off-shell. There is no kinetic term for  $D^a$  in the Lagrangian, so therefore it does not propagate or represent

any real particle. Its equation of motion, from  $\delta\mathcal{L}/\delta D^a = 0$ , yields a simple algebraic expression for  $D^a$  that can be used to eliminate it from the Lagrangian if desired.

To build a fully supersymmetric and gauge-invariant Lagrangian, the ordinary derivatives in  $\mathcal{L}_{\text{chiral}}$  (Eq. 3.2) must be replaced by covariant derivatives

$$D_\mu \phi_i = \partial_\mu \phi_i - igA_\mu^a(T^a\phi)_i \quad (3.9)$$

$$D_\mu \phi^{*i} = \partial_\mu \phi^{*i} + igA_\mu^a(\phi^*T^a)^i \quad (3.10)$$

$$D_\mu \psi_i = \partial_\mu \psi_i - igA_\mu^a(T^a\psi)_i. \quad (3.11)$$

This leads to the full Lagrangian

$$\begin{aligned} \mathcal{L} &= \mathcal{L}_{\text{chiral}} + \mathcal{L}_{\text{gauge}} \\ &\quad - \sqrt{2}g(\phi^{*i}T^a\psi_i)\lambda^a - \sqrt{2}g\lambda^{\dagger a}(\psi^{\dagger i}T^a\phi_i) + g(\phi^{*i}T^a\phi_i)D^a \\ &= -\partial^\mu \phi^{*i} \partial_\mu \phi_i - i\psi^{\dagger i} \bar{\sigma}^\mu \partial_\mu \psi_i + ig\partial^\mu \phi^{*i} A_\mu^a(T^a\phi)_i - ig\partial_\mu \phi_i A^{\mu a}(\phi^*T^a)^i \\ &\quad - g^2 A^{\mu a}(\phi^*T^a)^i A_\mu^a(T^a\phi)_i - g\psi^{\dagger i} \bar{\sigma}^\mu A_\mu^a(T^a\psi)_i - V_{\text{chiral}}(\phi, \phi^*) \\ &\quad - \frac{1}{2}M^{ij}\psi_i\psi_j - \frac{1}{2}M_{ij}^*\psi^{\dagger i}\psi^{\dagger j} - \frac{1}{2}y^{ijk}\phi_i\psi_j\psi_k - \frac{1}{2}y_{ijk}^*\phi^{*i}\psi^{\dagger j}\psi^{\dagger k} \\ &\quad - \frac{1}{4}F_{\mu\nu}^a F^{\mu\nu a} - i\lambda^{\dagger a} \bar{\sigma}^\mu \partial_\mu \lambda^a - ig\lambda^{\dagger a} \bar{\sigma}^\mu f^{abc} A_\mu^b \lambda^c + \frac{1}{2}D^a D^a \\ &\quad - \sqrt{2}g(\phi^{*i}T^a\psi_i)\lambda^a - \sqrt{2}g\lambda^{\dagger a}(\psi^{\dagger i}T^a\phi_i) + g(\phi^{*i}T^a\phi_i)D^a. \end{aligned} \quad (3.12)$$

Writing out  $F_{\mu\nu}^a$  and  $V_{\text{chiral}}(\phi, \phi^*)$  explicitly combining the  $D^a$  terms using the equation of motion  $D^a = -g\phi^{*i}T^a\phi_i$ , and rearranging some terms, the final unbroken SUSY Lagrangian is

$$\begin{aligned}
\mathcal{L} = & -\partial^\mu \phi^{*i} \partial_\mu \phi_i - i\psi^{\dagger i} \bar{\sigma}^\mu \partial_\mu \psi_i \\
& - \frac{1}{4} (\partial_\mu A_\nu^a - \partial_\nu A_\mu^a) (\partial^\mu A^{\nu a} - \partial^\nu A^{\mu a}) - i\lambda^{\dagger a} \bar{\sigma}^\mu \partial_\mu \lambda^a \\
& - M_{ik}^* M^{kj} \phi^{*i} \phi_j - \frac{1}{2} M^{ij} \psi_i \psi_j - \frac{1}{2} M_{ij}^* \psi^{\dagger i} \psi^{\dagger j} \\
& + ig \partial^\mu \phi^{*i} A_\mu^a (T^a \phi)_i - ig \partial_\mu \phi_i A^{\mu a} (\phi^* T^a)^i - g \psi^{\dagger i} \bar{\sigma}^\mu A_\mu^a (T^a \psi)_i \\
& - ig \lambda^{\dagger a} \bar{\sigma}^\mu f^{abc} A_\mu^b \lambda^c \\
& - \frac{1}{4} g f^{abc} [(\partial_\mu A_\nu^a - \partial_\nu A_\mu^a) A^{\mu b} A^{\nu c} + A_\mu^b A_\nu^c (\partial^\mu A^{\nu a} - \partial^\nu A^{\mu a})] \\
& - \frac{1}{2} M_{in}^* y^{jkn} \phi^{*i} \phi_j \phi_k - \frac{1}{2} M^{in} y_{jkn}^* \phi_i \phi^{*j} \phi^{*k} \\
& - \frac{1}{2} y^{ijk} \phi_i \psi_j \psi_k - \frac{1}{2} y_{ijk}^* \phi^{*i} \psi^{\dagger j} \psi^{\dagger k} \\
& - \sqrt{2} g (\phi^{*i} T^a \psi_i) \lambda^a - \sqrt{2} g \lambda^{\dagger a} (\psi^{\dagger i} T^a \phi_i) \\
& - g^2 A^{\mu a} (\phi^* T^a)^i A_\mu^a (T^a \phi)_i - \frac{1}{4} g^2 f^{abc} A_\mu^b A_\nu^c f^{abc} A^{\mu b} A^{\nu c} \\
& - \frac{1}{4} y^{ijn} y_{kln}^* \phi_i \phi_j \phi^{*k} \phi^{*l} - \frac{1}{2} g^2 (\phi^{*i} T^a \phi_i)^2. \tag{3.13}
\end{aligned}$$

The above Lagrangian applies to chiral supermultiplets interacting with one kind of gauge supermultiplet (i.e. one SM gauge group). In the general case, there are additional terms corresponding to interactions with all three SM gauge groups.

The following list gives a description of the terms in Eq. 3.13:

- First two lines: kinetic terms for the four types of fields  $\phi_i$ ,  $\psi_i$ ,  $A_\mu^a$ , and  $\lambda^a$
- Third line: mass terms for the  $\phi_i$  and  $\psi_i$  (see Figs. 3.1(a) and 3.1(b))
- Fourth and fifth lines: cubic couplings in which  $\phi_i$ ,  $\psi_i$ , or  $\lambda^a$  radiates an  $A_\mu^a$  (see Figs. 3.1(c), 3.1(d), and 3.1(e))
- Sixth line: triple gauge boson couplings (see Fig. 3.1(f))
- Seventh line: triple sfermion couplings (see Fig. 3.1(g))

- Eighth line: cubic couplings in which  $\psi_i$  radiates a  $\phi_i$  (see Fig. 3.1(h))
- Ninth line:  $\phi_i$ - $\psi_i$ - $\lambda^a$  vertices (see Fig. 3.1(i))
- 10<sup>th</sup> line:  $A_\mu^a$ - $A_\mu^a$ - $\phi_i$ - $\phi_i$  and quadruple gauge boson couplings (see Figs. 3.1(j) and 3.1(k))
- 11<sup>th</sup> line:  $\phi_i^4$  vertices (see Figs. 3.1(l) and 3.1(m))

### 3.3 Soft SUSY Breaking

Since quadratic divergences in sfermion masses vanish to all orders in perturbation theory in plain unbroken SUSY [20] due to the presence of gauge and Yukawa interactions with the necessary relationships between coupling constants (i.e. chiral symmetry inherited from the partner fermion protects the sfermion masses, as explained in Sec. 2.2), it is desirable that the terms that break SUSY not disturb this property. In addition, SUSY should be broken spontaneously, as electroweak symmetry is broken in the Standard Model, so that it is only made manifest at high energies. To satisfy these constraints, SUSY-breaking terms are simply added to the unbroken SUSY Lagrangian in Eq. 3.13 such that  $\mathcal{L}_{\text{total}} = \mathcal{L}_{\text{unbroken}} + \mathcal{L}_{\text{breaking}}$ . The coefficients of terms in  $\mathcal{L}_{\text{breaking}}$  must have positive mass dimension in order not to contribute quadratically divergent loop corrections to the scalar masses (like the Higgs mass); i.e. to not create a hierarchy problem (Sec. 2.2) for the scalars.<sup>1</sup> This form of SUSY

---

<sup>1</sup>This point can be argued via dimensional analysis. Radiative corrections take the form  $\Delta m_S^2$ , where  $m_S$  is the mass of the scalar particle in question. The dimensions of  $\Delta m_S^2$  are mass<sup>2</sup>.  $\Delta m_S^2$  is proportional to some coupling constant or mass coefficient  $k$  multiplied by a function of  $\Lambda_{\text{UV}}$ , the high energy cutoff scale. The function of  $\Lambda_{\text{UV}}$  is determined by a loop integral, and thus typically takes the form  $\Lambda_{\text{UV}}^2$  (quadratically divergent) or  $\ln \frac{\Lambda_{\text{UV}}}{m_{\text{low}}}$  (logarithmically divergent, where  $m_{\text{low}}$  is some other lower-mass scale in the problem). Now, if  $k$  already contributes at least one power of mass to  $\Delta m_S^2$ , then the high-energy behavior—the function of  $\Lambda_{\text{UV}}$ —can only contribute at most one power of the dimensionful parameter  $\Lambda_{\text{UV}}$ . However, there are typically no loop integrals that diverge linearly in  $\Lambda_{\text{UV}}$ , so by forcing  $k$  to have positive mass dimension, the form of the radiative corrections contributed by SUSY-breaking terms is limited to  $\Delta m_S^2 \sim m_{\text{low}}^2 \ln \frac{\Lambda_{\text{UV}}}{m_{\text{low}}}$ . In effect, the possibility of dangerous corrections proportional to  $\Lambda_{\text{UV}}^2$  is excluded by dimensional analysis if the requirement that  $k$  contribute at least one power of mass is enforced.

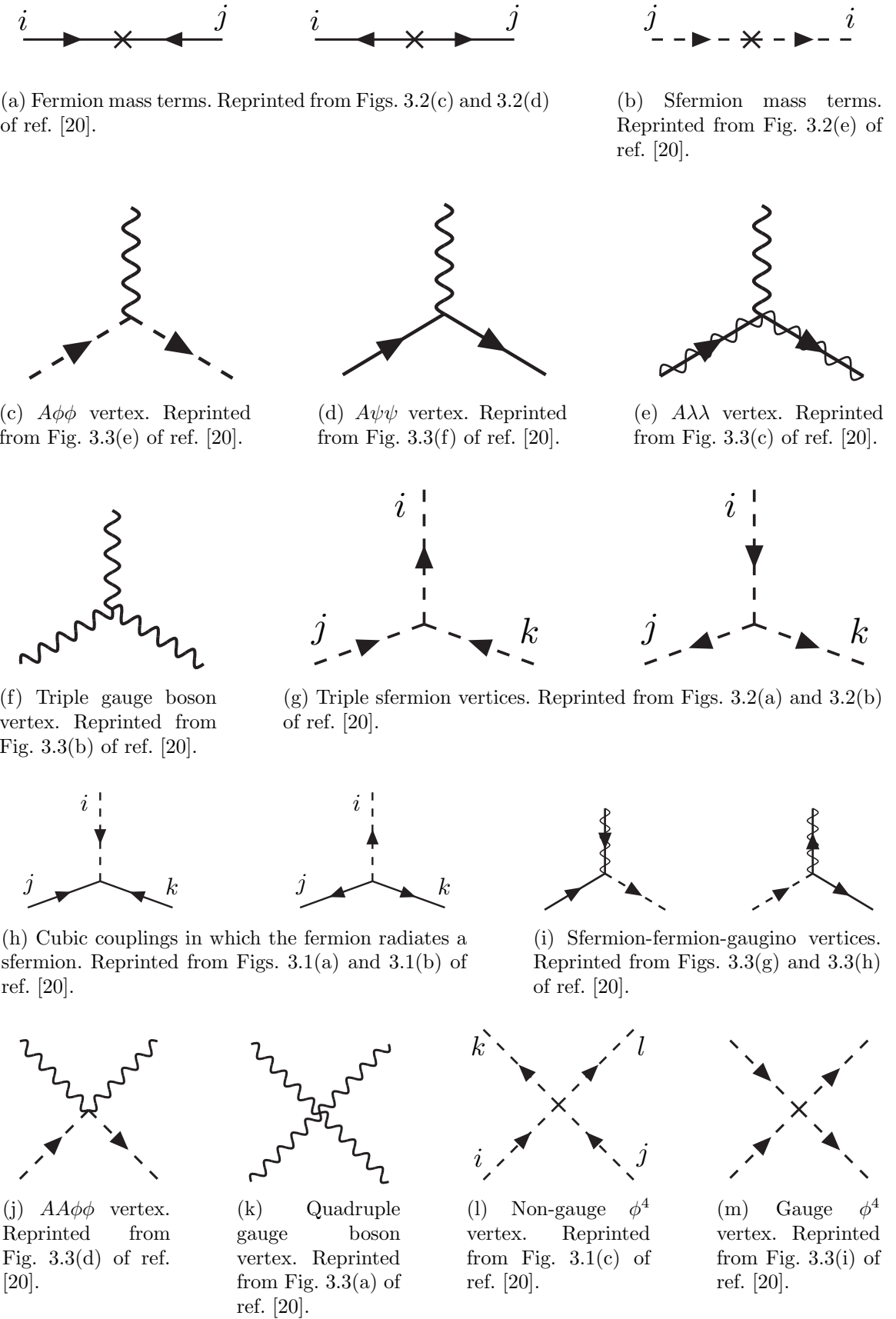


Figure 3.1: Interactions in the unbroken SUSY Lagrangian.

breaking is called *soft*, and all coefficients of soft SUSY breaking terms are expected to be of order  $m_{\text{soft}}$  or  $m_{\text{soft}}^2$ .

Soft SUSY breaking terms give masses to the sfermions and gauginos and introduce a cubic sfermion vertex. The soft terms are given by

$$\begin{aligned}
 \mathcal{L}_{\text{soft}} = & -\frac{1}{2}(M_3\tilde{g}^a\tilde{g}^a + M_2\tilde{W}^a\tilde{W}^a + M_1\tilde{B}\tilde{B} + \text{h.c.}) \\
 & - (a_u^{ij}\tilde{u}_{Ri}^*\tilde{Q}_j H_u - a_d^{ij}\tilde{d}_{Ri}^*\tilde{Q}_j H_d - a_e^{ij}\tilde{e}_{Ri}^*\tilde{L}_j H_d + \text{h.c.}) \\
 & - m_{\tilde{Q}_{ij}}^2 \tilde{Q}_i^\dagger \tilde{Q}_j - m_{\tilde{L}_{ij}}^2 \tilde{L}_i^\dagger \tilde{L}_j \\
 & - m_{\tilde{u}_{ij}}^2 \tilde{u}_{Ri} \tilde{u}_{Rj}^* - m_{\tilde{d}_{ij}}^2 \tilde{d}_{Ri} \tilde{d}_{Rj}^* - m_{\tilde{e}_{ij}}^2 \tilde{e}_{Ri} \tilde{e}_{Rj}^* \\
 & - m_{H_u}^2 H_u^* H_u - m_{H_d}^2 H_d^* H_d - (b H_u H_d + \text{h.c.})
 \end{aligned} \tag{3.14}$$

where  $a$  runs from 1-8 for  $\tilde{g}^a$  and from 1-3 for  $\tilde{W}^a$ , and  $i, j$  run over the three families. The color indices are not shown. The first line of Eq. 3.14 contains the gaugino mass terms. The second line contains cubic scalar couplings that contribute to mixing between the left- and right-handed third generation sfermions (it is assumed in the supersymmetric Standard Model that the  $a_u^{ij}$ ,  $a_d^{ij}$ , and  $a_e^{ij}$  are negligible unless  $i = j = 3$ ). The third and fourth lines of Eq. 3.14 contain squark and slepton mass terms, and finally the last line contains the Higgs mass terms.

Many viable models of achieving soft SUSY breaking have been studied over the last 30 years. For an overview, see Sec. 6 of ref. [20]. However, this thesis will only cover *gauge-mediated SUSY breaking* (GMSB), because the two-photon search performed is far more sensitive to this model than to other models of SUSY breaking.

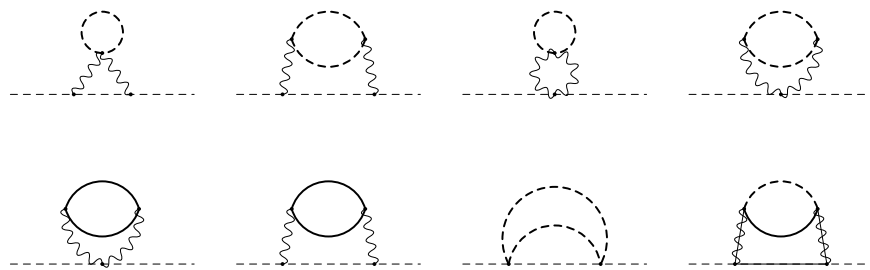
### 3.4 Gauge-Mediated SUSY Breaking

In gauge-mediated models [24–29], “hidden” fields spontaneously break the supersymmetry of very heavy chiral *messenger* supermultiplets. There are a number of competing models (see refs. [24–29]) that attempt to explain the precise mechanism of spontaneous SUSY breaking, but fortunately the details of those models mostly decouple from the phenomenology of GMSB. The messengers then communicate the SUSY breaking to the sparticles via self-energy loop diagrams of gauge interaction strength (i.e. via vertices like those shown in Figs. 3.1(c), 3.1(d), 3.1(i), 3.1(j), and 3.1(m), which are proportional to the SM gauge couplings constants). The messengers are very heavy, so they cannot be detected in current collider experiments. Feynman diagrams corresponding to gaugino and sfermion mass terms are shown in Figure 3.2.

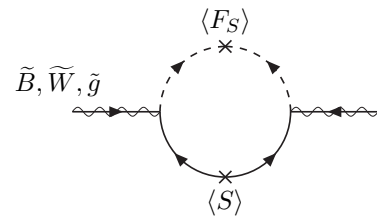
Historically, GMSB and gravity-mediated SUSY breaking, or mSUGRA [30–36], have been the two most thoroughly experimentally studied scenarios of SUSY breaking. One advantage of GMSB over mSUGRA is that it naturally suppresses flavor violation, a generic prediction of supersymmetry. Flavor violation is introduced in the scalar<sup>3</sup> couplings and sfermion mass terms of  $\mathcal{L}_{\text{soft}}$  (second, third, and fourth lines of Eq. 3.14). Since  $a_u^{ij}$ ,  $a_d^{ij}$ ,  $a_e^{ij}$ ,  $m_{\tilde{Q}ij}$ ,  $m_{\tilde{L}ij}$ ,  $m_{\tilde{u}ij}$ ,  $m_{\tilde{d}ij}$ , and  $m_{\tilde{e}ij}$  are matrices in family space, any nonzero off-diagonal elements will lead to mixing between sfermions of different families. This can lead, for example, to contributions to the diagram  $\mu \rightarrow e\gamma$  (Figure 3.3) exceeding the experimental bounds. To avoid this disaster, *universality* conditions are assumed:

$$\mathbf{m}_{\tilde{\mathbf{Q}}}^2 = m_{\tilde{Q}}^2 \mathbf{1}, \mathbf{m}_{\tilde{\mathbf{L}}}^2 = m_{\tilde{L}}^2 \mathbf{1}, \mathbf{m}_{\tilde{\mathbf{u}}}^2 = m_{\tilde{u}}^2 \mathbf{1}, \mathbf{m}_{\tilde{\mathbf{d}}}^2 = m_{\tilde{d}}^2 \mathbf{1}, \mathbf{m}_{\tilde{\mathbf{e}}}^2 = m_{\tilde{e}}^2 \mathbf{1} \quad (3.15)$$

i.e. all sfermion mass matrices arising from the soft terms are assumed to be proportional to the unit matrix  $\mathbf{1}$ , such that there can be no flavor mixing from these terms



(a) Sfermion mass terms. Heavy dashed lines denote messenger sfermions; solid lines denote messenger fermions. Reprinted from Fig. 6.4 of ref. [20].



(b) Gaugino mass term. The  $\langle S \rangle$  part of the loop is a messenger fermion contribution; the  $\langle F_S \rangle$  part is a messenger sfermion contribution. Reprinted from Fig. 6.3 of ref. [20].

Figure 3.2: Contributions to sfermion and gaugino masses from loop interactions with messenger particles in the GMSB framework.

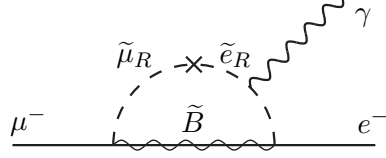


Figure 3.3: Possible contribution to  $\mu \rightarrow e\gamma$  from  $m_{\tilde{e}ij}$  soft term. Reprinted from Fig. 5.6(a) of ref. [20].

and contributions to flavor-changing processes are drastically reduced.<sup>2</sup> In mSUGRA models, universality is assumed from the beginning, while in GMSB it is a natural consequence of the fact that the sparticle-messenger vertices are the ordinary flavor-blind gauge couplings that prevent things like flavor-changing neutral currents.

In minimal GMSB (mGMSB), there are four messenger supermultiplets  $q, \bar{q}, l, \bar{l}$  providing the messenger (s)quarks and (s)leptons. There is one breaking scale  $\Lambda$ . The gaugino masses computed from diagrams like Fig. 3.2(b) are given by

$$M_a = \frac{\alpha_a}{4\pi} \Lambda \quad (3.16)$$

where  $a$  runs from 1-3 and the  $\alpha_a$  are the SM gauge coupling constants. The sfermion masses computed from diagrams like Fig. 3.2(a) are given by

$$m_{\phi_i}^2 = 2\Lambda^2 \sum_{a=1}^3 \left(\frac{\alpha_a}{4\pi}\right)^2 C_a(i) \quad (3.17)$$

where  $C_a(i)$  are group theory factors that are identical for all particles residing in the same type of supermultiplet (e.g. for all left-handed (s)quarks or left-handed (s)leptons). As explained in the previous paragraph, the gaugino and sfermion masses do not depend on fermion family.

---

<sup>2</sup>Universality also includes some assumptions about the form of  $a_{uij}$ ,  $a_{dij}$ , and  $a_{eij}$  and the stipulation that the soft terms not introduce any CP-violating phases.

In recent years, much theoretical progress has been made in unifying models of gauge mediation and developing less restrictive models than mGMSB. *General gauge mediation* (GGM) [37] retains the essential features of mGMSB, such as flavor degeneracy and communication of SUSY breaking via messengers, but does not make assumptions about the specific messenger sector or SUSY breaking scale. Many different collider final states can be interpreted in terms of GGM, and conversely, GGM implies a wealth of signatures, only a small fraction of which have been searched for at colliders [38–40]. The following section discusses the aspects of GGM collider phenomenology relevant to this thesis.

### 3.5 Phenomenology of General Gauge Mediation

The main distinguishing feature of all GMSB phenomenology is that the gravitino  $\tilde{G}$  is very light (eV-keV). In general, the gravitino mass is proportional to  $\langle F \rangle / M_P$ , where  $\langle F \rangle$  is the vacuum expectation value (VEV) of a field  $F$  that spontaneously breaks SUSY in the vacuum state and  $M_P$  is the Planck mass. In GGM models,  $\langle F \rangle \sim 10^8$  GeV, leading to a very light gravitino. In contrast, mSUGRA predicts  $\langle F \rangle \sim 10^{20}$  GeV. The fact that the gravitino is so much lighter than any other particles in the supersymmetric Standard Model, and that it interacts only gravitationally (and thus extremely feebly), leads to two important phenomenological consequences:

1. All sparticle decay chains in GMSB end with the production of a gravitino.
2. The gravitino escapes  $4\pi$ , hermetic collider detectors without interacting, leaving a signature of “missing” momentum transverse to the beam direction.

Even if the gravitino were lighter than any other sparticle, but heavier than an ordinary SM particle, it still could not decay to the SM particle due to *R-parity*. R-parity is a conserved quantity of the supersymmetric Standard Model introduced to

enforce baryon and lepton number conservation, which would otherwise be generically allowed at levels in conflict with experiment (e.g. the non-observation of baryon- and lepton-number-violating proton decay). All sparticles have R-parity -1, while all ordinary SM particles have R-parity +1, and R-parity conservation dictates that at any vertex, the product of the R-parities of each leg must be +1. This leads to two more important consequences:

1. Since conservation of energy only allows it to decay to ordinary SM particles, but R-parity prevents a sparticle-particle-particle vertex, the *lightest supersymmetric particle* (LSP) must be absolutely stable. All sparticle decays proceed through the *next-to-lightest supersymmetric particle* (NLSP), which in turn decays to the LSP. The fact that it is stable and only gravitationally interacting makes the gravitino a candidate dark matter particle (see Sec. 3.6).
2. In colliders, sparticles are produced in pairs (particle + particle  $\rightarrow$  sparticle + sparticle).

In GMSB, then, the gravitino is the LSP. If the NLSP is a gaugino,<sup>3</sup> then the possible decays depend on mixing among the gauginos. The four neutral gauginos  $\tilde{H}_u^0$ ,  $\tilde{H}_d^0$ ,  $\tilde{B}$ ,  $\tilde{W}^0$  mix into four *neutralino* mass eigenstates  $\tilde{\chi}_1^0$ ,  $\tilde{\chi}_2^0$ ,  $\tilde{\chi}_3^0$ ,  $\tilde{\chi}_4^0$ , and the four charged gauginos  $\tilde{H}_u^+$ ,  $\tilde{H}_d^-$ ,  $\tilde{W}^+$ ,  $\tilde{W}^-$  mix into two *chargino* mass eigenstates  $\tilde{\chi}_1^\pm$ ,  $\tilde{\chi}_2^\pm$  (two mass eigenstates each with two possible charges = four particles). In the limit that EWSB effects are small, the neutralino and chargino masses can be written as the gauge eigenstate masses plus a small perturbation:

---

<sup>3</sup>In principle, the NLSP could be anything, but in most popular GGM models, it is either a gaugino or a stau. The stau NLSP search is not the subject of this thesis, so it will not be considered in this section.

$$m_{\tilde{\chi}_1^0} = M_1 - \frac{m_Z^2 \sin^2 \theta_W (M_1 + \mu \sin 2\beta)}{\mu^2 - M_1^2} + \dots \quad (3.18)$$

$$m_{\tilde{\chi}_2^0} = M_2 - \frac{m_W^2 (M_2 + \mu \sin 2\beta)}{\mu^2 - M_2^2} + \dots \quad (3.19)$$

$$m_{\tilde{\chi}_3^0} = |\mu| + \frac{m_Z^2 (\text{sgn}(\mu) - \sin 2\beta)(\mu + M_1 \cos^2 \theta_W + M_2 \sin^2 \theta_W)}{2(\mu + M_1)(\mu + M_2)} + \dots \quad (3.20)$$

$$m_{\tilde{\chi}_4^0} = |\mu| + \frac{m_Z^2 (\text{sgn}(\mu) + \sin 2\beta)(\mu - M_1 \cos^2 \theta_W - M_2 \sin^2 \theta_W)}{2(\mu - M_1)(\mu - M_2)} + \dots \quad (3.21)$$

$$m_{\tilde{\chi}_1^\pm} = M_2 - \frac{m_W^2 (M_2 + \mu \sin 2\beta)}{\mu^2 - M_2^2} + \dots \quad (3.22)$$

$$m_{\tilde{\chi}_2^\pm} = |\mu| + \frac{m_W^2 \text{sgn}(\mu)(\mu + M_2 \sin 2\beta)}{\mu^2 - M_2^2} + \dots \quad (3.23)$$

where  $\tan \beta = \langle H_u^0 \rangle / \langle H_d^0 \rangle$ .

The two scenarios studied in ref. [40] are the following:

- **Bino NLSP:**  $M_1 \sim$  few hundred GeV,  $M_2, |\mu| \gg M_1$ . All but the lightest neutralino (Eq. 3.18) are effectively inaccessible at the LHC due to their large masses. The NLSP can always decay to  $\gamma + \tilde{G}$ , and if it is heavy enough, to  $Z + \tilde{G}$  or  $H + \tilde{G}$ .
- **Wino NLSP:**  $M_2 \sim$  few hundred GeV,  $M_1, |\mu| \gg M_2$ . The lightest neutralino (Eq. 3.18) and the lightest chargino (Eq. 3.22) are nearly degenerate in mass, and are the only two particles to play a role at the LHC. The decays described in the previous bullet point can happen, as well as chargino decays to  $W + \tilde{G}$ .

The search described in this thesis is optimized for the classic bino NLSP decay  $\gamma + \tilde{G}$ , but sensitivity to the wino co-NLSP scenario is also studied (see Chapter 8).

Since strong production of SUSY particles, for instance via  $gg \rightarrow \tilde{g}\tilde{g}$ , dominates over electroweak production, for instance via  $q\bar{q} \rightarrow \tilde{\chi}_1^\pm \tilde{\chi}_1^\mp$ , at the LHC due to the enhanced  $gg$  parton luminosity over the  $q\bar{q}$  parton luminosity, early LHC searches are particularly sensitive to light squarks and gluinos. General gauge mediation makes no

a priori restrictions on the mass splitting between the strongly interacting sparticles and the weakly interacting sparticles, so models with light squarks and gluinos are viable. In fact, such models could not be probed as well at the Tevatron<sup>4</sup> as they are at the LHC due to the aforementioned parton luminosities.

Typical LHC signatures of the bino and wino NLSP scenarios are shown in Figure 3.4.

### 3.6 Experimental Status of SUSY

Collider searches for evidence of supersymmetry began in earnest in the 1980s [42–50] and continue to this day. Most recently, the LHC and Tevatron experiments have set the strictest limits on a variety of SUSY breaking scenarios, including GMSB and mSUGRA.

Figure 3.5 shows the current limits set by the CMS experiment on the mSUGRA model (with  $\tan \beta = 10$ ) in the  $m_0$ - $m_{1/2}$  plane. (Note that although the plot is truncated at  $m_0 = 1000 \text{ GeV}/c^2$ , some searches are sensitive out to  $m_0 \sim 2000 \text{ GeV}/c^2$ .) Although the LHC has pushed  $m_0$  above  $\sim 1 \text{ TeV}/c^2$  for  $m_{1/2}$  up to  $\sim 400 \text{ GeV}/c^2$ , casting some doubt onto the theory’s prospects for solving the hierarchy problem, there is still a sizable chunk of mSUGRA parameter space that is not ruled out by collider experiments. Furthermore, parts of the CMS unexplored regions overlap with areas allowed by astrophysics experiments [51].

Figure 3.6 shows the most up-to-date limit (using  $1 \text{ fb}^{-1}$  of integrated luminosity collected by the ATLAS experiment [54] at the LHC) on the Snowmass Points and Slopes (SPS) model of mGMSB, dubbed SPS8 [53]. In general, the lifetime of the lightest neutralino in GMSB models can take on any value between hundreds of nanometers to a few kilometers depending on the mass of the lightest neutralino and

---

<sup>4</sup>Located on the Fermilab site in Batavia, Illinois, the Tevatron was a proton-antiproton collider operating at  $1.96 \text{ TeV}$  center-of-mass energy. The Tevatron ran from 1987 to 2011 [41].

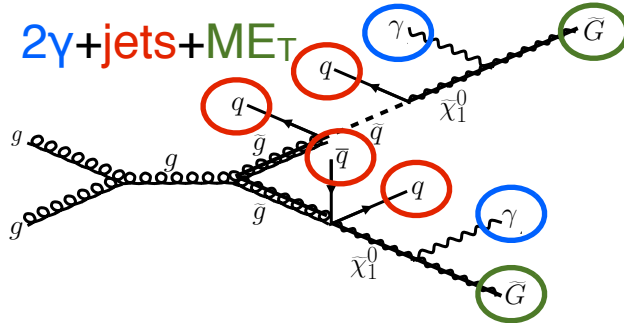
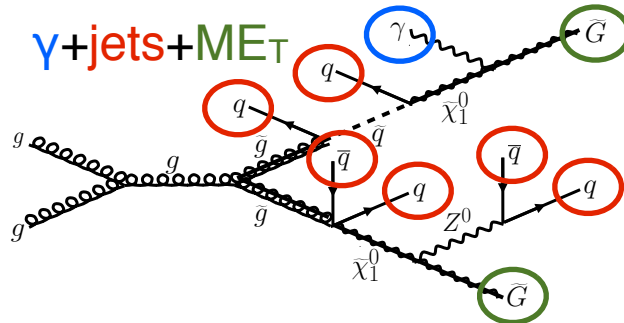
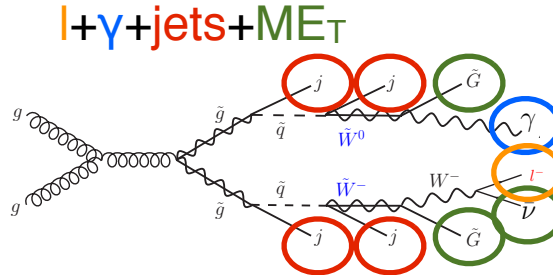
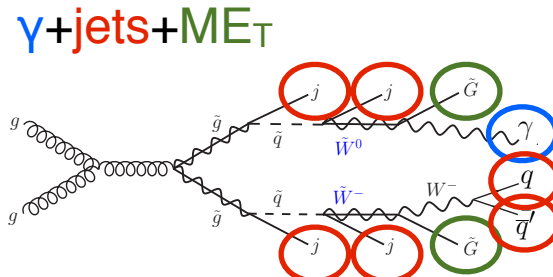
(a) Two gluinos each decay via  $\tilde{\chi}_1^0 \rightarrow \gamma \tilde{G}$ .(b) One gluino decays via  $\tilde{\chi}_1^0 \rightarrow \gamma \tilde{G}$ , the other via  $\tilde{\chi}_1^0 \rightarrow Z(\rightarrow q\bar{q})\tilde{G}$ .(c) One gluino decays via  $\tilde{\chi}_1^0 \rightarrow \gamma \tilde{G}$ , the other via  $\chi_1^\pm \rightarrow W^\pm(\rightarrow l^\pm \nu_l)\tilde{G}$ .(d) One gluino decays via  $\tilde{\chi}_1^0 \rightarrow \gamma \tilde{G}$ , the other via  $\chi_1^\pm \rightarrow W^\pm(\rightarrow q\bar{q}')\tilde{G}$ .

Figure 3.4: Typical LHC signatures of the bino and wino NLSP scenarios.

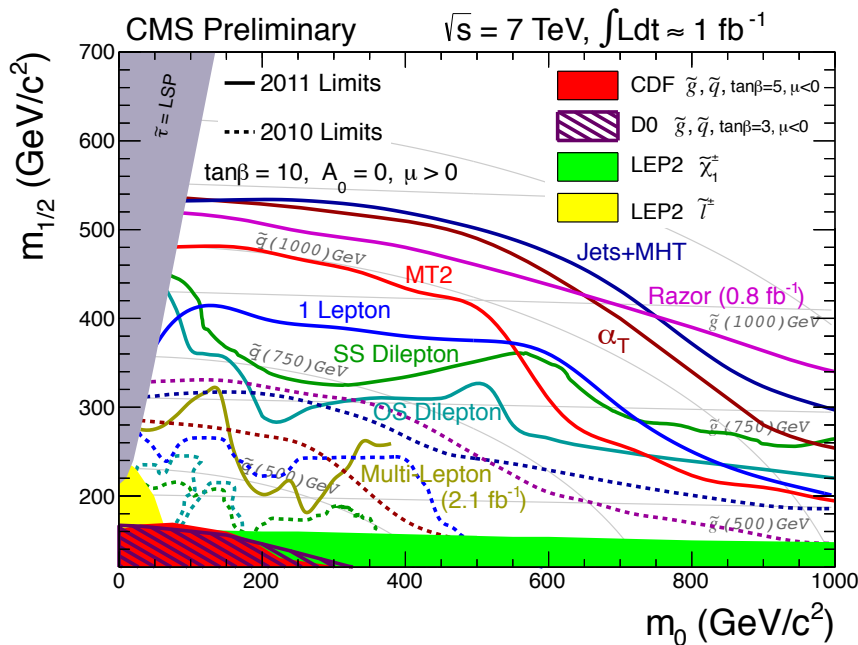


Figure 3.5: CMS limits on mSUGRA with  $\tan\beta = 10$ , corresponding to a model with third-generation squarks and sfermions somewhat lighter than their first- and second-generation counterparts. The limits set by individual searches are shown as separate colored lines. Solid lines refer to 2011 searches (i.e. using an integrated luminosity of  $\sim 1$  fb $^{-1}$ ), while dashed lines refer to 2010 searches ( $\sim 36$  pb $^{-1}$ ). Reprinted from ref. [52].

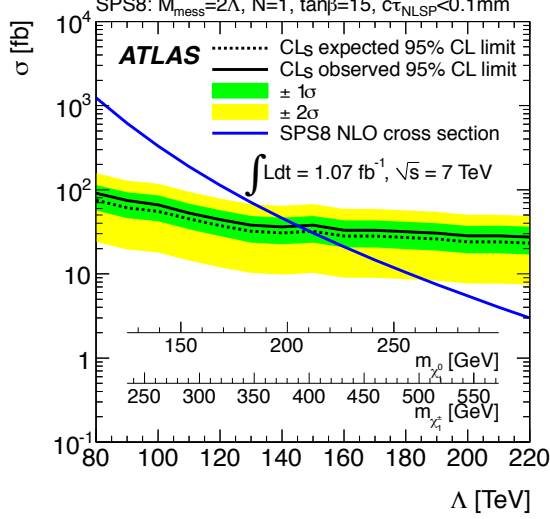


Figure 3.6: ATLAS cross section upper limit on the SPS8 [53] model of mGMSB as a function of SUSY breaking scale  $\Lambda$ , lightest neutralino mass  $m_{\tilde{\chi}_1^0}$ , or lightest chargino mass  $m_{\tilde{\chi}_1^\pm}$ . Values of  $\Lambda$ ,  $m_{\tilde{\chi}_1^0}$ , or  $m_{\tilde{\chi}_1^\pm}$  below the intersection point between the blue (predicted SPS8 cross section) and black (observed cross section upper limit) curves are excluded. The model parameters listed above the plot are defined in Secs. 3.4 and 3.5, except for  $\tau_{\text{NLSP}}$ , which is the neutralino lifetime. Reprinted from ref. [38].

the SUSY breaking scale [20]. The search published in ref. [38] (from which Fig. 3.6 is culled) considers only *prompt* neutralino variants, i.e. with neutralino lifetime short enough that the distance traveled by the neutralino before decay cannot be resolved by the detector. The most recent limits on non-prompt SPS8-style neutralino models were set by the Collider Detector at Fermilab (CDF) collaboration with  $570 \text{ pb}^{-1}$ , and are shown in Figure 3.7 [39].

Finally, if the gravitino is to make up some or all of the dark matter, constraints on the form of gauge mediation must come from cosmological considerations and astronomical observations. The gravitino in gauge mediation models is usually very light ( $\mathcal{O}(\text{eV-MeV})$ ) because it is proportional to the SUSY breaking scale divided by the Planck mass, and in GMSB the breaking scale is typically only of order a few hundred TeV ([20] and Sec. 3.5). A light, highly relativistic dark matter particle might have been produced, for instance, in the early, radiation-dominated period of the universe [55]. This *warm dark matter* (WDM) may be responsible for all of

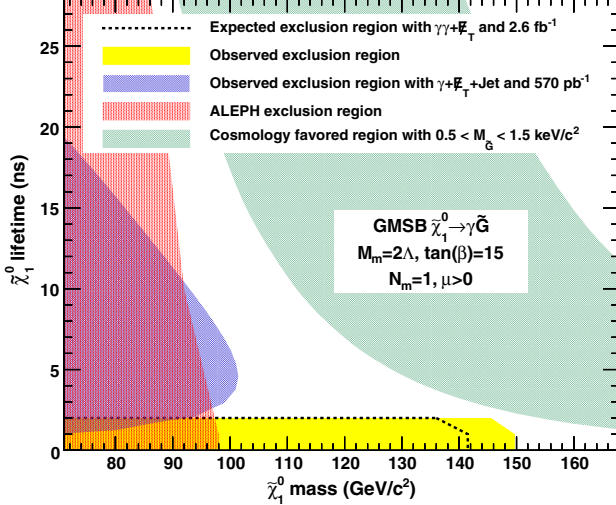


Figure 3.7: CDF exclusion contour in the  $\tau_{\tilde{\chi}_1^0}$ - $m_{\tilde{\chi}_1^0}$  plane, where  $\tau_{\tilde{\chi}_1^0}$  is the lifetime of the neutralino. Reprinted from ref. [39].

the dark matter needed to account for galactic structure, or it may share the duties with *cold dark matter* (CDM, weakly interacting particles with masses in the GeV range). In any viable model, the predicted relic density of the dark matter species must match the observed value of  $\Omega h^2 \sim 0.1$  [56]. For many GMSB models, this measurement constrains the gravitino mass to the keV range [57]. This constraint, however, does not translate into a very strong bound on the lifetime of the lightest neutralino. Using the following equation (taken from [57]):

$$\tau_{\tilde{\chi}_1^0} \sim 130 \left( \frac{100 \text{ GeV}}{m_{\tilde{\chi}_1^0}} \right)^5 \left( \frac{\sqrt{\langle F \rangle}}{100 \text{ TeV}} \right)^4 \mu \text{m} \quad (3.24)$$

and applying the gravitino mass constraint  $\sqrt{\langle F \rangle} \lesssim 3000 \text{ TeV}$  (cf. the first paragraph of Sec. 3.5 with  $m_{\tilde{G}} \sim \text{keV}$ ) and  $m_{\tilde{\chi}_1^0} = 100 \text{ GeV}$ , the upper bound on the neutralino lifetime is 100 meters. For  $\sqrt{\langle F \rangle} \sim 100 \text{ TeV}$ , the neutralino lifetime is detectable on collider time scales.

Recently, a lower bound on the WDM particle mass in either pure warm or mixed warm and cold dark matter scenarios was set using observations of the Lyman- $\alpha$  forest. For pure WDM,  $m_{\text{WDM}} > 8 \text{ keV}$ , while for some mixed WDM-CDM scenarios,

$m_{\text{WDM}} > 1.1\text{-}1.5 \text{ keV}$  [55, 58]. These bounds and others have motivated the development of more complicated gauge mediation models [58].

However, rather than focus on a specific GMSB model, of which there are many, the search detailed in the following chapters is interpreted in a minimally model dependent way. With this approach, the results can be applied to many competing models. The remainder of this thesis is devoted to the experimental details of the search, analysis strategy, and presentation of the results. The work described in this thesis forms the basis for the CMS public result “Search for Supersymmetry in Events with Photons and Missing Energy” [59], published in April 2012 (see Chapters 7 and 8 for results). Ref. [59] contains the best limits on bino-like NLSP and wino-like NLSP GGM models to date.

## Chapter 4

# The Large Hadron Collider

At a 2010-2011 energy of 3.5 TeV/beam (7 TeV/beam design [60]) and maximum instantaneous luminosity of  $3.55 \times 10^{33} \text{ cm}^{-2} \text{ s}^{-1}$  [61] ( $10^{34} \text{ cm}^{-2} \text{ s}^{-1}$  design [60]), the CERN Large Hadron Collider (LHC) is the highest energy and highest intensity proton-proton collider ever built. Its purpose is to allow the four LHC experiments to explore TeV scale physics. For CMS and ATLAS, this implies examining the origins of EWSB via searches for the SM Higgs boson and physical phenomena not predicted by the SM that may explain the mass hierarchy in the SM. It also includes searches for possible dark matter candidates that are often proposed to have masses at the weak scale. The LHC needs to provide high energy proton collisions because the masses of the sought-after particles are higher than those already incorporated into the SM. It must also provide an unprecedented collision rate because signatures of the Higgs boson and physics beyond the SM are very rare compared to SM processes.

The rest of this chapter is devoted to an overview of the LHC machine. Section 4.1 gives the overall layout of the machine and design choices made in light of energy and luminosity demands. Section 4.2 describes the LHC injection scheme. The different types of magnets and their functions is illustrated in Section 4.3, and finally the radiofrequency cavities are covered in Section 4.4. Unless otherwise noted, all

information in this chapter comes from ref. [60].

## 4.1 Design Considerations and Performance Limitations

The layout of the 26.7-km long [62] LHC ring, located  $\sim 100$  m underground on the border between France and Switzerland northwest of Geneva, is shown in Figure 4.1. The two circulating beams of protons travel in opposite directions, colliding only at the experimental points. There are eight straight sections, each  $\sim 528$  m long, and eight arcs, each made of 23 106.9-m long arc cells. Beam crossings occur in four of the straight sections. The arcs contain six 14.3-m long dipole magnets, the cryogenics to cool the magnets, and short straight sections (SSS) with focusing and corrector magnets. The high luminosity experiments CMS and ATLAS are located diametrically opposite each other on the ring, ensuring that in principle each should receive the same integrated luminosity from the LHC. In Fig. 4.1, ATLAS is located at Point 1, ALICE at Point 2, CMS at Point 5, and LHCb at Point 8.

To achieve a maximum energy per beam of 7 TeV, the peak magnetic field produced by the dipole magnets must be 8.33 T, demanding the use of superconducting technology. Due to the like charges of the two beams, two separate magnet systems and evacuated beam pipes must be used to accelerate the protons in opposite directions. Space limitations in the LHC tunnel, which was previously used for the LEP  $e^+e^-$  collider, prevent the installation of two separate rings of magnets, so each dipole instead contains two beam pipe bores and two sets of superconducting coils to produce two fields in opposite directions. In order to safely operate the magnets at 8.33 T, the cryogenic superfluid helium bath temperature is chosen to be 1.9 K (at a pressure of 0.13 MPa), colder than any other accelerator cryogen and well below the critical temperature of the niobium-titanium (NbTi) superconducting wires of 9.2 K

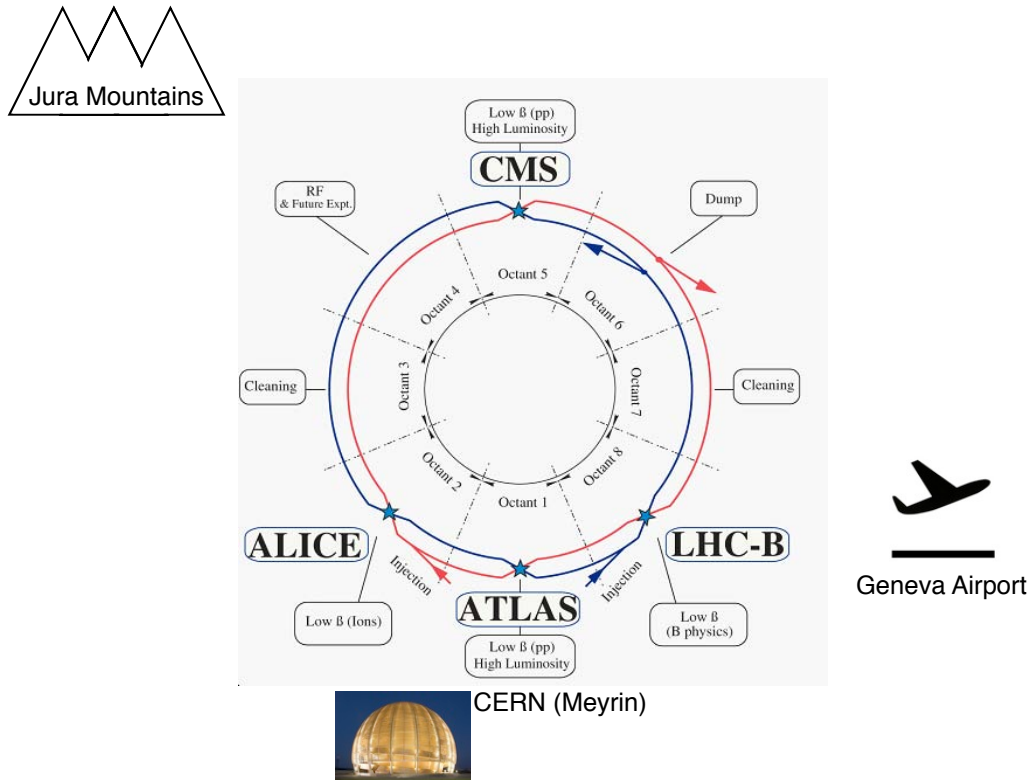


Figure 4.1: Bird's-eye view of the LHC ring, showing the locations of the experiments and local landmarks. Arrows show the beam direction. ATLAS is located at Point 1, ALICE at Point 2, CMS at Point 5, and LHCb at Point 8. The ring figure is reprinted from Fig. 2.1 of ref. [60]. The CERN Globe of Innovation photo comes from ref. [63] and the airplane cartoon comes from ref. [64].

[65]. The extremely low bath temperature leads to a lessened heat capacity in the wires and consequently a lower energy threshold for heating the wires above the temperature needed to maintain the superconducting state. In order to avoid a disastrous magnet quench caused by huge resistive losses if the wires were to transition to the normal conducting state, movements and heat dissipation within the cables must be controlled more tightly than in previous accelerators.

The LHC beams are arranged in bunches of protons, with each bunch separated by an integer multiple of the 25 ns minimum bunch spacing. The machine luminosity  $L$  is given by

$$L = \frac{N_b^2 n_b f_{\text{rev}} \gamma_r}{4\pi \epsilon_n \beta^*} F \quad (4.1)$$

where  $N_b$  is the number of protons per bunch (squared for the two beams),  $n_b$  is the number of bunches per beam,  $f_{\text{rev}}$  is the bunch revolution frequency,  $\gamma_r$  is the relativistic  $\gamma$  of the protons,  $\epsilon_n$  is the normalized transverse beam emittance,  $\beta^*$  is the value of the  $\beta$  function at the collision point, and  $F$  is a geometrical factor less than one related to the *crossing angle* of the bunches with respect to the horizontal (ATLAS) or vertical (CMS) planes and the beam size. The normalized transverse beam emittance is a measure of the RMS spread of the beam in the plane transverse to its direction of motion, irrespective of its energy. A smaller emittance implies that particles are squeezed into a smaller area in phase space, leading to larger luminosity. The  $\beta$  function is defined as the square of the transverse beam size divided by the emittance. It describes the oscillations of the transverse beam size as a function of position in the ring. To achieve high luminosity,  $\beta^*$  is the minimum of the  $\beta$  function, and it is related to the focusing strength of the triplet magnets near the interaction points. In accelerating sections of the ring, the  $\beta$  function gets large so that the proton

momenta may be more uniform. Each piece of Eq. 4.1 is limited by safety or design considerations.

Above some saturated bunch intensity, nonlinear beam-beam interactions experienced by the protons during collisions cause the luminosity to scale as  $N_b$ , not  $N_b^2$  [66]. The scale of these interactions is set by  $N_b/\epsilon_n$ , and the size of the beam pipe and maximum  $\beta$  function limit  $\epsilon_n$  to  $3.75 \mu\text{m}$ . Instabilities are also introduced through interactions between the protons and the wall of the beam pipe that scale with the beam current. Last but not least, the beam dump and magnet safety systems limit the total stored energy in the ring. For these reasons, the maximum number of protons per bunch is limited to  $1.15 \times 10^{11}$  for a 25 ns bunch spacing. In bunches of this proton multiplicity, the average number of proton-proton collisions per bunch crossing, or *pileup*, in CMS and ATLAS is approximately 20. This unprecedented level of pileup poses unique triggering, event reconstruction, and analysis challenges for the experiments.

$n_b$  can range from zero to 2808 and had a maximum of  $\sim 1400$  in 2011, corresponding to 50 ns bunch spacing.  $f_{\text{rev}}$  is set by the circumference of the ring to 11.2 kHz [67].  $\gamma_r$  is set by the beam energy, which was 3.5 TeV in 2011.

The mechanical aperture of the triplet assemblies of quadrupole magnets limit the minimum  $\beta^*$  to 0.55 [67] and maximum crossing angle to  $285 \mu\text{rad}$  [67] at the interaction points. The purpose of the crossing angle is to prevent parasitic collisions in the 23-m length of shared beam pipe upstream and downstream of the interaction points.

## 4.2 Beam Injection

The ultimate source of protons for the LHC is a bottle of hydrogen connected to the CERN Linac2 linear accelerator, which accelerates the protons up to 50 MeV. From

## The LHC injection complex

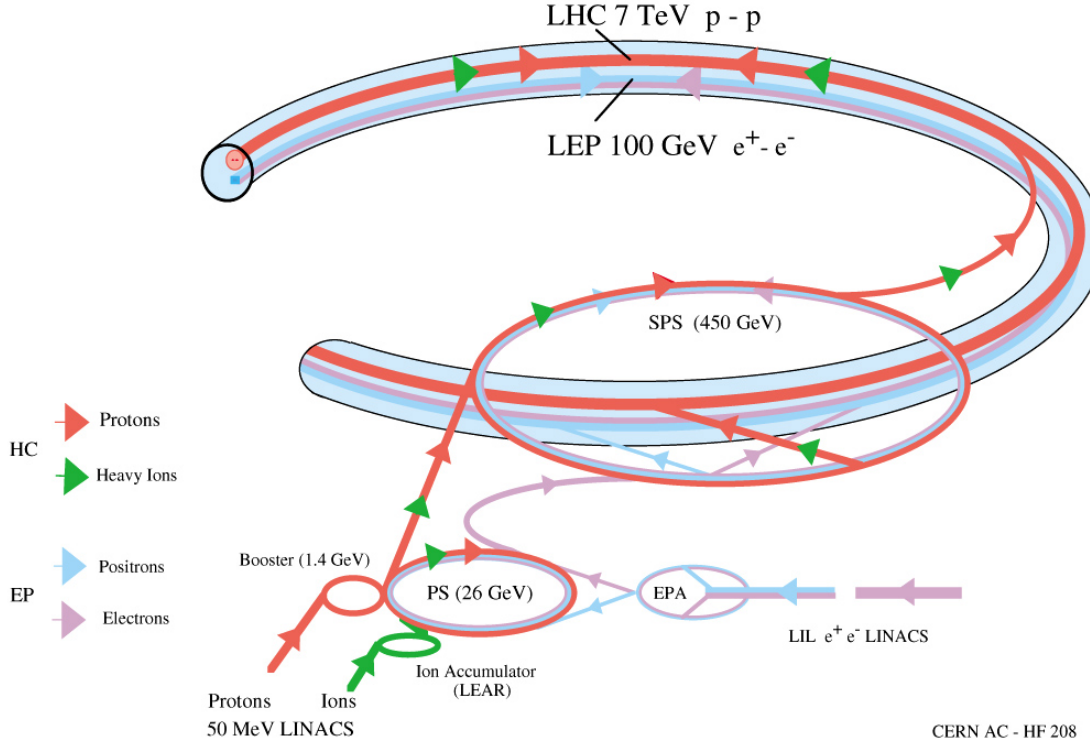


Figure 4.2: Overview of the LHC injector complex at CERN [68].

there they enter the Proton Synchrotron Booster (PSB), which accelerates them to 1.4 GeV, and then the Proton Synchrotron (PS) itself, which brings them to 25 GeV. The Super Proton Synchrotron (SPS) is the next stage, accelerating the protons to an energy of 450 GeV. Finally, they leave the SPS and enter the LHC, where they are accelerated to the desired beam energy (3.5 TeV in 2011). An overview of the LHC injector complex is shown in Figure 4.2.

The 25-ns spaced bunches (or 50 ns for 2011 operation) are produced in trains of 72 in the PS via a process of splitting six initial bunches into 12 smaller bunches at specified points along the ring. At the end of each train is a 300 ns (12 bunch) gap, which is an artifact of the splitting process. The SPS is limited by its maximum allowed bunch intensity to storing three or four PS trains at a time. There is an 220 ns (8 bunch) gap at the end of each train due to the SPS injection kicker rise time.

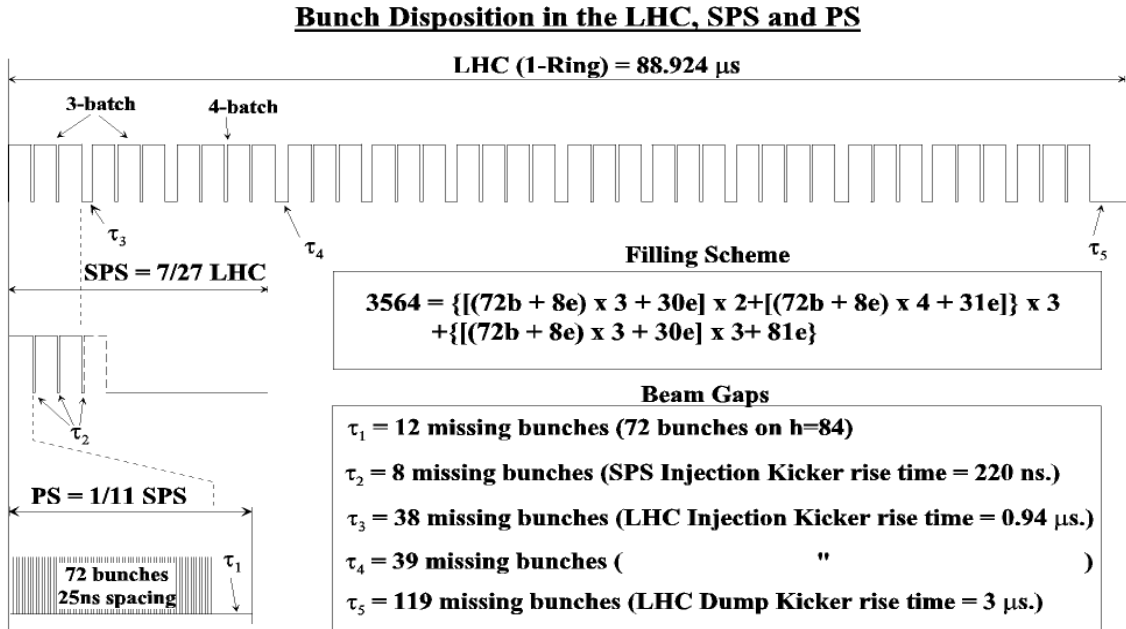


Figure 4.3: LHC injection scheme. Reprinted from Fig. 12.2 of ref. [60].

The LHC is filled three or four trains at a time from the SPS. At the end of each three-train and four-train group is a gap of  $0.94\ \mu s$  (38 or 39 bunches) due to the LHC injection kicker rise time. Finally, at the end of an entire  $88.924\text{-}\mu s$  long LHC orbit is a gap of  $3\ \mu s$  (119 bunches), known as the *abort gap*, to allow for the LHC dump kicker rise time. The injection scheme is shown in Figure 4.3.

LHC injection occurs at points 2 and 8. At the intersection of the SPS-LHC transfer line and the LHC beam pipe are five septum magnets that deflect the bunches 12 mrad horizontally into orbit. The septum magnets have a gap into which the beam is injected as well as two separate holes for the circulating beams, as shown in Figure 4.4. Four kicker magnets then deflect the bunches 0.85 mrad vertically into orbit. The kicker magnets supply a pulsed magnetic field with a  $0.94\ \mu s$  rise time (see Fig. 4.3) and a  $5.84(7.86)\ \mu s$  flat top for three-train(four-train) injection (see Figure 4.5). To limit emittance growth at injection due to over- or under-kicking the injected bunches such that they miss the core of the LHC orbit, the kicker current is limited to  $< 0.5\%$  flat top ripple in any direction.

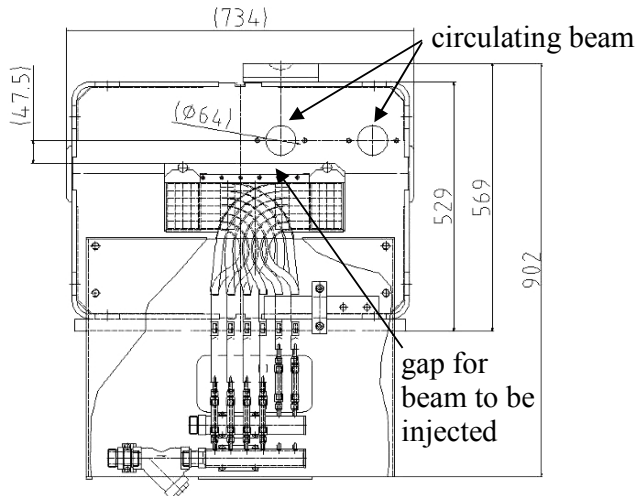


Figure 4.4: Cross-sectional view of septum magnet (beam direction is into or out of the page) showing the holes for the circulating beams and the separate gap for injected particles. Reprinted from Fig. 11.2 of ref. [60].

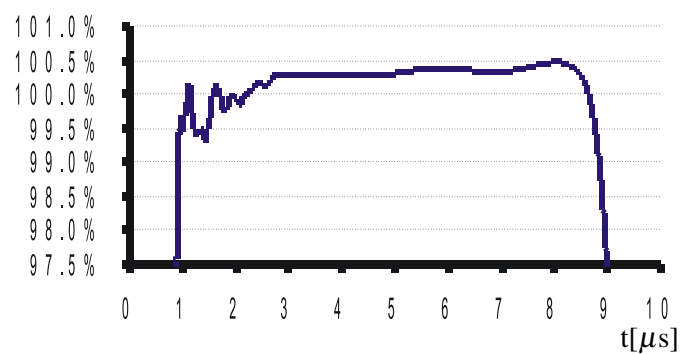


Figure 4.5: LHC injection kicker pulse shape. The  $y$ -axis measures percentage of maximum current. Reprinted from Fig. 11.7 of ref. [60].

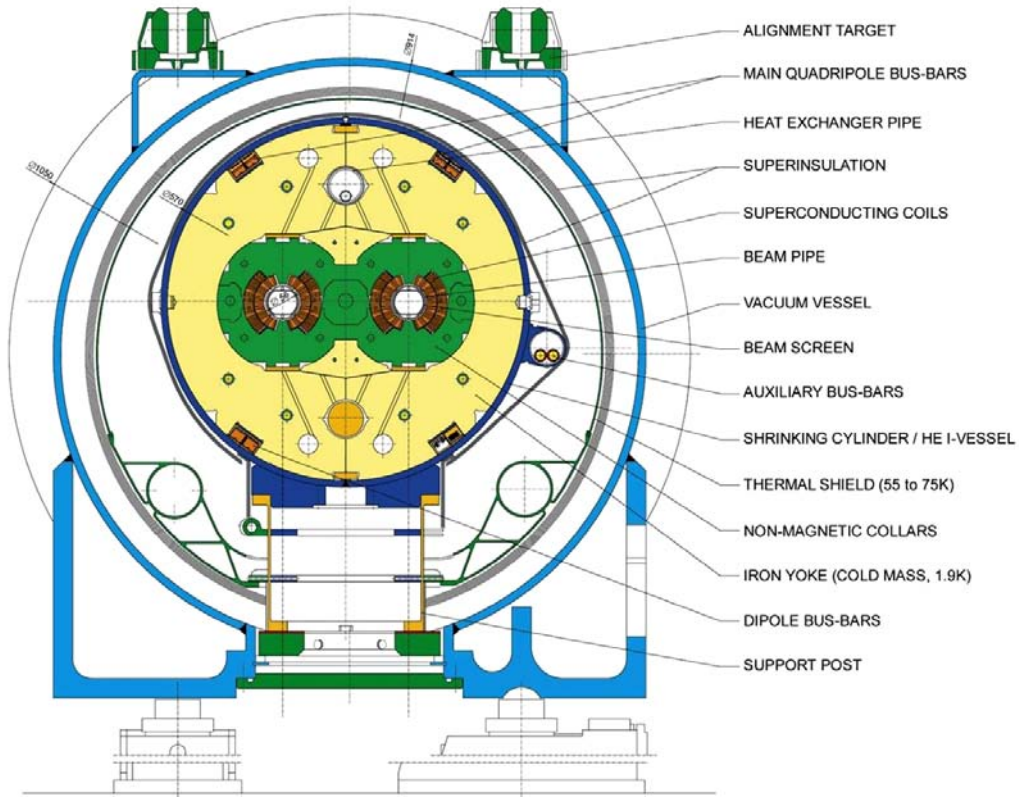


Figure 4.6: Cross-sectional view of LHC dipole + cryostat. Reprinted from Fig. 3.3 of ref. [60].

### 4.3 Magnets and Cryogenics

There are 1232 twin-bore dipole magnets along the LHC ring used for establishing the circular orbit of the protons. They consist of two evacuated beam pipes, each flanked by its own set of superconducting coils, inside an iron yoke which serves as the 1.9 K cold mass. The entire assembly sits inside a helium vessel, which is itself surrounded by a vacuum chamber thermally insulating the cold mass from the room temperature LHC cavern. The entire dipole + cryostat device is  $\sim 16.5$  m long and weighs about 27.5 t. A cross-sectional view of the dipole is given in Figure 4.6.

To provide a centripetal Lorentz force on the protons, the dipole field points vertically up or down, depending on the direction of the beam. The magnetic field lines for a single beam pipe are shown in Figure 4.7. Figure 4.8 shows the coil windings in two

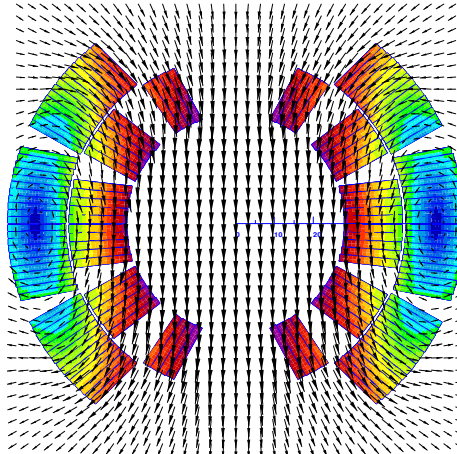


Figure 4.7: Magnetic field lines of the dipole field. The beam direction is into the page. Reprinted from Fig. 4 of ref. [69].

bores. To provide the correct field direction, the coils are wound around blocks that are  $\sim 14$  m long (the length of the dipole), so that each winding has a circumference of  $\sim 28$  m.

In addition to the dipoles, a number of different types of orbit corrector magnets are installed throughout the ring. The main quadrupole magnets, as well as higher order field corrector magnets, are located in the arcs and short straight sections. The function of these magnets is to provide fine grained control over the magnetic field in order to keep the bunches in the proper orbit and control the emittance and  $\beta$  functions.

In the straight sections, there are four specialized types of magnets related to SPS extraction and bringing the beams into collision. Matching section quadrupoles near the transfer lines help to match the injected bunch orbit to the circulating bunch orbit. Dispersion suppressors, consisting of dipoles and quadrupoles, help to reduce beam dispersion near the collision points due to off-momentum protons. Matching section separation dipoles control the separation between the two beams near the collision points. The magnets that perform the final squeeze of the beams before collision, called the low- $\beta$  inner triplets, must provide a very high field gradient of 215 T/m,

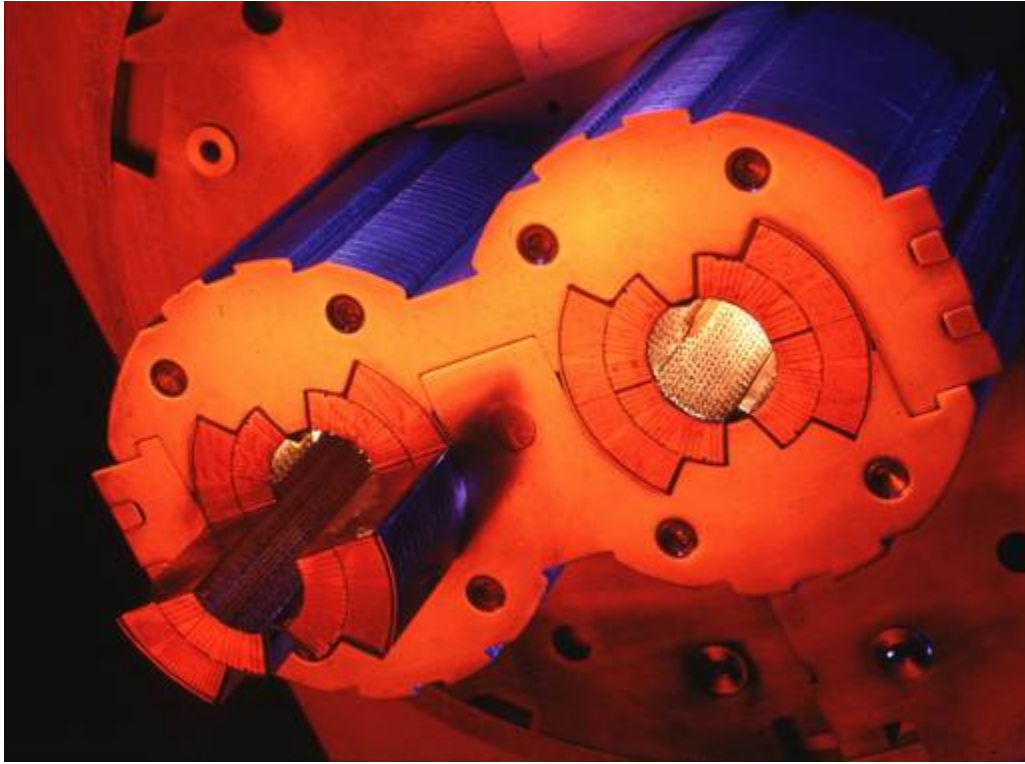


Figure 4.8: Superconducting coils in a twin-bore dipole [70].

withstand a high radiation dose, and sustain high heat loads in the superconducting coils.

The superfluid helium cryogen is delivered to the magnets via a distribution line from the main refrigerator. A cross section of the LHC tunnel, showing the cryogen delivery apparatus for a dipole, is shown in Figure 4.9.

## 4.4 Radiofrequency Cavities

LHC bunches are captured and accelerated in 400 MHz superconducting radiofrequency (RF) cavities. 400 MHz defines the bunch length of  $\lesssim 2$  ns. As bunches pass through the cavities, the oscillating electric field is at its peak and accelerates the protons through a potential difference of 2 MV per cavity (16 MV per turn). The finite bunch length is due to particles that arrive out of phase with the electric field due to deviations in their momenta from the nominal. During a ramp of the beam

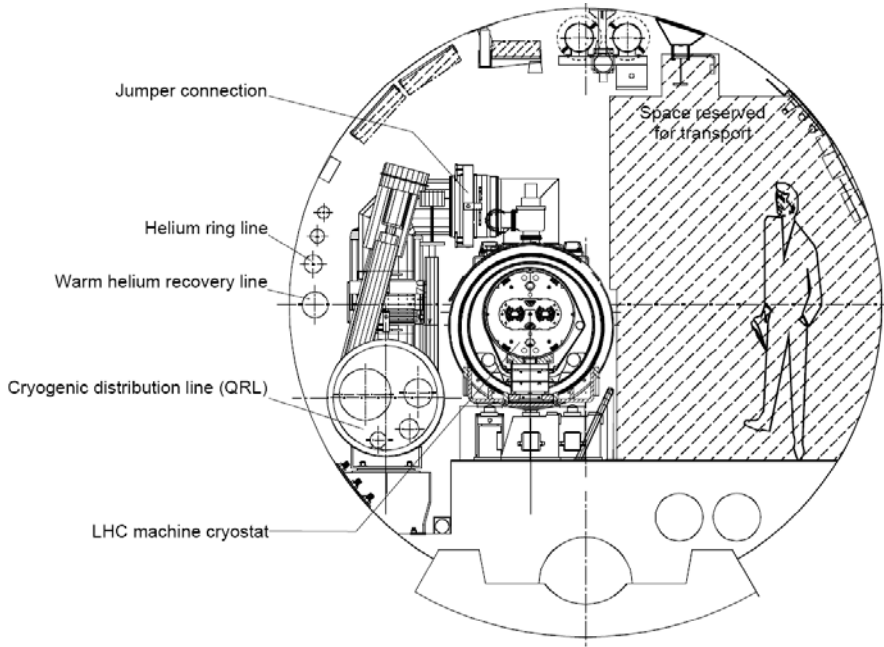


Figure 4.9: Cross section of the LHC tunnel, showing the cryogen delivery apparatus for a dipole. Reprinted from Fig. 7.1 of ref. [60].

energy from 450 GeV to 3.5 or 7 TeV, bunches repeatedly travel around the ring, receiving an energy kick each time, until the desired energy is reached. Feedback from the RF accelerating system causes an increase in magnet current to keep the bunches in a fixed orbit.

Superconducting material (niobium) coats the cylindrical walls of the cavity. RF power is coupled to the cavity via a klystron. The RF electric field standing wave is set up across the cavity in the beam direction. The transverse magnetic field dissipates some energy into the walls, but much less than in a normal conducting cavity.

# Chapter 5

## The Compact Muon Solenoid Experiment

The Compact Muon Solenoid (CMS) detector sits at point 5 of the LHC ring, diametrically opposite the ATLAS detector at point 1. It is a  $4\pi$  hermetic general purpose detector, meaning that it has the capability to detect charged and neutral hadrons, photons, electrons, muons, taus, neutrinos, and non-Standard-Model particles with good efficiency over a large range of rapidity. Its main distinguishing feature is a superconducting solenoid that provides a 3.8T magnetic field parallel to the beam line. This strong magnetic field allows precise determination of the momentum and charge of muons and electrons up to a momentum of  $\sim 1$  TeV.

The origin of the CMS coordinate system is at the nominal interaction point. The  $y$ -axis points skyward, the  $x$ -axis points towards the center of the LHC ring, and the  $z$ -axis points counterclockwise along the LHC ring.  $r$  denotes radial distances from the beam line,  $\phi$  is the azimuthal angle measured with respect to the positive  $x$ -axis, and  $\theta$  is the polar angle measured with respect to the positive  $z$ -axis. The *pseudorapidity*  $\eta$  is defined as  $\eta = -\ln \tan(\theta/2)$ , and is a good approximation to rapidity  $y = (1/2) \ln((E + p_z c)/(E - p_z c))$  for relativistic particles. The transverse

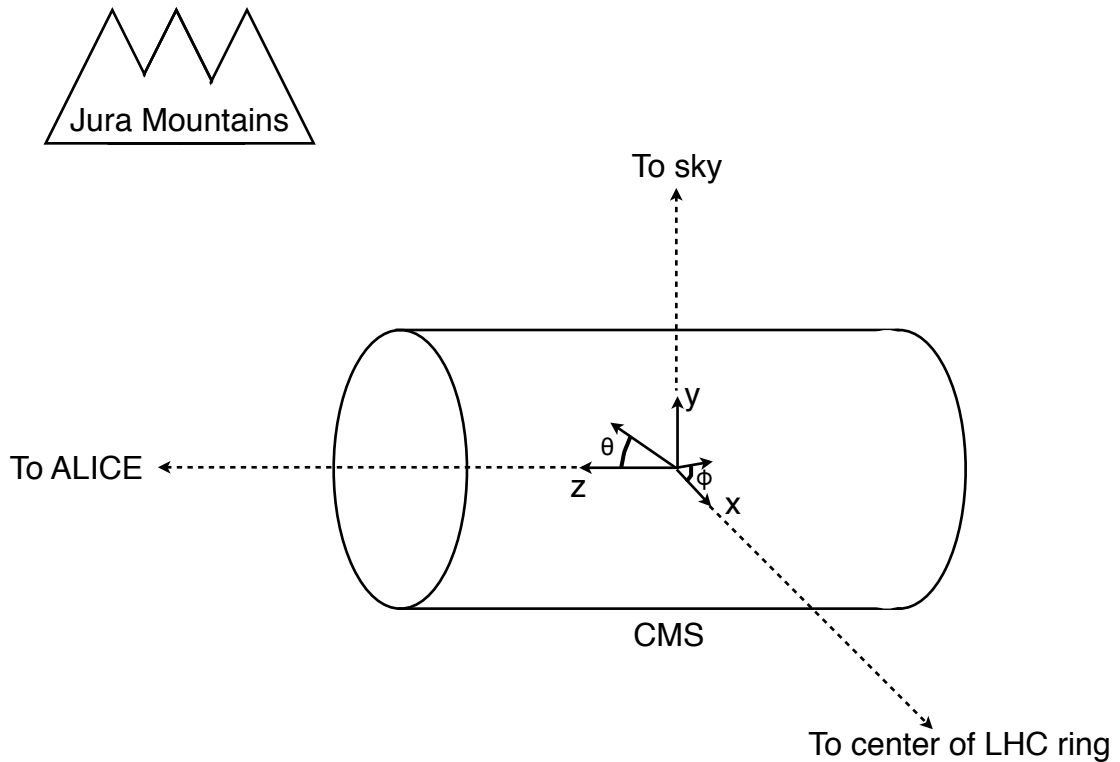


Figure 5.1: CMS coordinate system.

momentum and energy ( $p_T$  and  $E_T$ ) of a particle are defined as  $p_T = p \cos \phi$  and  $E_T = E \cos \phi$ , where  $p$  and  $E$  are the magnitude of the particle's momentum vector and the particle's total energy, respectively. A depiction of the CMS coordinate system is shown in Figure 5.1.

The CMS sub-detectors are arranged in concentric cylindrical layers, plus “end-caps,” around the beam line, as shown in Figure 5.2. Closest to the beam line are three layers of silicon pixel detectors, with the innermost at radius 4.4 cm and outermost at radius 10.2 cm [71]. Including the pixel endcaps, the total pixel coverage extends to  $\eta = 2.5$  [71]. The pixel detector plays an important role in determining the

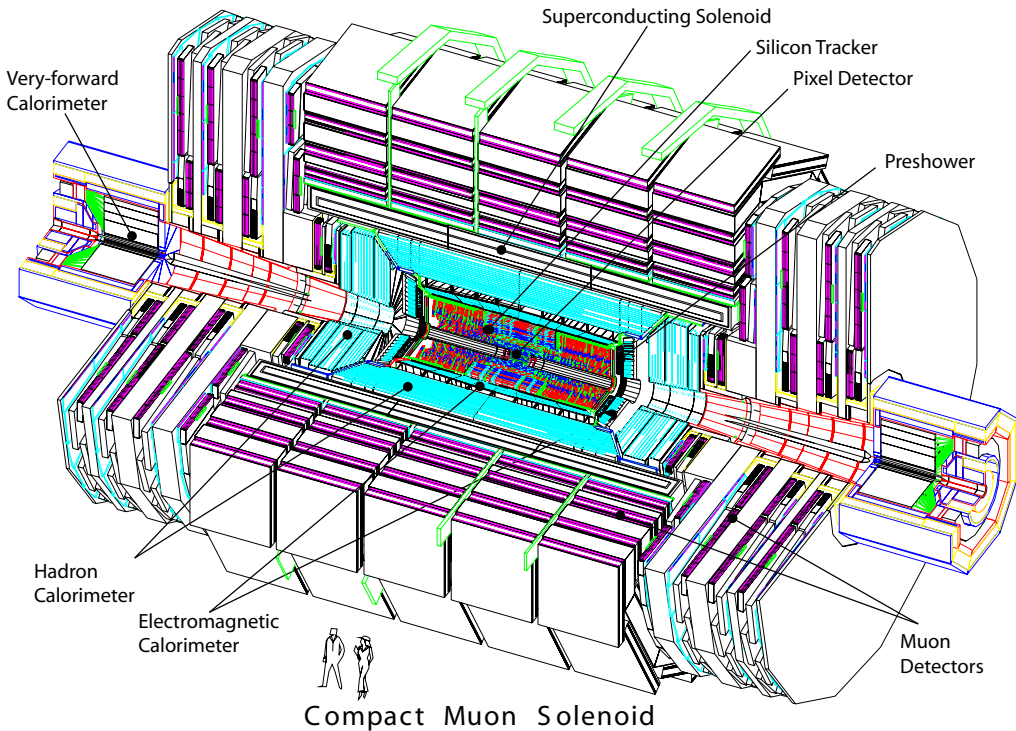


Figure 5.2: Cutaway view of CMS. Reprinted from Fig. 1.1 of ref. [71].

proton-proton interaction position (*beam spot*) and the impact parameters of charged particle trajectories, and is critical for the measurement of decay positions some distance from the beam spot (*displaced vertices*), such as those due to the showering and hadronization of a  $b$  quark.

The 10 next layers of CMS are comprised of silicon microstrip detectors, with the outermost layer at a radius of 1.3 m from the beam line [71]. As for the pixel detectors, the silicon strip endcaps extend tracking coverage to  $\eta = 2.5$ . The silicon microstrip layers are the workhorse of the CMS tracking system, and provide excellent charged particle momentum resolution and track finding efficiency.

Outside the tracking detectors are the calorimeters, starting with the single-layer lead tungstate crystal electromagnetic calorimeter at a radius of 1.3 m from the beam line (location of crystal front faces) [71]. Each crystal is 23 cm long, corresponding to 25.8 radiation lengths ( $X_0$ ) [71]. The crystal dimensions are such that most of one

electromagnetic shower, and no more, can be contained in a single crystal, leading to excellent energy resolution for photons and electrons. The electromagnetic calorimeter radial and endcap layers cover a pseudorapidity range up to 3.0. A lead/silicon sampling calorimeter sits in front of the crystal endcaps to provide better rejection of neutral pions.

The last layer of calorimetry inside the solenoid is the brass/scintillator sampling hadronic calorimeter, which has a radial extent from 1.77-2.95 m [71]. The hadronic barrel and endcap calorimeters cover up to  $|\eta| = 3.0$ , while the iron/quartz-fiber forward hadronic calorimeter covers the region  $3.0 \leq |\eta| \leq 5.2$ .<sup>1</sup> There is one more layer of hadronic calorimetry outside the solenoid in  $|\eta| < 1.3$  which, together with the layers inside the solenoid, provides approximately 12 hadronic interaction lengths of instrumented absorber. Because of its large  $|\eta|$  coverage and depth, the hadronic calorimeter provides good missing transverse energy resolution and accurate measurements of high energy jets.

The iron return yoke of the solenoidal magnetic field is interleaved with muon detectors from 4.1-7.4 m in  $r$  and 6.6-10.6 m in  $z$ , providing muon detection up to  $|\eta| = 2.4$  [71]. In the barrel region of  $|\eta| < 1.2$ , drift tubes are used to read out the muon tracks, while in the endcaps cathode strip chambers are used. Due to their speed, resistive plate chambers are used throughout the muon system to provide an independent trigger and timing measurement. Combining the tracker and muon system hits, the momenta and charge of muons up to  $p_T = 1$  TeV can be precisely reconstructed.

A longitudinal quarter cross-sectional view of CMS is shown in Figure 5.3. The remainder of this chapter is devoted to explaining the CMS subdetectors and readout systems. Section 5.1 describes the subdetector technologies and performance bench-

---

<sup>1</sup>The Centauro and Strange Object Research (CASTOR) and Zero Degree Calorimeter (ZDC) detectors provide additional calorimetry beyond  $|\eta| = 5.2$ . However, they are mainly used in the heavy ion and diffractive physics programs of CMS, and play no role in the detection of heavy SUSY particles. Therefore, they will not be discussed here.

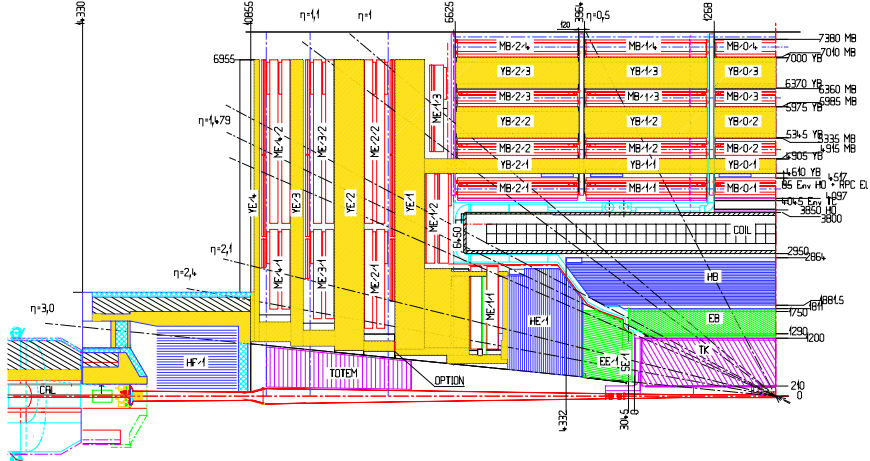


Figure 5.3: Longitudinal quarter cross-sectional view of CMS. The nominal interaction point is at the lower right-hand corner of the drawing. The tracker is shown in purple diagonal hashing, the electromagnetic calorimeter in green, the hadronic calorimeter in blue, and the muon stations in red. The solenoid is shown in black and white and labeled COIL, and the magnet return yoke is shown in yellow. Radial and longitudinal distances are measured in millimeters. Reprinted from Fig. CP 1 of ref. [72].

marks, while Section 5.2 details the CMS trigger and data acquisition systems and framework for promptly reconstructing and transferring data worldwide. For a thorough description of CMS, see ref. [71]. Unless otherwise noted, all information in this chapter comes from ref. [71].

## 5.1 The Detectors and Their Operating Principles

### 5.1.1 Tracking System

Given the LHC design instantaneous luminosity, efficient reconstruction of charged particle tracks from transverse momenta of 1 GeV up to 1 TeV can only be achieved with a low occupancy tracker. For  $r < 10$  cm, the hit rate density is highest, leading to the choice of  $100 \mu\text{m} \times 150 \mu\text{m}$  silicon pixel sensors for hit detection. For  $20 \text{ cm} < r < 110 \text{ cm}$ , the lower hit rate allows the use of silicon strips, with length along  $z$  of order centimeters and length along the  $r \cdot \phi$  curve of order hundreds of microns. This

design leads to a pixel hit occupancy of  $\sim 10^{-4}$ /pixel/BX and a strip hit occupancy of  $\sim 10^{-2}$ /pixel/BX, where BX refers to 1 LHC bunch crossing.

As radiation dose from hadrons accumulates over the lifetime of the tracker, silicon leakage current through the semiconductor junctions increases, heating up the sensors. Since the leakage current itself depends on temperature, this can lead to *thermal runaway* that damages the detector. To avoid this, the tracker must be cooled to approximately  $-10^{\circ}\text{C}$ . Operating at this temperature, the signal:noise ratio in the silicon sensors is 10:1, and should remain at that level over the 10-year lifetime of the tracker.

At its thickest ( $|\eta| \sim 1.5$ ), the tracker depth (including services) is  $\sim 1.8X_0$ , and the depth falls off to  $\sim 1X_0$  in thinner areas. Unfortunately, the large mass of the tracker degrades somewhat the performance of the electromagnetic calorimeter behind it, as  $\sim 50\%$  of photons will convert to  $e^+e^-$  pairs in the tracker.

## Pixel Detector

A longitudinal quarter view of the three barrel pixel (BPix) layers and two forward pixel (FPix) disks is shown in Figure 5.4. There are 768 BPix modules in total. Each BPix layer is divided into 32  $\phi$ -wedges, with eight modules per wedge arranged end-to-end in  $z$ . The  $\phi$ -wedges operate nearly independently in terms of clock and readout. Each FPix disk consists of 24  $\phi$ -wedges, with pie-shaped modules attached to the front and back of the disk, for a total of 192 modules. The front- and back-side modules of the FPix disks are constructed of different sized *plaquettes*, or multi-pixel sensor chips, such that the gaps in the front-side module are covered by plaquette area in the back-side module and vice versa. An illustration of the BPix and FPix mechanical layouts is given in Figure 5.5.

Since the electric field in the depletion region of the BPix sensors is perpendicular (i.e. pointing along  $r$ ) to the magnetic field of CMS (i.e. pointing along  $z$ ), the charge

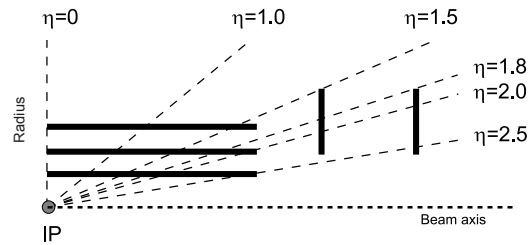
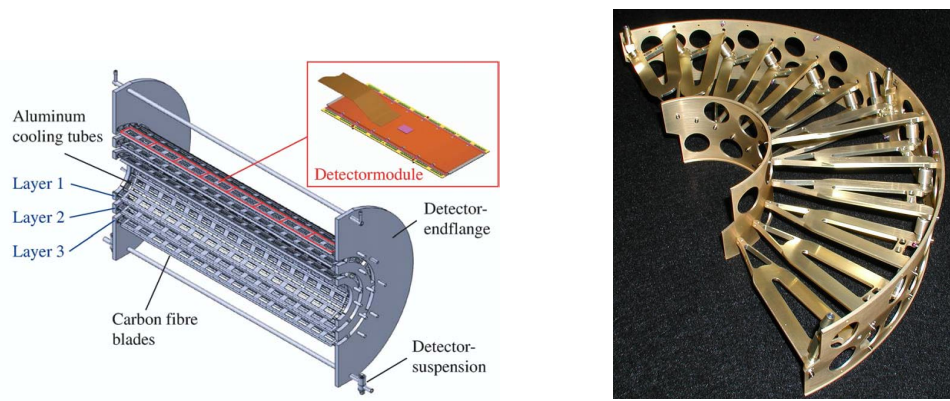


Figure 5.4: Longitudinal quarter view of the pixel detector. Reprinted from Fig. 3.6 of ref. [71].



(a) Cutaway view of the barrel pixel layers, showing the three layers and the eight end-to-end modules along  $z$ . Reprinted from Fig. 3.11 of ref. [71].

(b) Half-disk of the forward pixel detector, showing the 12 pie-shaped module mounts. Reprinted from Fig. 3.15 of ref. [71].

Figure 5.5: BPix and FPix mechanical structures.

carriers in the silicon experience a Lorentz drift along  $\phi$ . The multi-pixel sensor pitch is such that this causes the charge from one particle hit to be shared among multiple pixels. Particle hits are reconstructed reading out the analog pixel signal and interpolating between signals in multiple pixels. This method achieves a 15-20  $\mu\text{m}$  spatial resolution, which is comparable to the sensor pitch. To induce this effect in FPix, the sensor wedges are tilted by the approximate BPix Lorentz angle of 20° [73] with respect to the  $y$ -axis.

Each multi-pixel sensor consists of an array of  $52 \times 80$  n-type pixels implanted onto an n-type substrate with 320  $\mu\text{m}$  thickness. The other face of the substrate is covered with a thin layer of p-type semiconductor. Except for the outer edges, which are held at ground potential to prevent sparking between the sensor edges and the connected readout chip [74], the p-side is reverse biased at 150 V (BPix) or 300 V (FPix). The pixels are held at ground potential. A particle entering through the p-side will cause a burst of current to flow across the p-n junction. The charge will be collected by the pixels, which are bump-bonded to the readout. The BPix and FPix sensors employ slightly different technologies for electrically isolating the individual pixels, but both rely on the idea of surrounding the pixels with a p-type material to provide a p-n junction that acts as a barrier to current flow.

Each  $52 \times 80$  pixel sensor is bump bonded to a readout chip (ROC). The ROCs provide zero suppression and amplify, buffer, and communicate the signals from the sensors. A single token bit manager (TBM) controls  $\sim 16$  ROCs in the barrel or  $\sim 24$  ROCs in the endcaps. Its purpose is to distribute the clock and trigger to the ROCs (the latter initiates a transmission of the signal further upstream to be assembled into the full event readout of CMS). The clock and trigger are supplied by the pixel front end controller (pFEC), which interfaces to the central clock and data acquisition systems. Analog signals that are collected from the pixel front ends are digitized by the pixel front end digitizer (pxFED). A diagram of the readout system is shown in

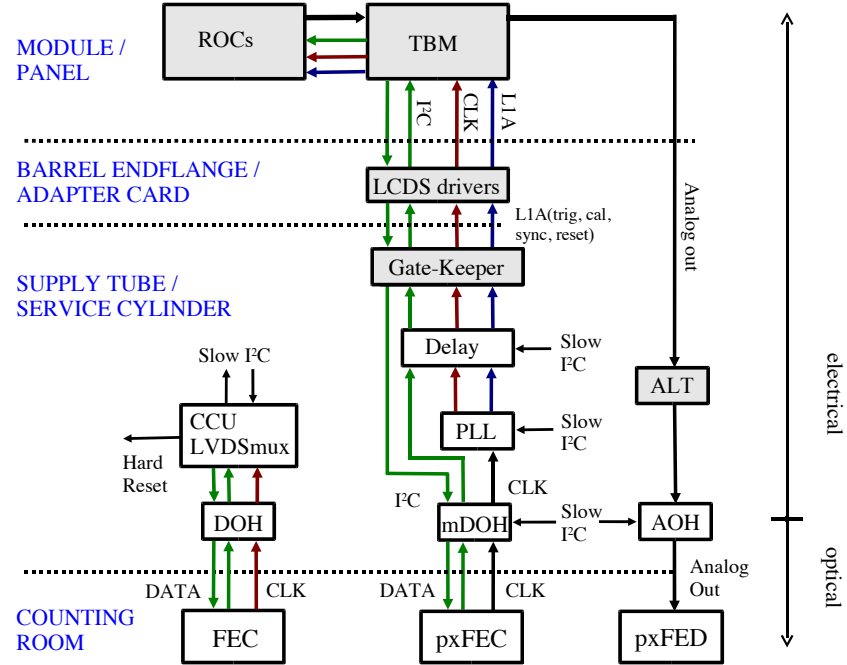


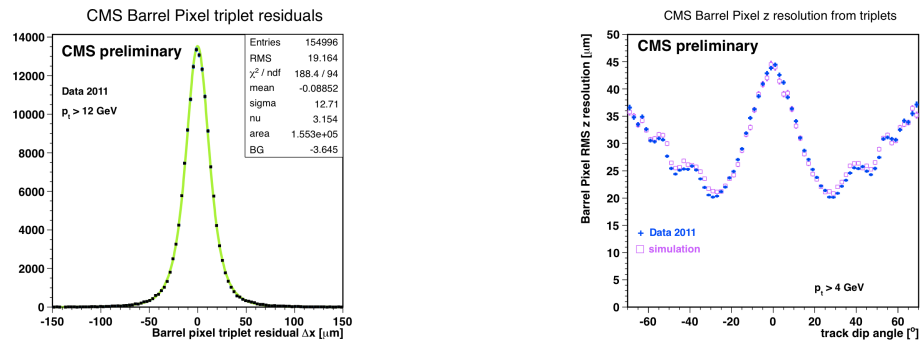
Figure 5.6: Pixel control and readout system. Reprinted from Fig. 3.9 of ref. [71].

Figure 5.6.

Figure 5.7 shows some results highlighting the performance of the pixel detector.

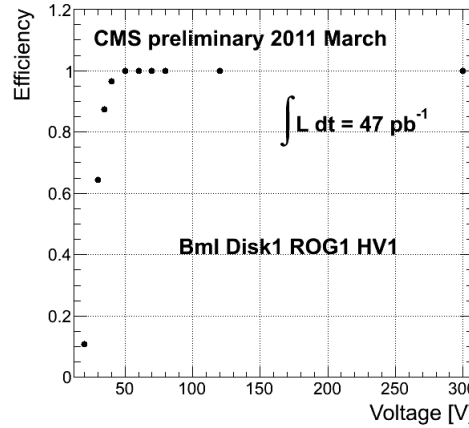
### Silicon Strip Tracker

The silicon strip tracker is divided into four parts: the inner barrel (TIB) and inner disks (TID), covering the radial extent  $20 \text{ cm} < r < 55 \text{ cm}$  and  $z$  extent  $80 \text{ cm} < |z| < 90 \text{ cm}$ ; and the outer barrel (TOB) and endcap (TEC), covering the radial extent  $61 \text{ cm} < r < 108 \text{ cm}$  and  $z$  extent  $124 \text{ cm} < |z| < 282 \text{ cm}$ . A number of the tracker layers and endcaps hold double-sided strip modules (shown as double lines in Figure 5.8), with the rear module tilted at an angle of 100 mrad with respect to the front module, to provide a measurement in two coordinates. There are a total of 15,148 modules in the tracker, arranged as shown in the longitudinal cross-sectional view of Fig. 5.8. For the TIB and TOB, the modules are arranged in straight rows end-to-end along  $z$ , with repeating rows covering the full  $2\pi$  extent in  $\phi$ . In each of the



(a) BPix hit resolution in the  $r \cdot \phi$  coordinate [75].

(b) BPix hit resolution in the  $z$  coordinate vs. track dip angle, showing the effect of charge sharing on resolution [76].



(c) Pixel reconstruction efficiency vs. bias voltage for a group of three wedges in FPix [77].

Figure 5.7: Pixel detector performance highlights.

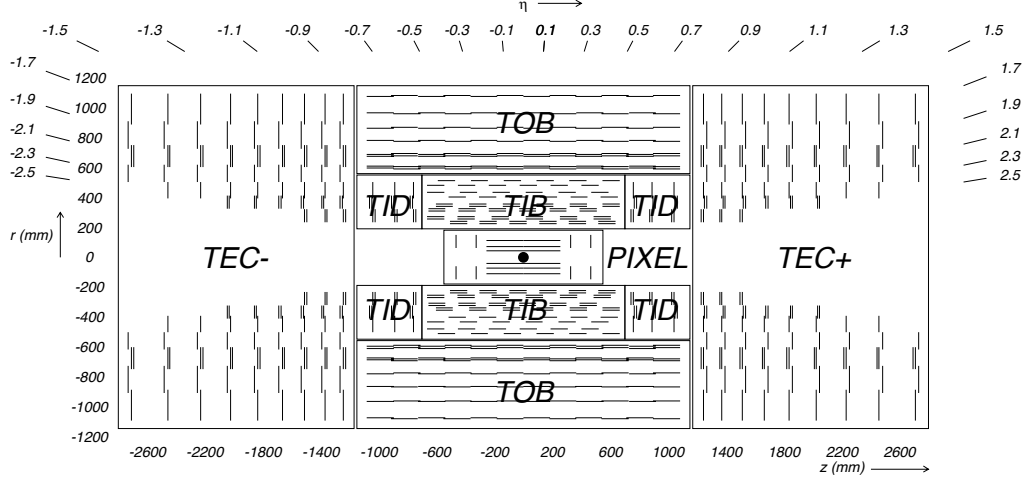


Figure 5.8: Longitudinal cross section of the silicon strip detector. Reprinted from Fig. 3.1 of ref. [71].

TID disks, the modules are arranged into three concentric circular rings of increasing  $r$ . In the TEC, the modules are affixed to  $\phi$ -wedges called *petals*. One side of the TEC and its petal structure is shown in Figure 5.9.

Like the pixels, the strip sensors generate a signal when current flows across a p-n junction in response to interaction with a charged particle. Whereas the pixels are n-type implants on an n-type substrate, with a solid p-type rear layer to which the high voltage is connected, the strips are p-type implants on an n-type substrate, with a solid n-type rear layer connecting to the high voltage. The p-n junction in the strip sensors is at the strip-substrate boundary, whereas in the pixel sensors it is at the boundary between the rear layer and the substrate. Each sensor has either 512 or 768 electrically isolated strips, with pitch varying from 80-205  $\mu\text{m}$  depending on location. Strip lengths in  $z$  range from  $\sim 10$  to  $\sim 25$  cm. Thin (320  $\mu\text{m}$ ) sensors are used in the TIB, TID, and inner four rings of the TEC, while thick (500  $\mu\text{m}$ ) sensors are used in the TOB and the outer rings of the TEC. The thicker sensors compensate for the increased strip capacitance (and hence electronics noise) of the longer strips in the outer layers/disk of the tracker such that strip signal:noise is maintained above 10 everywhere.

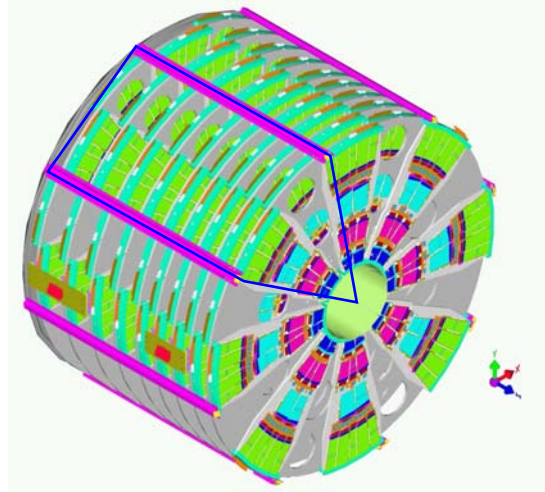


Figure 5.9: View of one tracker endcap, with the outline of a petal shown in blue. There are nine petals per wedge-shaped sector (one per TEC disk). Reprinted from Fig. 3.30 of ref. [71].

The strips are wire bonded to a front end readout chip called the APV25. The APV25 amplifies and shapes the strip signals before sending the full analog pulse information to an APVMUX, which multiplexes the output of two APV25s. Then, the electrical signal from the APVMUX is sent differentially a few centimeters to an optical driver, where it is converted to an optical signal and sent to one of the 450 front end drivers (FEDs). The FEDs convert the signal back to an electrical pulse and digitize it for use in the global event assembly. As for the pixels, analog readout is used on detector so that hit reconstruction may benefit from charge sharing.

Clock, trigger, and control signals are sent from the front end controllers (FECs) to phase locked loop (PLL) chips on the front ends. The FECs interface to the global clock and trigger system. Four or six APV25s, an APVMUX, and a PLL chip all sit on a *hybrid*, two of which one thin or two thick sensors are also affixed. The sensor-hybrid combination and its frame form a module. Figure 5.10 shows a diagram of a module, while Figure 5.11 shows a block diagram of the strip readout architecture.

As an example of the strip capabilities, strip hit resolution and signal:noise measurements are shown in Figure 5.12. The entire pixel + strip tracker has been used

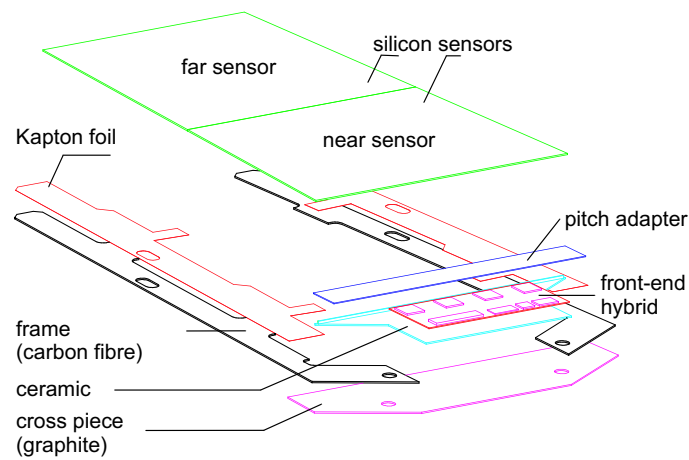


Figure 5.10: Exploded view of a strip module with two sensors. Reprinted from Fig. 3.22 of ref. [71].

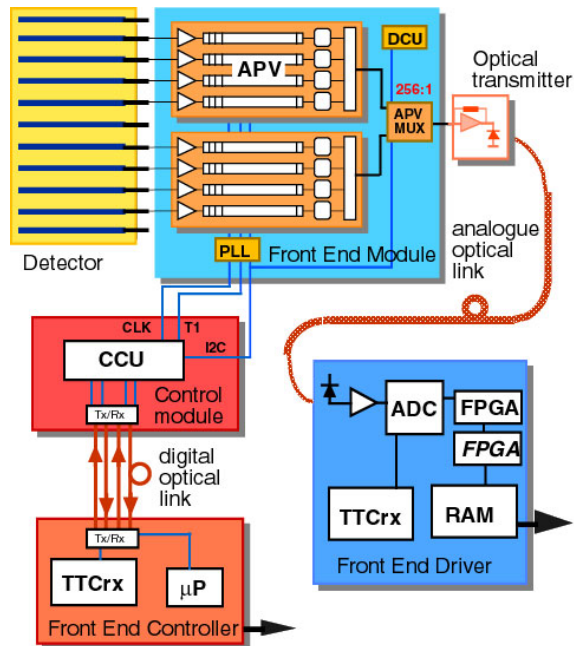


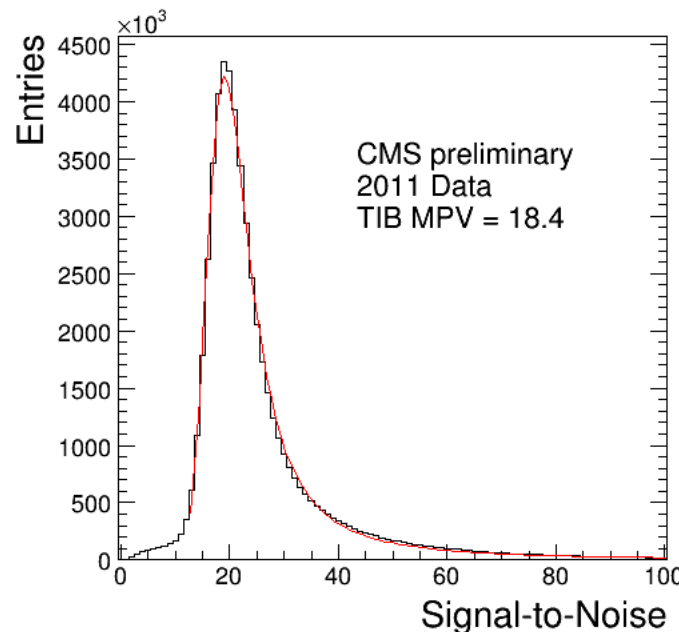
Figure 5.11: Block diagram of the strip readout architecture. Reprinted from Fig. 3.20 of ref. [71].

successfully in the reconstruction of primary and secondary vertices, electrons, muons, tau decays, and charm and bottom hadron decays. In addition, the superior performance of the tracker over the hadronic calorimeter for low energy charged hadrons has been exploited in the the particle flow jet and  $\cancel{E}_T$  reconstruction technique (see Sec. 6.1.3). The CMS silicon strips, as well as the pixels, are well aligned and operating at close to design performance.

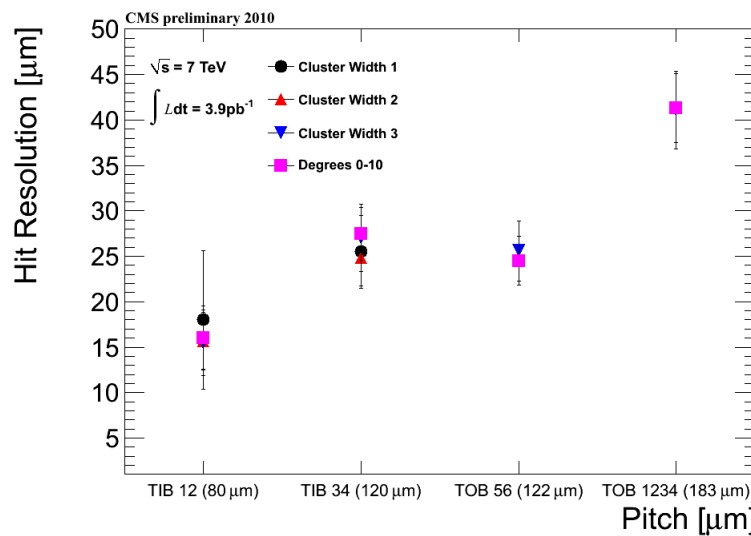
### 5.1.2 Electromagnetic Calorimeter

The electromagnetic calorimeter (ECAL) is composed of 75,848 lead tungstate ( $\text{PbWO}_4$ ) crystals, divided into one barrel (EB) layer and two endcap (EE) disks. In EB, there are 1700 crystals per *supermodule* (SM), arranged in a  $20 \times 85$  grid in  $\phi \times \eta$ . Two SMs are laid out end-to-end to form one row at fixed  $\phi$ , with a total of 18 rows needed to cover the entire  $2\pi$  extent in  $\phi$ . The SMs may be operated independently. In EE, the independent unit is a wedge-shaped sector, with nine sectors covering each endcap side. The 14,648 EE crystals are divided approximately evenly between the 18 EE sectors. A two-layer preshower detector is placed in front of the EE disks, each layer consisting of a lead absorber followed by 1.9 mm pitch silicon strip detectors (the strips in the first layer are rotated 90° with respect to the second layer). The ECAL layout is shown in Figure 5.13.

The electromagnetic energy resolution can be parametrized as  $(\sigma/E)^2 = (S/\sqrt{E})^2 + (N/E)^2 + (C)^2$ , where  $S$  characterizes the size of photostatistical fluctuations,  $N$  characterizes the contribution from electronics noise, and  $C$  is a constant accounting for imperfect intercalibration between crystals, non-uniformity of crystal performance, and incomplete shower containment within one crystal. The design goal of the ECAL is to achieve  $C = 0.5\%$ . Therefore, fast, dense, and relatively radiation hard  $\text{PbWO}_4$  was chosen as the crystal material. When a photon or electron strikes the crystal, it initiates an electromagnetic (EM) shower. Due to the density, short radiation length,



(a) TIB signal:noise [78].



(b) TIB and TOB hit resolution as a function of strip pitch [79].

Figure 5.12: Strip detector performance highlights.

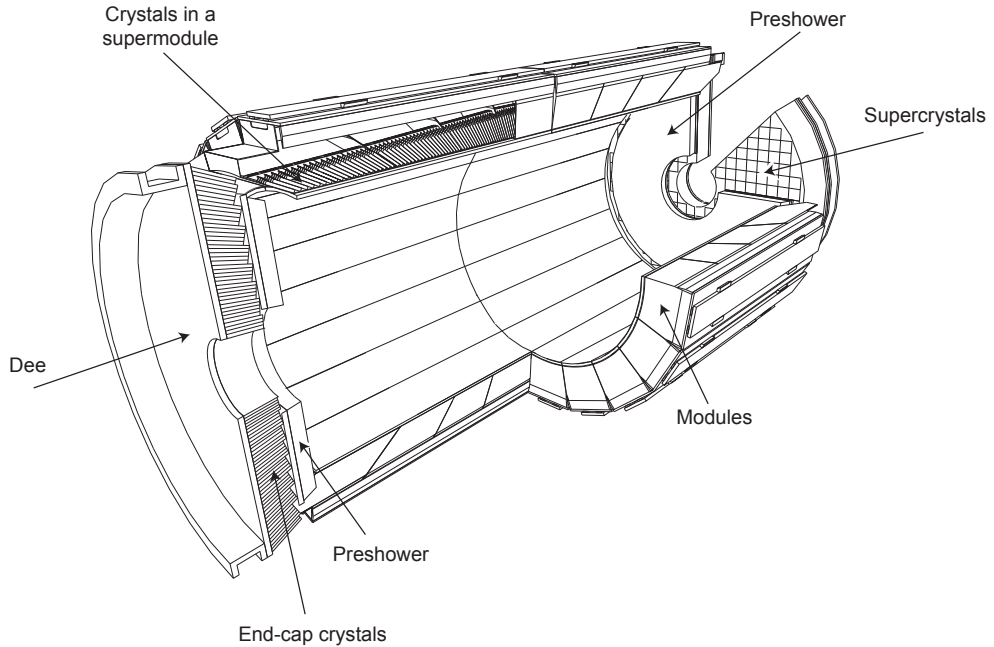


Figure 5.13: Layout of the ECAL detector. Reprinted from Fig. 4.5 of ref. [71].

and small Molière radius of  $\text{PbWO}_4$ , nearly the entirety of an EM shower can be contained in a single 23-cm long crystal with front face dimensions  $2.2 \text{ cm} \times 2.2 \text{ cm}$ . The crystals scintillate in the blue-green part of the spectrum at 440 nm, emitting  $\sim 80\%$  of the scintillation light within 25 ns. Light is transmitted along the length of the crystals and collected at the rear with avalanche photodiodes (APDs; semiconductor diodes) in EB or vacuum phototriodes (VPTs; conventional photomultipliers) in EE. Since the light output is low and varies with temperature, the crystals must be kept precisely at  $18^\circ\text{C}$ . The EB and EE crystals, which are slightly tapered to match the lateral shower development, are shown in Figure 5.14.

For each trigger, 10 samples, each separated by 25 ns, are read out. The 10-sample pulse is amplified and shaped by a multi-gain preamplifier (MGPA) residing on a very front end (VFE) card serving five crystals. The MGPA can switch between gains 1, 6, and 12 to avoid saturation of the electronics, and affords a dynamic range up to 3 TeV. The samples are digitized on the VFE card, then sent to the front end (FE)

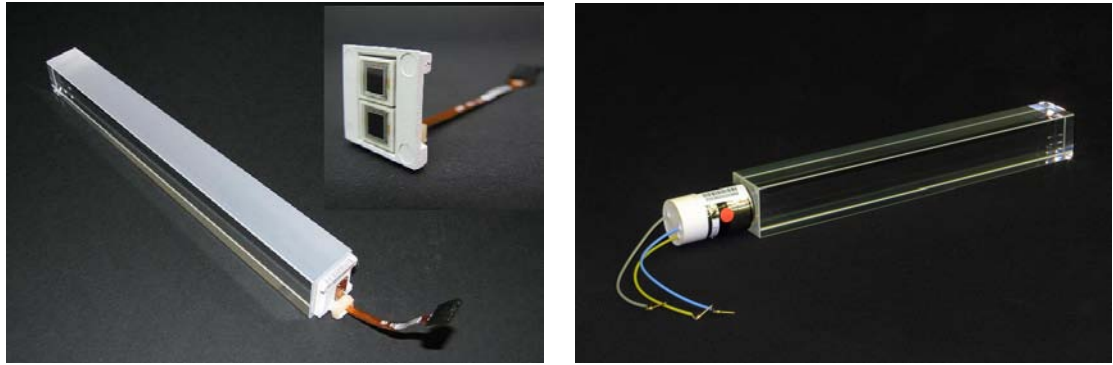


Figure 5.14: Left: EB crystal with attached APD. Right: EE crystal with attached VPT. Reprinted from Fig. 4.2 of ref. [71].

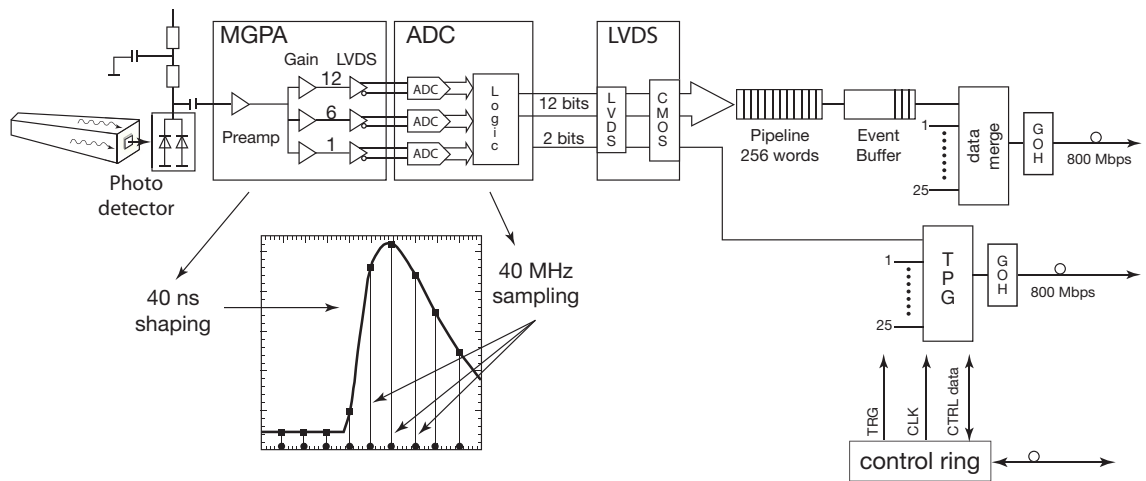


Figure 5.15: Flow chart of the crystal readout, showing the 10-sample pulse shape. Reprinted from Fig. 4.9 of ref. [71].

card serving five VFEs. Digitized samples are buffered in the FE card until receipt of a trigger, when they are sent over an optical link to the data concentrator card (DCC) that interfaces to the global DAQ. The DCC interfaces to the *selective readout* processor, which decides whether a crystal should be read out with or without zero suppression based on its proximity to a high-energy hit. The clock is transmitted to the FE cards from the Clock and Control System (CCS) boards. A flow chart of the crystal readout is given in Figure 5.15.

At each bunch crossing, the trigger concentrator cards (TCC) of the ECAL com-

pute *trigger primitives* from  $5 \times 5$  non-overlapping transverse energy sums (in the endcaps the geometry is not always  $5 \times 5$ ). This information, along with a special bit in EB only characterizing the transverse shower profile that is used for rejection of anomalous APD hits (see Sec. 6.1.1), is transmitted from the TCCs to the synchronization and link boards (SLBs), and then on to the global trigger system. The trigger decision is communicated to the DCCs, which request the buffered data from the front ends if the decision is affirmative.

Despite the radiation hardness of lead tungstate relative to other types of crystals, it still suffers from transparency loss due to radiation-induced lattice damage, as shown in Figure 5.16. In addition, any unforeseen change in the gains of the MGPAs and VPTs, or in the pedestal levels, will degrade the energy resolution. For this reason, a continuously running calibration system is installed with the ECAL. The system makes use of the LHC abort gaps to read out the pedestal levels, test pulses fired into the MGPAs, and laser (EB and EE) or LED (EE only) pulses fired into the crystals at regular intervals. Laser and LED events are used to compute corrections to the crystal gains for transparency loss, while the other types of calibration events serve to monitor changes in the electronics performance due to magnetic field or high voltage cycling. The mean time between transparency measurements is  $\sim 40$  minutes. Figure 5.17 shows the architecture of the laser monitoring system. The additional EE light monitoring system consisting of LEDs serves to (a) stabilize the response of the VPTs and (b) corroborate the laser calibration measurements. I describe it here in some detail because it is my principal contribution to the CMS detector.

VPT gains are known to be sensitive to the frequency and amplitude of incident light [81]. In general, as the pulsing frequency increases the gain decreases and vice versa, but some VPTs may exhibit a different dependence on rate changes. The gain changes are most abrupt when a source of pulsed light (i.e. the LHC) is suddenly turned on or off. Deviations of a few percent to over ten percent have been observed

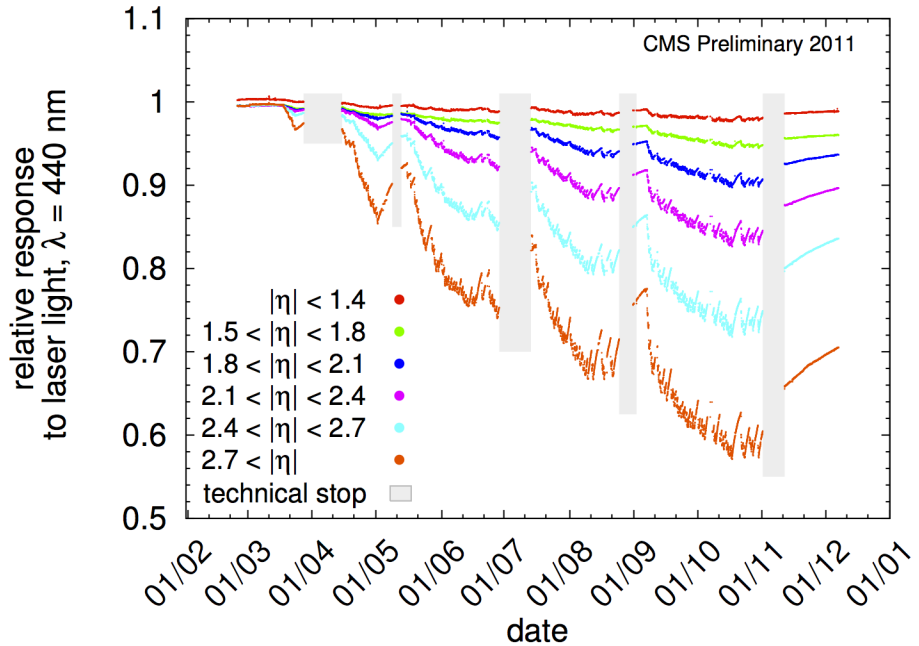


Figure 5.16: Relative response of the crystals to blue laser pulses from February 1, 2011 to January 1, 2012 [80]. Technical stops, during which the LHC is turned off for maintenance and development, are shown in gray. These periods of inactivity correspond to growth in the crystal response, as radiation damage recovery occurs.

in the lab (see Figure 5.18). The EE LED system mitigates the effects of LHC beam injections and dumps on the stability of the VPTs by continuously providing light pulses to the VPTs, irrespective of the state of the beam. At LHC on/off transitions, the frequency change seen by the VPTs is therefore less severe due to the continuous presence of the background LED pulse, leading to a reduced change in gain. Note that although the VPT effect is strongly suppressed in the 3.8 T magnetic field of CMS, the LED system is still required in light of the stringent requirements on ECAL stability imposed by the  $C = 0.5\%$  resolution goal. At present, there is no indication of a significant VPT effect discernible on top of the radiation damage, but in the future improved calibration precision will demand control over small effects like VPT gain fluctuations.

In addition to their stabilizing effect, the LED pulses are also read out as part of the ECAL calibration cycle and used to correct for crystal transparency loss and

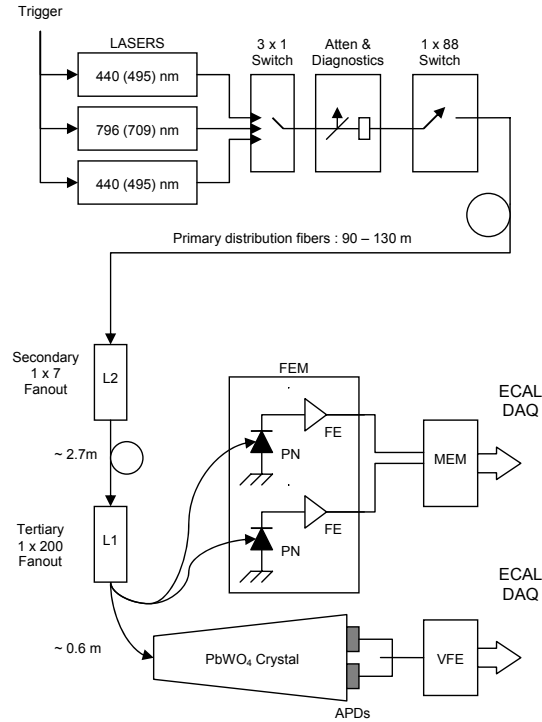


Figure 5.17: Architecture of the laser monitoring system. Reprinted from Fig. 4.16 of ref. [71].

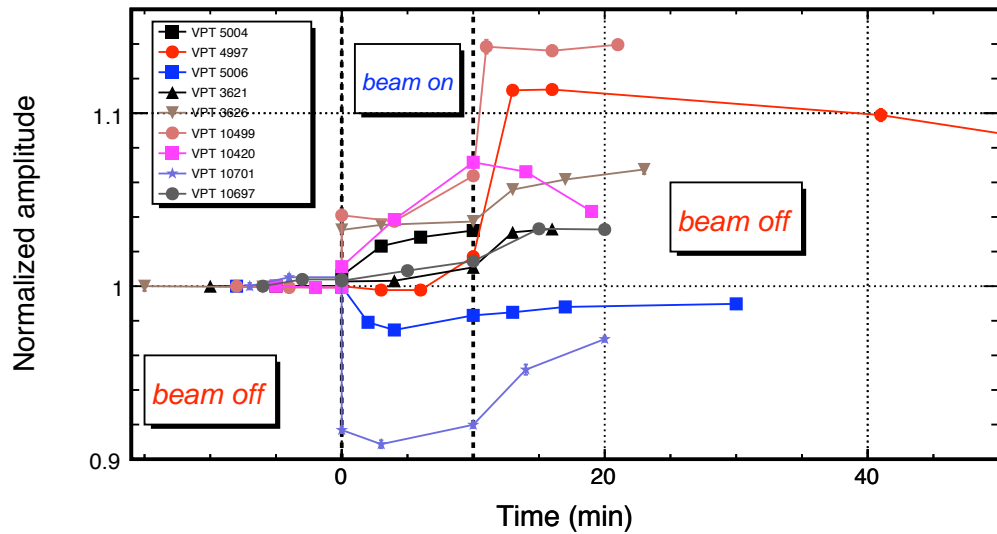


Figure 5.18: Change in response of nine different VPTs in zero magnetic field vs. time. The response of each VPT is normalized to its response for the earliest data point taken. For times less than 0, no light pulsing is applied to the VPTs. For times between 0 and 20 minutes, pulsed LED light was applied to the VPTs. For times later than 20 minutes, the pulsing source was again removed.

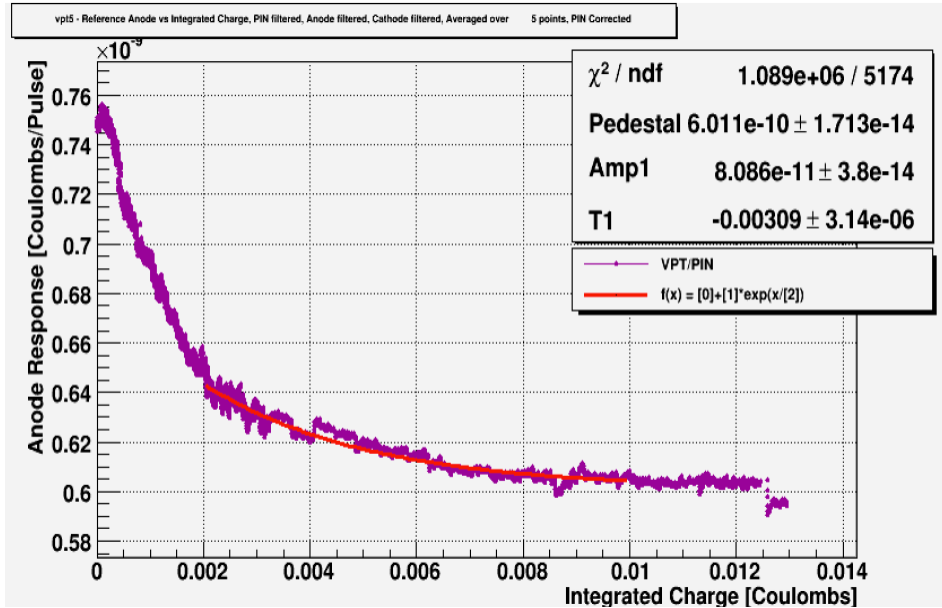


Figure 5.19: VPT response in a 3.8 T laboratory magnetic field to blue LED light vs. integrated charge at photocathode [82]. The response is corrected for changes in the LED light output by PIN diode normalization. For integrated charge less than  $\sim 0.003$  C, the average current draw at the photocathode is  $\sim 1$  nA, delivered by blue LED triggered at 2 kHz. For integrated charge greater than  $\sim 0.003$  C, the average current draw is  $\sim 10$  nA from a 20 kHz trigger rate.

VPT gain loss due to aging. Figure 5.19 shows the decrease in response of a VPT in the lab at 3.8 T as a function of integrated charge at the VPT photocathode. The loss of response due to photocathode aging differs from VPT to VPT, but a typical value is  $\sim 25\%$  per 0.05 C of integrated charge. The intrinsic time stability of LEDs (sub-percent) over the laser (few percent) used for ECAL calibration makes the LED information very useful despite the smaller light intensity delivered. LED data are used to correct for transparency loss and VPT aging whenever laser data are missing due to technical problems.

The LED system utilizes two wavelengths. Blue LEDs, at 450 nm wavelength, are near the peak of the crystal scintillation and VPT photocathode efficiency, and therefore are ideal for transmitting the maximum amount of light to VPTs for stability pulsing. Orange LED light, at 617 nm wavelength, is transparent to the crystals but still somewhat efficient for the VPT photocathode, allowing loss of response from

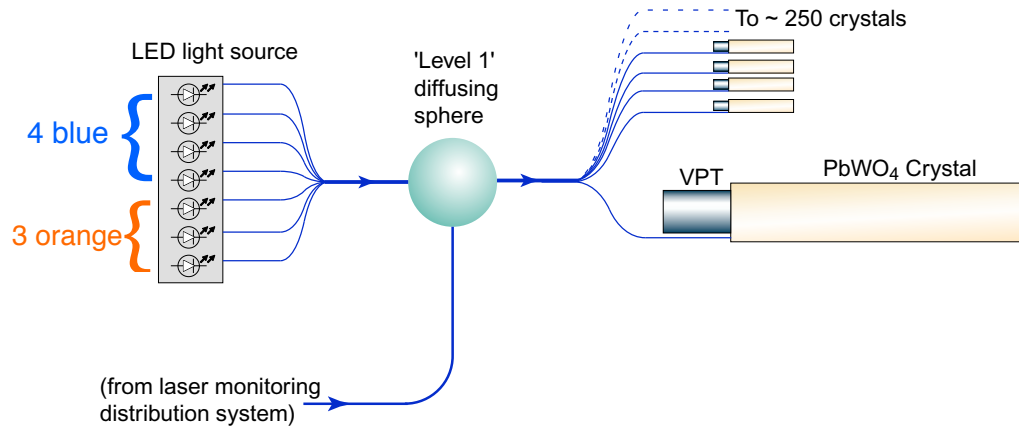


Figure 5.20: Diagram of the LED inputs to a diffusing sphere and the fanout to the crystals. Adapted from Fig. 4.8 of ref. [71].

crystal damage to be disentangled from VPT gain changes. In addition, the orange wavelength serves as a second calibration wavelength in EE, where there is only a blue laser. Each endcap disk holds 38 LED circuits, with each circuit driving four blue and three orange LEDs. Each of the seven LEDs of a circuit is coupled to the same diffusing sphere by an optical fiber whose cleaved end is stuck inside a hole drilled into the LED surface. The light entering the diffusing sphere is fanned out to  $\sim 200$  crystals + two PN diodes for tracking of the stability of the LED itself. A diagram of the inputs and outputs of a single diffusing sphere is shown in Figure 5.20. 38 diffusing spheres cover a single endcap disk.

The LED driver circuits are grouped into boxes that serve six, four, or three diffusing spheres each, for a total of four boxes per half-endcap “dee” (eight per disk). Each box is powered from supplies residing in the underground control room at Point 5. One power supply channel feeds four LED boxes. The four boxes per

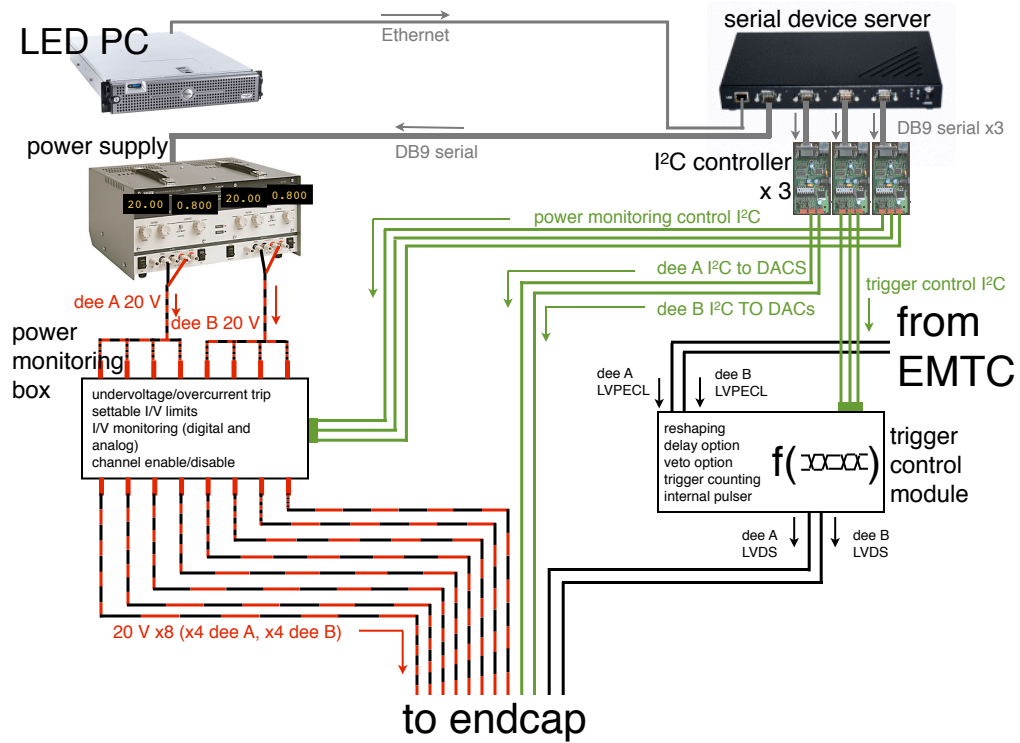


Figure 5.21: Hardware setup of the LED system.

dee receive a common clock signal and LED pulse trigger from a control box in the underground control room. The amplitude of a group of four blue or three orange LEDs is controlled by a single digital-to-analog converter (DAC) chip. For the blue LED groups, the amplitude ranges from zero to  $\sim 50$  GeV equivalent. Due to the lower photocathode efficiency for orange light, the amplitude of orange groups ranges from zero to  $\sim 5$  GeV equivalent. Power distribution, LED amplitudes, and pulse widths and delays are set by a computer program that interfaces to the hardware via an Ethernet-to-serial converter. The hardware setup of the LED system is shown in Figure 5.21.

The LED system has two modes: calibration, in which both blue and orange LED pulses are read out and processed for calibration purposes; and stability, in which blue LED pulses are fired continuously but not read out. During a calibration cycle, the LED system is in stability mode except during the calibration mode readout

periods. For a given EE wedge, these calibration periods occur approximately every 40 minutes and last  $\sim 6$  seconds. Orange or blue LED triggers are read out during the calibration periods. Once they end, the EE wedge returns to stability mode. Critically, stability pulsing occurs both inside and outside of a CMS data taking run, insuring the stability of the VPTs. The calibration and stability pulsing rates, as well as the overall health of the LED hardware, is monitored every ten minutes.

Calibration and stability triggers come once per LHC abort gap (see Sec. 4.2). The calibration trigger readout rate is always 100 Hz, corresponding to a trigger every 114 abort gaps, while the stability pulsing rate can range between 100 Hz and 11.4 kHz (corresponding to a trigger every abort gap) in steps of 100 Hz. The stability pulsing rate cannot go below 100 Hz (unless it is exactly 0 Hz) because the pulse itself is generated upon receipt of a calibration trigger. For calibration events, the entire 119-bunch-crossing long abort gap is dedicated to calibration triggers. However, in the rest of the abort gaps, only the last 35 bunch crossings of the gap are reserved for LED stability pulses. This arrangement allows the rest of the abort gap to be used to search for long-lived exotic particles decaying at random with respect to the LHC collision frequency [83]. A very small portion of the tail of the triggered VPT pulse “leaks” into the first few bunch crossings of the orbit following the abort gap, leading to an increase in the pedestal level of  $\sim 0.7$  ADC counts (compared to a noise level of  $\sim 2$  ADC counts).

Transitions between calibration and stability modes are executed by selectively zeroing the amplitudes of certain LED groups and maximizing the amplitudes of others. The computer program that controls the DACs of the LED system is itself controlled by a server running on a dedicated PC at Point 5. This server listens to commands from a program that coordinates the calibration cycles and consequently dictates the state of the LEDs (on or off) at any given time. Status information is sent back to the master program from the LED server. The master program is an XDAQ

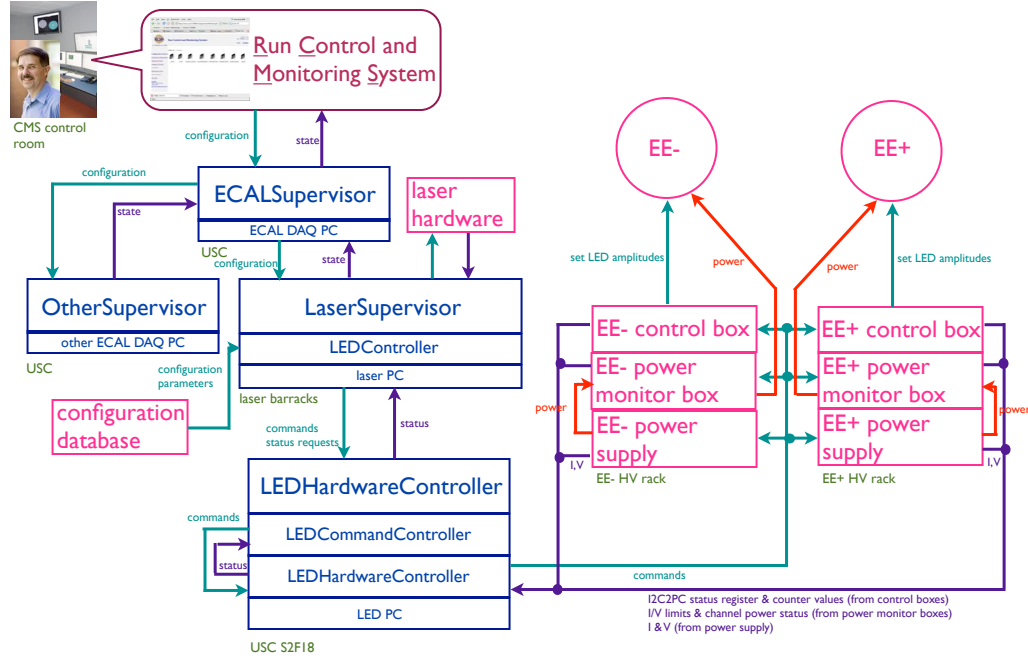


Figure 5.22: Software control flow of the LED system.

executive (see Sec. 5.2.2) that itself interfaces to the top level CMS run control. A diagram of the software control flow is given in Figure 5.22.

The current ECAL energy resolution is somewhat worse than the design goal of 0.5%. An incomplete understanding of (a) the transparency loss and (b) the photon conversion and electron bremsstrahlung processes in the  $\sim 1X_0$  of tracker material in front of the ECAL are the main limiting factors in improving the resolution. However, as more data accumulate, more refined models of transparency loss and EM interactions in the tracker can be built, leading to better resolution. Energy resolution vs.  $|\eta|$  can be seen in Figure 5.23.

The 10-sample readout coupled with the fast scintillation time of lead tungstate allows for a very precise reconstruction of the time of ECAL hits. ECAL timing is used for searches for long-lived particles that decay to photons or jets, such as long-lived neutralinos in GMSB [86]. Figure 5.24 shows the timing resolution in EE.

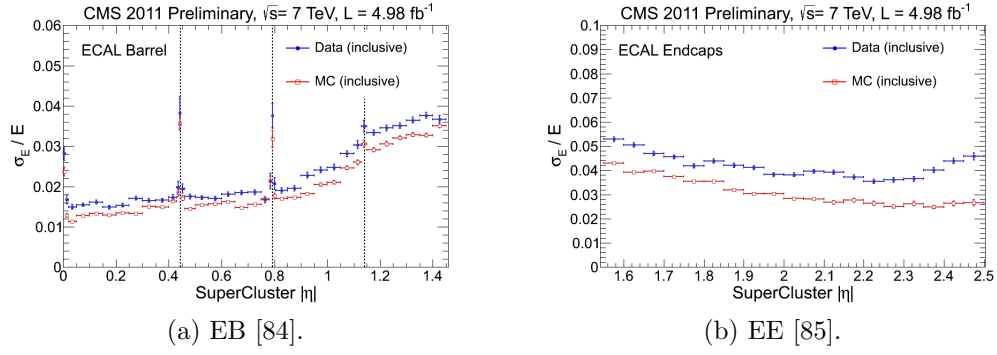


Figure 5.23: Energy resolution vs.  $|\eta|$  for  $Z$  decay electrons for data (filled blue circles) and MC (empty red squares). The dotted lines show the locations of module gaps (three per SM).

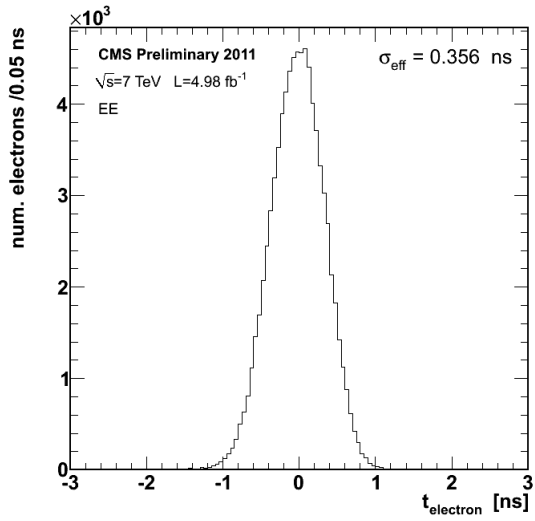


Figure 5.24: Distribution of reconstructed times of  $Z$  decay electrons in EE [87].

### 5.1.3 Hadronic Calorimeter

The CMS hadronic calorimeter (HCAL) has four parts: HCAL barrel (HB), HCAL endcap (HE), and HCAL outer (HO), which all utilize the same brass absorber / plastic scintillator sandwich technology; and HCAL forward (HF), which is a Čerenkov detector made of quartz fibers. A quarter longitudinal cross-sectional view of HCAL is shown in Figure 5.25. Like EB, HB is formed of 36  $\phi$ -wedges (18 cover  $2\pi$  in positive  $\eta$ , 18 cover  $2\pi$  in negative  $\eta$ ). Each wedge is divided into 16 along  $\eta$  and four along  $\phi$ , for a total of 64 readout towers per wedge (compare 1700 individually read out crystals per EB wedge). HE is divided into 36  $\phi$ -wedges containing 38 readout towers each. HO consists of five rings around HB and HE distributed symmetrically along  $z$ . There are 72  $\phi$ -slices per ring, with each  $\phi$ -slice further divided into 5, 6, or 8 along  $z$  depending on ring. The HF fibers are distributed within the steel absorber. HF is divided into 18  $\phi$ -wedges per endcap side, each containing 24 readout towers. All HB towers have a single readout channel except for the two in each wedge at highest  $|\eta|$ , which are segmented into two longitudinal layers for readout. In HE, all towers have two longitudinal readout layers, except for the three rings of towers closest to the beam line, which have three. There are also two longitudinal depths of HF fibers.

HB, HE, and HO are all sampling calorimeters consisting of alternating layers of brass absorber and plastic scintillator. The absorber initiates the hadronic shower, and as shower particles travel through the scintillator the scintillation light is read out by wavelength-shifting (WLS) fibers connected to the scintillator tiles.<sup>2</sup> The full development of the shower is sampled by the layers of instrumented scintillator. The scintillator tiles are staggered so that there are no cracks in coverage along the direction projected back to the beam spot. Light output from all tiles in a single readout tower is collected via the WLS fibers and merged into a single signal that is amplified

---

<sup>2</sup>By contrast, in the ECAL, the crystal material acts as both absorber and scintillator, greatly reducing the contribution to energy resolution from sampling fluctuations.

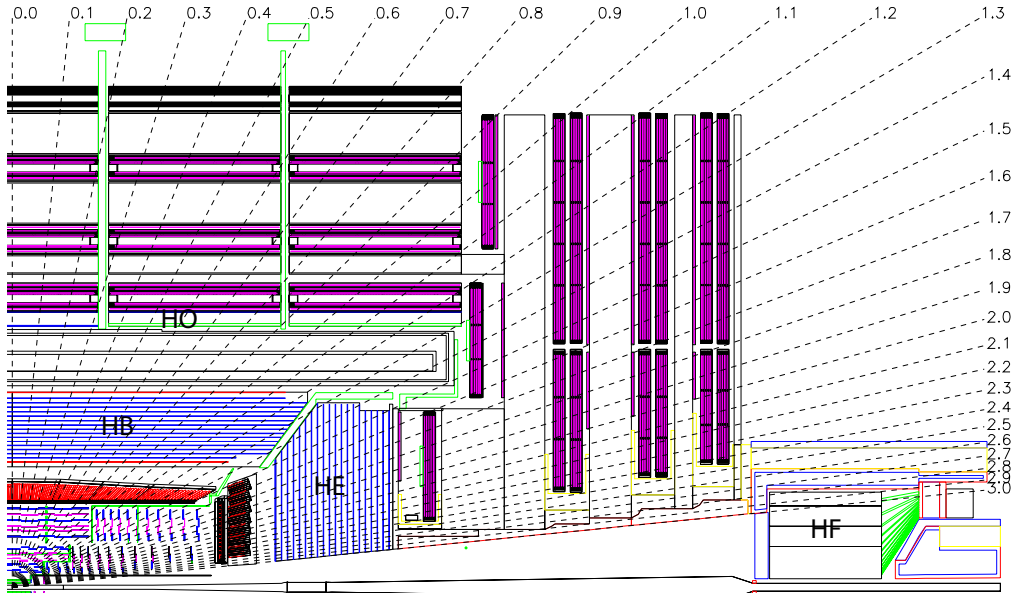


Figure 5.25: Quarter longitudinal cross-sectional view of HCAL (and muon stations in purple). Reprinted from Fig. 5.1 of ref. [71].

by a hybrid photodiode (HPD). A diagram of the optical readout of HB (similar for HE and HO) is shown in Figure 5.26.

Due to the extremely harsh radiation environment near the beam line, HF is constructed of a 1.2-m thick, 1.7-m long ring of steel absorber with radiation hard quartz fibers distributed within the steel and running parallel to the beam line. Hadronic showers develop in the steel and are sampled in the quartz fibers when charged shower particles hit the the fibers and emit Čerenkov light. The light is transmitted by total internal reflection down the fibers to a photomultiplier tube (PMT), where the signals from all fibers in an HF tower are merged into one. Since only relativistic particles emit Čerenkov light in these fibers, it is mostly the EM component of the hadronic shower, consisting of neutral pions decaying to photons that interact electromagnetically with the absorber, that is sampled [88]. The charged hadrons produced in hadronic showers are typically too slow to generate Čerenkov light. Figure 5.27 shows a cross-sectional view of one side of HF.

Electrical signals from either HPDs (HB/HE/HO) or PMTs (HF) are digitized on

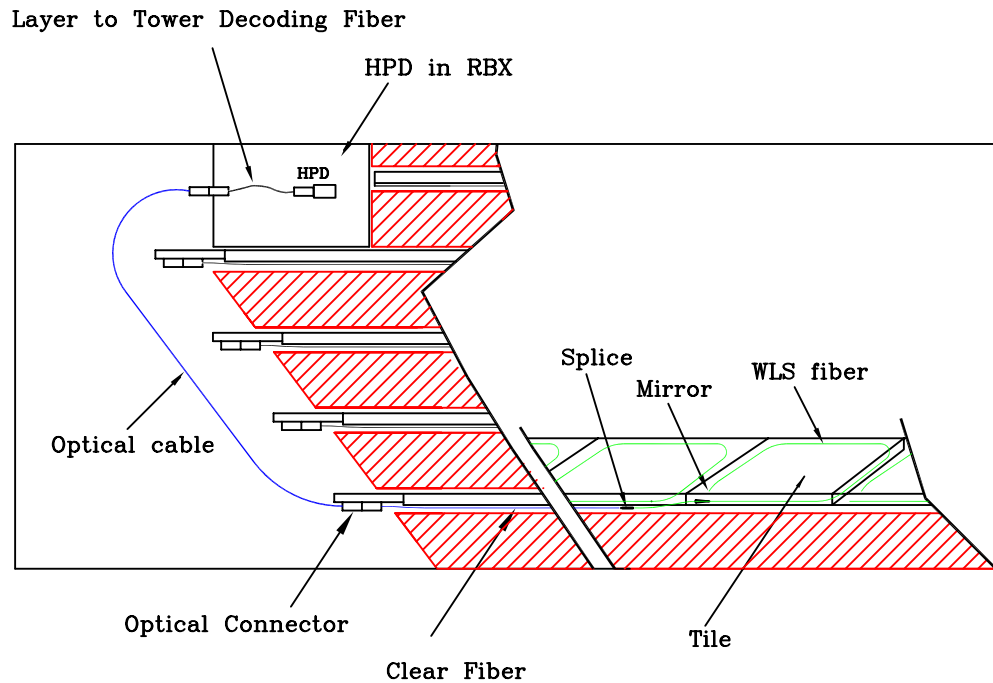


Figure 5.26: Diagram of the optical readout of HB. Reprinted from Fig. 5.7 of ref. [71].

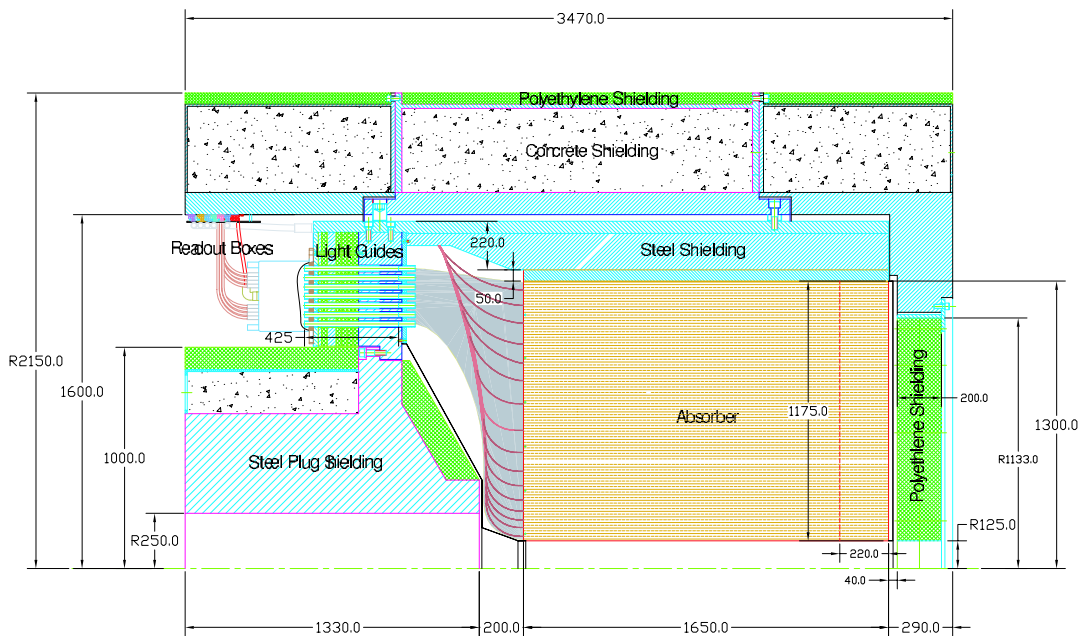


Figure 5.27: Cross-sectional view of one side of HF. The z-axis is horizontal. Reprinted from Fig. 5.28 of ref. [71].

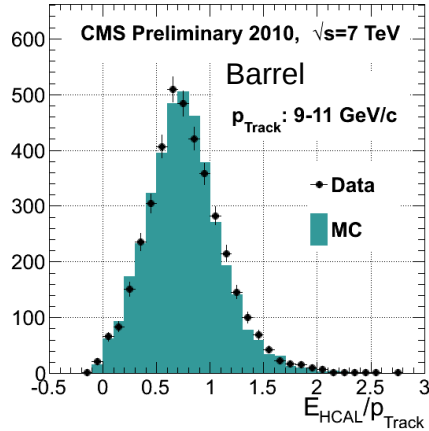
the front ends by means of a fast charge-integrating ADC. The digitized signals are sent off-detector to the HCAL Trigger/Read-Out (HTR) boards, where they await a trigger decision. If the trigger is accepted, the signals are sent on to the HCAL data concentrator cards (DCCs), which interface to the global DAQ system. HCAL trigger primitives, consisting of transverse energy sums over an entire tower, are calculated in the HTR boards and sent to the global trigger system.

Selected HCAL performance results can be seen in Figure 5.28.

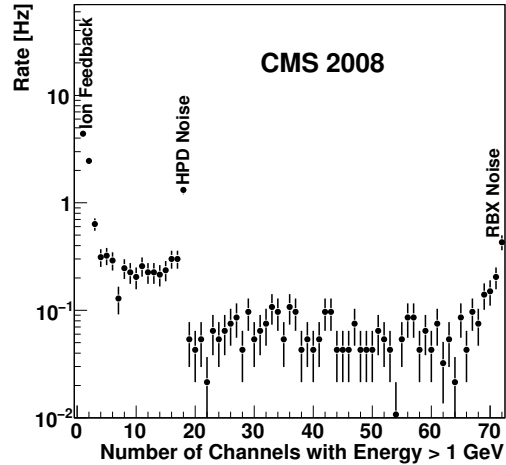
### 5.1.4 Muon System

Beginning at a radius of  $\sim 10$  interaction lengths from the beam line, where all particles except muons should have been stopped by the HCAL, are the muon chambers, interspersed with the iron return yoke of the CMS magnetic field. Three technologies are employed: drift tubes in the barrel section (MB), cathode strip chambers (CSCs) in the endcap section (ME), and resistive plate chambers (RPCs) in both sections to provide an independent trigger with superior time resolution. There are four barrel layers of stations extending out to  $|\eta| = 1.2$ . Each endcap consists of five disks of stations as shown in Figure 5.29(b), covering  $1.4 < |\eta| < 2.4$ . RPCs populate the barrel and endcap muon systems alongside the DT chambers and CSCs. Since they have time resolution much better than a few ns, they are used to assign the bunch crossing of muon tracks and provide a  $p_T$  trigger with sharp turn-on.

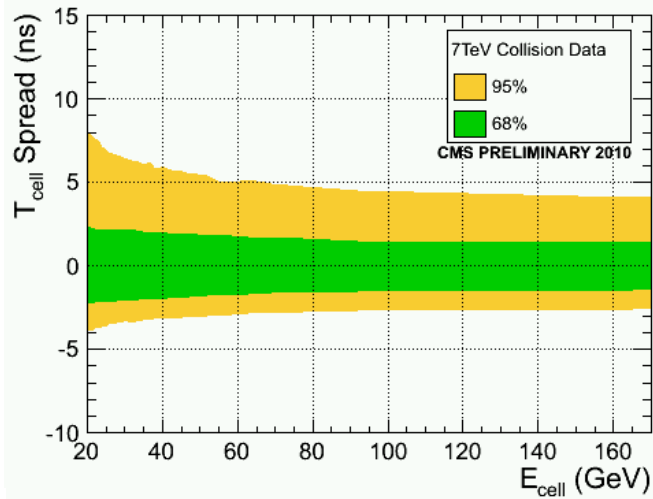
Each DT chamber consists of two  $r \cdot \phi$  superlayers (SLs) and optionally one  $z$  SL (in all chambers except those in the fourth layer). The SLs contain four rows of drift tubes, with the rows staggered such that there are no gaps in the coverage. The  $r \cdot \phi$  SLs have the tube axis parallel to the beam line, while the  $z$  SL is perpendicular to the beam line. The tubes are  $\sim 2.4$  m in length and 13 mm  $\times$  42 mm in cross section. Each chamber therefore records eight  $r \cdot \phi$  tracking points and optionally four  $z$  tracking points. The tubes are filled with an 85%Ar + 15% CO<sub>2</sub> gas mixture. An



(a) Data/MC comparison of HB response to charged tracks of 9-11  $\text{GeV}/c$  momentum [89].

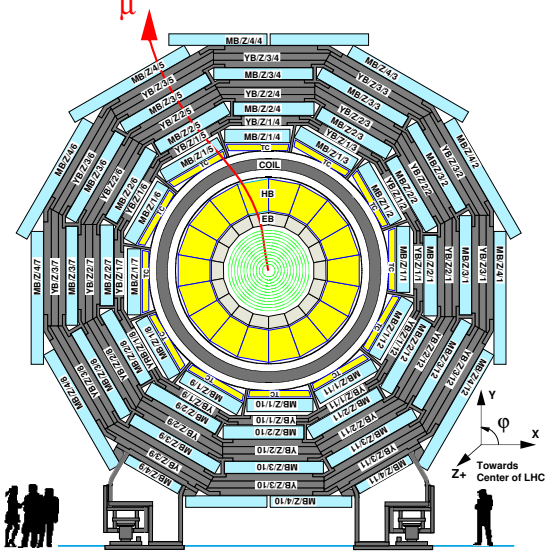


(b) Distribution of tower multiplicity, clearly showing three peaks in rate corresponding to noise sources (see Sec. 6.3) [90].

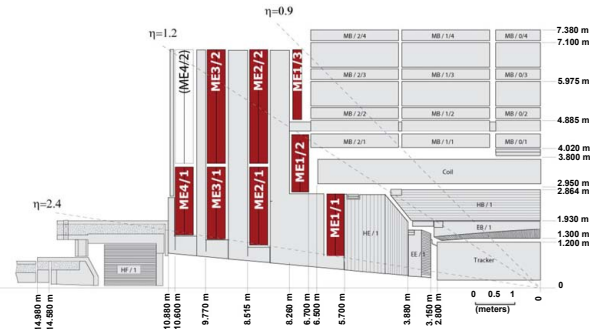


(c) Timing resolution vs. tower energy [89].

Figure 5.28: Selected HCAL performance results.



(a) One of the five wheels of MB, showing the four layers of muon stations. The five wheels are spaced symmetrically in  $z$  about  $z = 0$ . As a muon traverses the muon detectors, its curvature in the transverse plane changes direction and magnitude due to the magnetic field in the return yoke, which is of opposite sign and reduced strength relative to the field within the solenoid volume. Reprinted from Fig. 7.3 of ref. [71].



(b) Quarter longitudinal cross section of CMS highlighting the location of the ME disks. Reprinted from Fig. 7.47 of ref. [71].

Figure 5.29: View of the MB and ME layout in CMS.

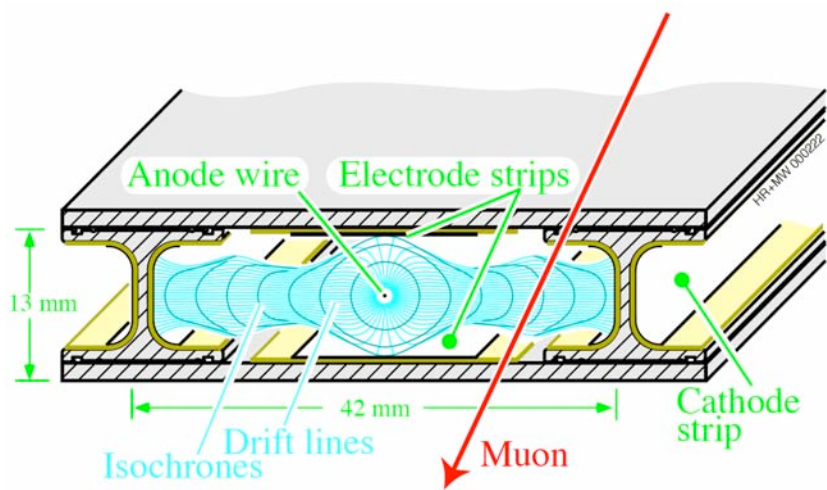


Figure 5.30: Electric field lines within a drift tube as well as the contours of equal drift time. Reprinted from Fig. 7.5 of ref. [71].

anode wire at 3600 V runs the length of the tube, while the walls are covered with electrodes held at 1800 V or -1200 V depending on wall. When a muon passes through the tube, it ionizes the gas atoms. The liberated electrons drift along the electric field lines created by the electrodes to the anode, which is read out. Figure 5.30 shows the electric field lines within a drift tube as well as the contours of equal drift time. The maximum drift time is 380 ns.

CSCs consist of alternating layers of cathode strips (four planes oriented along  $r$ ) and anode wires (three planes oriented along  $\phi$ ). A 40%Ar + 50%CO<sub>2</sub> + 10%CF<sub>4</sub> gas mixture fills the space between two successive planes, forming six gas gaps. When a muon ionizes the gas atoms, the positive ions drift toward the anode and are read out to provide a measurement of  $r$ , just as in the DTs. However, an image charge is induced on the cathode strips, which is also read out to provide a measurement of  $\phi$ . The wires are spaced 3.2 mm apart. The cathode strips have pitch varying from 8.4 mm at the end closest to the beam line to 16 mm at the other end, and are spaced 0.5 mm apart. A trapezoidal CSC is shown in Figure 5.31.

Track stubs from the muon system are combined with tracks from the tracking

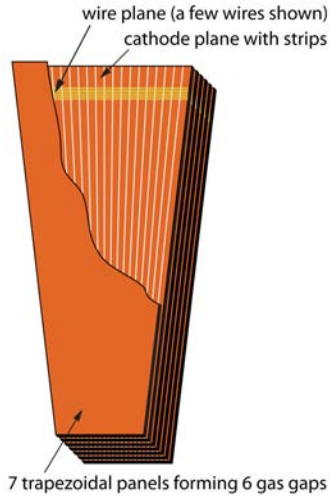


Figure 5.31: CSC wedge, showing the cathode and wire planes. Reprinted from Fig. 7.49 of ref. [71].

system to form more precise muon tracks than either system could form alone, as shown in Figure 5.32. This leads to extremely good di-muon invariant mass resolution (Figure 5.33) over a large  $p_T$  range.

## 5.2 Triggering, Data Acquisition, and Data Transfer

### 5.2.1 Level 1 and High Level Trigger Systems

The Level-1 (L1) trigger system, which encompasses dedicated hardware processors to construct trigger objects (typically high  $p_T$  jets, electrons, photons, taus, and muons) out of the calorimeter and muon hits, distributes a L1 accept or reject to all subdetectors at the LHC bunch crossing frequency of 40 MHz. Further data filtering is performed by the High Level Trigger (HLT) system, a farm of  $\sim 1000$  commercially available processors running a slimmed down version of the CMS event reconstruction software CMSSW. The data rate received by the HLT is  $\sim 100$  kHz; the output rate of

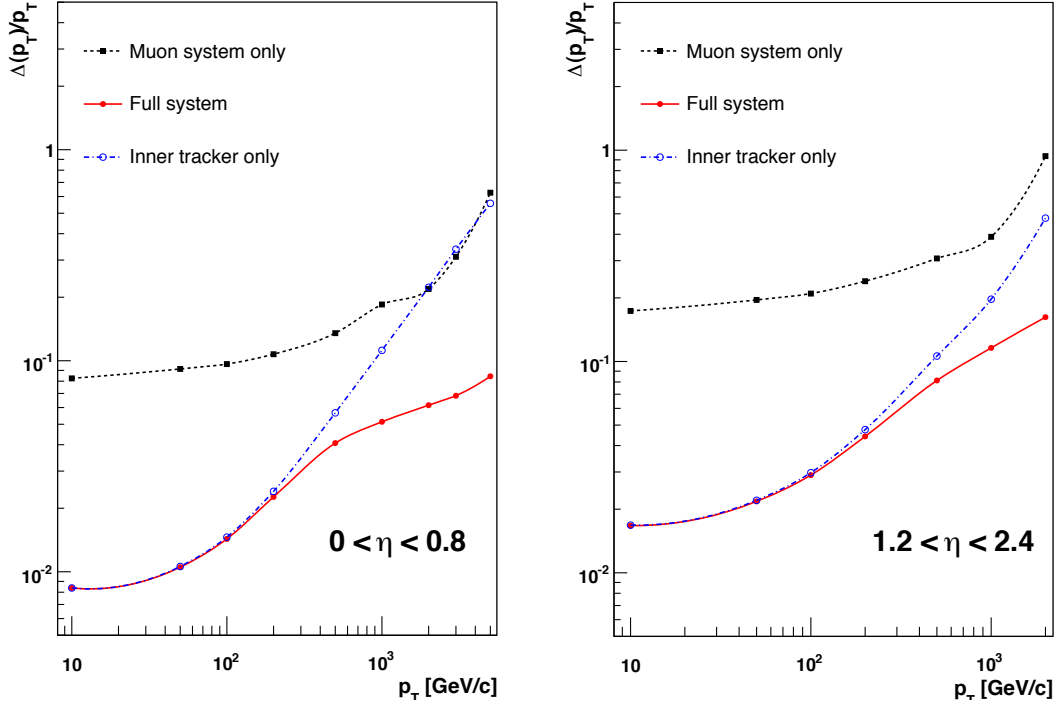


Figure 5.32: Muon  $p_T$  resolution as a function of muon  $p_T$  for tracker information only (blue), muon information only (black), and both tracker and muon information combined (red). Reprinted from Fig. 1.2 of ref. [71].

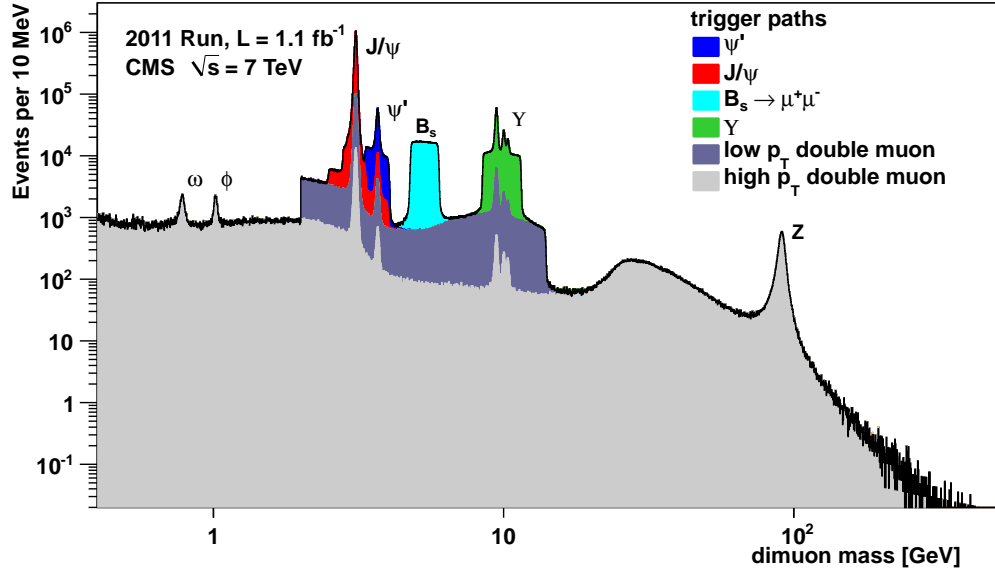


Figure 5.33: Di-muon invariant mass spectrum broken down by trigger path [91]. The light(dark) gray regions show the contribution from high- $p_T$ (low- $p_T$ ) di-muon triggers. Note that no  $B_s \rightarrow \mu^+ \mu^-$  decays have been observed [92]; the light blue region just shows the amount of triggers dedicated to the  $B_s \rightarrow \mu^+ \mu^-$  search.

events permanently written to disk is  $\sim 100$  Hz. An L1 trigger *latency* (time between the collision and the distribution of the L1 decision to the subdetectors) of  $3.2\ \mu\text{s}$  is achieved via the use of fast electronics and sufficiently deep buffers to pipeline trigger primitives waiting to be analyzed. This latency corresponds to the length of the LHC abort gap, so in principle CMS may be operated with zero *dead time* (during which LHC bunches are missed because the L1 system is blocked while processing other triggers).

At the bottom, the L1 trigger consists of trigger primitive generators (TPGs) in the calorimeter and muon systems that send  $E_T$  sums or muon track stubs to the regional calorimeter trigger (RCT) or muon track finders, respectively. The EB TPG also sends a *fine grain veto bit* [93], which encodes information about the EM shower pattern in the  $5 \times 5$  array of crystals, and is used to reject anomalous signals (see Sec. 6.1.1). The RCT, DT track finder (DTTF), and CSC track finder (CSCTF) sort and rank the regional trigger primitives based on  $p_T$  and quality. The ranked RCT candidates and muon track stubs are sent to the global calorimeter trigger (GMT) and global muon trigger (GMT), respectively, where high-level objects like isolated and non-isolated muons and EM candidates, jets, taus, and  $\cancel{E}_T$  are constructed from all the regional inputs and ranked. Calorimeter isolation sums for muons are also sent from the RCT to the GMT. The highest ranked global objects are sent to the global trigger (GT), which sits at the top of the L1 trigger. The GT issues the final L1 accept or reject to all subdetectors based on a comparison of the GMT and GCT candidates with the requirements of its programmed trigger menu. A block diagram of the L1 trigger is shown in Figure 5.34.

A region in the RCT consists of a matrix of  $4 \times 4$  trigger towers. A trigger tower in EB/HB is one HCAL tower + the  $5 \times 5$  matrix of ECAL crystals in front of it; in EE/HE the idea is similar but the counting of crystals and HE towers is slightly more complicated. An EM RCT candidate is built around a high  $E_T$  seed tower.

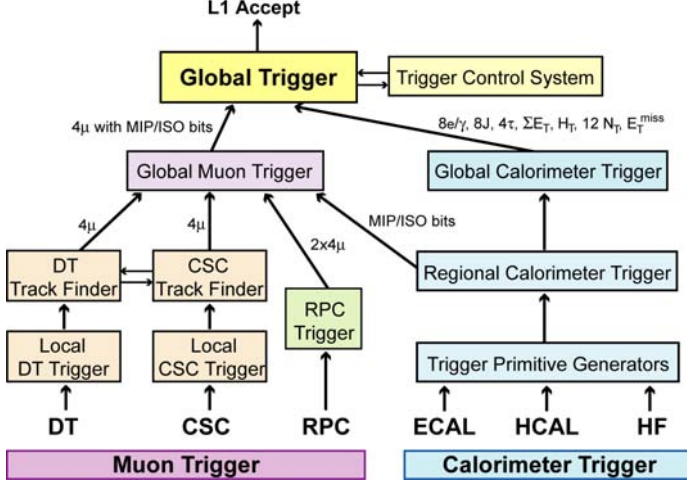


Figure 5.34: Block diagram of the L1 trigger. Reprinted from Fig. 8.1 of ref. [71].

The  $E_T$  of the candidate is the sum of the tower  $E_T$  and the  $E_T$  of its highest- $E_T$  broad side neighbor (see Figure 5.35 for a definition of the broad side neighbors). Two isolation criteria are defined based on (a) the ratio of the EM energy to the HCAL energy in the tower and (b) the shower shape. For a non-isolated EM candidate, the highest- $E_T$  broad side neighboring tower must pass these two isolation criteria; for an isolated EM candidate, all eight neighboring towers must pass the criteria, and there must also be at least one quiet corner with the  $E_T$  of all five towers in the corner below some threshold (see Fig. 5.35). The process is repeated until four isolated and four non-isolated EM candidates are found, starting with the highest- $E_T$  tower in the region and moving down in tower  $E_T$ . An RCT region is flagged as consistent with tau decay only if the pattern of tower transverse energy sums defines at most a  $2 \times 2$  matrix of energetic towers within the  $4 \times 4$  RCT region.

From the tower transverse energy sums, eight EM candidates, and tau flag received from each RCT, the GCT computes the total  $E_T$  in the calorimeter (and the total  $E_T$  above some programmable threshold, called  $H_T$ ), and the  $\cancel{E}_T$ . It also classifies the towers into jets and determines the globally highest ranked isolated and non-isolated EM candidates. The jet finding uses a clustering algorithm based on the energy of a

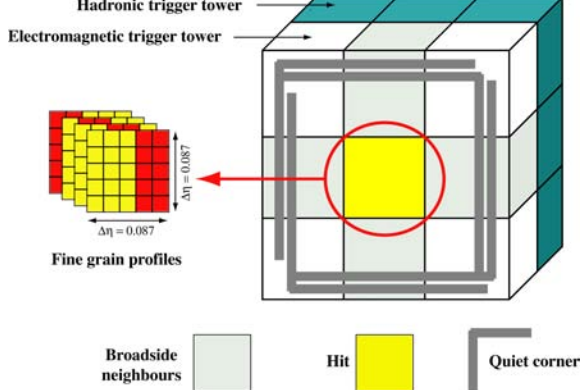


Figure 5.35: Geometry of an EM RCT candidate. Reprinted from Fig. 8.2 of ref. [71].

sub-cluster with respect to its neighbors [94]. Jets are classified as tau decays if all of the RCT regions participating in the jet clustering had energy patterns consistent with tau decay. Counts of jets above 12 different programmable  $E_T$  thresholds are calculated. The jet counts, energy sums,  $E_T$ , and highest ranked EM candidates are sent to the GT, where the final L1 decision is taken and transmitted to the sub-detectors. The GT can execute a maximum of 128 trigger algorithms in parallel. If any one of these algorithms yields an accept, the event is accepted, and all trigger information is sent on to the HLT for further filtering. The double-photon HLT paths used in this analysis (see Sec. 6.2) require isolated L1 seeds (i.e. EM candidates built by the RCT) with  $E_T > 12$  or 20 GeV, depending on path.

No muon triggers are used in the two-photon analysis. A description of the muon trigger system can be found in ref.[71].

### 5.2.2 Data Acquisition System

The CMS data acquisition (DAQ) system takes event fragments (calorimeter hits, track hits, etc.) from each of the 626 subdetector front end drivers (FEDs), assembles them into a data structure representing the full event, and sends the event on to the HLT for further filtering. The DAQ must operate at an input rate of  $\sim 100$

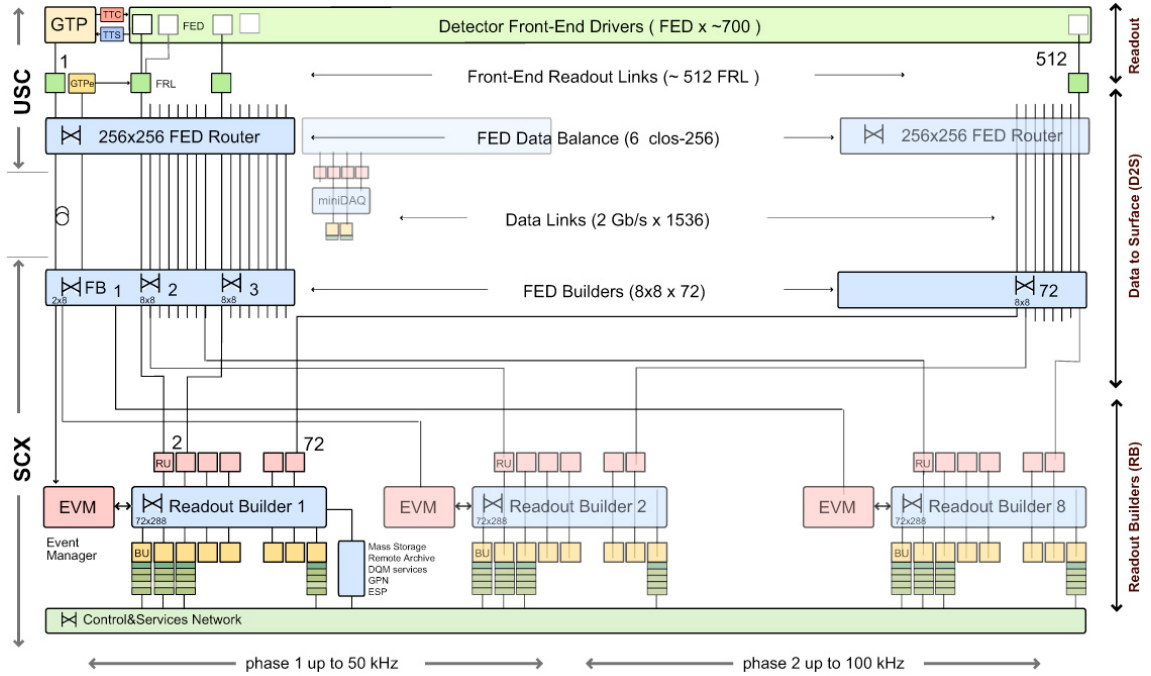


Figure 5.36: Diagram of the DAQ system. The identical event builder systems, shown as inputs and outputs to the boxes labeled “Readout Builder 1”, “Readout Builder 2”, etc., represent the eight slices. Within one slice, data can flow from the detector front ends to the readout systems to the builder network (which assembles the event fragments) to the filter systems (HLT) independently of the other slices. Reprinted from Fig. 9.8 of ref. [71].

GB/s, corresponding to an input rate from the L1 trigger of  $\sim 100$  kHz. To facilitate expansion of the system as the need arises, the DAQ is composed of eight nearly independent slices. Each slice functions as a smaller version of the whole DAQ that can handle an input event rate up to  $\sim 12.5$  kHz. A diagram of the DAQ system, showing schematically the eight slices, is given in Figure 5.36.

Data from the front ends is collected by the FEDs and pushed to the front end readout links (FRLs), which may take inputs from up to two FEDs simultaneously. The FRLs check for transmission errors, generate event fragments with size  $\sim 2$  kB, buffer the fragments in 64 kB memories, and finally send them to the FED builders. The FEDs, FRLs, and FED builders are located in the underground control room. The 72 FED builders each construct one  $\sim 16$  kB *super-fragment* from the input

event fragments, then send the super-fragment on to a readout unit (RU) located in the surface control room  $\sim 80$  m away. Super-fragments belonging to the same event are sent to RUs in the same DAQ slice. There are 72 RUs per readout builder, one for each super-fragment of an event, with each DAQ slice built around one readout builder (see Fig. 5.36). Each readout builder hosts a number of builder units (BUs) that perform the final integration of super-fragments into complete events.

Resource brokers (RBs) in the HLT filter farm request complete events from the BUs and distribute those events to the filter units (FUs) for HLT selection. If an event passes any one of the HLT paths in the predefined menu, it is sent back to the RB for transfer to the storage manager (SM). The SM nodes transfer accepted events to the CERN Tier-0 prompt reconstruction facility for unpacking of the raw data into ROOT [95] files that can be accessed by physicists wishing analyze the data. The lag time between recording of an event in the DAQ and availability of the fully reconstructed event for analysis is typically 48 hours.

If the buffers of the upstream DAQ elements (the filter farm, readout builders, FED builders, or FRLs) are full, those elements will not request new events from downstream. This can lead to a buildup of events in the downstream element buffers, *back-pressuring* all the way down to the FEDs themselves. The CMS trigger throttling system (TTS) consists of dedicated lines between the FEDs and the GT for the purpose of sending predefined signals to the GT about the state of the FED buffers. If the buffer of a particular FED is getting full, it can alert the GT to reduce the trigger rate so as to prevent FED buffer overflows and loss of time synchronization between event fragments. The TTS latency is  $\sim 1\mu\text{s}$ . Causes of back-pressure (hence dead time) include: problems with the FED electronics (in this case, the upstream elements request events but the FEDs have trouble sending them), increases in the L1 accept rate (perhaps due to a noisy detector channel) beyond what the upstream DAQ elements can handle, increases in the event size due to high pileup or a poor

quality beam that scrapes against the beam pipe, failures of the DAQ transmission lines or DAQ hardware such that events are not requested from the FEDs fast enough, or bottlenecks at the SM nodes or filter farm due to hardware failures or large event sizes.

All components of the DAQ, from the FEDs up to the SMs, are controlled by cross-platform DAQ (XDAQ) [96] processes, or *executives*. The Simple Object Access Protocol (SOAP) [97] protocol is used to transmit control and monitoring data between XDAQ-enabled devices and to the end user, who can view the running of a XDAQ executive via a Web interface called HyperDAQ [98]. The Run Control and Monitoring System (RCMS) handles the configuration and control of all XDAQ executives via a hierarchical structure. At the top of the hierarchy is the Level-0 *function manager* (FM), controlling the Level-1 sub-detector FMs, which in turn control their Level-2 system-specific XDAQ executives. The central DAQ and L1 trigger each have their own Level-1 FM. A unit of data acquisition, called a *run*, may be configured, started, and stopped by an end user interacting with the RCMS Web interface.

### 5.2.3 Data Processing and Transfer to Computing Centers

Data leaving the filter farm are grouped into datasets based on HLT path, i.e. there are different datasets for events passing diphoton triggers, jet triggers, muon + electron triggers, etc. At the Tier-0 facility, the datasets go through three levels of processing to create three *data tiers*. The first layer produces RAW data by unpacking the detector byte streams sent from the DAQ and L1 trigger into data structures holding the ADC counts recorded for each channel of the detector, digitized trigger primitives, and the L1 decision. A single event has  $\sim 1.5$  MB of RAW data. The next layer of processing is the reconstruction, which forms channel energies in GeV, applies calibrations, and creates high-level objects like photons, electrons, muons, taus, jets,  $\cancel{E}_T$ , and charged tracks. The RECO data tier occupies  $\sim 0.5$  MB per event.

Finally, analysis object data (AOD) is a subset of the RECO data, comprising the high-level objects but usually excluding the individual channel hit information if it is not associated to a physics object. This tier occupies  $\sim 0.1$  MB per event. One copy of the RAW data is stored permanently at CERN and another copy is distributed amongst the Tier-1 facilities (see below) for permanent storage. Changes in the reconstruction algorithms periodically require reprocessing of the RAW data to form a new RECO tier. In general, only the AOD tier is available to physicists wishing to perform analyses due to the smaller size and faster replication and transfer time of AOD with respect to RAW or RECO.

There are three tiers of computing and data storage sites within the Worldwide LHC Computing Grid (WLCG) [99]. The tier closest to CMS is Tier-0, which is located at CERN and performs archiving of the RAW data, prompt reconstruction of the data within  $\sim 48$  hours of its being collected, and transferral of copies of the RECO datasets to Tier-1 facilities. There are a few Tier-1 centers worldwide, hosted by national computing facilities and laboratories. They store parts of the RAW dataset and copies of the RECO datasets, participate in subsequent reconstruction passes after the prompt reconstruction at Tier-0, and ship AOD datasets upon request to the Tier-2 centers. Analysts interact primarily with the Tier-2 centers, which store AOD datasets and run batch processing queues for running analysis jobs over the datasets. Different layers of WLCG software control data transfer between sites, data storage, and batch processing. A diagram of the WLCG tier system is given in Figure 5.37.

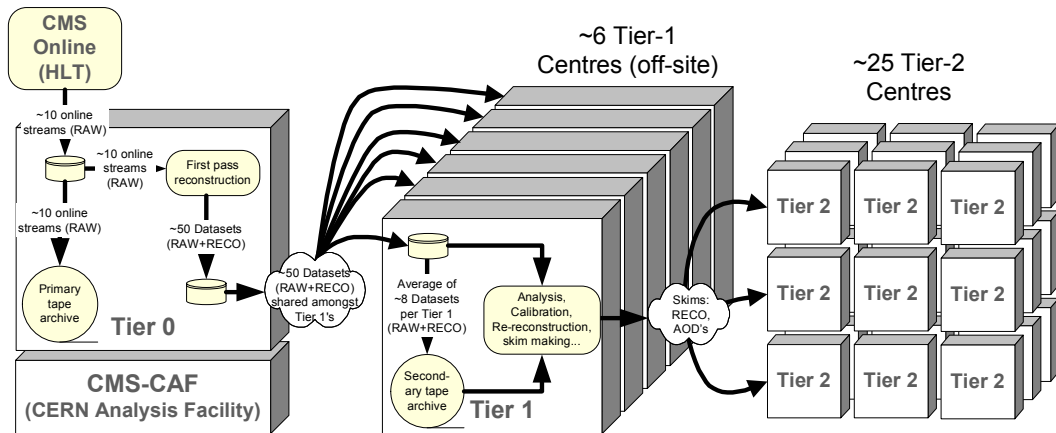


Figure 5.37: Diagram of the WLCG tier system showing data archival and reconstruction at each tier along with data transfer between tiers. Reprinted from Fig. 11.2 of ref. [71].

# Chapter 6

## Event Selection

In keeping with the phenomenology described in Sec. 3.5, the candidate GGM events selected in this search consist of two high- $E_T$  photons and a significant momentum imbalance transverse to the beam, indicating the production of an escaping gravitino. This momentum imbalance is usually referred to as *missing transverse energy* and is denoted by the symbols  $\cancel{E}_T$  or  $\text{ME}_T$ . The GGM signature is shown in Figure 6.1.

However, in order to use real CMS data (as opposed to simulation) to derive predictions for the backgrounds to the search, *control samples* that are not expected to contain any GGM signal events and are distinct from the *candidate* two-photon sample must be collected from the LHC data. These samples consist of different numerical combinations of photons, electrons, and jets, and are explained in more detail in Chapter 7. Since this search is performed in the high- $E_T$  tail of the  $\cancel{E}_T$  distribution, where adequate detector simulation is very difficult, it is advantageous to use *data-driven* background estimates, which capture the true detector response, over numbers derived from simulation.

In the following sections, the reconstruction of photons, electrons, jets, and  $\cancel{E}_T$  is explained. Sec. 6.1 begins with an explanation of the high level reconstruction. It is followed by Sec. 6.2, which describes the triggers used to collect the candidate

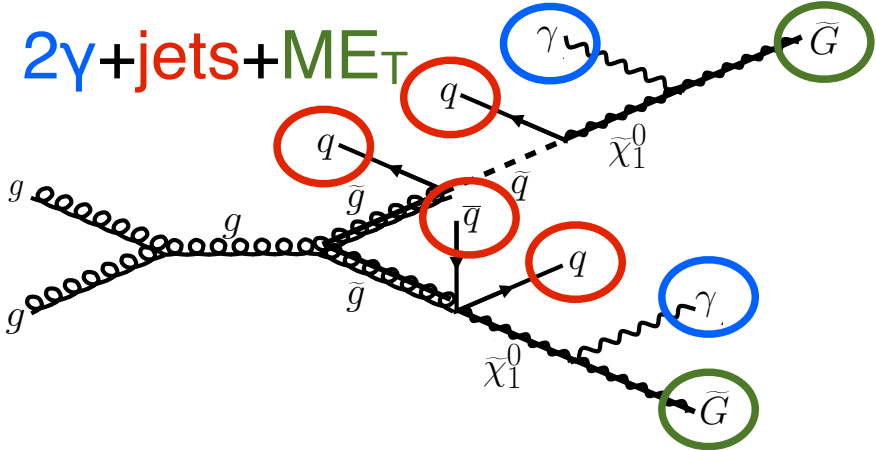


Figure 6.1: Two gluinos each decay via  $\tilde{\chi}_1^0 \rightarrow \gamma \tilde{G}$ .

and control samples. Sec. 6.3 describes event cleaning cuts that are applied to the candidate and control samples. Finally, the chapter concludes with a measurement of the photon identification efficiency in Sec. 6.4.

## 6.1 Object Reconstruction

This section describes the *offline* object reconstruction, i.e. the reconstruction of particle objects from events that have already been triggered and written to permanent storage, as opposed to the building of trigger objects explained in Secs. 5.2.1 and 6.2.

### 6.1.1 Photons

#### Uncalibrated EB/EE Hits

Photon reconstruction begins with the ADC count value for each of the 10 recorded time samples per ECAL crystal per trigger. To construct an *uncalibrated hit*, the gain (1, 6, or 12; see Sec. 5.1.2) of each sample is determined and the ADC count value scaled appropriately. The pedestal is estimated from the average of the first three samples, which, for a properly timed in hit, should contain no signal. This pedestal

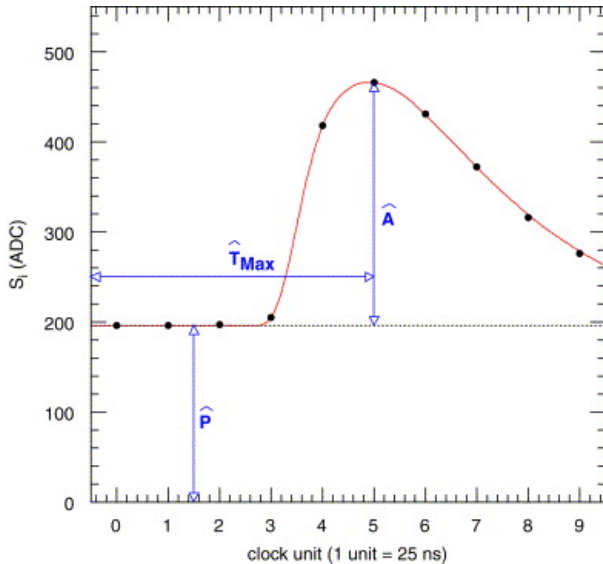


Figure 6.2: Typical ECAL channel pulse shape.  $\hat{P}$  is the pedestal value,  $\hat{A}$  is the pulse amplitude, and  $\hat{T}_{\max}$  is the hit time. The red line is the assumed pulse shape from which the weights are derived. Reprinted from ref. [100].

value is subtracted from the rest of the samples. Finally, the amplitude of the pulse is reconstructed using a predetermined weight for each sample [100]. The weights correspond to the pulse shape expected from the MGPA and shaping circuit response. The time of the hit is also reconstructed using the ratios between neighboring time samples [101]. A typical ECAL channel pulse shape is shown in Figure 6.2.

### Calibrated EB/EE Hits

In the next phase of the photon reconstruction, calibrations are applied to the uncalibrated hits to form *calibrated hits* with energy measured in GeV. Channels are excluded from seeding calibrated hits if

- they are excessively noisy,
- they are stuck in fixed gain (i.e. the MGPA gain does not change properly to avoid saturation),
- they are totally dead,

- they have one or more neighboring dead channels, or
- they do not have good trigger primitives (i.e. trigger primitive is missing, saturated, or *spike-like*; cf. Secs. 5.1.2 and 5.2.1).

*ECAL spikes* are hits in which low energy protons and heavy ions from jets ionize in the sensitive volume of the EB APD (Sec. 5.1.2), causing the APD to register a fake large-amplitude hit. Because they are not the result of a real electromagnetic shower, spikes tend to be isolated. They may also appear to arrive early or late with respect to the nominal bunch crossing. Most spikes are reconstructed with a hit time  $\sim 10$  ns earlier than real EM hits because unlike real hits, whose pulse shapes include the time constant associated with crystal scintillation, the reconstructed spikes only involve the rise time of the electronics. There also is a long tail of late arriving spikes due to slow neutrons from jets [102].

Because of their particular timing and topological characteristics, cuts have been developed to effectively identify and reject spike-like hits. This analysis utilizes both the “Swiss cross” cut  $1 - E_4/E_1 > 0.95$ , where  $E_1$  is the energy of the spike candidate crystal and  $E_4$  is the sum of the energies in the four crystals whose edges are next to the four edges of the spike candidate crystal, and a timing cut  $t \geq 3$  ns, to flag spikes. More information about these cuts can be found in ref. [102]. A simpler algorithm using the fine grain veto bit of the ECAL L1 TPG (Sec. 5.2.1) is used to reject spikes at the trigger level.

In addition to the trigger primitives, no uncalibrated hits that are spike-like are eligible for calibration. The calibrations applied are corrections to account for crystal transparency and VPT photocathode loss (leading to signal loss), measured continuously by the laser/LED system; energy intercalibrations (relative energy calibration between crystals); absolute scale calibrations between ADC counts and GeV;<sup>1</sup> and

---

<sup>1</sup>The ADC-GeV scale factors (one for EB and one for EE) are defined such that the sum of fully calibrated and scaled hits in a particular  $5 \times 5$  cluster of crystals (plus the associated energy deposited in ES) is 50 GeV for a 50 GeV incident unconverted photon [103].

time intercalibrations (relative time calibration between crystals).

The ECAL crystals were pre-calibrated before installation in CMS using laboratory light yield and photodetector gain measurements [104]. In addition, some EB and EE crystals were intercalibrated using test beams [105], and all EB crystals were intercalibrated with cosmic ray muons [106]. EE precalibrations were validated with LHC *splash events* in 2009 [106, 107], in which the beam was dumped onto a collimator approximately 150 meters upstream of CMS, causing a spray of muons to enter CMS at one endcap and exit at the other. Splash events were also used to derive time intercalibration constants. Before colliding beam operations commenced, the intercalibration precision was estimated to be 0.5%-2.2% in EB and 1%-5% in EE [108].

Three calibration methods were employed once colliding beam operations began:

- $\phi$  symmetry relative calibration between crystals, exploiting the azimuthal symmetry of CMS
- $\pi^0$  and  $\eta$  relative calibration between crystals, using the diphoton decays of these particles
- $E/p$  absolute calibration, comparing the momentum measured in the tracker  $p$  to the energy measured in the ECAL  $E$  of a sample of electrons from  $Z$  decay

By September 2011, the intercalibration precision in EB was measured to be between 0.3% and 1.1% using the  $\pi^0/\eta$  method [109]. Figure 6.3 shows the improvement in  $Z$  reconstruction from pre-LHC calibration constants to the latest  $\pi^0/\eta$ -derived constants.

### Calibrated ES Hits

ES calibrated hits are formed from the three samples read out per sensor. Just as in the case of EB/EE crystals, ES uncalibrated hits are gain-adjusted, pedestal-subtracted,

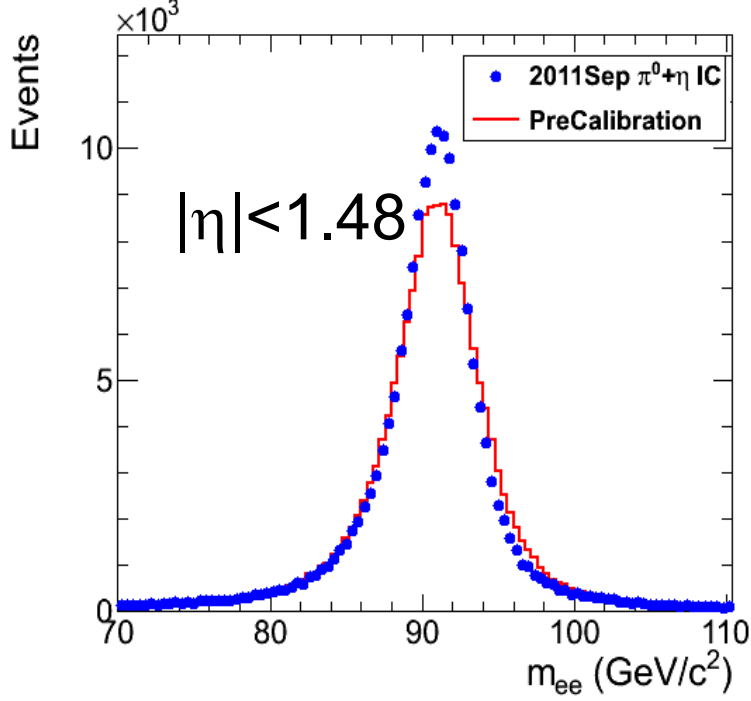


Figure 6.3:  $Z$  peak reconstructed using pre-LHC calibration constants (red) or September 2011  $\pi^0/\eta$ -derived intercalibration constants (blue). Reprinted from ref. [109].

and reconstructed using weights. To make a calibrated ES hit, intercalibration constants, angle correction constants (for the non-uniformity of sensor angle with respect to the vertical across ES), and a MIP-GeV absolute scale factor are applied.

### Clustering

After calibrated ECAL hits are formed, they must be clustered into shapes that represent the energy deposit from a single particle. *Basic clusters* are formed around seed hits, defined as a hit that

- has calibrated  $E_T > 1(0.18)$  GeV in EB(EE),
- does not originate from a dead channel or one with faulty hardware,
- is not poorly calibrated,

- was reconstructed with the standard algorithm (i.e. not a special recovery algorithm for channels with subpar data integrity),
- is not saturated,
- is not spike-like, and
- is in time (EB).

EB basic clusters are formed around the seeds via the *hybrid* algorithm, while EE basic clusters are formed with the `multi5x5` algorithm [110]. In addition to handling non-radiating electrons and unconverted photons, both algorithms are designed to also recover all of the energy associated with electron bremsstrahlung deposits and photon conversions. The geometry of the CMS magnetic field means that bremsstrahlung and conversions will tend to spread the shower out in  $\phi$ , not  $\eta$ . Both algorithms work by forming basic clusters around seeds, then combining the basic clusters into *superclusters* (SC) by searching in a window extended in the  $\phi$  direction for all basic clusters consistent with bremsstrahlung radiation from the primary electron, or with a photon conversion. Figure 6.4 illustrates the hybrid algorithm in EB. In EE, the energy deposited in ES must also be added into the total clustered energy sum.

Figure 6.5 shows the effect of superclustering on  $Z \rightarrow ee$  reconstruction.

## Supercluster Corrections

The total clustered ECAL energy is defined as

$$E = F \times \sum_{i=1}^{n_{\text{crystal}}} G \times c_i \times A_i \quad (6.1)$$

where  $G$  is the ADC-GeV or MIP-GeV scale factor,  $c_i$  are the intercalibration constants,  $A_i$  is the uncalibrated hit amplitude in ADC counts, and  $F$  is a SC correction

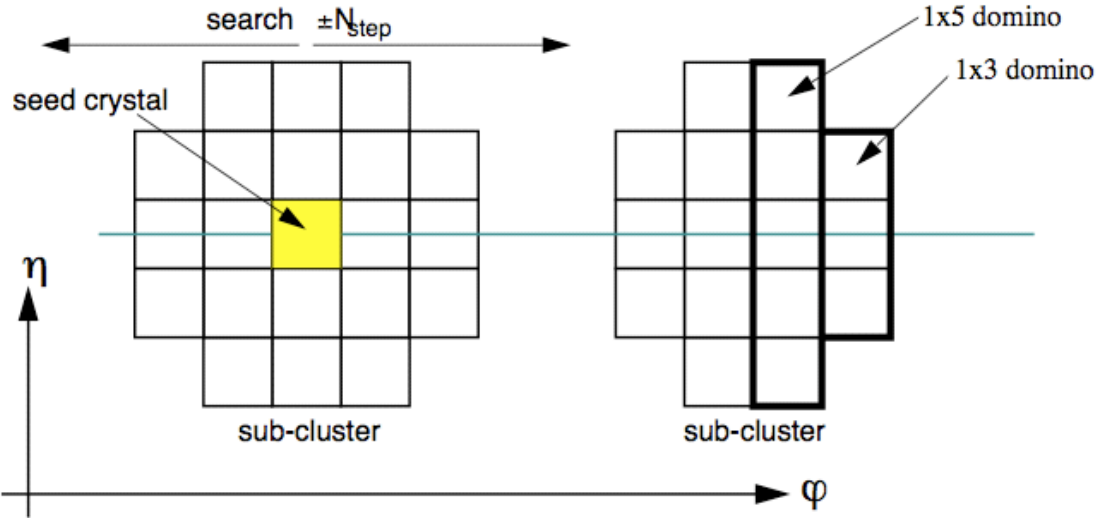


Figure 6.4: Hybrid algorithm in EB. The shower extent is constant in  $\eta$  (five crystals), but spreads out in  $\phi$  as the two sub-clusters (or basic clusters) are grouped into the same supercluster. The maximum extent in  $\phi$  is 17 crystals. Reprinted from ref. [110].

factor.  $G$  and  $c_i$  were explained in Sec. 6.1.1.  $F$  is a product of three factors for hybrid SCs (two for `multi5x5` SCs in EE, items 2 and 3 below) [110]:

1.  $C_{\text{EB}}(\eta)$ , which compensates for lateral energy leakage due to the crystal off-pointing in EB only. These corrections are taken from MC simulation [110] and were confirmed in test beams [105].
2.  $f(\text{brem})$ , which corrects for biases in the clustering algorithms for showers characterized by differing amounts of bremsstrahlung. These corrections are taken from MC simulation [110].
3. Residual correction  $f(E_T, \eta)$ , due to the variation in  $\eta$  of detector material traversed by a primary electron or photon, and to any residual  $E_T$  dependence of the reconstruction. These corrections are determined from MC and validated on  $Z \rightarrow ee$  data samples [112].

As a benchmark of ECAL calibration performance, the extra energy smearing in MC needed to achieve data/MC agreement in the  $Z$  width was between  $\sim 0.9\%$  (in

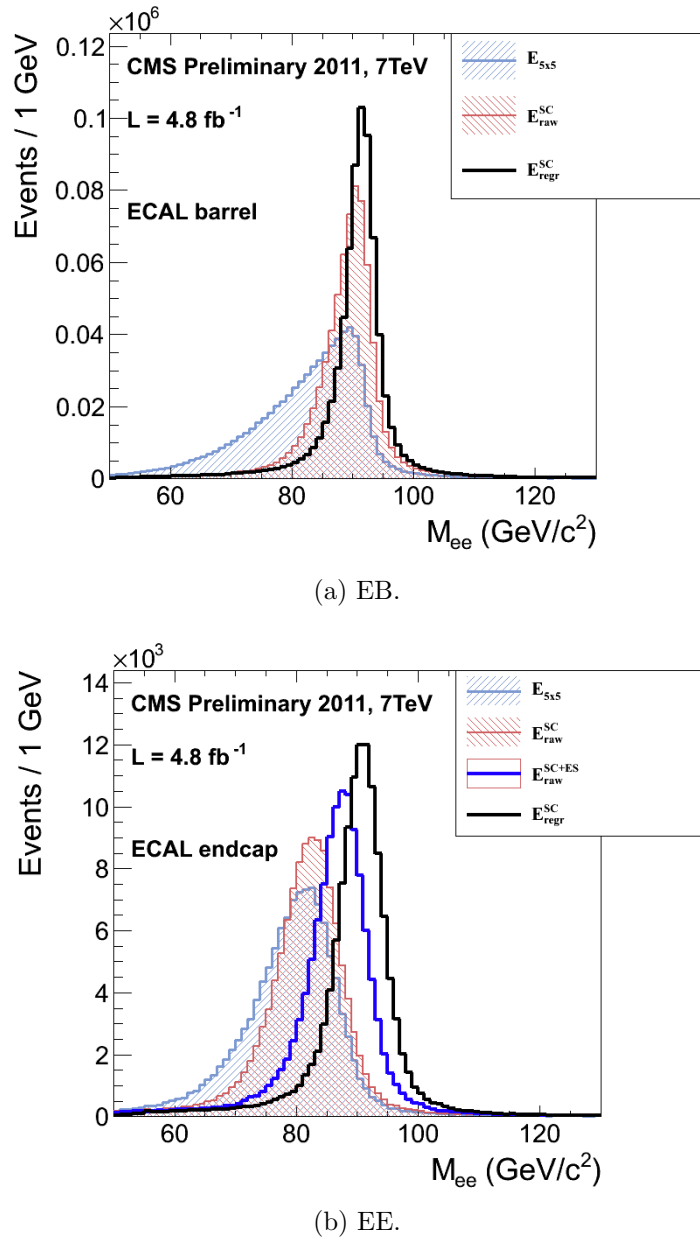


Figure 6.5:  $Z$  peak reconstructed in the dielectron channel for different kinds of clustering. The constituent hits were calibrated with the best available intercalibrations and laser calibrations as of December 2011. The light blue histogram shows the reconstruction using a  $5 \times 5$  energy sum, the red histogram shows the reconstruction using the SC energy for crystals only (the dark blue histogram in the EE plot adds in the energy from ES), and the black histogram shows the reconstruction after the SCs are corrected using a multivariate method [111]. Reprinted from Fig. 30 of ref. [111].

the central part of EB for electrons with little bremsstrahlung) and  $\sim 3.3\%$  (in the outer part of EE for heavily radiating electrons) [111].

## From Supercluster to Photon

The CMS photon object is any SC with  $E_T > 10$  GeV and  $H/E < 0.5$ , unless the SC  $E_T > 100$  GeV, in which case the  $H/E$  requirement is dropped.  $H/E$  is defined as the ratio of energy in the HCAL in a 0.15 cone around the SC centroid, directly behind the SC, to the SC energy. SCs with  $R9 > 0.94(0.95)$  in EB(EE), where  $R9$  is defined as the ratio of the energy in the central  $3 \times 3$  cluster of crystals divided by the SC energy  $E_{3 \times 3}/E_{\text{SC}}$ , are the best calibrated and most accurate type of electromagnetic shower. Therefore, for these objects, the photon energy is defined as the energy sum of the fully calibrated hits in the central  $5 \times 5$  cluster around the seed (with  $C_{\text{EB}}(\eta)$  applied for EB photons). For all other SCs, the photon energy is equal to the fully corrected SC energy (cf. Sec. 6.1.1).

In this search, candidate photons and *fake photons* ( $f$ , “fakes”) are further selected according to the criteria listed in Table 6.1. Fakes are used in the determination of the QCD background, as explained in Chapter 7.

Table 6.1: Selection criteria for photons and fakes. “Pixel seed,”  $I_{\text{comb}}$ , and  $\sigma_{i\eta i\eta}$  are defined in the text.

Variable	Cut ( $\gamma$ )	Cut ( $f$ )
SC $ \eta $	$< 1.4442$	$< 1.4442$
$H/E$	$< 0.05$	$< 0.05$
$R9$	$< 1$	$< 1$
Has pixel seed	No	No
$I_{\text{comb}}, \sigma_{i\eta i\eta}$	$< 6$ GeV AND $< 0.011$	$(\geq 6 \text{ AND } < 20 \text{ GeV}) \text{ OR } \geq 0.011$

$I_{\text{comb}}$  is defined as

$$I_{\text{comb}} = I_{\text{ECAL}} - 0.093\rho + I_{\text{HCAL}} - 0.0281\rho + I_{\text{track}} \quad (6.2)$$

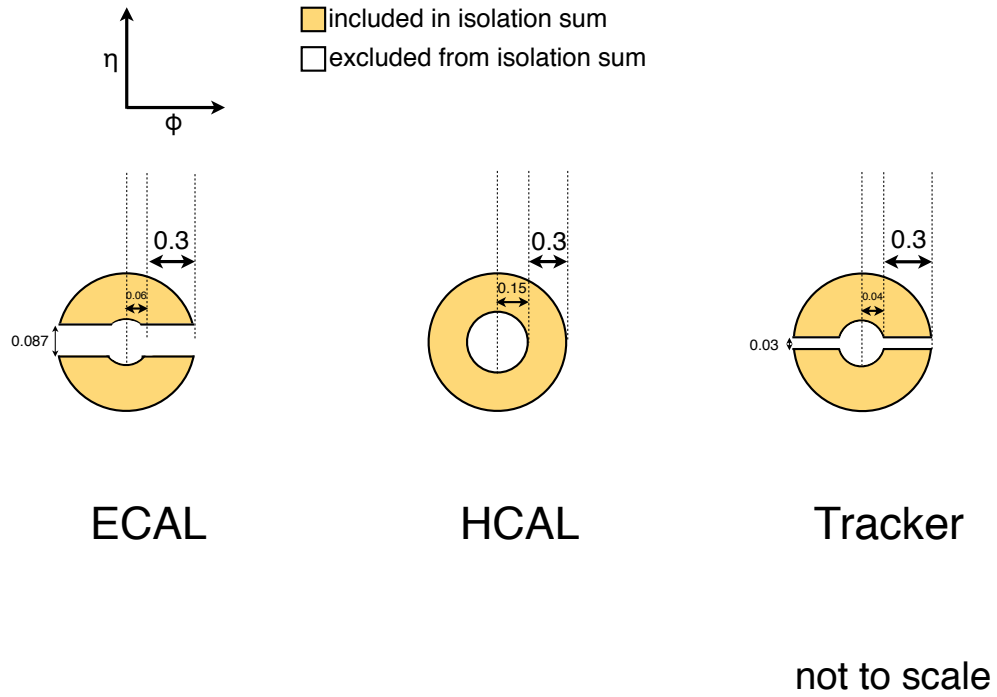


Figure 6.6: ECAL, HCAL, and track isolation cones.

where  $I_{\text{ECAL}}$ ,  $I_{\text{HCAL}}$ , and  $I_{\text{track}}$  are  $E_T$  sums in the annular regions defined in Figure 6.6 and  $\rho$  is the average pileup energy density in the calorimeters (per unit  $\eta \cdot \phi$ , or unit calorimeter surface area) as measured with the Fastjet algorithm [113, 114].  $\rho$  is constant over the  $\eta$  range of the calorimeter. Note that the ECAL and track isolation veto strips at constant  $\eta$  ensure that the isolation cuts are similarly efficient for converted photons, radiating electrons, and unconverted photons.

$\sigma_{i\eta i\eta}$  is the log energy weighted extent of the shower in  $\eta$  and is defined as

$$\sigma_{i\eta i\eta} = \frac{\sum_{i=1}^{25} w_i (\eta_i - \bar{\eta})^2}{\sum_{i=1}^{25} w_i} \quad (6.3)$$

where the sums run over the  $5 \times 5$  matrix of crystals surrounding the seed,  $w_i = \max(0, 4.7 + \ln(E_i/E))$ ,  $E_i$  is the energy of the  $i^{\text{th}}$  crystal,  $E$  is the total energy in the

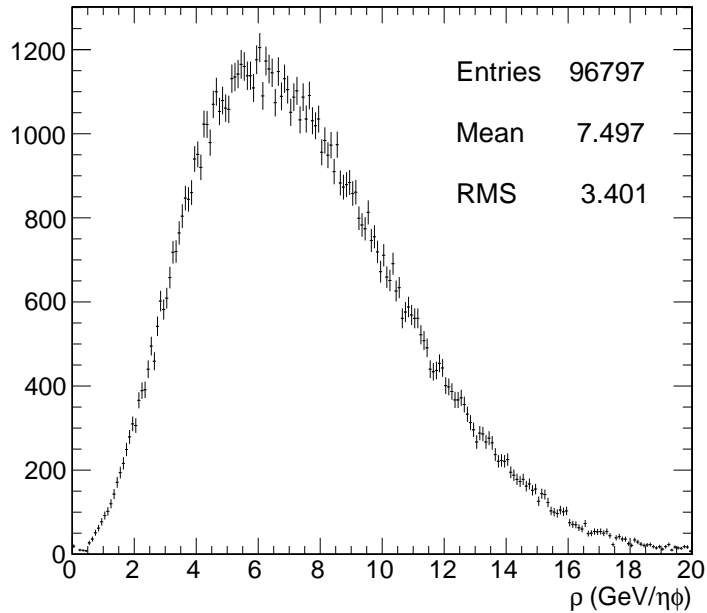


Figure 6.7:  $\rho$  distribution for a sample of two-photon events, with at least one 40 GeV and one 25 GeV photon, passing the selection requirements in Table 6.1 and the trigger requirements in Table 6.3. This sample covers the full 2011 dataset of  $4.7 \text{ fb}^{-1}$ .

25 crystals,  $\eta_i$  is the offset in  $\eta$  of the  $i^{\text{th}}$  crystal from the seed, and  $\bar{\eta}$  is the weighted average  $\eta$  of the 25 crystals (using the  $w_i$  as weights) [115].

Figure 6.7 shows the  $\rho$  distribution for a sample of two-photon events, with at least one 40 GeV and one 25 GeV photon, passing the selection requirements in Table 6.1 and the trigger requirements in Table 6.3. This sample represents the full 2011 dataset of  $4.7 \text{ fb}^{-1}$ . Since the average  $\rho$  is  $\sim 7.5 \text{ GeV}$ , and there is a long tail above this average value, it is necessary to subtract pileup energy from the ECAL and HCAL isolation cones to recover otherwise clean photons in events with large pileup. The ECAL and HCAL *effective areas* of 0.093 and 0.0281, respectively, are calculated by fitting the average ECAL or HCAL isolation energy vs.  $\rho$  in a sample of  $Z \rightarrow ee$  events to a straight line. The slope of the line—which has the units of  $\eta \cdot \phi$ , or area—is the effective area.

The cut on combined isolation of 6 GeV (Table 6.1) is the result of an  $S/\sqrt{B}$

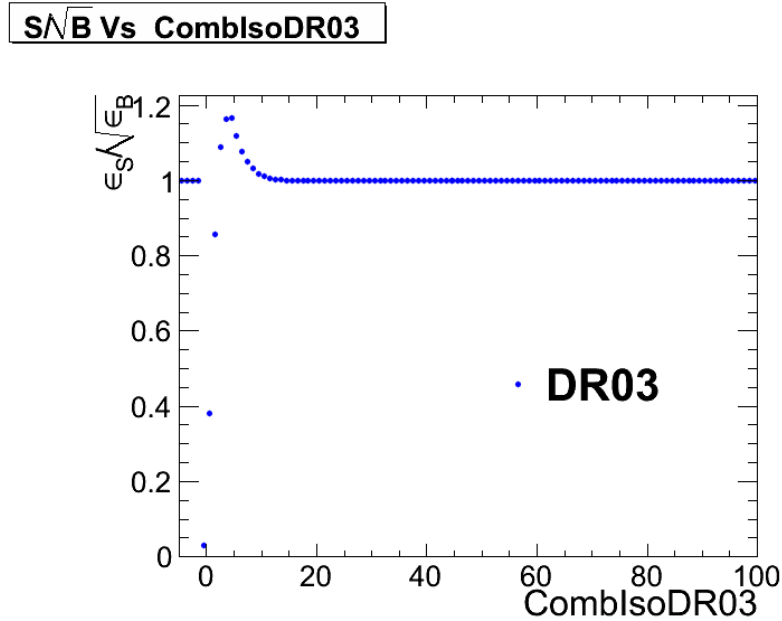


Figure 6.8:  $S/\sqrt{B}$  ( $S$  and  $B$  defined in the text) vs.  $I_{\text{comb}}$ . ‘‘DR03’’ in the legend indicates that this combined isolation was calculated in  $\Delta R = 0.3$  cones, as used throughout this analysis. Reprinted from Fig. 7 of ref. [116].

optimization procedure [116].  $S$  is a sample of photons in simulated GGM events that are products of neutralino decay, while  $B$  is a sample of photons matched to generated hadronic jets in simulated QCD events. Figure 6.8 shows the value of  $S/\sqrt{B}$  vs. combined isolation, in particular the pronounced peak around 6 GeV.

The upper bound on fake photon combined isolation guarantees that poorly isolated dijet events, with  $\cancel{E}_T$  resolution dissimilar to the candidate diphoton events, do not enter the  $ff$  sample. The exact value of 20 GeV (cf. Table 6.1) arises from a low- $\cancel{E}_T$   $ff/\gamma\gamma \chi^2$  optimization procedure [116]. Figure 6.9 shows the value of the Neyman’s  $\chi^2$  between the  $ff$  and  $\gamma\gamma \cancel{E}_T$  distributions, truncated at either 25 or 50 GeV, vs. upper bound on fake combined isolation. As shown in the figure, 20 GeV keeps the  $\chi^2$  small while also being large enough that a sufficient number of  $ff$  events may be collected.

Finally, a ‘‘pixel seed’’ is defined as a hit in the pixel detector consistent with a

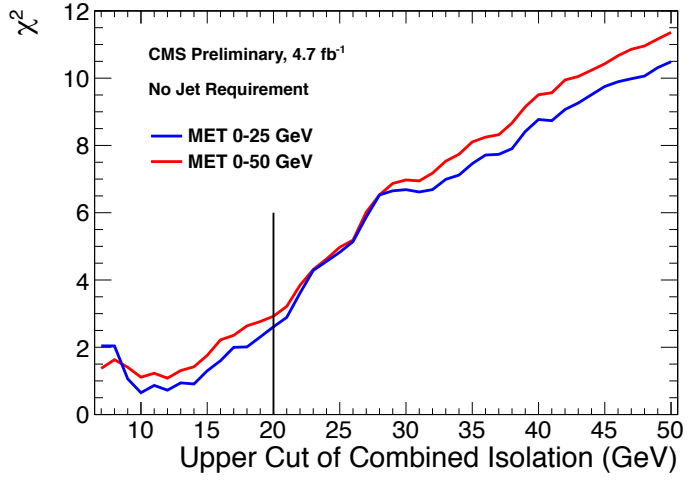
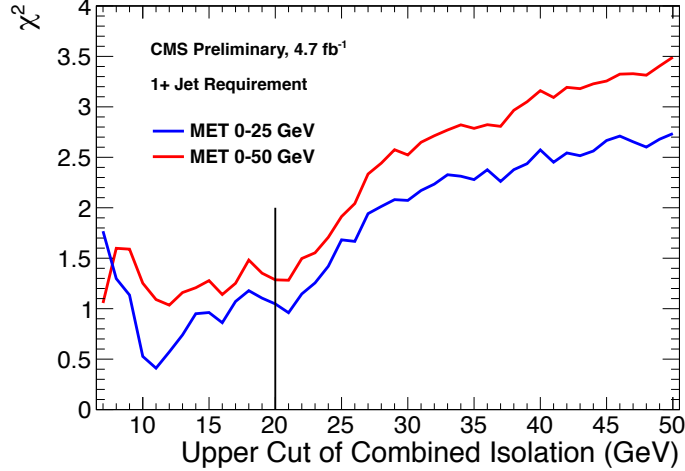
(a) Events with  $\geq 0$  jets.(b) Events with  $\geq 1$  jet.

Figure 6.9: Neyman's  $\chi^2$  between the  $ff$  and  $\gamma\gamma$   $\cancel{E}_T$  distributions, truncated at either 25 (red) or 50 (blue) GeV, vs. upper bound on fake combined isolation. A jet is defined as in Table 6.2, but with the  $\Delta R$  cleaning criteria of Table 6.2 applied to the two primary EM objects and all additional electrons, photons, and fake photons. The full reweighting and normalization procedure is employed in the  $\cancel{E}_T$  calculation (see Sec. 7.2). Reprinted from Fig. 9 of ref. [116].

track extrapolated from the position of the ECAL SC back to the primary vertex. Real photons, having no charge and therefore no bending in the magnetic field, should not have a pixel seed.

### 6.1.2 Electrons

Electrons are reconstructed identically to photons, except that in the electron case the presence of a pixel seed is enforced, rather than vetoed.<sup>2</sup> Photons and electrons are defined by very similar criteria so that  $Z \rightarrow ee$  events can be used to model the QCD background in the two-photon sample without introducing any bias in the electron energy measurement (cf. Sec. 7.2).

### 6.1.3 Jets and Missing Transverse Energy

#### Particle Flow

In this analysis, jets and  $E_T$  are formed from *particle flow* (PF) candidates. The particle flow algorithm [118, 119] uses information from all CMS subdetectors to reconstruct as accurately as possible the positions and momenta of all visible jet constituents, exploiting the fine granularity of the tracker and ECAL to achieve a greatly improved momentum resolution over calorimeter-only jets [120]. The PF algorithm is summarized below [118].

1. Reconstruct the fundamental detector objects via iterative procedures
  - Tracks in the inner silicon layers
    - High efficiency and low fake rate for charged hadrons in jets

---

<sup>2</sup>In many CMS analyses, electrons are reconstructed very differently from photons. In particular, a special tracking algorithm [117] is used to best follow a radiating electron. However, in this analysis, the electron tracking is not used.

- Relaxed primary vertex constraint allows photon conversions, particles originating from nuclear interactions in the silicon, and long-lived particles to be reconstructed
  - Calorimeter clusters
  - Muon tracks in the outer muon layers
2. Create a “block” of linked fundamental objects
- Link silicon tracks to calorimeter clusters via  $\Delta R_{\text{track-cluster}}$  (account for electron bremsstrahlung)
  - Link clusters in one calorimeter layer to clusters in a separate layer via  $\Delta R_{\text{cluster-cluster}}$
  - Link silicon tracks to muon tracks via global track  $\chi^2$
3. ID the particles in the block
- If global (silicon + muon layers) muon  $p_T$  is compatible with silicon track  $p_T$ , ID as a muon and remove corresponding tracks from block
  - ID electron tracks via special algorithm and removed all corresponding tracks and cluster from block
  - Remove fake tracks from the block
  - Allow multiple tracks to be associated to one HCAL cluster, but not multiple HCAL clusters to be associated to one track—for each track, keep only the HCAL cluster link that is closest in  $\Delta R$  to the track
  - If the cluster energy is significantly larger than the energy of the linked tracks, ID as a PF photon or PF neutral hadron
  - If the cluster is not linked to a track, ID as a PF photon or PF neutral hadron

- If the cluster energy is smaller than the energy of the linked tracks, ID each track as a PF charged hadron

## Jets

PF candidates are clustered into jets by means of the anti- $k_T$  algorithm with  $R = 0.5$  [121]. In this algorithm, all possible pairs of PF candidates  $i, j$  are looped over, and the pairs that minimize the distance variable

$$d_{ij} = \frac{\Delta R_{ij}^2}{R^2 \max(k_{Ti}^2, k_{Tj}^2)} \quad (6.4)$$

are clustered together, where  $k_{Ti}$  is the transverse momentum of PF candidate  $i$ . The process is repeated, using the pairwise-clustered PF candidates as input objects to the next round of clustering, until  $d_{ij} > 1/k_{Ti}^2$  for all pairs of clustered PF candidates [122]. An illustration is given in Figure 6.10. The anti- $k_T$  algorithm is infrared and collinear safe, leading to well-behaved theoretical predictions and ease of comparison between data and MC simulation. It also tends to form circular jets, making it easy for experimental effects such as expected out-of-cone energy and fiducial acceptance to be measured or simulated. For these reasons, the anti- $k_T$  jet clustering algorithm was chosen for this analysis.

Once jets are found, they must be corrected for biases in the energy measurement due to non-compensation [123], invisible energy (lost to overcoming nuclear binding energy, in neutrinos, or in unclustered muons, for example) [123], detector geometry and cracks [124], zero suppression and trigger inefficiencies [125], pileup, and effects of the clustering algorithm [124]. Four multiplicative correction factors are applied to the raw jet four-momentum  $p_\mu^{\text{raw}}$  [120]:

- $C_{\text{offset}}(p_T^{\text{raw}})$ , which accounts for extra energy due to noise, pileup, and the un-

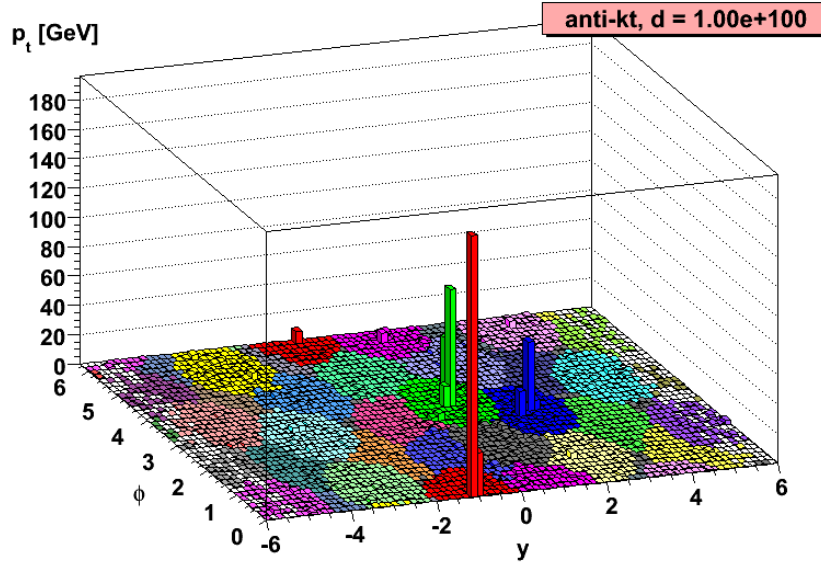


Figure 6.10: Example event display showing jets clustered via the anti- $k_T$  algorithm.  $y$  is pseudorapidity. Reprinted from slide 85 of ref. [122].

derlying event;

- $C_{\text{MC}}(C_{\text{offset}}p_T^{\text{raw}}, \eta)$ , which is derived from MC and accounts for most of the  $p_T$  and  $\eta$  dependence;
- $C_{\text{rel}}(\eta)$ , which accounts for the remaining differences in uniformity over the entire calorimeter between data and MC; and
- $C_{\text{abs}}(C_{\text{rel}}C_{\text{MC}}C_{\text{offset}}p_T^{\text{raw}})$ , which accounts for the remaining differences in linearity over the full  $p_T$  range between data and MC.

Figure 6.11 shows the total jet energy correction factor  $C_{\text{offset}}C_{\text{MC}}C_{\text{rel}}C_{\text{abs}}$  vs.  $\eta$  for jets reconstructed with the anti- $k_T$  algorithm,  $R = 0.5$ . The PF jet corrections are more uniform across  $\eta$  than those of CALO jets (composed of simple calorimeter towers) or JPT jets (Jet Plus Tracks; composed of calorimeter energies replaced, where possible, with matching track  $p_T$ ) [126]. In addition, for  $p_T$  in the range 30-200 GeV and  $|\eta|$  up to 2.0, the PF jet energy correction uncertainty is lower than that of the other two types of jets, and never exceeds  $\sim 3\%$  [120]. The superior performance

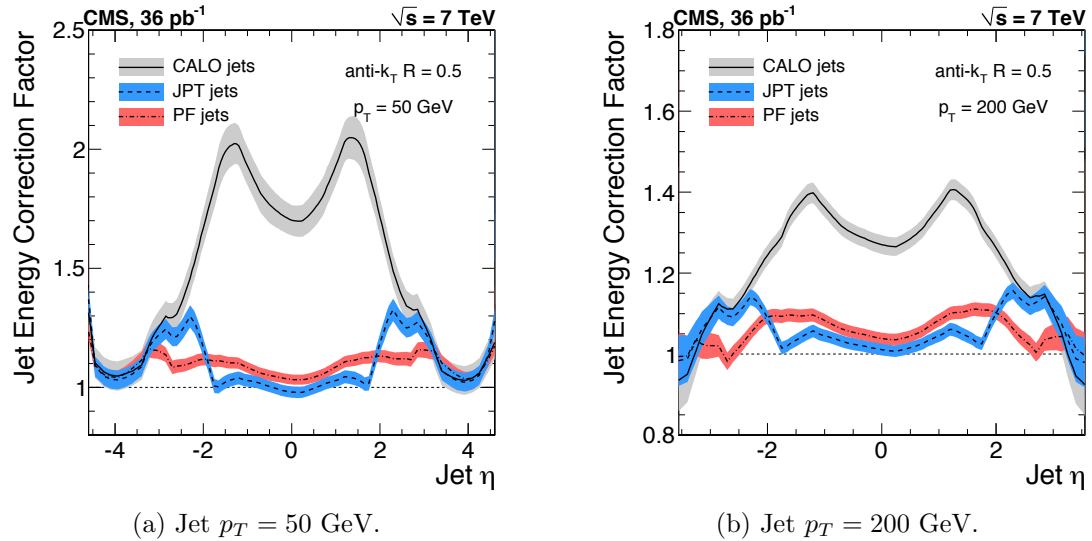


Figure 6.11: Total jet energy correction factor  $C_{\text{offset}}C_{\text{MC}}C_{\text{rel}}C_{\text{abs}}$  vs.  $\eta$ , including uncertainty band, for jets reconstructed with the anti- $k_T$  algorithm,  $R = 0.5$ . Reprinted from Fig. 26 of ref. [120].

of PF jets motivates their use in this search.

In this analysis, candidate and QCD control events are binned by number of jets satisfying the criteria in Table 6.2.

## Missing Transverse Energy

To be consistent with the jet reconstruction,  $\cancel{E}_T$  in this analysis is also reconstructed from PF candidates. Raw  $\cancel{E}_T$  is defined as

$$\mathcal{L}_{T\text{raw}} = \left| - \sum_{i=1}^{n_{\text{PF}}} \vec{p}_T i \right| \quad (6.5)$$

where  $n_{\text{PF}}$  is the number of PF candidates in the event.  $\cancel{E}_{T,\text{raw}}$  may be corrected for the same effects that necessitate jet corrections, since  $\cancel{E}_{T,\text{raw}}$  is usually the result of jet mis-measurement (except, of course, in electroweak physics processes that include an energetic neutrino, or SUSY production). CMS *Type-I*  $\cancel{E}_T$  corrections simply involve

Table 6.2: Definition of HB/HE hadronic jets.

Variable	Cut
Algorithm	L1FastL2L3Residual corrected PF
$p_T$	$> 30 \text{ GeV}$
$ \eta $	$< 2.6$
Neutral hadronic energy fraction	$< 0.99$
Neutral electromagnetic energy fraction	$< 0.99$
Number of constituents	$> 1$
Charged hadronic energy	$> 0.0 \text{ GeV}$ if $ \eta  < 2.4$
Number of charged hadrons	$> 0$ if $ \eta  < 2.4$
Charged electromagnetic energy fraction	$< 0.99$ if $ \eta  < 2.4$
$\Delta R$ to nearest PF electron <sup>a</sup> , muon <sup>b</sup> , or one of the two primary EM objects	$> 0.5$

<sup>a</sup>A PF electron is defined as an electron reconstructed with the PF algorithm [127] with  $p_T > 15 \text{ GeV}$ ,  $|\eta| < 2.6$ , and  $(I_{\text{charged}} + I_{\text{photon}} + I_{\text{neutral}})/p_T < 0.2$ , where  $I_{\text{charged}}(I_{\text{photon}})(I_{\text{neutral}})$  is the sum of PF charged hadron(PF photon)(PF neutral hadron) momenta in a  $\Delta R = 0.4$  cone around the PF electron.

<sup>b</sup>Muons are reconstructed [128] from a combination of muon station and inner tracker hits. Here, a muon must have track  $\chi^2 < 10$ , at least one good muon station hit, inner track transverse impact parameter  $< 0.02 \text{ cm}$ , inner track longitudinal impact parameter  $< 0.5 \text{ cm}$ ,  $p_T > 15 \text{ GeV}$ ,  $|\eta| < 2.6$ , and  $(I_{\text{ECAL}} + I_{\text{HCAL}} + I_{\text{track}})/p_T < 0.2$ , where  $I_{\text{ECAL}}(I_{\text{HCAL}})(I_{\text{track}})$  is the sum of ECAL(HCAL)(track) momenta in a  $\Delta R = 0.3$  cone around the muon.

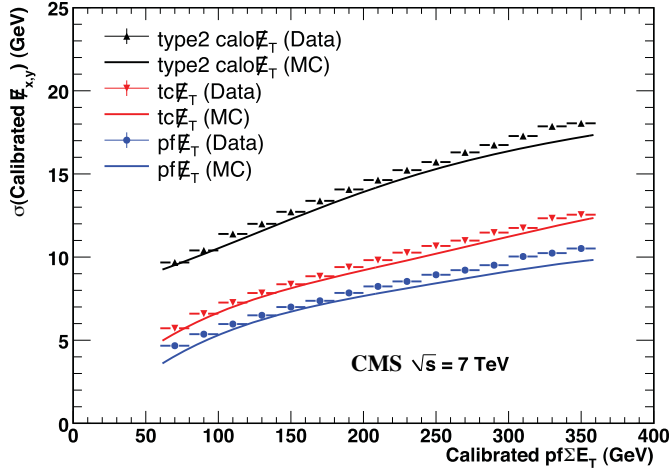


Figure 6.12:  $\sigma$  of a Gaussian fit to the x- and y-components of calibrated  $E_T$  vs. the calibrated PF  $E_T$  sum in a sample of events containing at least two jets with  $p_T > 25$  GeV.  $\sigma$  is calibrated such that the  $E_T$  scale is equal for all three algorithms. PF  $\sum E_T$  is corrected, on average, to the particle level using a Pythia v8 simulation [129]. The blue markers (data) and line (MC) refer to PF jets. Reprinted from Fig. 13 of ref. [125].

replacing the PF jets with their corrected energies (cf. Sec 6.1.3) and recalculating  $E_T$ . Only jets with electromagnetic fraction (EMF) below 90% and  $p_T > 20$  GeV are replaced. This ensures that very electromagnetic jets (as well as isolated leptons, which also receive no correction), which consist chiefly of neutral pions and are measured accurately by the ECAL, do not receive a correction derived for jets with a large fraction of their energy in charged hadrons. In addition, the  $p_T$  cut guarantees that jet corrections are only applied where they are known to within a few percent. For this search, the level of agreement between the SM background estimate and the two-photon search sample in a low- $E_T$  control region is the same regardless of whether the  $E_T$  is corrected or not, so for simplicity the Type-I  $E_T$  corrections are not used (see Sec. 7.4).

Figure 6.12 shows the  $\sigma$  of a Gaussian fit to the x- and y-components of calibrated  $E_T$  vs. the calibrated PF  $E_T$  sum in a sample of events containing at least two jets with  $p_T > 25$  GeV. Again, PF  $E_T$  outperforms  $E_T$  constructed of calorimeter towers or track-corrected calorimeter deposits.

## 6.2 HLT

From the objects described in Sec. 6.1, four samples of events are formed:

- $\gamma\gamma$  candidate sample, in which the two highest  $E_T$  objects are photons,
- $e\gamma$  control sample, in which the two highest  $E_T$  objects are one electron and one photon,
- $ee$  control sample, in which the two highest  $E_T$  objects are electrons, and
- $ff$  control sample, in which the two highest  $E_T$  objects are fakes.

In all samples, the leading EM object is required to have offline reconstructed  $E_T > 40$  GeV, while the trailing EM object is required to have offline reconstructed  $E_T > 25$  GeV. The high level triggers used to select the four samples, by run range, are listed in Table 6.3. No trigger is prescaled.

Each piece of the HLT path name is defined as follows.

- **Photon**: Energy deposit in the ECAL that fired an L1 trigger (cf. Sec. 5.2.1).  
For `Photon26_IsoVL_Photon18`, the L1 seed  $E_T$  threshold is 12 GeV, while for all other triggers in Table 6.3 it is 20 GeV (cf. Sec. 5.2.1).
- Integer following the word **Photon**:  $E_T$  threshold in GeV for offline reconstructed photon, using the full photon reconstruction of Sec. 6.1.1 minus the laser calibrations and assuming the primary vertex at (0, 0, 0).
- **CaloIdL**: For EB photons,  $H/E < 0.15$  and  $\sigma_{i\eta i\eta} < 0.014$ .
- **IsoVL**:  $I_{\text{ECAL}} < 0.012E_T + 6$  GeV,  $I_{\text{HCAL}} < 0.005E_T + 4$  GeV, and  $I_{\text{track}} < 0.002E_T + 4$  GeV.
- **R9Id**:  $R9 > 0.8$ .

Table 6.3: HLT paths triggered by the  $\gamma\gamma$ ,  $e\gamma$ ,  $ee$ , and  $ff$  samples, by run range. No triggers are prescaled.

Run range	$\gamma\gamma$	$e\gamma$	$ee$	$ff$
160404-163261	Photon26_ IsoVL_ Photon18	Photon26_ IsoVL_ Photon18	Photon26_ IsoVL_ Photon18	Photon26_ IsoVL_ Photon18
161216-166967	Photon36_ CaloIdL_ Photon22_ CaloIdL	Photon36_ CaloIdL_ Photon22_ CaloIdL	Photon36_ CaloIdL_ Photon22_ CaloIdL	Photon36_ CaloIdL_ Photon22_ CaloIdL
166347-180252	Photon36_ CaloIdL_ IsoVL_ Photon22_ CaloIdL_ IsoVL	Photon36_ CaloIdL_ IsoVL_ Photon22_ CaloIdL_ IsoVL	Photon36_ CaloIdL_ IsoVL_ Photon22_ CaloIdL_ IsoVL	Photon36_ CaloIdL_ IsoVL_ Photon22_ CaloIdL_ IsoVL  Photon36_ CaloIdL_ IsoVL_ Photon22_ R9Id  Photon36_ R9Id_ Photon22_ CaloIdL_ IsoVL  Photon36_ R9Id_ Photon22_ R9Id

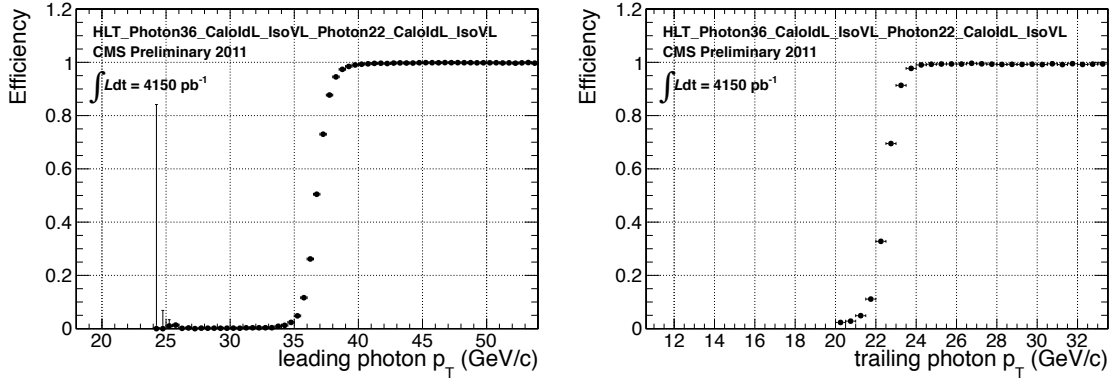


Figure 6.13: Efficiency of `HLT_Photon36_CaloIdL_IsoVL_Photon22_CaloIdL_IsoVL` for offline selected leading photon (left) and trailing photon (right) vs. photon  $p_T$ . Reprinted from Fig. 2 of ref. [116].

In addition, the versions of `HLT_Photon26_IsoVL_Photon18` and `Photon36_CaloIdL_Photo22_CaloIdL` that were active during runs 160404-163268 included a cut  $E_{\max}/E_{5\times 5} < 0.98$  for spike rejection.  $E_{\max}$  is the energy in the highest energy crystal of the EM cluster and  $E_{5\times 5}$  is the energy in the  $5\times 5$  crystal matrix around the seed crystal. For runs after 163268, Swiss cross spike rejection of individual crystals from HLT quantities was performed (cf. Sec. 6.1.1). All information about the evolution of the CMS HLT settings can be found in the HLT configuration browser at <http://j2eeps.cern.ch/cms-project-confdb-hltdev/browser/>.

As an example of the naming convention just described, the HLT path `Photon36_CaloIdL_IsoVL_Photon22_R9Id` is fired if one photon is found with  $E_T > 36$  GeV passing the CaloIdL and IsoVL requirements, and another is found with  $E_T > 22$  GeV passing the R9Id requirement.

For the offline  $E_T$  cuts described in this section, the triggers are  $> 99\%$  efficient, as shown in Figure 6.13 [116]. The efficiencies are measured with respect to triggers with lower  $E_T$  thresholds.

## 6.3 Event Quality

To suppress instrumental backgrounds, a set of event quality cuts are applied to the  $\gamma\gamma$ ,  $e\gamma$ ,  $ee$ , and  $ff$  samples. First, all events are required to pass a good run selection, as determined by the CMS Physics Validation Team [130]. The good run selection excludes luminosity sections during which a sufficient part of the CMS detector was unpowered or malfunctioning. Such conditions could occur if, for example, a high voltage supply trips off in the middle of a run, or a DAQ error corrupts data quality but is not spotted until after the data have been collected. The severity of a detector problem is judged by its effect on a wide range of analyses and reconstruction algorithms. Of the  $\sim 5 \text{ fb}^{-1}$  of integrated luminosity delivered by the LHC in 2011,  $4.68 \text{ fb}^{-1}$  passed the good run selection. This analysis is performed on the entire 2011 certified dataset.

Second, all events must contain at least one good interaction vertex. The criteria for a good vertex are:

- $\chi^2 \neq 0$  OR  $\text{ndof} \neq 0$  OR  $N_{\text{tracks}} \neq 0$ , where  $\chi^2$  and  $\text{ndof}$  are calculated for the track fit to the vertex, and  $N_{\text{tracks}}$  is the number of tracks in the vertex fit
- $\text{ndof} > 4$
- $|z| < 24 \text{ cm}$ , where  $z$  is the  $z$ -coordinate of the vertex position
- $|\rho| < 2 \text{ cm}$ , where  $\rho$  is the transverse displacement of the vertex position from the beam line

The good vertex requirement eliminates non-collision backgrounds such as beam scraping, beam halo, cosmic muon interactions, and instrumental effects.

Third, the two electromagnetic objects in the  $\gamma\gamma$ ,  $e\gamma$ ,  $ee$ , and  $ff$  events must be separated in  $\phi$  by at least 0.05. This requirement protects against beam halo bremsstrahlung, in which a halo muon traveling parallel to the beam line radiates an

energetic photon while itself depositing a large amount of energy in the ECAL. In this case, the two ECAL hits would likely be at the same  $\phi$  (and  $\rho$ ).

Fourth, the two EM objects must be separated in  $R$  by at least 0.6. Since the isolation cone size used is 0.3, this ensures that the isolation energy of one EM object cannot be in the veto strip (Fig. 6.6) of the other.

Finally, the  $\gamma\gamma$ ,  $e\gamma$ ,  $ee$ , and  $ff$  events must pass an HCAL noise filter and ECAL dead channel filter. The HCAL noise filter guarantees that all HCAL reconstructed hits are inconsistent with any noise source. Noise sources [90] include:

- Ion feedback in the HPDs absent any true incident photons, in which a thermal electron ionizes a molecule in the HPD acceleration gap, faking a real signal
- HPD discharge affecting nearly all channels in the same HPD [131], partially explained by the effect of the 4 T CMS magnetic field on the flashover voltage of the dielectric [132]
- Concurrent signals in nearly all 72 channels of a single RBX, as yet unexplained
- HF PMT window hits (as opposed to the usual quartz fiber hits)
- ADC saturation

Since HCAL noise may induce fake jets or  $E_T$ , events are rejected if any of the following criteria are true:

- Any HPD has  $> 17$  hits
- A single HPD has  $> 10$  hits, but every other HPD has zero hits
- An RBX has  $> 10$  zero-ADC-count hits
- Any HB/HE reconstructed hit corresponding to an RBX with  $> 50$  GeV of energy fails a two-dimensional cut defined by the variables  $(TS4 - TS5)/(TS4 + TS5) < 0.05$

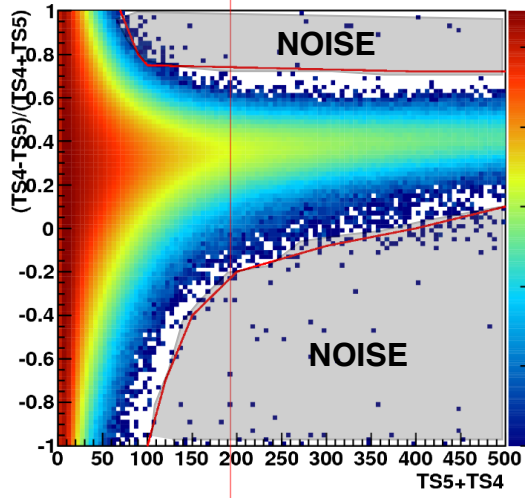


Figure 6.14:  $(TS4 - TS5)/(TS4 + TS5)$  vs.  $TS4 + TS5$  for a minimum bias sample. HB/HE hits are considered noisy if they lie in the sparsely populated gray region labeled "NOISE" defined by the curved red lines. Adapted from ref. [133].

$TS5)$  vs.  $TS4 + TS5$ , where  $TS4(TS5)$  is the hit amplitude in the fourth(fifth) time sample read out for that hit. The cut is defined in Fig. 6.14.

The ECAL dead channel filter is designed to flag events in which significant EM energy was deposited in a masked region of the ECAL by using the trigger primitive information for the corresponding trigger tower. Energy deposited in a masked region of ECAL can cause fake  $E_T$ . Events are rejected if the trigger primitive  $E_T$  exceeds the maximum value of 63.75 GeV in any trigger tower that is masked in the readout.

## 6.4 Photon Identification Efficiency

In order to determine the cross section (or cross section upper limit) for a GGM signal, the photon identification efficiency is needed. Since no suitably large sample of  $Z \rightarrow \mu\mu\gamma$  events in CMS exists yet, the efficiency calculation relies on the similarity between detector response to electrons and photons. A scale factor to correct the MC photon ID efficiency to the real photon efficiency for the data is obtained from the ratio of the electron efficiency from the data to the electron efficiency from MC.

The different types of photon ID variables—calorimeter and track isolation, ratio of hadronic to electromagnetic energy of the shower, and transverse shower shape—are chosen so that their distributions for isolated electrons and photons are similar.<sup>3</sup>

The photon selection efficiency is

$$\epsilon_\gamma = \epsilon_\gamma^{\text{MC}} \times \frac{\epsilon_e^{\text{data}}}{\epsilon_e^{\text{MC}}} \quad (6.6)$$

where

- $\epsilon_\gamma$  is the photon ID efficiency in data,
- $\epsilon_\gamma^{\text{MC}}$  is the photon ID efficiency in MC,
- $\epsilon_e^{\text{data}}$  is the electron ID efficiency obtained using  $Z \rightarrow ee$  electrons in the data that satisfy the photon ID cuts, and
- $\epsilon_e^{\text{data}}$  is the electron ID efficiency obtained using  $Z \rightarrow ee$  electrons in MC that satisfy the photon ID cuts.

The ratio  $\epsilon_e^{\text{data}}/\epsilon_e^{\text{MC}}$  is defined as the scale factor by which the GGM signal MC photon ID efficiency must be multiplied to give an estimate of the photon ID efficiency in data. The photon ID requirements of Table 6.1 plus the IsoVL HLT requirement described in Sec. 6.2 and Table 6.3 are repeated in Table 6.4.

### 6.4.1 Tag and Probe Method

A *tag and probe* method using  $Z$  events is utilized to measure the efficiency of the photon ID cuts in Table 6.1. The tag is a well-identified electron. The probe, by contrast, is as loosely identified as possible, and all tags must pass the probe criteria

---

<sup>3</sup> $R9$  differs between photons and radiating electrons, but the requirement  $R9 < 1$  is loose enough not to introduce problems with the use of electrons to measure the photon ID efficiency.

in addition to the stringent tag criteria. The tag and probe criteria used in this study are shown in Table 6.5.

The invariant mass of the tag and probe are required to be within a narrow window around  $Z$  mass. Assuming that the probabilities of the tag and probe legs of the  $Z$  decay to pass the photon ID cuts are uncorrelated, the efficiency can be estimated as

$$\epsilon = \frac{N_{\text{tag-pass}}}{N_{\text{tag-pass}} + N_{\text{tag-fail}}} \quad (6.7)$$

where  $N_{\text{tag-pass}}$  is the number of tag-probe pairs in which the probe leg passes the photon ID cuts under study and  $N_{\text{tag-fail}}$  is the number of tag-probe pairs in which the probe leg fails the cuts. Implicit in these definitions is a double counting of pairs in which both electrons pass the tag and probe criteria [135]. In addition, in the rare circumstance (less than 1% in MC [135]) that two or more probes may be matched to one tag, the pair with invariant mass closest to the  $Z$  mass is chosen.

In practice,  $N_{\text{tag-pass}}$  and  $N_{\text{tag-fail}}$  are returned by a simultaneous unbinned maximum likelihood fit to the invariant mass distributions of tag-pass and tag-fail events, with appropriate signal and background PDF assumptions. The fit form used is

Table 6.4: Candidate photon ID requirements.

Variable	Cut
$I_{\text{ECAL}}$	$< 0.012E_T + 6 \text{ GeV}$
$I_{\text{HCAL}}$	$< 0.005E_T + 4 \text{ GeV}$
$I_{\text{track}}$	$< 0.002E_T + 4 \text{ GeV}$
$H/E$	$< 0.05$
$\sigma_{i\eta i\eta}$	$< 0.011$
$I_{\text{ECAL}} - 0.0792\rho + I_{\text{HCAL}} - 0.0252\rho + I_{\text{track}}$	$< 6 \text{ GeV}$
$R9$	$< 1$

Table 6.5: Tag and probe criteria. The superscript 0.4 indicates that the isolation variable was calculated in a cone of  $\Delta R = 0.4$  around the photon candidate. The isolations without superscripts use the standard  $\Delta R = 0.3$  cones.

Variable	Cut	
	Tag	Probe
RECO object	photon	photon
HLT	HLT_Ele17_CaloIdVT_CaloIsoVT_TrkIdT_TrkIsoVT_SC8_Mass30_v* (must have fired the 17 GeV leg)	—
$H/E$	$< 0.05$	$< 0.15$
$I_{\text{ECAL}}^{0.4}$	$< 0.006E_T + 4.2 \text{ GeV}$	—
$I_{\text{HCAL}}^{0.4}$	$< 0.0025E_T + 2.2 \text{ GeV}$	—
$I_{\text{track}}^{0.4}$	$< 0.001E_T + 2.0 \text{ GeV}$	—
$E_T$	$> 25 \text{ GeV}$	—
SC $E_T$	—	$> 15 \text{ GeV}$
SC $ \eta $	$< 1.4442$	$< 1.4442$
$\sigma_{i\eta i\eta}$	$< 0.009$	—
Has pixel seed	Yes	—
Track match type	General track <sup>a</sup>	—
Track match $\Delta R$	$< 0.04$	—
Track match $p_T$	$> 15 \text{ GeV}$	—
Track match $ \eta $	$< 1.479$	—

<sup>a</sup>A general track is reconstructed with the CMS standard combinatorial track finder [134].

$$\begin{aligned} f_{\text{tag-pass}}(m_{\text{tag-pass}}) &= \epsilon N_S f_S^{\text{pass}}(m_{\text{tag-pass}}) + N_B^{\text{pass}} f_B^{\text{pass}}(m_{\text{tag-pass}}) \\ f_{\text{tag-fail}}(m_{\text{tag-fail}}) &= (1 - \epsilon) N_S f_S^{\text{fail}}(m_{\text{tag-fail}}) + N_B^{\text{fail}} f_B^{\text{fail}}(m_{\text{tag-fail}}) \end{aligned} \quad (6.8)$$

where  $f_{\text{tag-pass}}(m_{\text{tag-pass}})$  and  $f_{\text{tag-fail}}(m_{\text{tag-fail}})$  are the tag-pass and tag-fail PDFs, respectively;  $\epsilon$  is the efficiency;  $N_S$  is the total number of  $Z$  signal events summed over both samples;  $f_S^{\text{pass}}(m_{\text{tag-pass}})$  and  $f_S^{\text{fail}}(m_{\text{tag-fail}})$  are the tag-pass and tag-fail signal PDFs, respectively;  $N_B^{\text{pass}}$  and  $N_B^{\text{fail}}$  are the numbers of background events in the tag-pass and tag-fail samples, respectively; and  $f_B^{\text{pass}}(m_{\text{tag-pass}})$  and  $f_B^{\text{fail}}(m_{\text{tag-fail}})$  are the tag-pass and tag-fail background PDFs, respectively. This particular implementation of the tag and probe methodology is based on tag `CMSSW_4_2_5` of the CMSSW package `PhysicsTools/TagAndProbe`, and uses the MINUIT2 [136] library, as coded in RooFit [137], for the likelihood maximization. For this study, CMSSWv4.2.8 was used.

For both samples, the signal shape is assumed to be a Crystal Ball function [138] convoluted with the  $Z$  generated lineshape, while the background shape is a PDF that describes the falling background as well as the kinematic turn-on at low invariant mass. The background PDF, called `RooCMSShape` [135], is given by

$$f_{\text{RooCMSShape}}(x) = \begin{cases} 1e20 & \text{for } (x - \mu)\gamma < -70 \\ 0 & \text{for } (x - \mu)\gamma > 70 \\ \text{erfc}((\alpha - x)\beta) \exp(-(x - \mu)\gamma) & \text{otherwise} \end{cases} \quad (6.9)$$

where  $\alpha$ ,  $\beta$ ,  $\gamma$ , and  $\mu$  are parameters of the fit, most of which are held fixed. In the three lowest  $E_T$  bins, all parameters of the tag-pass and tag-fail background PDFs are left floating, because the effect of the relaxed  $E_T$  cuts has a significant effect on

the background shape. More details of the signal and background PDFs are given in Table 6.6. The fixed signal and background parameter values were determined by fitting a small sample ( $0.0 \leq \eta < 0.25$ ) of Fall11 MC signal (DYJetsToLL) and background (QCD\_Pt-20to30\_BCtoE, QCD\_Pt-30to80\_BCtoE, QCD\_Pt-80to170\_BCtoE, GJet\_Pt-20\_doubleEMEnriched, WJetsToLNu, TTJets) with parameters left floating.<sup>4</sup>

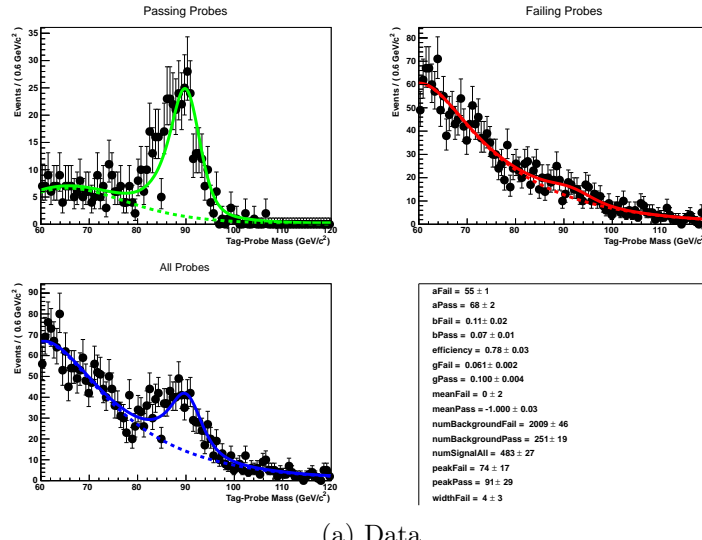
Table 6.6: Parameter values (parameter definitions are in the text) for the signal and background PDFs for the different samples. The background PDF applies to all efficiency bins except the four lowest  $E_T$  bins, which use a floating `RooCMSShape` background. When a bracketed range is given, the parameter is allowed to float within that range. When a constant is given, the parameter is fixed to that constant.

PDF	Crystal Ball fit parameters				RooCMSShape fit parameters			
	$\mu$	$\sigma$	$\alpha$	n	$\mu$	$\alpha$	$\beta$	$\gamma$
Tag-pass signal	[-1.0, 1.0]	[1.0, 3.0]	0.87	97.0	N/A	N/A	N/A	N/A
Tag-fail signal	[-1.0, 1.0]	[1.0, 3.0]	0.73	134.9	N/A	N/A	N/A	N/A
Tag-pass background	N/A	N/A	N/A	N/A	65.0	61.949	0.04750	0.01908
Tag-fail background	N/A	N/A	N/A	N/A	$\alpha$	[50.0, 100.0]	0.065	0.048

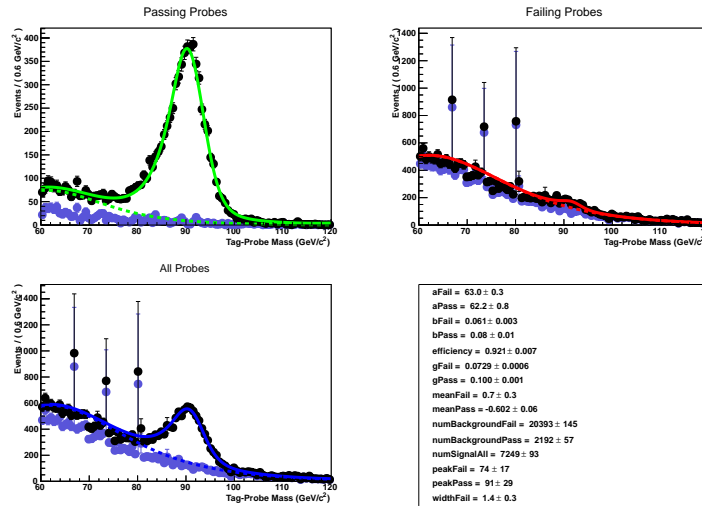
Some fit examples are shown in Figures 6.15 and 6.16. In Fig. 6.15, which shows fits to data and MC for  $15 \text{ GeV} \leq \text{probe } E_T < 20 \text{ GeV}$ , the kinematic turn-on is below the invariant mass range covered by the plot. The exponentially falling background is easily seen underneath the signal, and is especially pronounced in the background-dominated tag-fail sample.

---

<sup>4</sup>See Appendix A for a discussion of the MC samples.

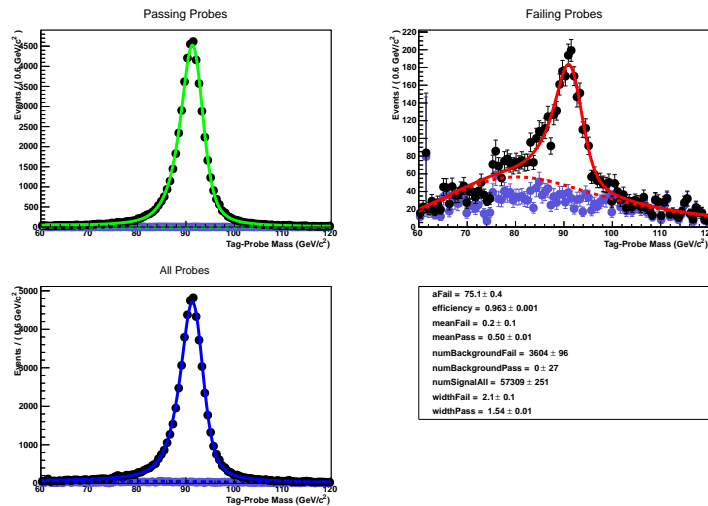
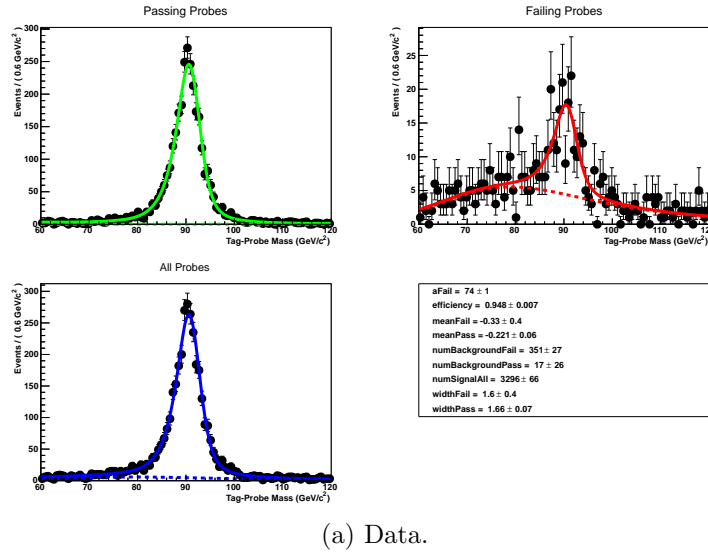


(a) Data.



(b) MC. The purple points are the background MC (photon + jet, W, QCD, and t̄t).

Figure 6.15: Tag and probe invariant mass fits for  $15 \text{ GeV} \leq \text{probe } E_T < 20 \text{ GeV}$ . Errors are statistical only. The tag-pass fit is shown in green in the upper-left-hand plot, the tag-fail fit in red in the upper-right-hand plot, and a fit to both samples in blue in the lower-left-hand plot. Dotted lines are the background components of the fits; solid lines are signal plus background.



(b) MC. The purple points are the background MC (photon + jet,  $W$ , QCD, and  $t\bar{t}$ ).

Figure 6.16: Tag and probe invariant mass fits for  $-0.25 \leq \text{probe } \eta < -0.5$ . Errors are statistical only. The tag-pass fit is shown in green in the upper-left-hand plot, the tag-fail fit in red in the upper-right-hand plot, and a fit to both samples in blue in the lower-left-hand plot. Dotted lines are the background components of the fits; solid lines are signal plus background.

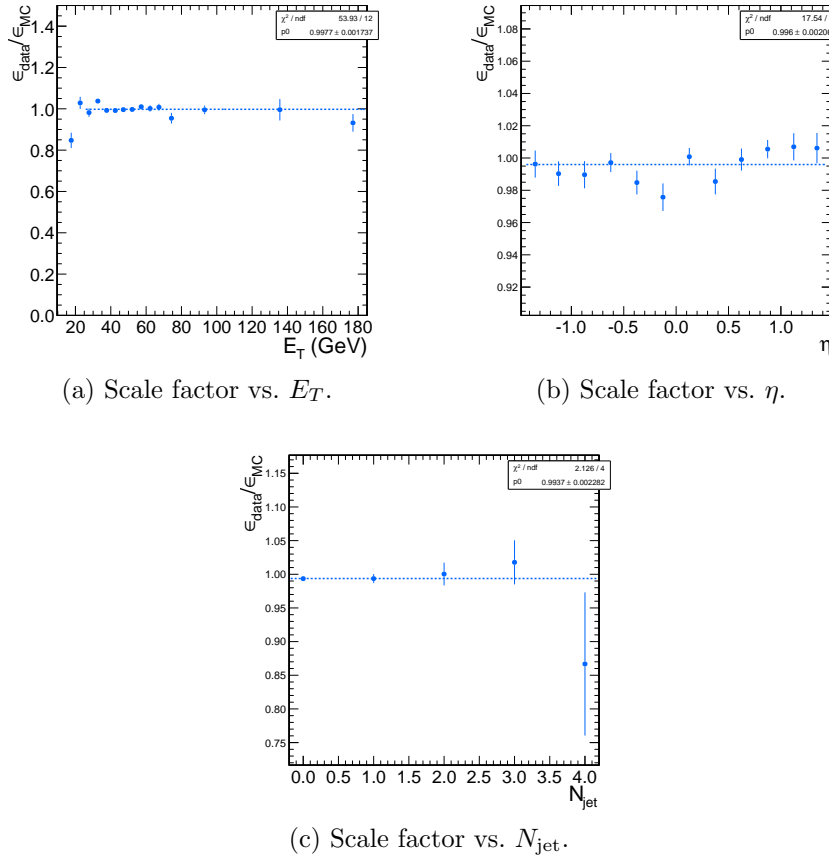


Figure 6.17: Dependence of the photon ID efficiency scale factor on some kinematic variables. Errors are statistical only.

#### 6.4.2 Photon Efficiency Scale Factor $\epsilon_e^{\text{data}} / \epsilon_e^{\text{MC}}$

Figure 6.17 shows the dependence of the photon ID efficiency scale factor  $\epsilon_e^{\text{data}} / \epsilon_e^{\text{MC}}$  on  $E_T$ ,  $\eta$ , and  $N_{\text{jet}}$ , where jets are defined as in Table 6.2, but with only the two  $Z$  electrons considered as candidates for overlap removal. Errors are statistical only. There is no significant dependence of the scale factor on these variables, so only one scale factor is computed from the entire dataset.

The effect of pileup is studied by comparing the efficiencies  $\epsilon_e^{\text{data}}$  and  $\epsilon_e^{\text{MC}}$  vs. the number of primary vertices ( $N_{\text{PV}}$ ) in the event. The efficiency only drops a few percent for events with large  $N_{\text{PV}}$  after using pileup-corrected isolation cuts, as can be seen in Figure 6.18(a). The MC tracks the data, and the scale factor is flat vs.  $N_{\text{PV}}$ , as

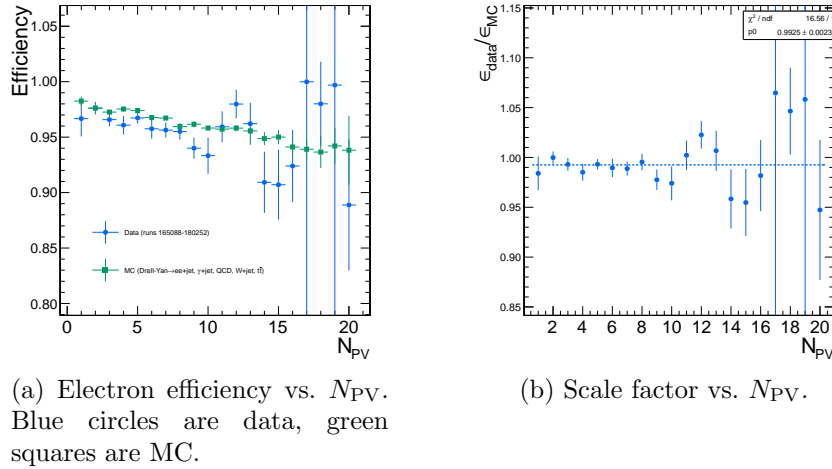


Figure 6.18: Dependence of the photon ID efficiency scale factor on the number of primary vertices per event. Errors are statistical only.

shown in Fig. 6.18(b).

The scale factor is measured to be  $\epsilon_e^{\text{data}}/\epsilon_e^{\text{MC}} = 0.994 \pm 0.002(\text{stat.}) \pm 0.035(\text{syst.})$ .

Four main sources of systematic error, in addition to the statistical error of 0.2%, were studied.

### Different behavior of electrons and photons in MC

Even though the photon ID cuts are designed to be similarly efficient for both electrons and photons, there might be a small difference in the performance between the two kinds of particles, e.g. because of electron bremsstrahlung. To check this effect, the MC electron ID efficiency was calculated using a  $Z \rightarrow ee$  sample and the MC photon ID efficiency was calculated using a  $\gamma + \text{jets}$  sample. Both samples were reconstructed in CMSSWv3.6. Half the difference between these two results, 0.5%, was taken as an error on the scale factor.

**Pileup** To account for the possibility that the MC simulation may not adequately reproduce the data in a high pileup environment, the data/MC scale factor for events with 1-4 good reconstructed primary vertices was calculated, along with the same for events with  $\geq 5$  good reconstructed primary vertices. The

difference between the scale factors from both samples, 2.4%, was taken as an error on the scale factor from pileup.

**Signal fit over/underestimation** It was found that the signal fit slightly underestimates the data in the tag-pass sample, and slightly overestimates it in the tag-fail sample. To cover this effect with a systematic error, the efficiencies in data and MC, and then the scale factor, were recalculated using the background (from fit) subtracted integrals of the tag-pass and tag-fail distributions, rather than the fitted signal yields in those distributions. The difference between the scale factor found in this way and the nominal scale factor, 1.9%, was taken as an error on the scale factor.

**Signal and background shape assumption** To assess the magnitude of the error from the signal and background shape assumptions, the tag-pass and tag-fail tail parameters (Crystal Ball  $\alpha$  and  $n$ ) were varied by  $\pm 1\sigma$ , and the background shape was varied between `RooCMSShape`, exponential, power law, and quadratic. All possible combinations of varied parameters were generated, and the data and MC were refit and new scale factors generated according to those combinations. The error was taken as the largest deviation of the scale factor from nominal, 1.8%.

Finally, the pixel veto efficiency was estimated from MC to be  $0.96 \pm 0.005$ (syst.), with error due to varying assumptions of the tracker material distribution [139]. In general, the photon ID selection used in this analysis is very efficient for GGM photons and robust to pileup, and its efficiency is fairly well measured.

# Chapter 7

## Data Analysis

The signature of GGM SUSY particle production in this search is an excess of two-photon events with high  $E_T$  above the Standard Model background.  $E_T$  is reconstructed using the particle flow algorithm as described in Sec. 6.1.3. Candidate two-photon events, as well as control events, are selected according to the offline object criteria presented in Secs. 6.1.1, 6.1.2, and 6.1.3; the event quality criteria in Sec. 6.3; and the trigger requirements in Sec. 6.2. These are summarized in Table 7.1.

Table 7.1: Selection criteria for  $\gamma\gamma$ ,  $e\gamma$ ,  $ee$ , and  $ff$  events.

Variable	Cut			
	$\gamma\gamma$	$e\gamma$	$ee$	$ff$
HLT match	IsoVL	IsoVL	IsoVL	IsoVL    R9Id
$E_T$	$> 40/$ $> 25 \text{ GeV}$			
SC $ \eta $	$< 1.4442$	$< 1.4442$	$< 1.4442$	$< 1.4442$
$H/E$	$< 0.05$	$< 0.05$	$< 0.05$	$< 0.05$
$R9$	$< 1$	$< 1$	$< 1$	$< 1$
Pixel seed	No/No	Yes/No	Yes/Yes	No/No
$I_{\text{comb}}$ , $\sigma_{i\eta i\eta}$	$< 6 \text{ GeV} \&\&$ $< 0.011$	$< 6 \text{ GeV} \&\&$ $< 0.011$	$< 6 \text{ GeV} \&\&$ $< 0.011$	$< 20 \text{ GeV} \&\&$ $(\geq 6 \text{ GeV} \parallel$ $\geq 0.011)$
JSON	Yes	Yes	Yes	Yes
No. good PVs	$\geq 1$	$\geq 1$	$\geq 1$	$\geq 1$
$\Delta R_{\text{EM}}$	$> 0.6$	$> 0.6$	$> 0.6$	$> 0.6$
$\Delta\phi_{\text{EM}}$	$\geq 0.05$	$\geq 0.05$	$\geq 0.05$	$\geq 0.05$

This search utilizes  $4.7 \text{ fb}^{-1}$  of CMS data collected during the period April–December 2011, corresponding to the following datasets [140]:

- `/Photon/Run2011A-05Jul2011ReReco-ECAL-v1/AOD`
- `/Photon/Run2011A-05Aug2011-v1/AOD`
- `/Photon/Run2011A-03Oct2011-v1/AOD`
- `/Photon/Run2011B-PromptReco-v1/AOD`

The search strategy is to model the backgrounds to the GGM SUSY signal using  $\cancel{E}_T$  shape templates derived from the control samples, and then to look for a high- $\cancel{E}_T$  excess above the estimated background in the  $\gamma\gamma$  sample. There are two categories of backgrounds: QCD processes with no real  $\cancel{E}_T$  and electroweak processes with real  $\cancel{E}_T$  from neutrinos. The relevant QCD background processes are multijet production with at least two jets faking photons, photon + jet production with at least one jet faking a photon, and diphoton production. The relevant electroweak background processes, which are small compared to the QCD background, involve  $W \rightarrow e\nu$  decay with a recoiling jet that fakes a photon or a real radiated photon (the  $W$  may come from the decay of a top quark in  $t\bar{t}$  events). In both cases, the electron is misidentified as a photon due to a small inefficiency in reconstructing the electron pixel seed. The main diagrams contributing to the QCD(electroweak) backgrounds are shown in Figure 7.1(7.2).

## 7.1 Control Samples

Data control samples are used to model all of the backgrounds. The primary control sample used to model the QCD background is the  $ff$  sample, which is similar to the candidate  $\gamma\gamma$  sample but with combined isolation or  $\sigma_{inj\eta}$  cuts inverted. The cuts

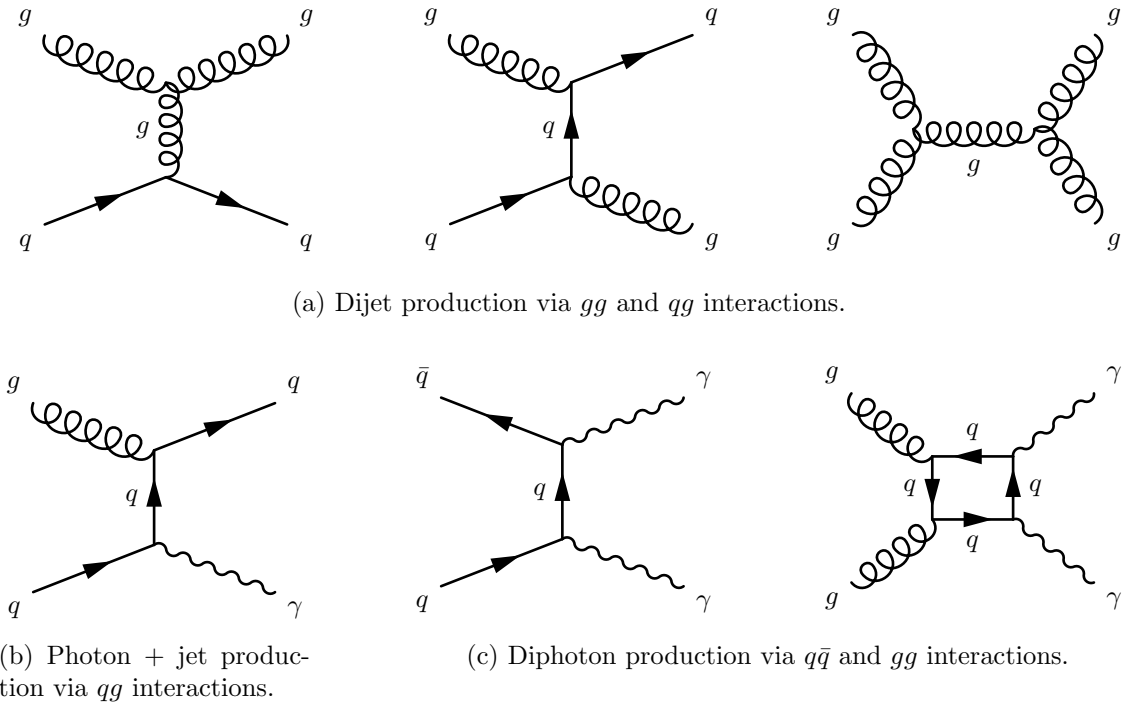


Figure 7.1: Representative Feynman diagrams of some QCD backgrounds to the GGM SUSY search.

on these variables are used to distinguish between photons and jets, so by inverting those cuts, the resulting  $ff$  sample becomes enriched with QCD dijets. Because the fake photons are still required to pass a tight cut on  $H/E$ , they are guaranteed to be very electromagnetic jets, with an EM energy scale and resolution similar to that of the candidate photons. This insures that the resulting estimate of the  $\cancel{E}_T$  shape does not have too long of a tail from severe HCAL mis-measurements that are actually rare in the  $\gamma\gamma$  sample.

As a cross-check, the  $ee$  sample is also used to model the QCD background. This sample of  $Z$  decays should have no true  $\cancel{E}_T$ , just like the  $ff$  sample, and the electron definition (differing from the photon definition only in the presence of a pixel seed) insures that the electron energy scale and resolution is similar to that of the photon.

Finally, the  $e\gamma$  sample is used to model the electroweak background from  $W \rightarrow e\nu$  decays. The  $e\gamma$   $\cancel{E}_T$  distribution is scaled by the electron $\rightarrow$ photon misidentification

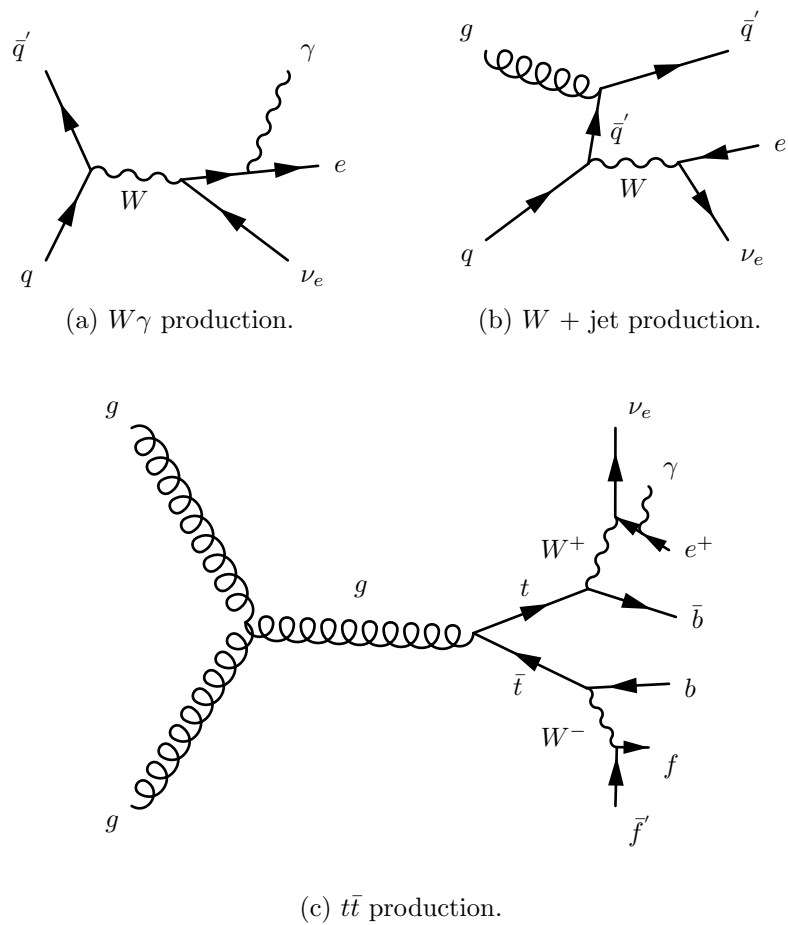


Figure 7.2: Representative Feynman diagrams of some electroweak backgrounds to the GGM SUSY search.

rate to predict the number of  $W\gamma$ ,  $W + \text{jet}$ , and  $t\bar{t}$  events in the  $\gamma\gamma$  sample.

The remainder of this chapter describes the data analysis procedures and the final results of the search. Sec. 7.2 addresses the QCD background estimation. Sec. 7.3 addresses the electroweak background estimation. The chapter concludes with a discussion of systematic errors in Sec. 7.4 and a presentation of the final results in Sec. 7.5.

## 7.2 Modeling the QCD Background

### 7.2.1 Outline of the Procedure

Due to the fact that the CMS ECAL energy resolution is much better than the HCAL energy resolution, the energies of the two candidate photons in the events of the  $\gamma\gamma$  sample are typically measured to far greater accuracy and precision than the energy of the hadronic recoil in those events. Therefore, fake  $E_T$  in the  $\gamma\gamma$  sample is almost entirely the result of hadronic mis-measurement in QCD dijet, photon + jet, and diphoton events. The strategy employed to model this background is to find a control sample in data consisting of two well-measured EM objects, just like the candidate  $\gamma\gamma$  sample, and assign each event a weight to account for the underlying kinematic differences between the control and candidate samples. Once the reweighted  $E_T$  spectrum of the control sample is created, it is then normalized in the low- $E_T$  region, the assumption being that GGM SUSY does not predict a significant amount of events at low  $E_T$ . There are three aspects of this QCD background estimation procedure that bear highlighting:

**Choice of control sample** Since the underlying cause of  $E_T$  in the candidate sample is mis-measured hadronic activity, a control sample with similar hadronic activity to the candidate sample should be chosen. Hadronic activity refers to number of jets, jet  $E_T$ , pileup, etc.

**Reweighting** The control sample is reweighted so that its  $\cancel{E}_T$  spectrum appears as it would if the control sample had the same kinematic properties as the candidate  $\gamma\gamma$  sample (i.e. particle  $p_T$  and  $\eta$  distributions, etc.). By choosing an appropriate control sample and reweighting it, the control  $\cancel{E}_T$  distribution should now match both the hadronic activity and the kinematics of the candidate sample.

**Normalization** Finally, the control  $E_T$  distribution is normalized in a region of low  $\cancel{E}_T$ , where contamination from the expected GGM SUSY signal is small. This implies an extrapolation of the low- $\cancel{E}_T$  QCD background prediction to the high- $\cancel{E}_T$  signal region.

As explained in the beginning of this chapter, the  $ff$  sample is used as the primary QCD control sample, while the  $ee$  sample is used as a cross-check. Both samples have two well-measured EM objects per event, no real  $\cancel{E}_T$ , and similar hadronic activity to the  $\gamma\gamma$  sample. Figures 7.3- 7.8 show a comparison of the shapes of some distributions relevant to hadronic activity between the  $\gamma\gamma$ ,  $ee$ , and  $ff$  samples. In general, the  $ee$  sample has less hadronic activity than the  $\gamma\gamma$  and  $ff$  samples, as shown by the more steeply falling  $ee$  distributions in Figs. 7.3, 7.4, 7.5, and 7.6. In addition to the kinematic reweighting, there is also a reweighting by number of jets per event, which attempts to correct for this difference (see Sec. 7.2.2).

### 7.2.2 Reweighting

To reweight the control sample events to match the kinematics of the candidate sample events, a weight based on the  $p_T$  of the di-EM-object system and the number of jets in the event is used. As explained in Sec. 7.2.1,  $E_T$  in the  $\gamma\gamma$ ,  $ff$ , and  $ee$  samples is due to the poorly measured hadronic recoil off the well-measured di-EM system. Therefore, the  $p_T$  of the di-EM system is a good handle on the true magnitude of the hadronic recoil, which affects the measured  $\cancel{E}_T$ . The di-EM system is depicted

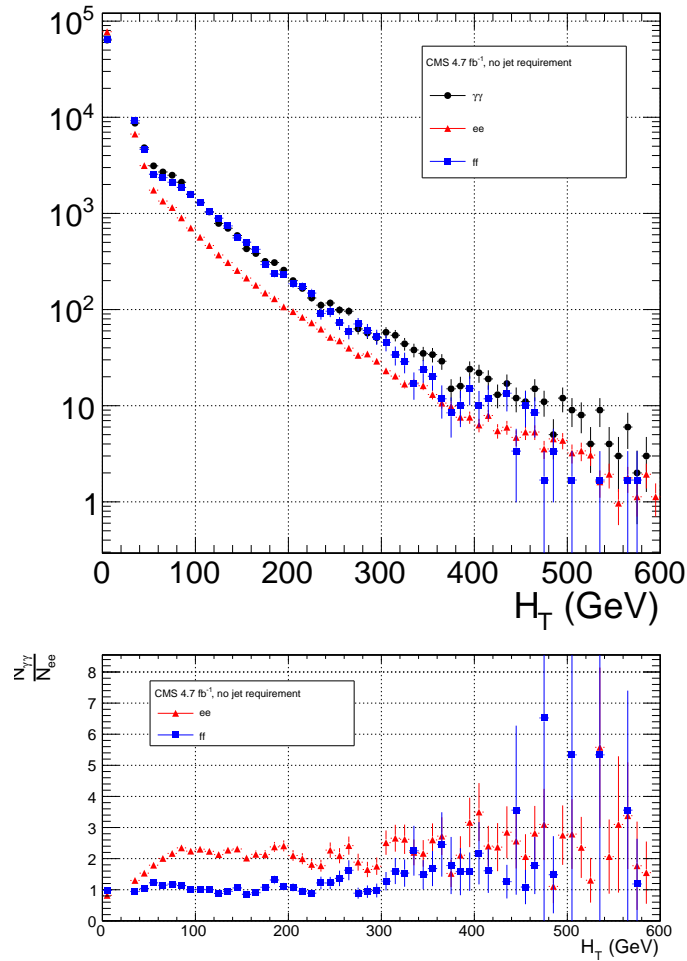


Figure 7.3:  $H_T$ , defined as the scalar sum of corrected jet  $E_T$  for jets defined as in Table 7.2.  $\gamma\gamma$  is in black,  $ee$  ( $81 \text{ GeV} \leq m_{ee} < 101 \text{ GeV}$ ) is in red, and  $ff$  is in blue. The  $ee$  and  $ff$  distributions are normalized to the number of events in the  $\gamma\gamma$  distribution. Errors are statistical only.

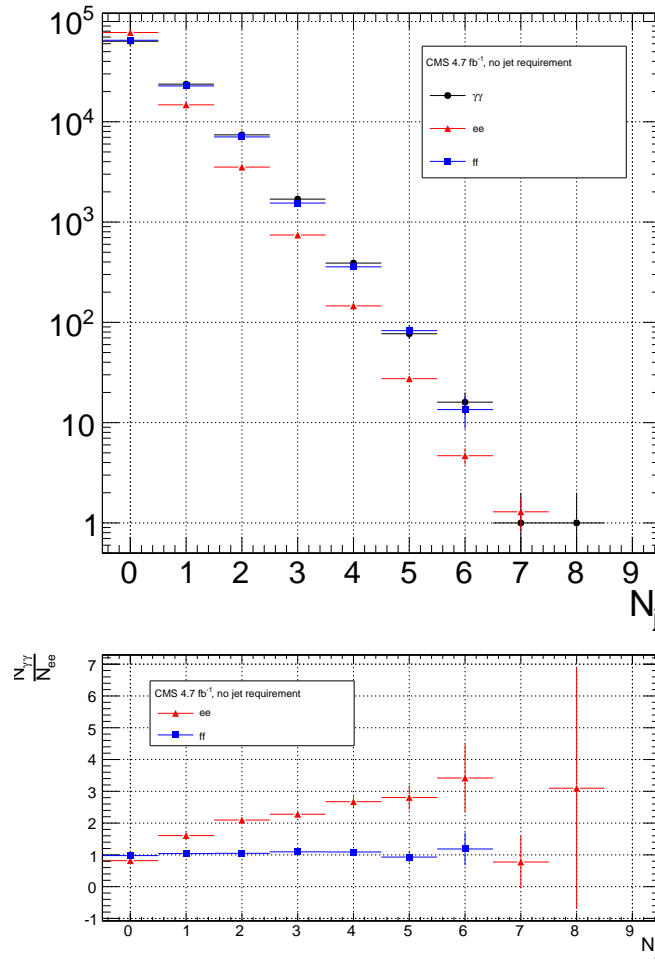


Figure 7.4: Number of jets per event for jets defined as in Table 7.2.  $\gamma\gamma$  is in black,  $ee$  ( $81 \text{ GeV} \leq m_{ee} < 101 \text{ GeV}$ ) is in red, and  $ff$  is in blue. The  $ee$  and  $ff$  distributions are normalized to the number of events in the  $\gamma\gamma$  distribution. Errors are statistical only.

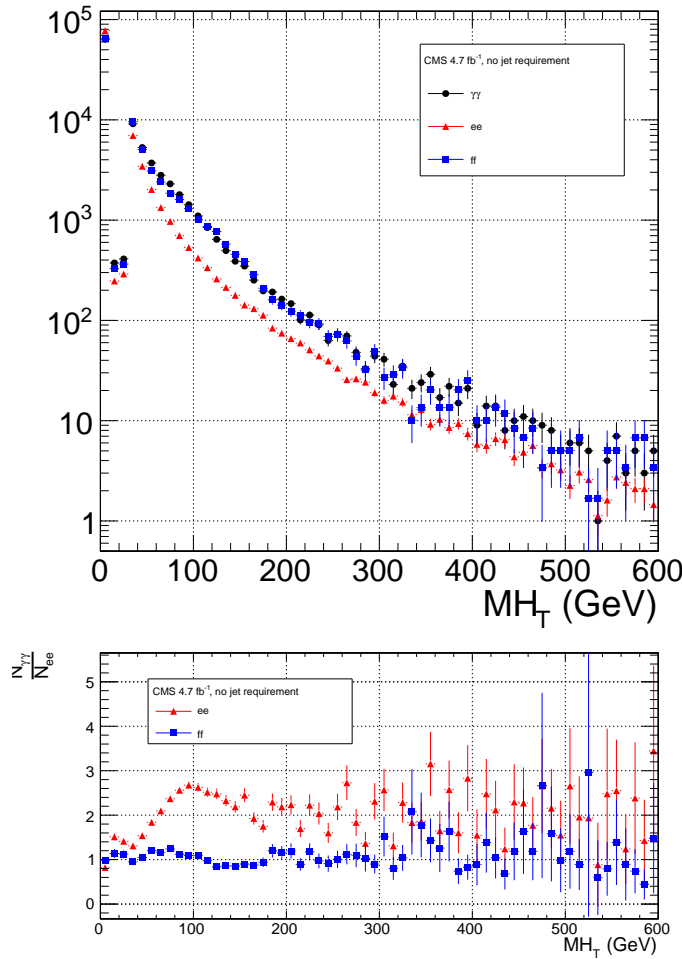


Figure 7.5:  $H_T$ , defined as the magnitude of the negative vectorial sum of corrected jet  $E_T$  for jets defined as in Table 7.2.  $\gamma\gamma$  is in black,  $ee$  ( $81 \text{ GeV} \leq m_{ee} < 101 \text{ GeV}$ ) is in red, and  $ff$  is in blue. The  $ee$  and  $ff$  distributions are normalized to the number of events in the  $\gamma\gamma$  distribution. Errors are statistical only.

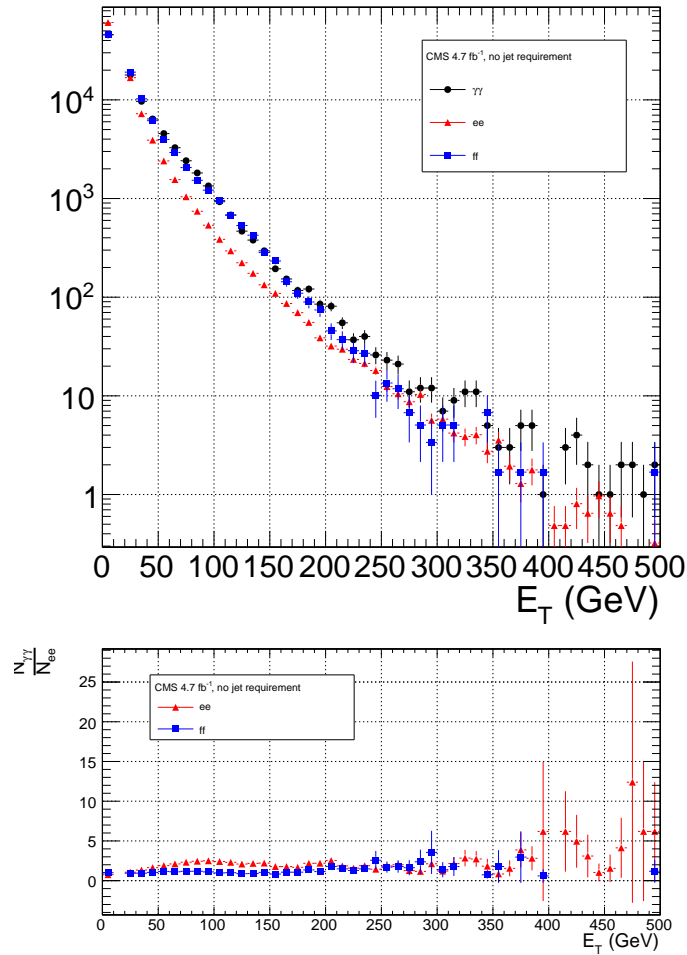


Figure 7.6: Corrected  $E_T$  for the jet with the largest corrected  $E_T$  per event, for jets defined as in Table 7.2 (excluding the  $p_T$  requirement).  $\gamma\gamma$  is in black,  $ee$  ( $81 \text{ GeV} \leq m_{ee} < 101 \text{ GeV}$ ) is in red, and  $ff$  is in blue. The  $ee$  and  $ff$  distributions are normalized to the number of events in the  $\gamma\gamma$  distribution. Errors are statistical only.

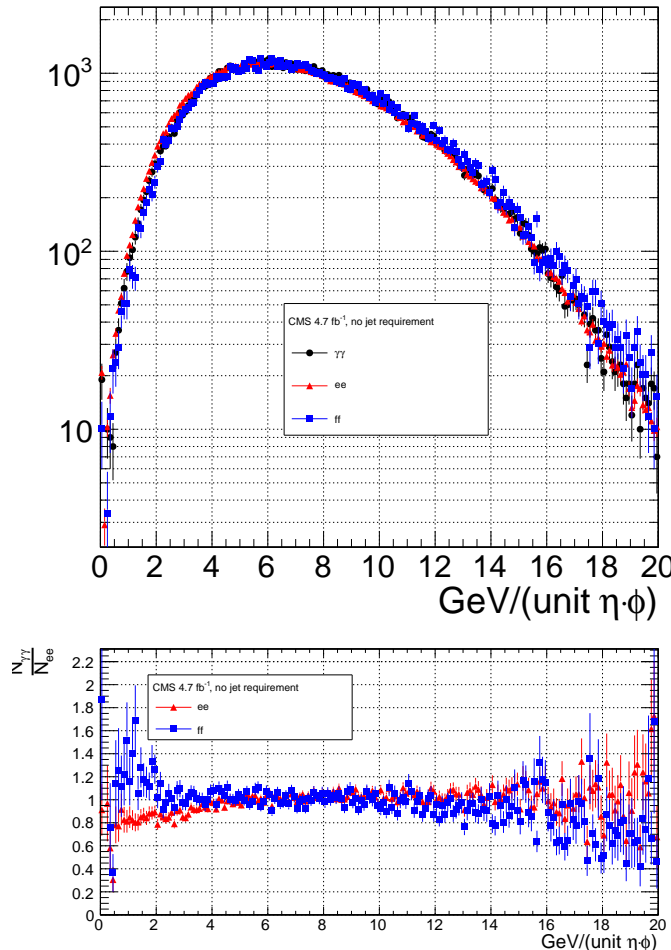


Figure 7.7:  $\rho$  (average pileup energy density in the calorimeters per unit  $\eta \cdot \phi$ , cf. Sec. 6.1.1).  $\gamma\gamma$  is in black,  $ee$  ( $81 \text{ GeV} \leq m_{ee} < 101 \text{ GeV}$ ) is in red, and  $ff$  is in blue. The  $ee$  and  $ff$  distributions are normalized to the number of events in the  $\gamma\gamma$  distribution. Errors are statistical only.

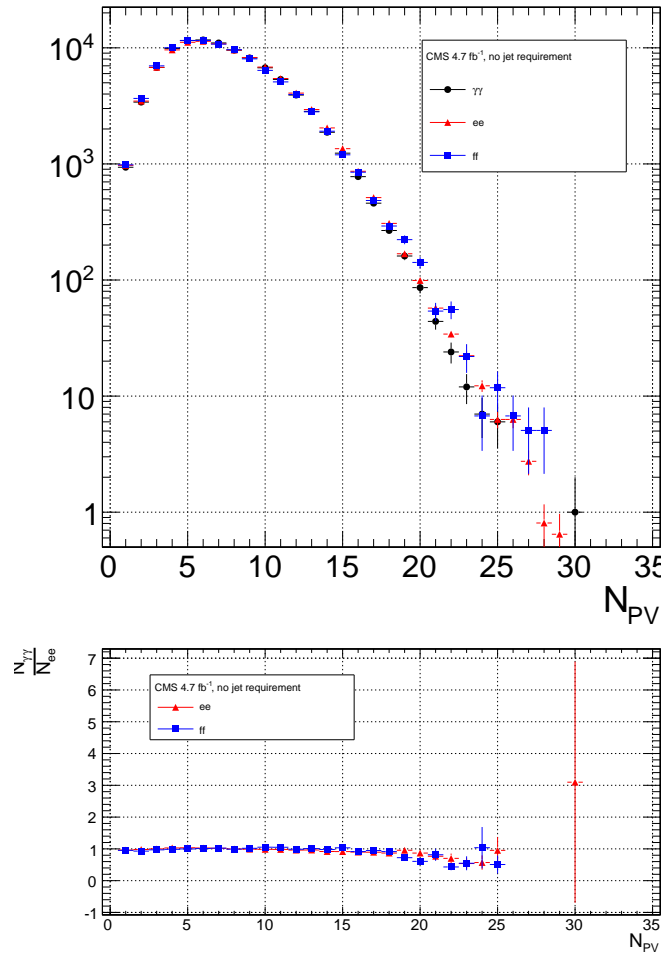


Figure 7.8: Number of good reconstructed primary vertices per event according to the criteria of Sec. 6.3.  $\gamma\gamma$  is in black,  $ee$  ( $81 \text{ GeV} \leq m_{ee} < 101 \text{ GeV}$ ) is in red, and  $ff$  is in blue. The  $ee$  and  $ff$  distributions are normalized to the number of events in the  $\gamma\gamma$  distribution. Errors are statistical only.

Table 7.2: Definition of HB/HE/HF hadronic jets.

Variable	Cut
Algorithm	L1FastL2L3Residual corrected PF (cf. Sec. 6.1.3)
$p_T$	$> 30 \text{ GeV}$
$ \eta $	$< 5.0$
Neutral hadronic energy fraction	$< 0.99$
Neutral electromagnetic energy fraction	$< 0.99$
Number of constituents	$> 1$
Charged hadronic energy	$> 0.0 \text{ GeV}$ if $ \eta  < 2.4$
Number of charged hadrons	$> 0$ if $ \eta  < 2.4$
Charged electromagnetic energy fraction	$< 0.99$ if $ \eta  < 2.4$
$\Delta R$ to nearest PF electron <sup>a</sup> , muon <sup>b</sup> , or one of the two primary EM objects	$> 0.5$

<sup>a</sup>A PF electron is defined as an electron reconstructed with the PF algorithm [127] with  $p_T > 15 \text{ GeV}$ ,  $|\eta| < 2.6$ , and  $(I_{\text{charged}} + I_{\text{photon}} + I_{\text{neutral}})/p_T < 0.2$ , where  $I_{\text{charged}}(I_{\text{photon}})(I_{\text{neutral}})$  is the sum of PF charged hadron(PF photon)(PF neutral hadron) momenta in a  $\Delta R = 0.4$  cone around the PF electron.

<sup>b</sup>Muons are reconstructed [128] from a combination of muon station and inner tracker hits. Here, a muon must have track  $\chi^2 < 10$ , at least one good muon station hit, inner track transverse impact parameter  $< 0.02 \text{ cm}$ , inner track longitudinal impact parameter  $< 0.5 \text{ cm}$ ,  $p_T > 15 \text{ GeV}$ ,  $|\eta| < 2.6$ , and  $(I_{\text{ECAL}} + I_{\text{HCAL}} + I_{\text{track}})/p_T < 0.2$ , where  $I_{\text{ECAL}}(I_{\text{HCAL}})(I_{\text{track}})$  is the sum of ECAL(HCAL)(track) momenta in a  $\Delta R = 0.3$  cone around the muon.

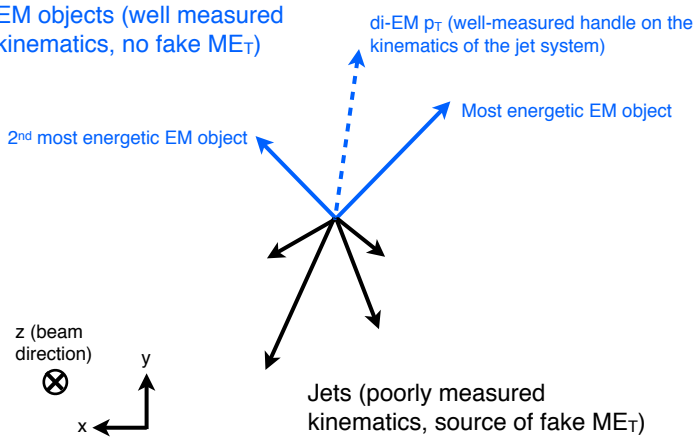
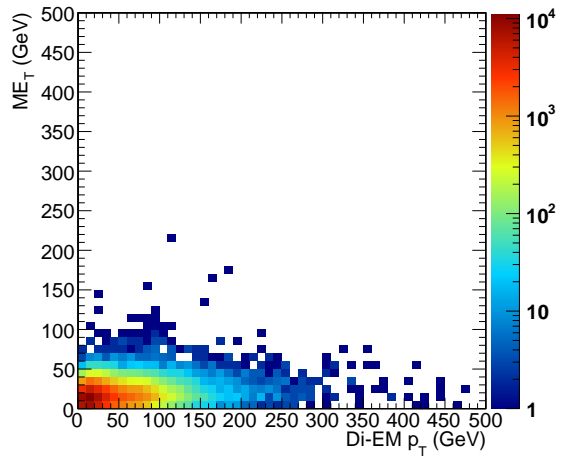
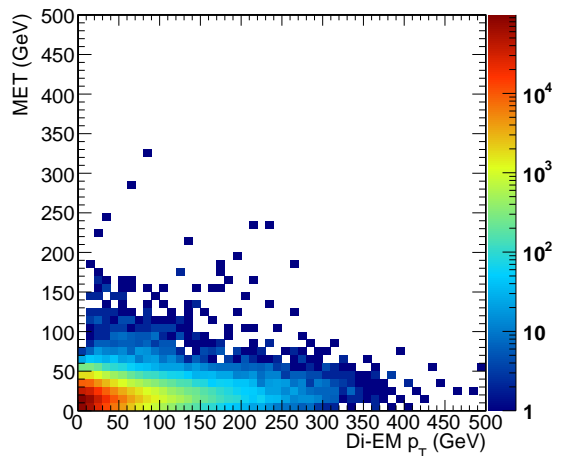
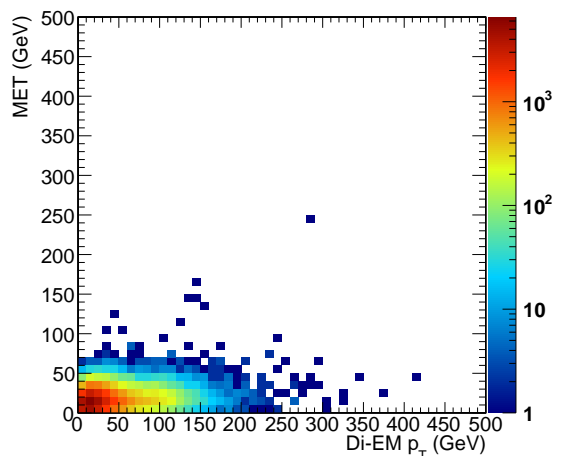


Figure 7.9: Cartoon showing the di-EM system in blue and the hadronic recoil in black. The di-EM  $p_T$  (dashed blue line) is used to reweight the control sample kinematic properties to match those of the candidate  $\gamma\gamma$  sample.

in Figure 7.9. As shown in Figure 7.10,  $\cancel{E}_T$  is largely uncorrelated with di-EM  $p_T$ , so there is little danger of reweighting away a true signal excess.

Whereas the di-EM  $p_T$  reweighting accounts for differences in production kinematics between the control and  $\gamma\gamma$  samples, a simultaneous reweighting based on the number of jets in the event accounts for differences in hadronic activity between the samples, especially between  $ee$  and  $\gamma\gamma$  (cf. Figs. 7.3- 7.8). Jets are defined as in Table 6.2. Figure 7.11 shows the effect of reweighting by number of jets per event, which is to increase(decrease) the tail of the  $ee$ ( $ff$ )  $\cancel{E}_T$  spectrum.

Although the electron and photon energies are well measured by the ECAL, the ECAL-only measurement of the fake photon energy (cf. Sec 6.1.1) is biased slightly low due to the fact that fakes (which are really jets) tend to deposit some energy in the HCAL. This can be seen in Figs. 7.12 and 7.13, which show the relative difference between the ECAL-only  $E_T$  measurement and the PF  $E_T$  measurement vs. EMF for electrons, photons, and fakes. PF  $E_T$  is defined as the L1Fast-corrected  $E_T$  of the nearest PF jet with  $p_T \geq 20$  GeV (i.e., the  $E_T$  of the PF jet object reconstructed from the same ECAL shower as the fake photon). On average, the high-EMF fakes, which

(a)  $\gamma\gamma$ .(b)  $ee$ .(c)  $ff$ .Figure 7.10:  $E_T$  vs. di-EM  $p_T$ .

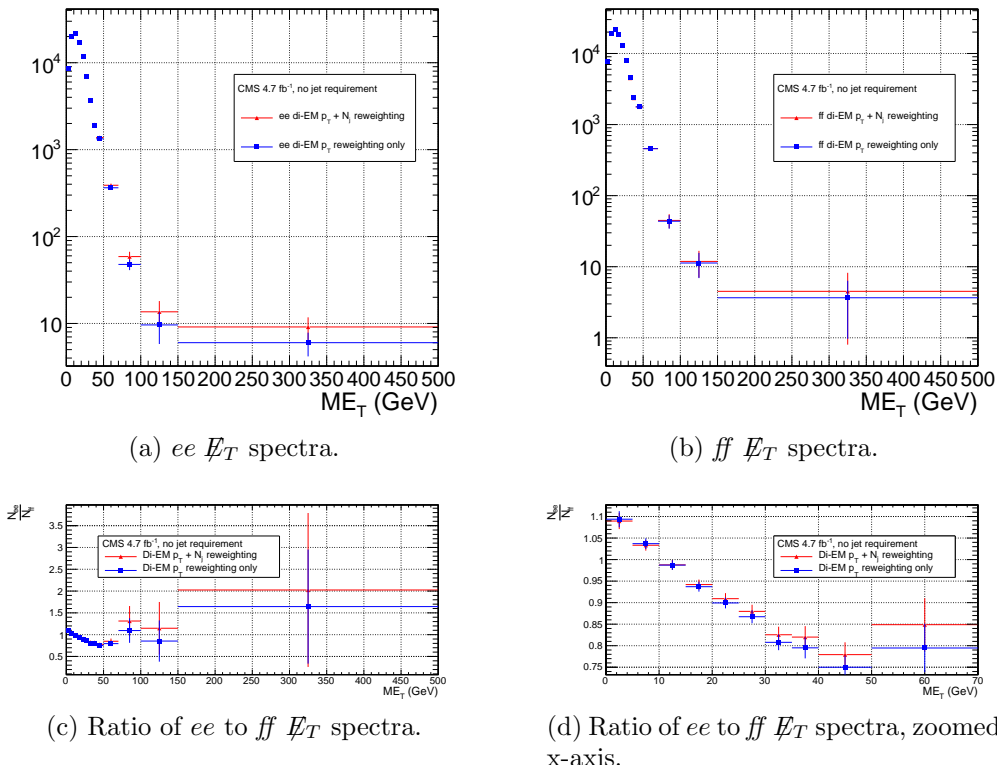


Figure 7.11:  $E_T$  spectra of the reweighted ee ( $81 \text{ GeV} \leq m_{\text{ee}} < 101 \text{ GeV}$ ) and ff control samples. Blue squares indicate di-EM  $p_T$  reweighting only; red triangles indicate di-EM  $p_T + \text{number of jets}$  reweighting. PF  $p_T$  (cf. p. 144) is used to calculate the di-EM  $p_T$ . The full normalization procedure is employed, along with ee sideband subtraction (discussed at the end of this section). Error bars are statistical only.

make up the bulk of the sample, tend to deposit a few percent more energy in the HCAL than the electrons or photons. This energy is recovered by the PF algorithm. For this reason, the PF  $p_T$  is used in the calculation of di-EM  $p_T$  rather than the ECAL-only  $p_T$ .<sup>1</sup> This leads to a modest improvement in the agreement between the  $ee$  and  $ff$   $\cancel{E}_T$  spectra, as shown in Figure 7.14.

The control sample event weights are defined as

$$w_{ij} = \frac{N_{\text{control}}}{N_{\gamma\gamma}} \frac{N_{\gamma\gamma}^{ij}}{N_{\text{control}}^{ij}} \quad (7.1)$$

where  $i$  runs over the number of di-EM  $p_T$  bins,  $j$  runs over the number of jet bins,  $N_{\text{control}}$  is the total number of events in the control sample,  $N_{\gamma\gamma}$  is the total number of events in the  $\gamma\gamma$  sample,  $N_{\gamma\gamma}^{ij}$  is the number of  $\gamma\gamma$  events in the  $i^{\text{th}}$  di-EM  $p_T$  bin and  $j^{\text{th}}$  jet bin, and  $N_{\text{control}}^{ij}$  is the number of control sample events in the  $i^{\text{th}}$  di-EM  $p_T$  bin and  $j^{\text{th}}$  jet bin. The effect of the reweighting is more significant for the  $ee$  sample than for the  $ff$  sample, as shown in Figure 7.15.

The  $ee$  sample contains a non-negligible background of  $t\bar{t}$  events in which both  $W$  bosons decay to electrons. These events have significant real  $\cancel{E}_T$  from the two neutrinos (unlike the  $\gamma\gamma$  events), and therefore inflate the background estimate at high  $\cancel{E}_T$ . In order to remove the  $t\bar{t}$  contribution from the  $ee$  sample, a sideband subtraction method is employed.

Only events in the  $ee$  sample with  $81 \text{ GeV} \leq m_{ee} < 101 \text{ GeV}$ , where  $m_{ee}$  is the di-electron invariant mass, are used in the QCD background estimate. This choice maximizes the ratio of  $Z$  signal to background. The sidebands used to estimate the background contribution within the  $Z$  window are defined such that  $71 \text{ GeV} \leq m_{ee} < 81 \text{ GeV}$  and  $101 \text{ GeV} \leq m_{ee} < 111 \text{ GeV}$ .

---

<sup>1</sup>In the few events ( $\mathcal{O}(10^{-3})$ ) in which two PF jet objects, corresponding to the two electrons or fakes, are not found, the ECAL-only  $p_T$  is used.

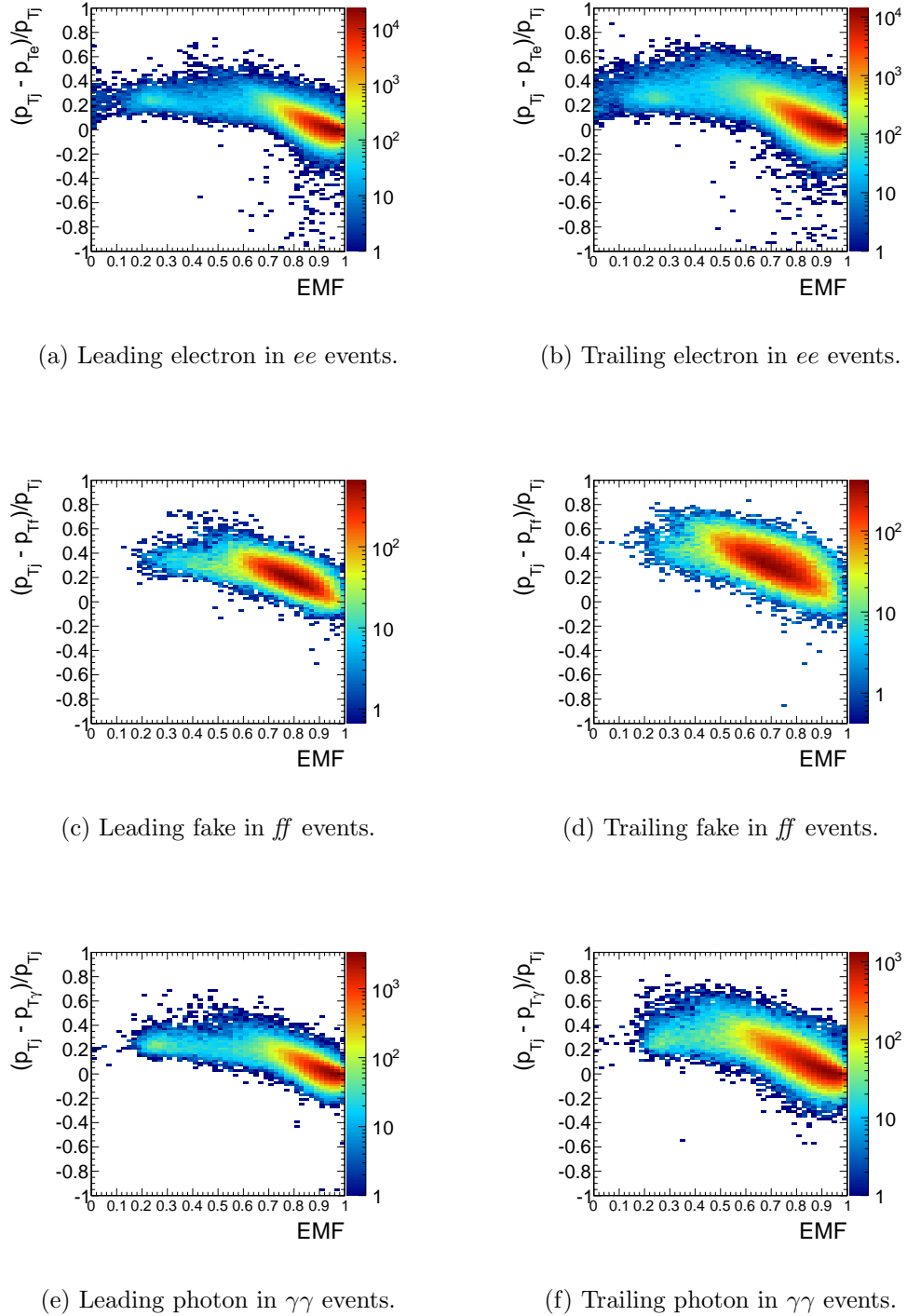


Figure 7.12: Relative difference between the ECAL-only  $E_T$  measurement and the PF  $E_T$  measurement vs. EMF. PF  $E_T$  is defined in the text.

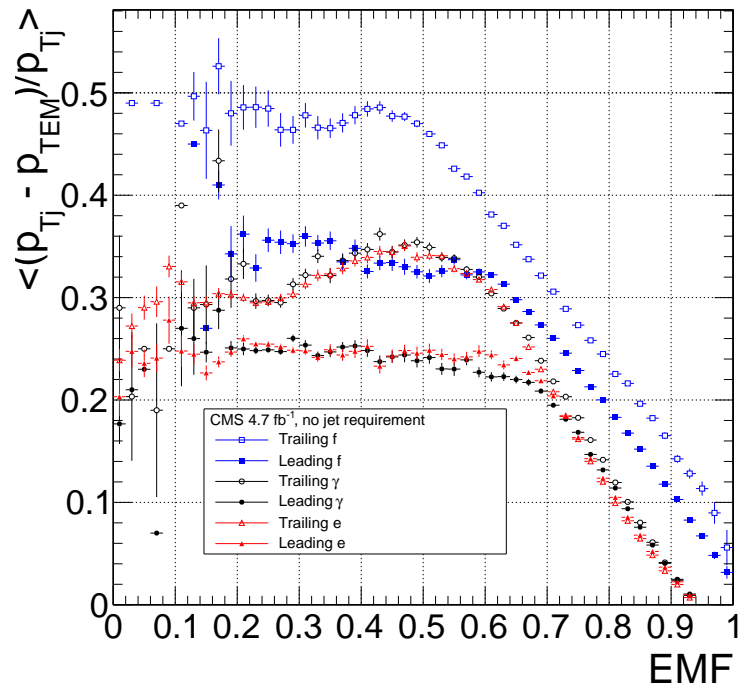


Figure 7.13: Average relative difference between the ECAL-only  $E_T$  measurement and the PF  $E_T$  measurement vs. EMF for the leading (filled marker) and trailing (open marker) electrons in  $ee$  events (red triangles), fakes in  $ff$  events (blue squares), and photons in  $\gamma\gamma$  events (black circles). These are nothing more than profile histograms of Fig. 7.12. PF  $E_T$  is defined in the text. Error bars are statistical only.

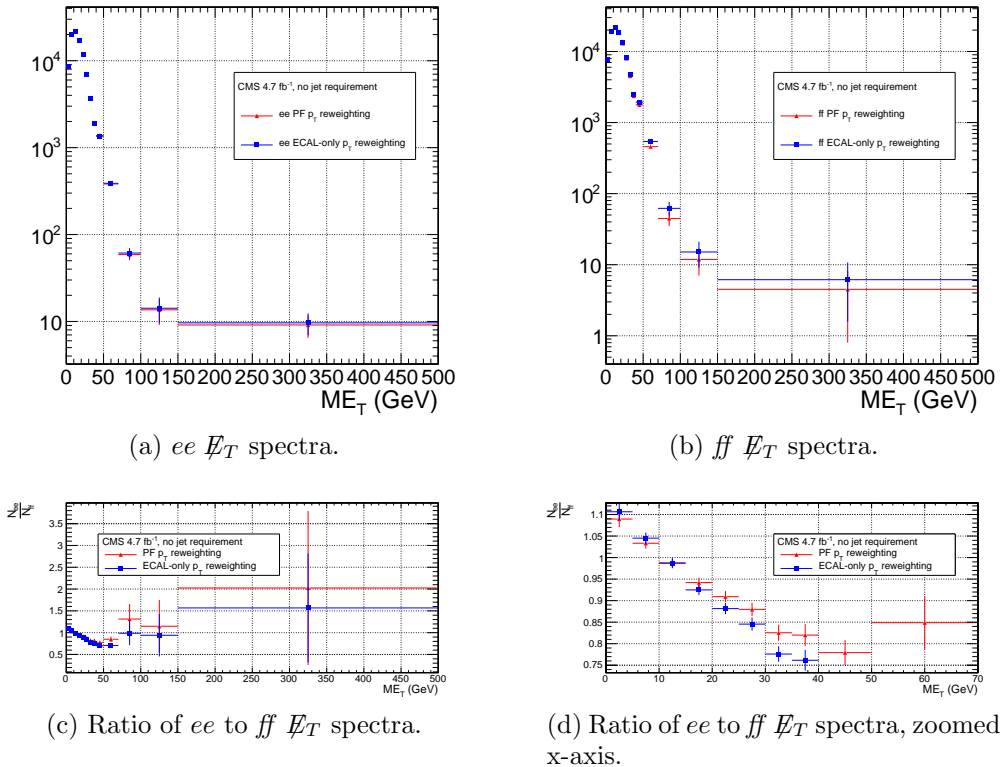


Figure 7.14:  $\cancel{E}_T$  spectra of the reweighted ee ( $81 \text{ GeV} \leq m_{\text{ee}} < 101 \text{ GeV}$ ) and ff control samples. Blue squares indicate reweighting using the ECAL-only  $p_T$  estimate; red triangles indicate reweighting using the PF  $p_T$  estimate. The full reweighting and normalization procedure is employed, along with ee sideband subtraction (discussed at the end of this section). Error bars are statistical only.

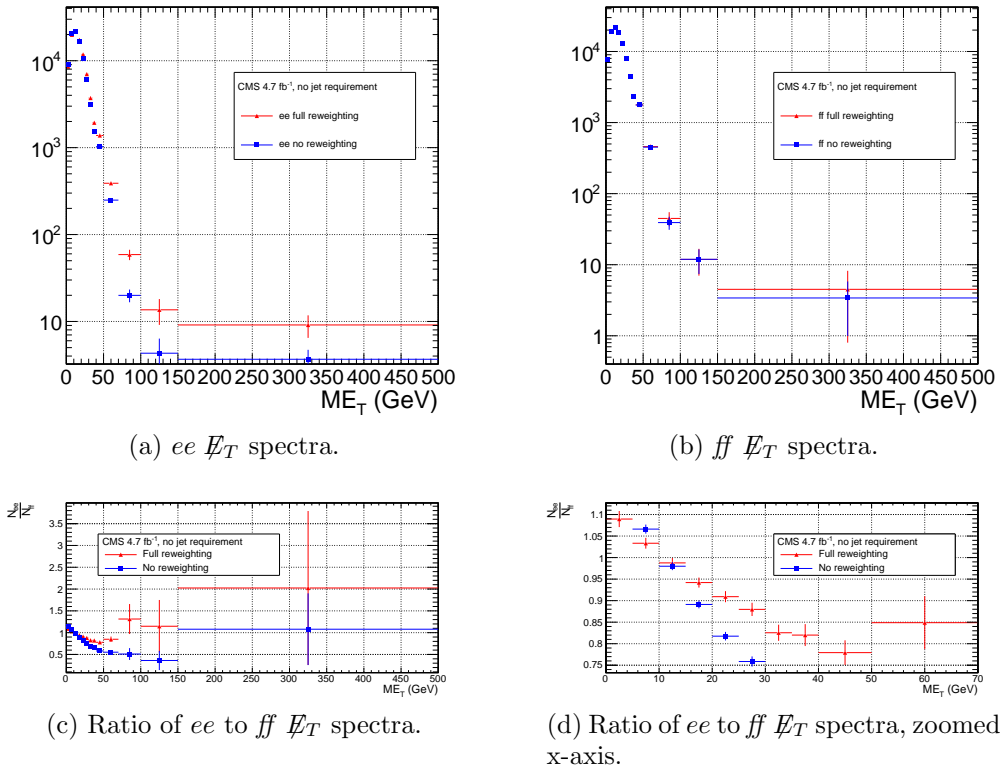


Figure 7.15:  $\cancel{E}_T$  spectra of the ee ( $81 \text{ GeV} \leq m_{ee} < 101 \text{ GeV}$ ) and ff control samples. Red triangles indicate full di-EM  $p_T +$  number of jets reweighting; blue squares indicate no reweighting. PF  $p_T$  (cf. p. 147) is used to calculate the di-EM  $p_T$ . The full normalization procedure is employed, along with ee sideband subtraction (discussed at the end of this section). Error bars are statistical only.

The full reweighting procedure is applied to the  $Z$  signal region and the two sideband regions independently. Only  $Z$  signal events are used in the calculation of the di-EM  $p_T$  weights for the  $Z$  signal region, and likewise only the events within a given sideband region are used in the calculation of the weights for that region. Assuming a constant  $t\bar{t}$  background shape, the resulting reweighted sideband  $\cancel{E}_T$  distributions are added together and subtracted from the reweighted  $Z$  signal  $\cancel{E}_T$  distribution. The sideband subtracted  $Z$  signal  $\cancel{E}_T$  distribution is then normalized as discussed in Secs. 7.2.1 and 7.2.3. The statistical and reweighting error from the sideband regions is propagated to the error on the final  $ee$  QCD  $\cancel{E}_T$  estimate.

The di-EM  $p_T$  weights for the two  $ee$  sideband regions are shown in Figure 7.16. The overall scale of the weights, as well as the trend with di-EM  $p_T$ , is similar for the two regions (except at high di-EM  $p_T$ , where the statistics are poor anyway). Figure 7.17 shows the  $\cancel{E}_T$  spectra for the two sideband regions and the  $Z$  signal region after subtraction. The shapes of the spectra indicate that the high- $\cancel{E}_T$  tail, present in the sideband distributions, was successfully subtracted from the  $Z$  signal distribution.

The  $ee$  ( $81 \text{ GeV} \leq m_{ee} < 101 \text{ GeV}$ ),  $ff$ , and  $\gamma\gamma$  di-EM  $p_T$  spectra for events with 0, 1, or  $\geq 2$  jets (as in Table 6.2) are shown in Figure 7.18. Broad humps in the  $ff$  and  $\gamma\gamma$  spectra are due to kinematic  $\Delta R$  and  $p_T$  turn-ons that are suppressed in the  $ee$  sample due to the invariant mass cut. Figure 7.19 shows the weights applied to the  $ee$  ( $81 \text{ GeV} \leq m_{ee} < 101 \text{ GeV}$ ) and  $ff$   $\cancel{E}_T$  spectra as a function of di-EM  $p_T$  and number of jets per event.

### 7.2.3 Normalization

After reweighting, the  $\cancel{E}_T$  distributions of the QCD control samples are normalized to the  $\cancel{E}_T < 20 \text{ GeV}$  region of the candidate  $\gamma\gamma$   $\cancel{E}_T$  spectrum, where signal contamination is low. The normalization factor is  $(N_{\gamma\gamma}^{\cancel{E}_T < 20 \text{ GeV}} - N_{e\gamma}^{\cancel{E}_T < 20 \text{ GeV}})/N_{\text{control}}^{\cancel{E}_T < 20 \text{ GeV}}$ ,

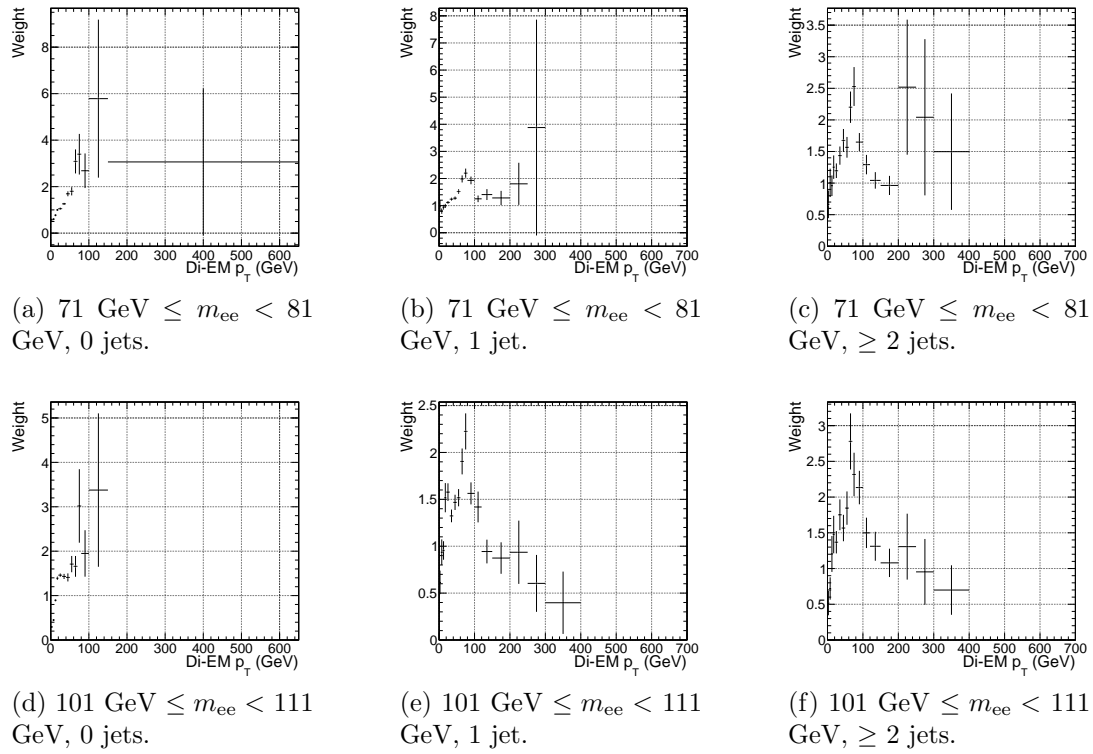


Figure 7.16:  $ee$  sideband di-EM  $p_T$  weights for events with 0, 1, or  $\geq 2$  jets (as in Table 6.2). Errors are statistical only.

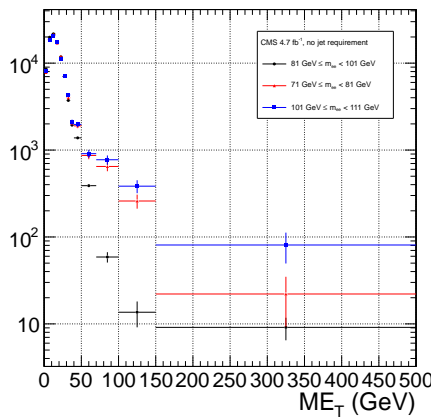
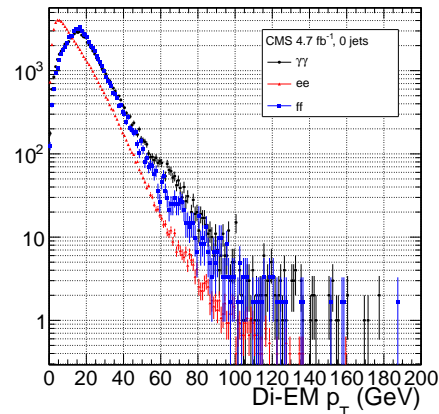
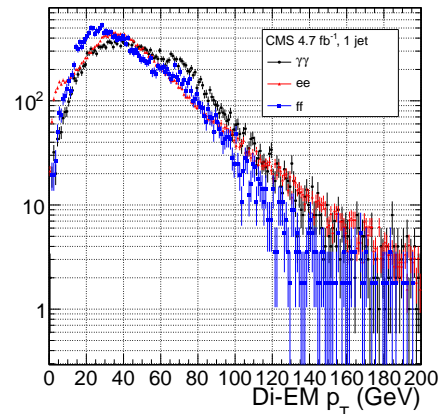


Figure 7.17:  $E_T$  spectra of the  $ee$  sample for  $71 \text{ GeV} \leq m_{ee} < 81 \text{ GeV}$  (red triangles),  $81 \text{ GeV} \leq m_{ee} < 101 \text{ GeV}$  (black circles), and  $101 \text{ GeV} \leq m_{ee} < 111 \text{ GeV}$  (blue squares). The two sideband distributions (red and blue) and the  $Z$  signal distribution (black) are normalized to the total number of  $\gamma\gamma$  events. Errors are statistical only.



(a) 0 jets.



(b) 1 jet.

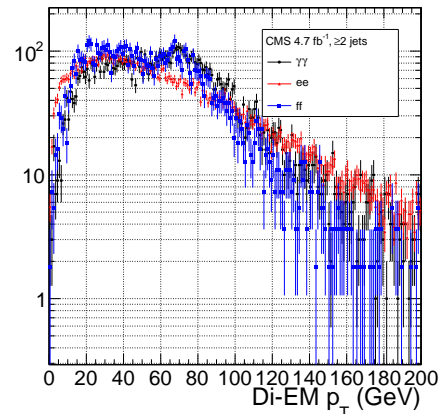
(c)  $\geq 2$  jets.

Figure 7.18:  $ee$  ( $81 \text{ GeV} \leq m_{ee} < 101 \text{ GeV}$ ) (red triangles),  $ff$  (blue squares), and  $\gamma\gamma$  (black circles) di-EM  $p_T$  spectra for events with 0, 1, or  $\geq 2$  jets (as in Table 6.2). Errors are statistical only.

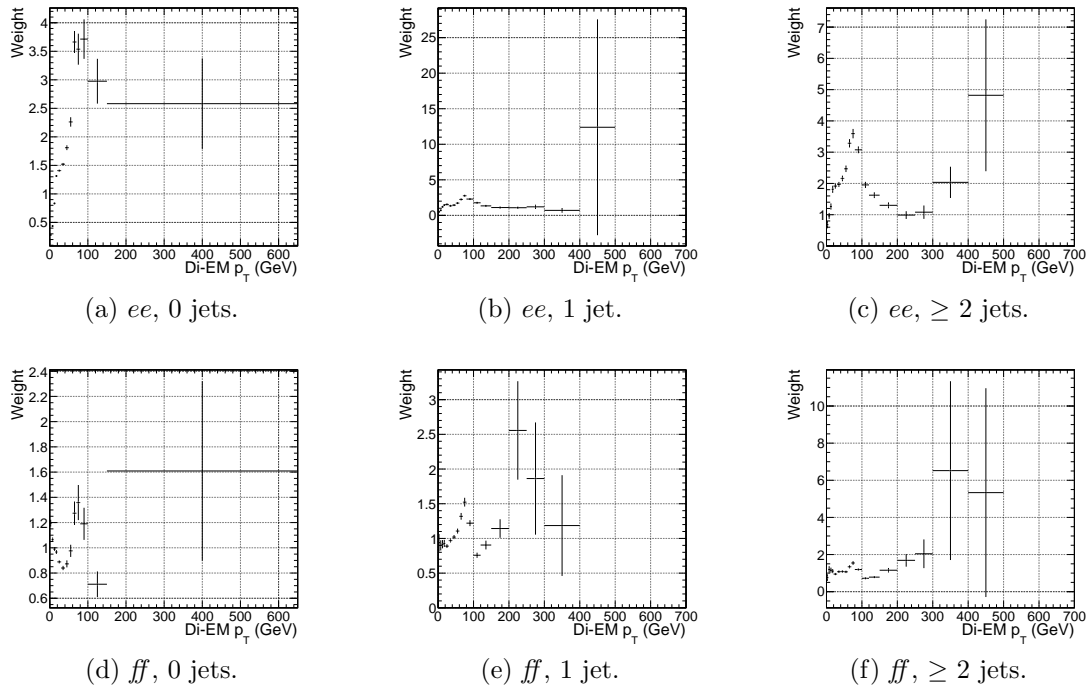


Figure 7.19:  $ee$  ( $81 \text{ GeV} \leq m_{ee} < 101 \text{ GeV}$ ) and  $ff$  di-EM  $p_T$  weights for events with 0, 1, or  $\geq 2$  jets (as in Table 6.2). Errors are statistical only.

where  $N_{e\gamma}^{E_T < 20 \text{ GeV}}$  is the expected number of electroweak background events with  $E_T < 20 \text{ GeV}$  (discussed in Section 7.3). The error on the QCD background prediction introduced by normalization is discussed in Sec. 7.4.

### 7.3 Modeling the Electroweak Background

$W\gamma$ ,  $W + \text{jet}$ , and  $t\bar{t}$  processes in which the  $W$  decay electron is misidentified as a photon (due to a failure to properly associate a pixel seed to the electron candidate) can contribute significantly to the high- $E_T$  tail of the  $\gamma\gamma E_T$  spectrum. To estimate this background, the  $e\gamma$  sample, which is enriched in  $W \rightarrow e\nu$  decays, is scaled by  $f_{e \rightarrow \gamma}/(1 - f_{e \rightarrow \gamma})$ , where  $f_{e \rightarrow \gamma}$  is the rate at which electrons are misidentified as photons. The derivation of this scaling factor comes from the two equations

$$N_{e\gamma}^W = f_{e \rightarrow e} N_W \quad (7.2)$$

$$N_{\gamma\gamma}^W = (1 - f_{e \rightarrow e}) N_W \quad (7.3)$$

where  $N_{e\gamma}^W$  is the number of  $W$  events in the  $e\gamma$  sample in which the electron was correctly identified,  $f_{e \rightarrow e}$  is the probability to correctly identify an electron,  $N_W$  is the true number of triggered  $W \rightarrow e\nu$  events, and  $N_{\gamma\gamma}^W$  is the number of  $W$  events in the  $\gamma\gamma$  sample in which the electron was misidentified as a photon. The contribution from  $Z \rightarrow ee$  can be neglected (i.e.  $f_{e \rightarrow \gamma}$  is small and the  $Z$  contribution involves  $f_{e \rightarrow \gamma}^2$ , since both electrons have to be misidentified). Since  $f_{e \rightarrow e} = 1 - f_{e \rightarrow \gamma}$ , solving for  $N_{\gamma\gamma}^W$  gives

$$N_{\gamma\gamma}^W = \frac{f_{e \rightarrow \gamma}}{1 - f_{e \rightarrow \gamma}} N_{e\gamma}^W \quad (7.4)$$

$f_{e \rightarrow \gamma}$  is measured by fitting the  $Z$  peaks in the  $ee$  and  $e\gamma$  samples. The number of  $Z$  events fitted in the  $ee$  and  $e\gamma$  samples, respectively, is given by

$$N_{ee}^Z = (1 - f_{e \rightarrow \gamma})^2 N_Z \quad (7.5)$$

$$N_{e\gamma}^Z = 2f_{e \rightarrow \gamma}(1 - f_{e \rightarrow \gamma}) N_Z \quad (7.6)$$

where  $N_Z$  is the true number of triggered  $Z \rightarrow ee$  events. Solving for  $f_{e \rightarrow \gamma}$  gives

$$f_{e \rightarrow \gamma} = \frac{N_{e\gamma}^Z}{2N_{ee}^Z + N_{e\gamma}^Z} \quad (7.7)$$

A Crystal Ball function is used to model the  $Z$  signal shape in both the  $ee$  and  $e\gamma$  samples, while an exponential convoluted with an error function (`RooCMSShape`, see Sec. 6.4.1) is used to model the background shape. The fixed fit parameters are identical for the two samples, but the other parameters are allowed to float independently. Table 7.3 shows the values and ranges of the fixed and floating fit parameters, respectively.

Table 7.3: Parameter values for the signal and background PDFs for the  $ee$  and  $e\gamma$  samples. When a bracketed range is given, the parameter is allowed to float within that range. When a constant is given, the parameter is fixed to that constant.

PDF	Crystal Ball fit parameters				<code>RooCMSShape</code> fit parameters			
	$\mu$	$\sigma$	$\alpha$	n	$\mu$	$\alpha$	$\beta$	$\gamma$
$ee$ signal	[86.2, 96.2]	[1.0, 5.0]	1.063	143.16	N/A	N/A	N/A	N/A
$e\gamma$ signal	[86.2, 96.2]	[1.0, 5.0]	1.063	143.16	N/A	N/A	N/A	N/A
$ee$ background	N/A	N/A	N/A	N/A	58	97.0	0.0922	0.191
$e\gamma$ background	N/A	N/A	N/A	N/A	56	72.02	0.098	0.0375

Fits to the  $ee$  and  $e\gamma$  invariant mass spectra are shown in Figure 7.20. Figure 7.21(a) indicates that there is some dependence of  $f_{e \rightarrow \gamma}$  on the electron  $p_T$ , but since the the bulk of the electrons have  $p_T \sim 45$  GeV, applying a  $p_T$ -dependent misidentification rate has a negligible effect on the final background estimate. (Note that all fit parameters are floating in the  $p_T$ -dependent fits.) The dependence on  $\eta$  is small, as shown in Figure 7.21(b). Therefore, a constant misidentification rate (derived from all  $ee$  and  $e\gamma$  events), rather than a  $p_T$ - and  $\eta$ -dependent misidentification rate, is used in the final electroweak background estimate, with the difference between the constant rate and the rate for electrons with  $p_T$  between 25 and 40 GeV (the range in which the bulk of the trailing photons in the  $\gamma\gamma$  sample lie) taken as a systematic error.

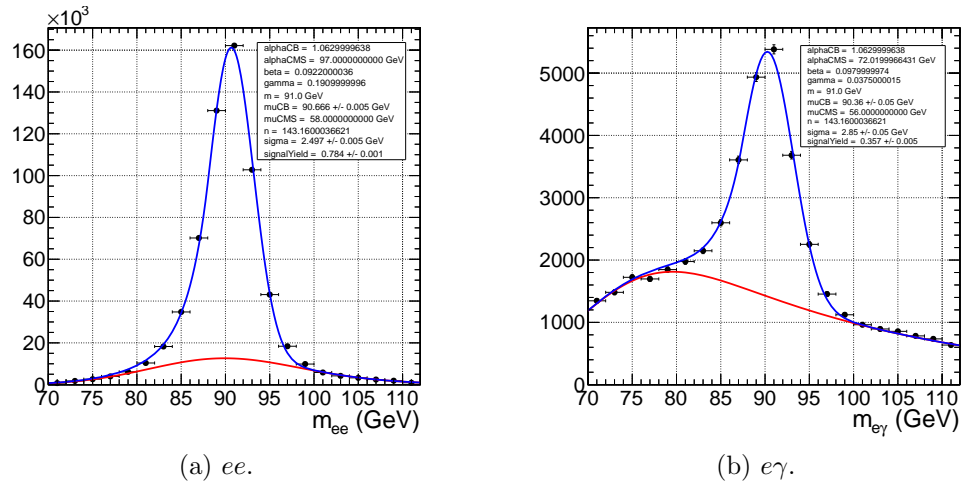
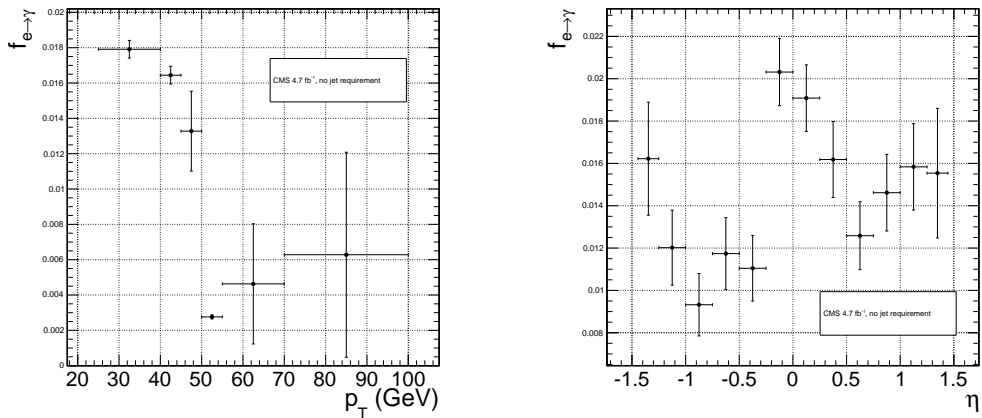


Figure 7.20: Fits to the  $ee$  and  $e\gamma$  invariant mass spectra using the Crystal Ball RooCMSShape function described in the text and in Table 7.3. The total fit is shown in blue, while the background component is shown in red.



(a)  $f_{e \rightarrow \gamma}$  vs. electron  $p_T$ . For the lowest  $p_T$  bin, the fit to the  $e\gamma$  spectrum does not converge well, so the  $Z$  signal fraction is fixed to the value in Fig. 7.20(b).

(b)  $f_{e \rightarrow \gamma}$  vs. electron  $\eta$ .

Figure 7.21:  $f_{e \rightarrow \gamma}$  vs. electron  $p_T$  and  $\eta$ .

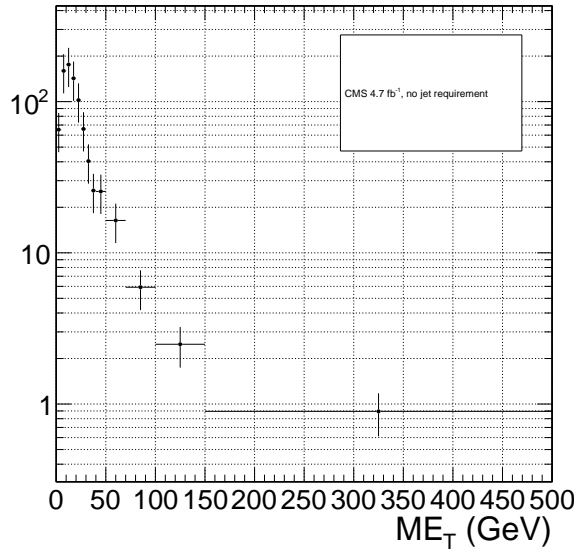


Figure 7.22:  $\cancel{E}_T$  spectrum of the  $e\gamma$  sample after scaling by  $f_{e \rightarrow \gamma}$ . The total error on  $f_{e \rightarrow \gamma}$  is propagated to the total error on the electroweak background estimate.

Using the integrals of the  $Z$  fits shown in Fig. 7.20, Eq. 7.7, and the  $p_T$  systematic discussed above,  $f_{e \rightarrow \gamma}$  is calculated to be  $0.014 \pm 0.000(\text{stat.}) \pm 0.004(\text{syst.})$ . The scaled  $e\gamma$  MET distribution is shown in Figure 7.22.

In the  $36 \text{ pb}^{-1}$  version of this analysis [141], it was shown that the  $ee$  sample could accurately predict the QCD and real  $Z$  contribution to the  $e\gamma$  sample at low  $\cancel{E}_T$ , and that the expectation from  $W \rightarrow e\nu$  MC accounted for the remaining  $W$  contribution at high  $\cancel{E}_T$ . A plot of the  $\cancel{E}_T$  distributions of the 2010  $e\gamma$  sample and the predicted components is shown in Figure 7.23. This exercise helps to validate both the QCD and electroweak background prediction methods.

## 7.4 Errors on the Background Prediction

The statistical error on the final background estimate in a particular  $\cancel{E}_T$  bin comes from three sources: the number of control sample events collected in that bin, the statistical error on the weights applied to events in that bin, and the statistics of the normalization region. In the case of the  $ee$  control sample, there are contributions

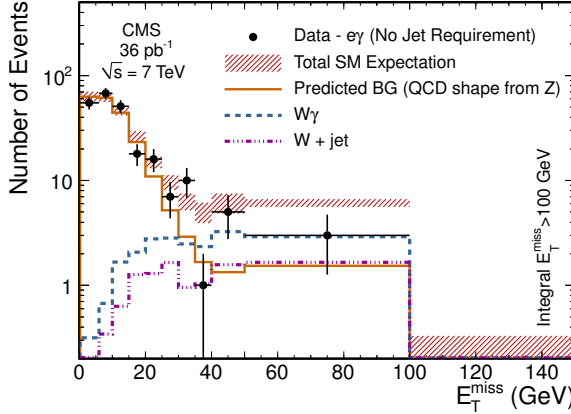


Figure 7.23:  $\cancel{E}_T$  spectrum of the  $e\gamma$  sample in  $35 \text{ pb}^{-1}$  of 2010 LHC data scaled by the 2010 measured  $f_{e \rightarrow \gamma}$  (black dots), QCD and real  $Z$  predicted background from the 2010  $ee$  sample (solid orange line), MC  $W + \text{jet}$  estimate (dash-dotted purple line), and MC  $W\gamma$  estimate (dashed blue line). The total  $e\gamma$  prediction (red band) is the sum of the  $ee$ ,  $W + \text{jet}$ , and  $W\gamma$  predictions. Reprinted from Fig. 2 of ref. [141].

from the statistics of the  $m_{ee}$  sidebands as well.

In order to propagate the statistical error due to the reweighting procedure to the shape of the final QCD  $\cancel{E}_T$  distribution, 1000 toy sets of weights are generated. Each set includes a weight for each (di-EM  $p_T$ ,  $N_j$ ) bin, with the values picked from a Gaussian distribution with mean and standard deviation equal to the observed weight for that bin and its statistical error. The effect of reweighting error is not correlated between  $\cancel{E}_T$  bins. For each of the 1000 experiments, the control sample data are reweighted according to the generated weights, and the background estimates are calculated for each  $\cancel{E}_T$  bin. Since the distribution of the toy background estimates follows a Gaussian distribution in each  $\cancel{E}_T$  bin, the RMS spread of the estimates is taken as the statistical error due to reweighting. This procedure is carried out for the  $ff$ ,  $ee$ , low sideband  $ee$ , and high sideband  $ee$  samples.

The total statistical error on the background estimate per  $\cancel{E}_T$  bin is given by

$$\sigma_{\text{stat}}^2 = \sigma_{\text{stat,QCD}}^2 + \sigma_{\text{stat,EW}}^2 \quad (7.8)$$

where  $\sigma_{\text{stat,QCD}}^2$  is the square of the total statistical error on the QCD prediction in the  $\cancel{E}_T$  bin

$$\sigma_{\text{stat,QCD}}^2 = \sigma_{\text{stat},s}^2 + \sigma_{\text{Poisson,QCD}}^2 + \sigma_{\text{reweight},s}^2 + \sigma_{\text{reweight,QCD}}^2 \quad (7.9)$$

and  $\sigma_{\text{stat,EW}}$  is the Poisson error on the number of  $e\gamma$  events in the  $\cancel{E}_T$  bin ( $= \sqrt{N_{e\gamma}}$ , where  $N_{e\gamma}$  is the prediction in the  $\cancel{E}_T$  bin after scaling by  $f_{e\rightarrow\gamma}$ ). The contributions to  $\sigma_{\text{stat,QCD}}^2$  are discussed below.

- $\sigma_{\text{stat},s}^2$  is the statistical error contributed by the normalization factor  $s$  (i.e. from Poisson error in the normalization region  $\cancel{E}_T < 20$  GeV):

$$\begin{aligned} \sigma_{\text{stat},s}^2 = & \frac{N_{\text{control}}^2}{(N_{\gamma\gamma}^{\text{norm}} - N_{e\gamma}^{\text{norm}})^2} ([\sigma_{\text{Poisson},\gamma\gamma}^{\text{norm}}]^2 + [\sigma_{\text{Poisson},e\gamma}^{\text{norm}}]^2) + \\ & \frac{N_{\text{control}}^2}{(N_{\text{control}}^{\text{norm}})^2} (\sigma_{\text{Poisson,control}}^{\text{norm}})^2 \end{aligned} \quad (7.10)$$

where  $N_{\text{control}}$  is the number of reweighted, normalized events in the  $\cancel{E}_T$  bin,  $N_{\gamma\gamma}^{\text{norm}}$  is the number of  $\gamma\gamma$  events in the normalization region,  $N_{e\gamma}^{\text{norm}}$  is the number of  $e\gamma$  events in the normalization region (after scaling by  $f_{e\rightarrow\gamma}$ ),  $\sigma_{\text{Poisson},\gamma\gamma}^{\text{norm}}$  is the Poisson error on the number of  $\gamma\gamma$  events in the normalization region ( $= \sqrt{N_{\gamma\gamma}^{\text{norm}}}$ ),  $\sigma_{\text{Poisson},e\gamma}^{\text{norm}}$  is the Poisson error on the number of  $e\gamma$  events in the normalization region ( $= \sqrt{N_{e\gamma}^{\text{norm}}}$ ),  $N_{\text{control}}^{\text{norm}}$  is the number of QCD control ( $ee$  or  $ff$ ) events in the normalization region, and  $\sigma_{\text{Poisson,control}}^{\text{norm}}$  is the Poisson error on the number of QCD control ( $ee$  or  $ff$ ) events in the normalization region ( $= \sqrt{\sum_{i=1}^{N_{\text{control}}^{\text{norm}}} w_i^2}$ , where  $w_i$  is the di-EM  $p_T$  weight applied to event  $i$ ). For the  $ee$  control region,  $N_{\text{control}}$  and  $N_{\text{control},\text{norm}}$  are sideband subtracted, and  $\sigma_{\text{Poisson,control}}^{\text{norm}}$  includes the Poisson error on the number of sideband events.

- $\sigma_{\text{Poisson,QCD}}$  is the Poisson error due to the number of QCD control ( $ee$  or  $ff$ ) events in the  $\cancel{E}_T$  bin, equal to  $\sqrt{\sum_{i=1}^{N_{\text{control}}} w_i^2}$ , where  $w_i$  is the di-EM  $p_T$  weight applied to event  $i$ . For the  $ee$  control region,  $\sigma_{\text{Poisson,QCD}}$  includes the Poisson error on the number of subtracted sideband events.
- $\sigma_{\text{reweight},s}$  is the error contributed by the control sample reweighting in the normalization region ( $= \frac{N_{\text{control}}^2}{(N_{\text{control}}^{\text{norm}})^2} \sigma_{\text{reweight,control}}^{\text{norm}}$ ).  $\sigma_{\text{reweight,control}}^{\text{norm}}$  is the quadrature sum of the RMS of the 1000 toy reweighting experiments for each  $\cancel{E}_T$  bin in the normalization region. For the  $ee$  control sample, it also includes (in quadrature) the RMS of the toys in the sideband samples.
- $\sigma_{\text{reweight,QCD}}$  is the error contributed by the control sample reweighting in the  $\cancel{E}_T$  bin ( $= s\sigma_{\text{reweight,control}}$ ).  $\sigma_{\text{reweight,control}}$  is the RMS of the 1000 toy reweighting experiments for the  $E_T$  bin. For the  $ee$  control sample, it also includes (in quadrature) the RMS of the toys in the sideband samples.

The difference in hadronic activity between the  $ee$ ,  $ff$ , and  $\gamma\gamma$  samples results in a small bias ( $\sim 1$  GeV) of the  $ee$   $\cancel{E}_T$  distribution towards lower values with respect to the  $ff$  and  $\gamma\gamma$  samples, as shown in Figure 7.24. Therefore, the  $ff$  sample is used as the primary QCD background estimator, and the difference between the  $ee$  and  $ff$  predictions is assigned as an error on the knowledge of the hadronic activity. For  $\cancel{E}_T > 100$  GeV, this error amounts to 43% of the total QCD + electroweak background estimate, and is the dominant source of systematic error.

The second largest source of systematic error comes from the  $p_T$  dependence of the  $e \rightarrow \gamma$  misidentification rate (see 7.3). For  $\cancel{E}_T > 100$  GeV, the expected electroweak background is  $3.4 \pm 1.0$  events, so this error amounts to 4.8% of the total QCD + electroweak background estimate.

The assumption of a constant  $t\bar{t}$  and  $W + \text{jets}$  background shape under the  $Z$  peak in the  $ee$  sample induces a systematic error on the  $ee$  sideband-subtracted back-

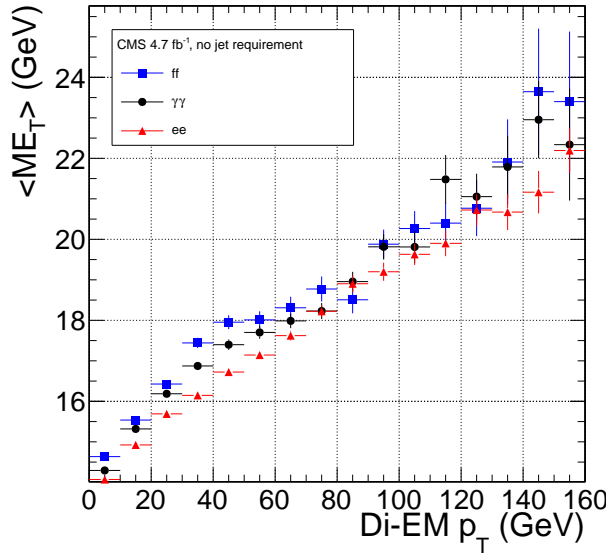


Figure 7.24: Average  $\cancel{E}_T$  vs. di-EM  $p_T$  for the  $ff$  (blue squares),  $ee$  (red triangles), and  $\gamma\gamma$  (black circles) samples.

ground prediction. To assess the magnitude of this error, the sideband subtraction (see Sec. 7.2.2) is performed once using only the prediction from the high sideband, and once using only the prediction from the low sideband. In each of these cases, the prediction is weighted by a factor of two, to account for the fact that the sideband regions are only half as wide (10 GeV) as the signal region (20 GeV). The maximum variation from the nominal  $ee$  estimate is taken as the error, which amounts to 11% for  $\cancel{E}_T > 100$  GeV.  $\cancel{E}_T$  distributions using the nominal  $ee$  sideband subtraction, the low-sideband-only subtraction, and the high-sideband-only subtraction are shown in Figure 7.25.

Finally, the few percent error on the jet energy correction factors introduces an error on the final background estimate through (a) the use of the PF  $p_T$  to measure the di-EM  $p_T$ , (b) the counting of jets passing a 30 GeV  $p_T$  threshold for placement of the event in an  $N_j$  bin for reweighting, and (c) the counting of jets above threshold for the  $\geq 1$ -jet version of the selection. To estimate this error, 100 pseudo-experiments are generated with identical properties as the true data sample, except with corrected jet energies (in all events) all shifted by an amount  $r\sigma(p_T, \eta)$ .  $r$  is a random number

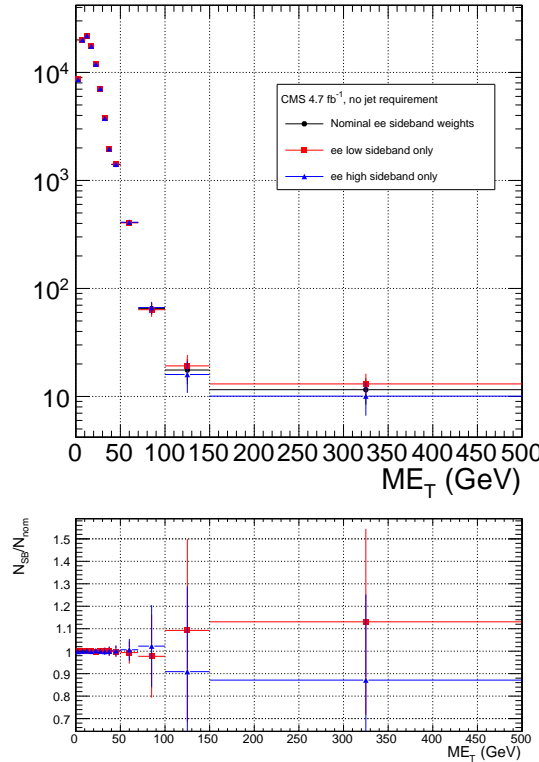


Figure 7.25:  $ee$   $\cancel{E}_T$  distributions using the nominal sideband subtraction (black circles), low sideband only (red squares), and high sideband only (blue triangles). The bottom plot shows the ratio of the low sideband distribution to the nominal (red squares) and the ratio of the high sideband distribution to the nominal (blue triangles).

drawn from a Gaussian distribution with mean 0 and width 1, and  $\sigma(p_T, \eta)$  is the uncertainty on the jet energy correction factor (which, like the correction factor itself, is a function of  $p_T$  and  $\eta$ ). The same factor  $r$  is applied to all jets in all events in the pseudo-experiment because the jet energy correction errors are correlated from jet to jet (they result from e.g. uncertainties in MC simulation or uncertainties in ECAL energy scale [120]). The standard error of the mean of the 100 resulting background estimates in each relevant  $\cancel{E}_T$  bin is taken as the error. The error in each  $\cancel{E}_T$  bin is assumed to be uncorrelated. This process is repeated for both the inclusive and  $\geq 1$ -jet selections. For  $\cancel{E}_T \geq 100$  GeV, the jet energy correction uncertainty is 1.5% (2.2%) of the total background for the inclusive ( $\geq 1$ -jet) selection.

The uncertainty in how to define the (di-EM  $p_T$ ,  $N_j$ ) bins, especially at high di-

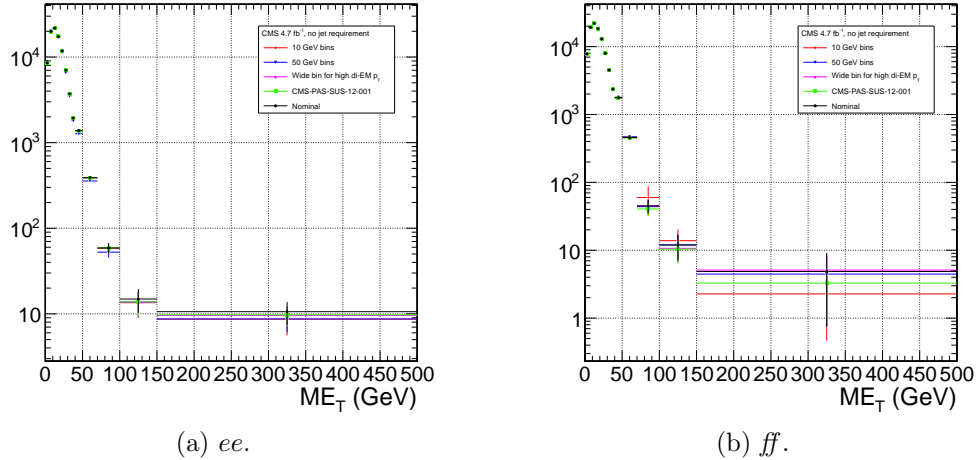


Figure 7.26: Comparison of  $\cancel{E}_T$  distributions for five different di-EM  $p_T$  bin definitions: uniform bins of width 10 GeV (red diamonds); uniform bins of width 50 GeV (blue downward-pointing triangles); bins with lower edges  $\{0.0, 5.0, 10.0, 15.0, 20.0, 30.0, 40.0, 50.0, 60.0, 70.0, 80.0, 100.0, 750.0\}$  GeV for 0-jet events and  $\{0.0, 5.0, 10.0, 15.0, 20.0, 30.0, 40.0, 50.0, 60.0, 70.0, 80.0, 100.0, 150.0\}$  GeV for  $\geq 1$ -jet events (magenta upward-pointing triangles), i.e. a single wide bin at high di-EM  $p_T$ ; bins with lower edges  $\{0.0, 5.0, 10.0, 15.0, 20.0, 30.0, 40.0, 50.0, 60.0, 70.0, 80.0, 100.0, 150.0\}$  GeV for 0-jet events and  $\{0.0, 5.0, 10.0, 15.0, 20.0, 30.0, 40.0, 50.0, 60.0, 70.0, 80.0, 100.0, 120.0, 150.0, 200.0, 700.0\}$  GeV for  $\geq 1$ -jet events (green squares), i.e. the bins used in ref. [59]; and the nominal bin definitions shown in Fig. 7.19 (black circles).

EM  $p_T$  where the statistics are low, is covered by the 1000-toys procedure as long as the bins are not too coarse. This is shown in Figure 7.26. If the bins are too coarse, the details of the shape of the di-EM  $p_T$  spectra are lost, and the reweighting has a smaller effect.

The use of uncorrected instead of corrected PF  $\cancel{E}_T$  (see Sec. 6.1.3) makes no difference in the agreement of the background predictions and the search sample in a control region at low  $\cancel{E}_T$ , as shown in Figure 7.27. Since the control samples are derived from the same data as the search sample, any biases in the  $\cancel{E}_T$  reconstruction due to jet energy scale are present equally in both samples.

Tables 7.4 and 7.5 list all the errors on the  $ee$  and  $ff$  QCD background predictions, respectively, for the  $\cancel{E}_T$  bins used in the search. Table 7.6 lists the errors on the

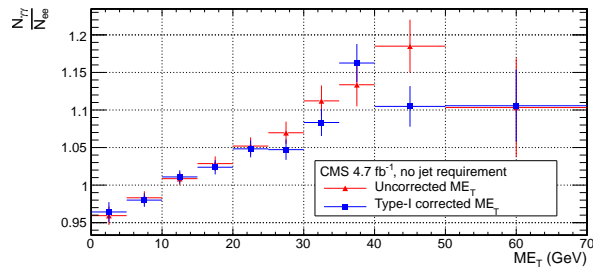
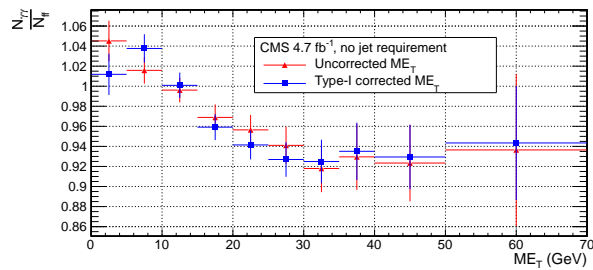
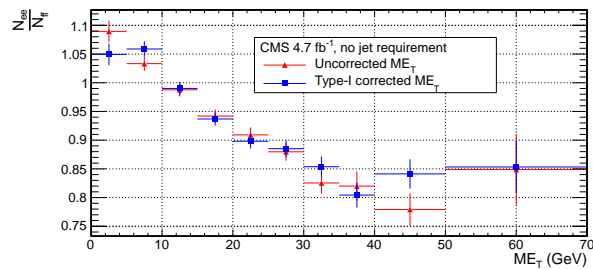
(a) Ratio of  $\gamma\gamma$  to  $ee$   $\cancel{E}_T$  distributions.(b) Ratio of  $\gamma\gamma$  to  $ff$   $\cancel{E}_T$  distributions.(c) Ratio of  $ee$  to  $ff$   $\cancel{E}_T$  distributions.

Figure 7.27: Agreement between  $\gamma\gamma$ ,  $ee$ , and  $ff$  samples for uncorrected (red triangles) and corrected (blue squares)  $\cancel{E}_T$ .

electroweak background prediction. Finally, Table 7.7 shows the errors on the total QCD + electroweak background prediction, broken down by origin (statistical or systematic) and QCD background estimation sample ( $ee$  or  $ff$ ). In the final result, only the  $ff$  QCD estimate is used.

Table 7.4: Errors on the  $ee$  QCD background prediction as a fraction of the  $ee$  prediction.

Source of error	Fractional uncertainty (%)				
	[50, 60)	[60, 70)	[70, 80)	[80, 100)	$\geq 100$
Total	3.9	8.1	16	25	25
Statistics	3.6	7.8	16	24	22
No. events	3.6	7.7	15	24	20
In norm. region	0.43	0.44	0.46	0.55	0.51
In this $E_T$ bin	3.5	7.7	15	24	20
Reweighting	0.73	1.2	3.5	4.3	7.7
In norm. region	0.19	0.19	0.2	0.24	0.23
In this $E_T$ bin	0.71	1.2	3.5	4.3	7.7
Systematics	2.6	4.4	1.2	7.5	14
$f_{e \rightarrow \gamma}$ (in norm. region)	0.0012	0.0012	0.0013	0.0015	0.0014
$m_{ee}$ background shape	1.4	2	0.72	5.5	12
Jet energy scale	2.2	3.9	0.96	5.1	6.9

## 7.5 Results

Figure 7.28( 7.29) shows the  $E_T$  distribution of the inclusive( $\geq 1$ -jet)  $\gamma\gamma$  search sample along with the predicted  $E_T$  distributions of the QCD and electroweak backgrounds. The observed number of two-photon events,  $ee$  and  $ff$  background estimates and their errors, and expected number of inclusive( $\geq 1$ -jet) two-photon events from two representative GGM SUSY models are listed in Table 7.8( 7.9). (Details of the SUSY MC production are given in Chapter 8.) The  $ee$  estimate is shown for comparison; the  $ff$  estimate is the official result used in the interpretation. No deviation from the Standard Model prediction is observed in the  $\gamma\gamma$  search sample.

Table 7.5: Errors on the  $ff$  QCD background prediction as a fraction of the  $ff$  prediction.

Source of error	Fractional uncertainty (%)				
	[50, 60)	[60, 70)	[70, 80)	[80, 100)	$\geq 100$
Total	15	25	61	34	64
Statistics	7.2	14	30	33	38
No. events	7.1	14	29	33	36
In norm. region	0.64	0.64	0.64	0.64	0.64
In this $E_T$ bin	7.1	14	29	33	36
Reweighting	0.85	2.7	5.1	6.9	13
In norm. region	0.27	0.27	0.27	0.27	0.27
In this $E_T$ bin	0.81	2.6	5.1	6.9	13
Systematics	13	21	53	6.6	52
$ee/ff$ difference	13	21	53	5.5	52
$f_{e \rightarrow \gamma}$ (in norm. region)	0.0012	0.0012	0.0012	0.0012	0.0012
Jet energy scale	0.099	1.7	1.8	3.5	1.8

Table 7.6: Errors on the  $e\gamma$  electroweak background prediction as a fraction of the  $e\gamma$  prediction.

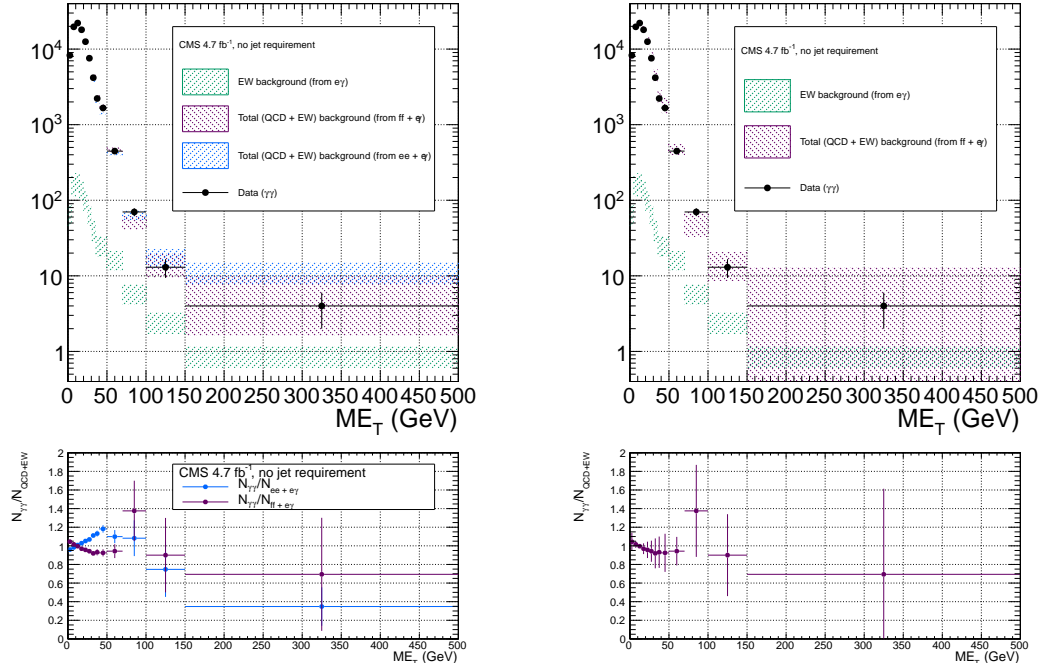
Source of error	Fractional uncertainty (%)				
	[50, 60)	[60, 70)	[70, 80)	[80, 100)	$\geq 100$
Total	29	29	30	30	30
Statistics	3.6	5.2	6.7	7.2	6.5
Systematics ( $f_{e \rightarrow \gamma}$ )	29	29	29	29	29

Table 7.7: Errors on the total QCD + electroweak background prediction as a fraction of the total prediction.

Source of error	Fractional uncertainty (%)				
	[50, 60)	[60, 70)	[70, 80)	[80, 100)	$\geq 100$
Total ( $ee + e\gamma$ )	3.9	7.8	15	22	22
Statistics	3.4	7.3	14	21	18
QCD	3.4	7.3	14	21	18
Electroweak	0.13	0.3	0.53	0.79	0.76
Systematics	2.7	4.5	2.6	7.4	13
QCD	2.5	4.1	1.1	6.7	12
Electroweak	1	1.7	2.3	3.2	3.4
Total ( $ff + e\gamma$ )	14	24	54	30	54
Statistics	6.9	13	26	29	30
QCD	6.9	13	26	29	30
Electroweak	0.11	0.24	0.79	0.83	1.1
Systematics	12	20	47	6.7	43
QCD	12	20	47	5.8	43
Electroweak	0.9	1.3	3.4	3.4	4.8

Table 7.8: Observed numbers of two-photon events,  $ee$  and  $ff$  background estimates and their errors, and expected numbers of two-photon events from two representative GGM SUSY models (details of MC simulation given in Chapter 8) for the  $E_T$  bins used in the search. The  $ee$  estimate is shown for comparison; the  $ff$  estimate is the official result used in the interpretation. Errors on the background estimates are detailed in Tables 7.4, 7.5, 7.6, and 7.7. Errors on the expected numbers of GGM events are purely statistical.

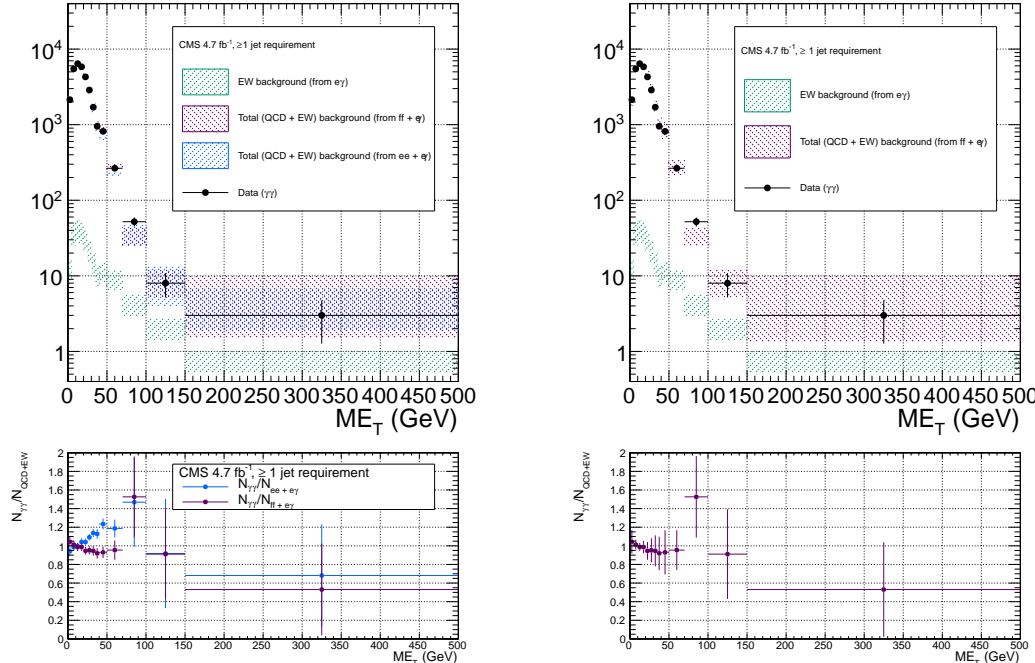
Source	No. events				
	[50, 60)	[60, 70)	[70, 80)	[80, 100)	$\geq 100$
Observation ( $\gamma\gamma$ )	354	93	37	33	17
Predicted background ( $ff + e\gamma$ )	$361 \pm 51.5$	$113 \pm 27.1$	$26.9 \pm 14.5$	$23.9 \pm 7.23$	$20.2 \pm 10.9$
Predicted background ( $ee + e\gamma$ )	$317 \pm 14.1$	$90.2 \pm 7.77$	$39.6 \pm 5.75$	$25.1 \pm 5.66$	$28.9 \pm 6.70$
$m_{\tilde{q}} = 720$ GeV $M_3 = 720$ GeV $M_1 = 375$ GeV	$13.3 \pm 2.13$	$17.7 \pm 2.46$	$15.3 \pm 2.33$	$42.9 \pm 3.82$	$966 \pm 18.3$
$m_{\tilde{q}} = 1440$ GeV $M_3 = 1440$ GeV $M_1 = 375$ GeV	$0.008 \pm 0.003$	$0.009 \pm 0.003$	$0.012 \pm 0.003$	$0.030 \pm 0.005$	$1.92 \pm 0.04$



(a)  $ee + e\gamma$  and  $ff + e\gamma$ . The widths of the bands correspond to the errors given in Table 7.7, excluding the error associated with the difference between the  $ee$  and  $ff$  QCD estimates for the  $ff + e\gamma$   $E_T$  distribution.

(b)  $ff + e\gamma$ . The widths of the bands correspond to the errors given in Table 7.7, including the error associated with the difference between the  $ee$  and  $ff$  QCD estimates.

Figure 7.28:  $\not{E}_T$  distribution of the  $\gamma\gamma$  search sample (black circles) along with the predicted  $\not{E}_T$  distributions of the QCD and electroweak backgrounds (blue band for  $ee$  QCD prediction + electroweak prediction, purple band for  $ff$  QCD prediction + electroweak prediction). The electroweak background prediction is shown in green. The bottom plots show the ratio of the  $\gamma\gamma$   $\not{E}_T$  distribution to the  $ee + e\gamma$  background distribution (blue) and  $ff + e\gamma$  background distribution (purple).



(a)  $ee + e\gamma$  and  $ff + e\gamma$ . The widths of the bands correspond to the errors given in Table 7.7, excluding the error associated with the difference between the  $ee$  and  $ff$  QCD estimates for the  $ff + e\gamma$   $E_T$  distribution.

(b)  $ff + e\gamma$ . The widths of the bands correspond to the errors given in Table 7.7, including the error associated with the difference between the  $ee$  and  $ff$  QCD estimates.

Figure 7.29:  $E_T$  distribution of the  $\gamma\gamma + \geq 1$  jet search sample (black circles) along with the predicted  $E_T$  distributions of the QCD and electroweak backgrounds (blue band for  $ee$  QCD prediction + electroweak prediction, purple band for  $ff$  QCD prediction + electroweak prediction). The electroweak background prediction is shown in green. The bottom plots show the ratio of the  $\gamma\gamma E_T$  distribution to the  $ee + e\gamma$  background distribution (blue) and  $ff + e\gamma$  background distribution (purple).

Table 7.9: Observed numbers of two-photon +  $\geq 1$ -jet events,  $ee$  and  $ff$  background estimates and their errors, and expected numbers of two-photon +  $\geq 1$ -jet events from two representative GGM SUSY models (details of MC simulation given in Chapter 8) for the  $E_T$  bins used in the search. The  $ee$  estimate is shown for comparison; the  $ff$  estimate is the official result used in the interpretation. Errors on the background estimates are detailed in Tables 7.4, 7.5, 7.6, and 7.7. Errors on the expected numbers of GGM events are purely statistical.

Source	No. events				
	[50, 60)	[60, 70)	[70, 80)	[80, 100)	$\geq 100$
Observation ( $\gamma\gamma + \geq 1$ jet)	202	63	27	25	11
Predicted background ( $ff + e\gamma$ )	$200 \pm 35.4$	$77.7 \pm 28.1$	$19.4 \pm 8.55$	$14.7 \pm 7.04$	$14.4 \pm 5.59$
Predicted background ( $ee + e\gamma$ )	$171 \pm 10.2$	$52.7 \pm 5.74$	$25.1 \pm 4.76$	$10.2 \pm 5.04$	$13.1 \pm 5.74$
$m_{\tilde{q}} = 720$ GeV $M_3 = 720$ GeV $M_1 = 375$ GeV	$13.3 \pm 2.13$	$17.7 \pm 2.46$	$15.3 \pm 2.33$	$42.9 \pm 3.82$	$965 \pm 18.3$
$m_{\tilde{q}} = 1440$ GeV $M_3 = 1440$ GeV $M_1 = 375$ GeV	$0.008 \pm 0.003$	$0.009 \pm 0.003$	$0.012 \pm 0.003$	$0.031 \pm 0.004$	$1.92 \pm 0.04$

# Chapter 8

## Interpretation of Results in Terms of GMSB Models

As shown in Figs. 7.28 and 7.29 and Tables 7.8 and 7.9, no excess of events above the Standard Model expectation is found in either the  $\geq 0$ - or  $\geq 1$ -jet analyses for the GMSB-sensitive region  $\cancel{E}_T \geq 50$  GeV. Therefore, upper limits on the production cross sections of various GMSB models are calculated and then translated into statements of exclusion. Section 8.1 describes the GMSB models that were generated with MC and tested for exclusion. The upper limit calculation and translation to model exclusions is laid out in Section 8.2. The upper limits themselves are presented in Section 8.3, and, finally, the exclusions are presented in Section 8.4.

### 8.1 Simplified Models

The exclusion reach of the two-photon search is presented for three different two-dimensional scans in GMSB parameter space. The first scan covers the bino NLSP scenario of Sec. 3.5. In this scan,  $M_2$ , which controls the amount of wino mixing, is set to 3.5 TeV.  $M_1$ , which controls the amount of bino mixing, is set to 375 GeV. This insures that all gauginos except the lightest neutralino are too heavy to be pro-

duced in significant numbers at the LHC. All other mass parameters except for  $M_3$  ( $\sim$ gluino mass) and  $m_{\tilde{q}}$  ( $\sim$ first- and second-generation squark mass) are set to 3.5 TeV, which insures that squark/gluino decay to intermediate states such as third-generation squarks or any flavor of lepton is strongly suppressed. Every mass parameter except for  $M_1$ ,  $M_3$ , and  $m_{\tilde{q}}$  is set so large that it has essentially no effect on the sparticle dynamics that can be observed in LHC collisions, which are completely determined by  $M_1$ ,  $M_3$ , and  $m_{\tilde{q}}$ . The high-mass parameters are decoupled from the relevant part of the spectrum.  $M_3$  and  $m_{\tilde{q}}$  are scanned over from  $M_3 = m_{\tilde{q}} = 400$  GeV to  $M_3 = m_{\tilde{q}} = 2$  TeV in 80-GeV steps. The resulting simplified model consists only of a gluino, first- and second-generation squarks, and the lightest neutralino and its decay products (the gravitino is forced to be the LSP). The scan in  $M_3$ - $m_{\tilde{q}}$  space illuminates the sensitivity of the two-photon search to different levels of signal hadronic activity.

The second scan is identical to the first except that the values of  $M_1$  and  $M_2$  are inverted ( $M_1 = 3.5$  TeV and  $M_2 = 375$  GeV). In this case,  $M_1$  is decoupled from the relevant part of the spectrum. This corresponds to the wino NLSP scenario of Sec. 3.5. Now, both the lightest neutralino and the lightest chargino have masses of order 375 GeV, and are therefore produced with approximately equal frequency in the gluino and squark decays. The chargino decays to  $W + \tilde{G}$ , so final states in this scan often include leptons or large jet multiplicity. Since there is no guarantee that two neutralinos will be produced and will decay to two photons, this search is not well optimized for the wino NLSP scenario. However, a related CMS search with one photon and  $\geq 3$  jets has an exclusion reach of  $\sim 1$  TeV in  $M_3$  and  $m_{\tilde{q}}$  for this scenario [59].

The third scan is  $M_3$  vs.  $M_1$  for  $m_{\tilde{q}}$ ,  $M_2$ , and all other mass parameters equal to 2.5 TeV (decoupled).  $M_3$  is scanned from 160 GeV to 2 TeV in 80-GeV steps, while  $M_1$  is scanned from 150 GeV to 1050 GeV in 100-GeV steps.  $M_3 < M_1$  is not allowed,

as this would imply that the gluino, not the lightest neutralino, is the NLSP. This scan highlights the performance of the two-photon search as a function of  $M_1$  (i.e. as a function of decays open to the neutralino), whereas the previous two scans keep  $M_1$  fixed.

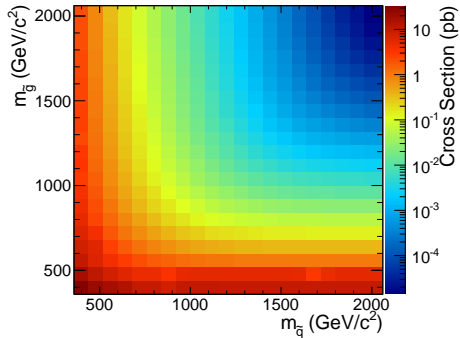
For each scan, the sparticle mass spectrum is generated with SuSpect 2.41 [142] and the decay widths with SDECAY 1.3 [143]. The event data (including production, unstable particle decay, parton showering, and hadronization) is generated with Pythia 6.422 [144], using the sparticle mass spectra and decay widths as inputs. The gravitino is always forced to be the LSP. The simulated data are reconstructed with CMSSWv4.2.2, which uses a detector simulation based on GEANT 4 [145]. Next to leading order cross sections are calculated with PROSPINO 2.1 [146], and shown in Figure 8.1 for the three signal MC scenarios.

## 8.2 Upper Limit Calculation and Model Exclusion

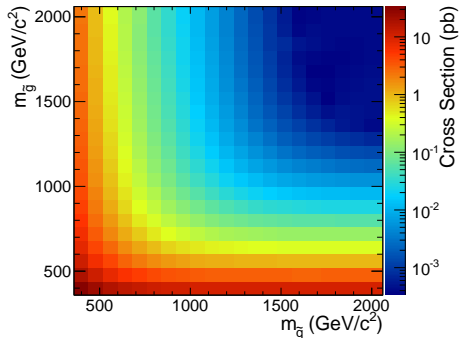
The upper limits are calculated according to the prescription followed for the 2011 ATLAS + CMS Higgs limit combination [147]. This prescription utilizes the frequentist  $\text{CL}_s$  method [148] with profile likelihood test statistic [149]. The  $\text{CL}_s$  method and the profile likelihood are explained in Section 8.2.2, using specific signal MC points to illustrate the procedure. First, however, the signal MC acceptance  $\times$  efficiency, which is an input to the limit setting procedure, is presented in Section 8.2.1.

### 8.2.1 Signal Acceptance $\times$ Efficiency

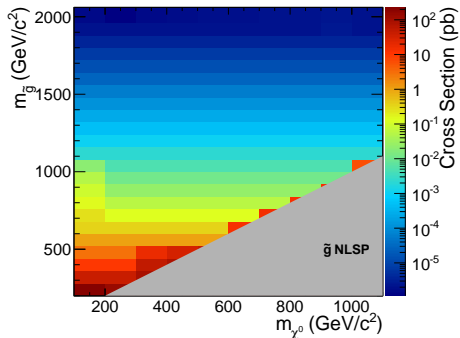
The signal acceptance  $\times$  efficiency (denoted  $\mathcal{A} \times \epsilon$ ), defined for each signal point as the number of  $\gamma\gamma$  events selected with  $\cancel{E}_T \geq 50$  GeV divided by the total number of events generated, is shown in Figure 8.2 for the three different scenarios described in Sec. 8.1. Acceptance refers to the fraction of true events that can be detected given



(a)  $M_2$  decoupled ( $M_2 = 3.5$  TeV),  $M_1 = 375$  GeV,  $M_3$  vs.  $m_{\tilde{q}}$ .



(b)  $M_1$  decoupled ( $M_1 = 3.5$  TeV),  $M_2 = 375$  GeV,  $M_3$  vs.  $m_{\tilde{q}}$ .



(c)  $m_{\tilde{q}}$  decoupled ( $m_{\tilde{q}} = 2.5$  TeV),  $M_3$  vs.  $M_1$ .

Figure 8.1: Next to leading order cross sections for the three different MC scenarios described in the text.

the fiducial extent of the detector and the  $E_T$  cuts on the photons. Efficiency denotes the fraction of accepted events (i.e. those events passing the  $E_T$  and  $\eta$  cuts) that have two photons passing the photon identification criteria.

In Figs. 8.2(a) and 8.2(b), the large drop in  $\mathcal{A} \times \epsilon$  for  $m_{\tilde{q}} > M_3$  is due to an increase in the number of jets produced per event and a consequent reduction in the number of photons that pass the  $I_{\text{comb}} < 6$  GeV cut. For  $m_{\tilde{q}} > M_3$ , there is more phase space available to produce gluinos in the hard scatter than squarks. However, since gluinos must decay via squarks, and in these models all squarks are heavier than the gluino, only the two-jet decay  $\tilde{g} \rightarrow q\tilde{q}\chi^0$  is available. Conversely, when  $m_{\tilde{q}} < M_3$ , there is more phase space available to produce squarks, which may then decay via one jet as  $\tilde{q} \rightarrow q\tilde{\chi}^0$ . Jets in SUSY events may be very close to the neutralino decay photons, and as a result the photons may fail the strict isolation requirements, leading to lower  $\mathcal{A} \times \epsilon$  for jet-rich events. The worsened acceptance along  $M_3 = 400$  GeV and  $m_{\tilde{q}} = 400$  GeV in Fig. 8.2(b) is due to efficiency of the jet cut, which decreases drastically as  $M_3$  and  $m_{\tilde{q}}$  approach  $M_1$  because of shrinking phase space to produce hard jets in the squark and gluino decays to neutralinos.

The broad peak in  $\mathcal{A} \times \epsilon$  shown in Fig. 8.2(a) for  $m_{\tilde{q}} < M_3$  and  $\sim 600$  GeV  $< m_{\tilde{q}} < \sim 1600$  GeV is due to the  $E_T > 50$  GeV cut. The efficiency of the cut decreases as  $m_{\tilde{q}}$  decreases because of the fixed  $M_1$  of 375 GeV. If the squark-neutralino mass splitting gets too small, the likelihood of producing an energetic enough gravitino to pass the  $E_T$  cut decreases.

$\mathcal{A} \times \epsilon$  is generally much lower for the  $M_2 = 375$  GeV grid (Figs. 8.2(c) and 8.2(d)) due to the larger contribution from chargino decays to  $W + \tilde{G}$ , which do not give rise to photons in the final state. The increased acceptance for  $M_3 > m_{\tilde{q}}$  is due to the same jet multiplicity issue affecting the  $M_1 = 375$  GeV grid. As  $M_3$  and  $m_{\tilde{q}}$  increase relative to the fixed  $M_2$ , the jets from squark and gluino decay get more energetic, increasing the chance that they will overlap with the neutralino decay photon and

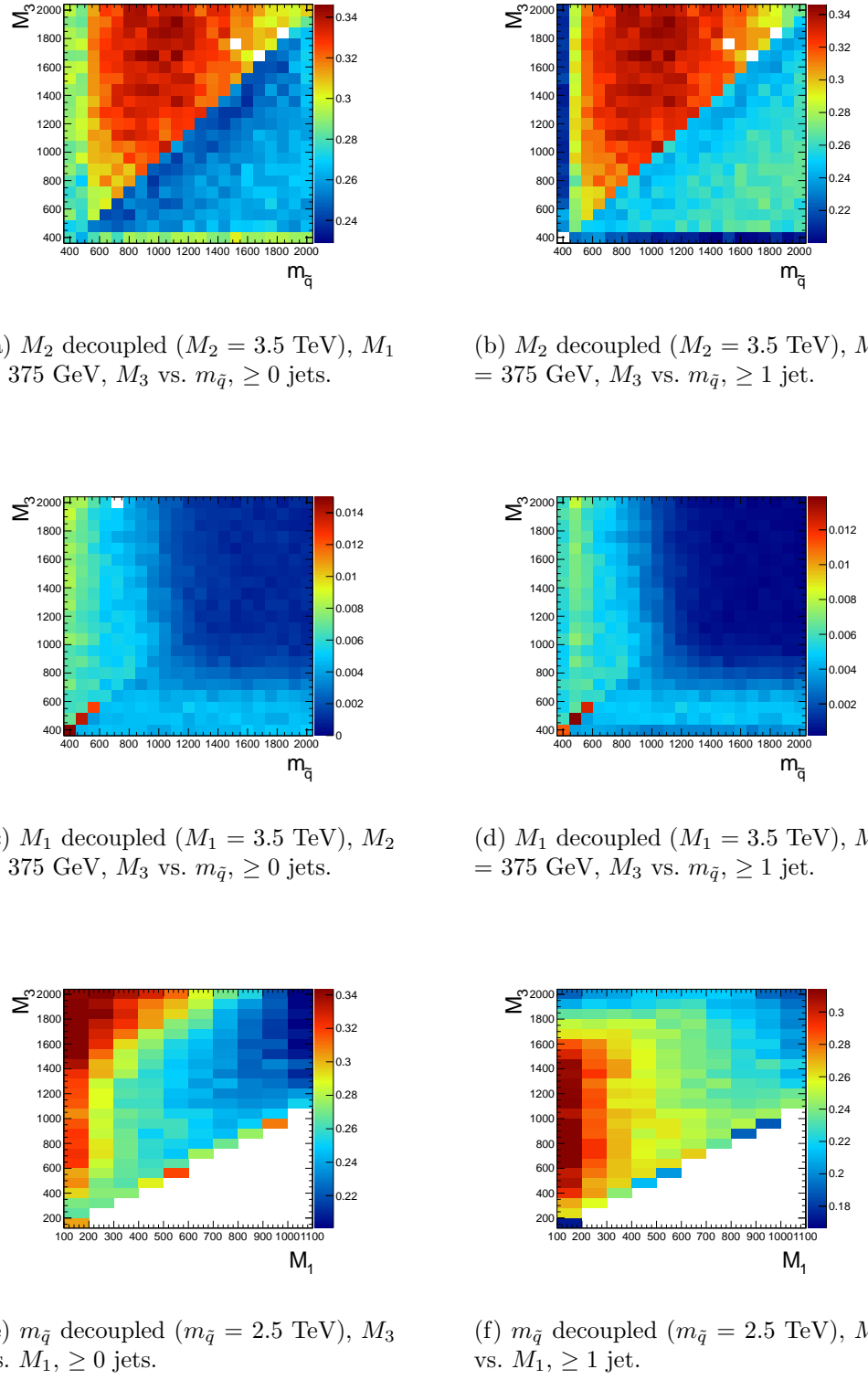


Figure 8.2: Signal acceptance  $\times$  efficiency (defined in the text) for the three different scenarios described in Sec. 8.1.

cause it to fail the isolation cut. For  $m_{\tilde{q}} \gtrsim 1$  TeV and  $M_3 \gtrsim 800$  GeV, the acceptance is so low that not enough events were simulated to see the acceptance decrease over the statistical error.

In Fig. 8.2(e), the neutralino is always heavy enough to guarantee decay to a photon that can pass the 40 GeV  $p_T$  cut.  $\mathcal{A} \times \epsilon$  increases as  $M_3$  increases because the larger gluino-neutralino mass splitting gives the neutralino a larger kinetic energy, increasing the chance that it will decay to a photon with 40 GeV  $p_T$  or higher. After the bino mass increases beyond the threshold needed to produce high  $p_T$  photons,  $\mathcal{A} \times \epsilon$  decreases with increasing  $M_1$ , independent of gluino mass, because higher  $M_1$  means more phase space is open to decays of the form  $\tilde{\chi}_1^0 \rightarrow Z\tilde{G}$  and  $\tilde{\chi}_1^0 \rightarrow H\tilde{G}$ . The two-photon search is naturally not as efficient for these decays.

There is a small chance that some real GMSB signal events could be reconstructed as  $ff$  events in the data. To correct the signal acceptance for this effect, the number of signal events reconstructed as  $ff$  events is subtracted from the number of signal  $\gamma\gamma$  events, effectively reducing the signal acceptance. This is generally a small correction ( $\sim 5\%$ ).

### 8.2.2 $\text{CL}_s$ and the Profile Likelihood Test Statistic

The process of setting a cross section upper limit entails (1) defining a test statistic, (2) generating a distribution for that test statistic under the signal + background and background-only hypotheses, and (3) deciding whether or not the observed value of the test statistic is more compatible with the signal + background (i.e. weaker upper limit) or background-only (i.e. stronger upper limit) hypotheses by considering where it falls within the test statistic distributions. An important requirement on the choice of test statistic is that it be able to effectively discriminate between the signal + background and background-only hypotheses, i.e. the shape of its distribution for these two hypotheses should be different. The procedure for determining the exclud-

ability of a particular model given the value of the test statistic observed should not give rise to pathological behavior in the presence of small signals, low statistics, or weak sensitivity to models, as is commonly the case in high energy physics. These demands on the test statistic and the limit setting procedure itself dictate the choice of the profile likelihood test statistic and  $\text{CL}_s$  procedure.

In the remainder of this section, the notation is taken from ref. [147].

### Profile Likelihood

For a specific model of GMSB, the limit setting procedure concerns the question of whether to reject the signal + background hypothesis  $\mu s + b$  in favor of the background-only (Standard Model) hypothesis of  $b$  ( $\mu = 0$ ).  $\mu$  is a dimensionless signal strength parameter.  $s$  is the expected number of signal events, calculated from MC simulated signal events as in Secs. 8.1 and 8.2.1.  $b$  is the expected number of background events, estimated in Chap. 7. By the Neyman-Pearson lemma [150], the ratio of the likelihood of  $\mu s + b$  to the likelihood of  $b$  is the test statistic with the highest power to reject  $\mu s + b$  at whatever confidence level is desired. In practice, this means that the likelihood ratio is the best discriminator between the GMSB and Standard Model hypotheses.

The likelihood of the signal + background hypothesis as a function of the data (either real or generated) is defined as

$$\mathcal{L}(\text{data}|\mu, \theta) = \prod_{i=1}^N \frac{(\mu s_i(\theta) + b_i(\theta))^{n_i}}{n_i!} e^{-\mu s_i(\theta) - b_i(\theta)} p(\tilde{\theta}|\theta) \quad (8.1)$$

where  $N = 5$  is the number of  $\cancel{E}_T$  bins used in the analysis ([50, 60) GeV, [60, 70) GeV, [70, 80) GeV, [80, 100) GeV, and  $[100, \infty)$  GeV);  $s_i(\theta)$  and  $b_i(\theta)$  are the expected number of signal and background events in  $\cancel{E}_T$  bin  $i$ , respectively;  $n_i$  is the number of events observed in  $\cancel{E}_T$  bin  $i$ ; and  $\theta$  represents all the nuisance parameters

(uncertainties).  $p(\tilde{\theta}|\theta)$  represents the product of probability distribution functions (PDFs) for the nuisance parameters, where  $\tilde{\theta}$  is the default value of the nuisance parameter. In this analysis, there are eight experimental nuisance parameters per  $E_T$  bin, given here as relative errors on the expected number of signal events:

- Uncertainty on the measured integrated luminosity (4.5% in all bins) [151]
- Uncertainty on the signal acceptance due to  $\epsilon_e^{\text{data}}/\epsilon_e^{\text{MC}}$  and the pixel veto efficiency error (cf. Sec. 6.4.2) (8% in all bins)
- Uncertainty on the signal acceptance due to imperfect pileup simulation (2.6% in all bins)
- Systematic uncertainty on QCD background prediction due to difference between  $ff$  and  $ee$  estimates (5.5%-53% of the QCD background depending on bin)
- Systematic uncertainty on electroweak background prediction due to  $p_T$  dependence of  $f_{e \rightarrow \gamma}$  (29%-30% of the electroweak background depending on bin)
- Statistical uncertainty on the signal acceptance (1.8%-100% depending on model and bin)
- Statistical uncertainty on the QCD background prediction (7.2%-38% of the QCD background depending on bin)
- Statistical uncertainty on the electroweak background prediction (3.6%-7.2% of the electroweak background depending on bin)

and one very small theoretical nuisance parameter: the uncertainty on the signal acceptance due to underlying parton distribution function (PDF) uncertainties. In the limit-setting code, the uncertainties on signal acceptance due to photon efficiency and PDF errors are added in quadrature and treated as one. The uncertainty on the

signal acceptance due to jet energy correction uncertainties is negligible, due to the presence of many hard jets in GMSB signal events. The uncertainties on integrated luminosity and pileup are 100% correlated between  $\cancel{E}_T$  bins, and the uncertainty on signal acceptance can usually be treated similarly because the error on  $\epsilon_e^{\text{data}}/\epsilon_e^{\text{MC}}$  often dominates the PDF error on acceptance (although these three uncertainties are 0% correlated with each other).

To estimate the uncertainty due to imperfect simulation of LHC pileup, the square of the average data efficiency for photons over the range 1-15 reconstructed primary vertices (see Fig. 6.18(a)), weighted by the number of  $\gamma\gamma$  events per primary vertex bin, is calculated. The efficiency per primary vertex bin is estimated from a linear fit to Fig. 6.18(a). The process is repeated for MC using the entire range of primary vertices in Fig. 6.18(a) (all MC signal points have the same pileup simulation). The error is taken as  $2 \times |\text{avg. data efficiency squared} - \text{avg. MC efficiency squared}| / (\text{avg. data efficiency squared} + \text{avg. MC efficiency squared})$ .

Each nuisance parameter PDF is modeled by a log-normal distribution:

$$p(\tilde{\theta}|\theta) = \frac{1}{\sqrt{2\pi} \ln \kappa} \exp\left(-\frac{(\ln \tilde{\theta}/\theta)^2}{2(\ln \kappa)^2}\right) \frac{1}{\tilde{\theta}} \quad (8.2)$$

where  $\tilde{\theta} = 1$  and  $\kappa = 1 + \text{the one-standard-deviation relative error on the nuisance parameter}$  (e.g. for the 4.5% error due to integrated luminosity,  $\kappa = 1.045$ ).

Similarly, the likelihood of the background-only hypothesis as a function of the data (either real or generated) is defined as

$$\mathcal{L}(\text{data}|0, \theta) = \prod_{i=1}^N \frac{b_i(\theta)^{n_i}}{n_i!} e^{-b_i(\theta)} p(\tilde{\theta}|\theta) \quad (8.3)$$

The profile likelihood test statistic is defined as

$$\tilde{q}_\mu = -2 \ln \frac{\mathcal{L}(\text{data}|\mu, \hat{\theta}_\mu)}{\mathcal{L}(\text{data}|\hat{\mu}, \hat{\theta})}, 0 \leq \hat{\mu} \leq \mu \quad (8.4)$$

where the  $\hat{\theta}_\mu$  maximize  $\mathcal{L}(\text{data}|\mu, \hat{\theta}_\mu)$  when it is evaluated at a particular  $\mu$ , and  $\hat{\mu}$  and  $\hat{\theta}$  are the global maximum likelihood estimators of  $\mu$  and  $\theta$ . The condition  $\hat{\mu} \leq \mu$  insures that the obtained cross section upper limit is one-sided, i.e. there is no possibility to find a lower limit on the cross section. The profile likelihood test statistic has the nice property that in the asymptotic (large statistics) limit its PDF can be approximated by analytic formulae, eliminating the need to generate multiple toy experiments to get the PDF. However, the approximation breaks down for small numbers of observed events, so in practice the asymptotic limit is only used as a first guess at the location of the true limit.

The PDFs  $f(\tilde{q}_\mu|\mu, \hat{\theta}_\mu^{\text{obs}})$  and  $f(\tilde{q}_\mu|0, \hat{\theta}_0^{\text{obs}})$  for the profile likelihood test statistic under the signal + background and background-only hypotheses, respectively, are obtained by generating toy MC pseudo-experiments.  $\hat{\theta}_\mu^{\text{obs}}$  and  $\hat{\theta}_0^{\text{obs}}$  maximize Eqs. 8.1 and 8.3, respectively, when they are evaluated for the observed data. For each  $\mu$  (and the background-only hypothesis  $\mu = 0$ ), the pseudo-experiments are generated by picking random values of  $s$  and  $b$  from a Poisson distribution with the  $\theta$  fixed as just described.

### **CL<sub>s</sub>**

In the classical frequentist approach, a signal model may be excluded at the 95% confidence level (CL) if the probability of any measurement of the test statistic to be greater than or equal to the observed value given the signal + background hypothesis is 5%. This means that the observed value of the test statistic is so incompatible with what one would expect to observe if the signal model were true that, under the

assumption that the signal model *is* true, the chance of observing a test statistic even further afield from the signal expectation is only 5%. Mathematically,

$$\begin{aligned} p_\mu &\equiv P(\tilde{q}_\mu \geq \tilde{q}_\mu^{\text{obs}} | \mu s + b) = \int_{\tilde{q}_\mu^{\text{obs}}}^{\infty} f(\tilde{q}_\mu | \mu, \hat{\theta}_\mu^{\text{obs}}) d\tilde{q}_\mu \\ p_\mu &\leq 0.05 \Rightarrow \text{exclude } \mu \end{aligned} \quad (8.5)$$

where  $\tilde{q}_\mu^{\text{obs}}$  is the observed value of the test statistic and  $p_\mu$  is the p-value. As indicated in Eq. 8.5, the p-value is simply the integral of the PDF of  $\tilde{q}_\mu$  from  $\tilde{q}_\mu^{\text{obs}}$  to infinity.

By construction, the classical 95% CL frequentist approach described above will reject a true signal + background hypothesis 5% of the time. This can happen if the experiment gets “unlucky” and the observation fluctuates low, causing  $\tilde{q}_\mu^{\text{obs}}$  to fall in the tail of the  $\tilde{q}_\mu$  distribution. This poses a problem for the case of very weak signals ( $\mu \sim 0$ ), because it will lead to spurious exclusions of models to which the experiment has little sensitivity. To avoid this pitfall, the  $\text{CL}_s$  limit setting method is used.

In the  $\text{CL}_s$  method, the classical frequentist p-value of Eq. 8.5 is simply divided by one minus the p-value of the background-only hypothesis, and it is this ratio, rather than the p-value of the signal + background hypothesis alone, that is required to be  $\leq 0.05$ . Mathematically,

$$1 - p_0 \equiv P(\tilde{q}_\mu \geq \tilde{q}_\mu^{\text{obs}} | b) = \int_{\tilde{q}_\mu^{\text{obs}}}^{\infty} f(\tilde{q}_\mu | 0, \hat{\theta}_0^{\text{obs}}) d\tilde{q}_\mu \quad (8.6)$$

$$\text{CL}_s(\mu) \equiv \frac{p_\mu}{1 - p_0} \quad (8.7)$$

$$\text{CL}_s(\mu) \leq 0.05 \Rightarrow \text{exclude } \mu$$

where  $p_0$  is the p-value for the background-only hypothesis ( $\mu = 0$ ). In the case of low sensitivity to  $\mu$ ,  $p_\mu \lesssim 1 - p_0$ , so  $\text{CL}_s(\mu) \lesssim 1$  and  $\mu$  will not be excluded. On the

contrary, for high sensitivity to  $\mu$  ( $\mu s \gg \sigma_b$ ),  $p_\mu \ll 1 - p_0$ , so models that can be excluded by the criterion  $p_\mu \leq 0.05$  will also be excluded by the criterion  $\text{CL}_s \leq 0.05$ . Compared to the classical frequentist method,  $\text{CL}_s$  limits can be a little stronger in the case of low signal sensitivity [147].

To determine the upper limit on the cross section of a particular model, the lowest value of  $\mu$  for which  $\text{CL}_s(\mu) \leq 0.05$ , denoted  $\mu^{95\% \text{ CL}}$ , is found. The cross section upper limit of that model is then simply  $\mu^{95\% \text{ CL}}$  multiplied by the expected cross section of the model (cf. Fig. 8.1).

In contrast to the observed upper limit, the expected upper limit is calculated from an ensemble of background-only MC pseudo-experiments. The distribution  $f(\mu_{\text{pseudo}}^{95\% \text{ CL}})$  is plotted (one entry per pseudo-experiment). The median expected upper limits and  $\pm 1\sigma$  and  $\pm 2\sigma$  bands are defined as

$$0.5 = \int_0^{\mu_{\text{exp}}^{95\% \text{ CL}}} f(\mu_{\text{pseudo}}^{95\% \text{ CL}}) d\mu_{\text{pseudo}}^{95\% \text{ CL}} \quad (8.8)$$

$$0.16 = \int_0^{\mu_{-1\sigma,\text{exp}}^{95\% \text{ CL}}} f(\mu_{\text{pseudo}}^{95\% \text{ CL}}) d\mu_{\text{pseudo}}^{95\% \text{ CL}} \quad (8.9)$$

$$0.84 = \int_0^{\mu_{+1\sigma,\text{exp}}^{95\% \text{ CL}}} f(\mu_{\text{pseudo}}^{95\% \text{ CL}}) d\mu_{\text{pseudo}}^{95\% \text{ CL}} \quad (8.10)$$

$$0.025 = \int_0^{\mu_{-2\sigma,\text{exp}}^{95\% \text{ CL}}} f(\mu_{\text{pseudo}}^{95\% \text{ CL}}) d\mu_{\text{pseudo}}^{95\% \text{ CL}} \quad (8.11)$$

$$0.975 = \int_0^{\mu_{+2\sigma,\text{exp}}^{95\% \text{ CL}}} f(\mu_{\text{pseudo}}^{95\% \text{ CL}}) d\mu_{\text{pseudo}}^{95\% \text{ CL}} \quad (8.12)$$

The technical procedure followed to calculate the 95% CL cross section upper limits for each GMSB model tested is given below.

1. Calculate a guess for the median expected limit and  $\pm 2\sigma$  error bands ( $\mu_{\pm 2\sigma, \text{guess}}^{95\% \text{ CL}}$ ) using the asymptotic formulae for  $f(\tilde{q}_\mu | 0, \hat{\theta}_0^{\text{obs}})$ .
2. Calculate observed ( $\mu_{\text{obs,asym}}^{95\% \text{ CL}}$ ), median expected ( $\mu_{\text{exp,asym}}^{95\% \text{ CL}}$ ), and  $\pm 1\sigma$  ( $\mu_{\pm 1\sigma, \text{asym}}^{95\% \text{ CL}}$ )

and  $\pm 2\sigma$  ( $\mu_{\pm 2\sigma, \text{asym}}^{\text{95\%CL}}$ ) expected  $\text{CL}_s$  limits using the asymptotic formulae for  $f(\tilde{q}_\mu | \mu, \hat{\theta}_\mu^{\text{obs}})$  and  $f(\tilde{q}_\mu | 0, \hat{\theta}_0^{\text{obs}})$ . Restrict the range of  $\mu_{\text{obs}, \text{asym}}^{\text{95\%CL}}$  and  $\mu_{\text{exp}, \text{asym}}^{\text{95\%CL}}$  to  $[0, 5 \times \mu_{\pm 2\sigma, \text{guess}}^{\text{95\%CL}}]$  (this avoids pathological behavior of the limit-setting code when the expected number of signal events is much greater than the observed number of events and only introduces a  $\sim 5\%$  upward bias in the observed limit, well within the  $\pm 1\sigma$  error bands).

3. Calculate median expected ( $\mu_{\text{exp}}^{\text{95\%CL}}$ ) and  $\pm 1\sigma$  ( $\mu_{\pm 1\sigma}^{\text{95\%CL}}$ ) and  $\pm 2\sigma$  ( $\mu_{\pm 2\sigma}^{\text{95\%CL}}$ ) expected  $\text{CL}_s$  limits using 100 toy MC pseudo-experiments to generate  $f(\tilde{q}_\mu | \mu, \hat{\theta}_\mu^{\text{obs}})$  and  $f(\tilde{q}_\mu | 0, \hat{\theta}_0^{\text{obs}})$ . Restrict the range of  $\mu_{\text{exp}}^{\text{95\%CL}}$  to  $[0, 5 \times \mu_{\pm 2\sigma, \text{guess}}^{\text{95\%CL}}]$ .
4. If  $\mu_{\pm 2\sigma}^{\text{95\%CL}}$  could not be calculated, set  $\mu_{\pm 2\sigma}^{\text{95\%CL}} = \mu_{\pm 2\sigma, \text{asym}}^{\text{95\%CL}}$  instead.
5. If  $\mu_{+2\sigma}^{\text{95\%CL}} \neq \mu_{-2\sigma}^{\text{95\%CL}}$  and  $\mu_{\text{obs}, \text{asym}}^{\text{95\%CL}} > 0.0001$ :
  - If  $\mu_{\text{obs}, \text{asym}}^{\text{95\%CL}} > \mu_{+2\sigma}^{\text{95\%CL}}$ , set  $\mu_{+2\sigma}^{\text{95\%CL}} = 1.3 \times \mu_{\text{obs}, \text{asym}}^{\text{95\%CL}}$ .
  - If  $\mu_{\text{obs}, \text{asym}}^{\text{95\%CL}} < \mu_{-2\sigma}^{\text{95\%CL}}$ , set  $\mu_{-2\sigma}^{\text{95\%CL}} = 0.7 \times \mu_{\text{obs}, \text{asym}}^{\text{95\%CL}}$ .
6. If  $\mu_{+2\sigma}^{\text{95\%CL}} = \mu_{-2\sigma}^{\text{95\%CL}}$ , set  $\mu_{\pm 2\sigma}^{\text{95\%CL}} = \mu_{\pm 2\sigma, \text{asym}}^{\text{95\%CL}}$  instead.
7. Scan over 100 equally spaced test values of  $\mu$  between  $\mu_{-2\sigma}^{\text{95\%CL}}$  and  $\mu_{+2\sigma}^{\text{95\%CL}}$  and, if  $\mu > 0.0001$ , calculate the  $\text{CL}_s$  p-value ( $p_\mu$ ) for this test value of  $\mu$  to  $10^{-6}$  precision using a minimum of 500 toy experiments to generate  $f(\tilde{q}_\mu | \mu, \hat{\theta}_\mu^{\text{obs}})$  and  $f(\tilde{q}_\mu | 0, \hat{\theta}_0^{\text{obs}})$ .
8. Determine the observed ( $\mu_{\text{obs}, \text{scan}}^{\text{95\%CL}}$ ), median expected ( $\mu_{\text{exp}, \text{scan}}^{\text{95\%CL}}$ ), and  $\pm 1\sigma$  ( $\mu_{\pm 1\sigma, \text{scan}}^{\text{95\%CL}}$ ) and  $\pm 2\sigma$  ( $\mu_{\pm 2\sigma, \text{scan}}^{\text{95\%CL}}$ ) expected  $\text{CL}_s$  limits from the scan p-values for the signal + background and background-only pseudo-experiments.

Finally, a particular GMSB model is excluded if the upper limit on the cross section for that model is less than the expected theoretical cross section.

## 8.3 Cross Section Upper Limits

Figure 8.3 shows the observed upper limits on the cross sections for the models described in Sec. 8.1. In some ( $\mathcal{O}(10^{-3})$ ) cases, the upper limit is zero due to a computational failure. The upper limit for these points is estimated from the average of the upper limits of the four neighboring points, as shown in Figure 8.4. If any of the four points is also missing a valid upper limit, it is dropped from the average. The errors on the individual upper limits used in the estimate are propagated to the error on the average.

## 8.4 Exclusion Contours

Exclusion contours for the GMSB models discussed above are shown in Figure 8.5. The contours are derived from plots of predicted cross section minus cross section upper limit ( $\sigma \times (1 - \mu^{95\%CL})$ ), where  $\sigma$  is the nominal value of the predicted cross section for a given GMSB model) vs. the two model parameters of interest, so the values are either negative (not excluded) or positive (excluded). Sometimes, a particular point may have a different sign than its four same-sign neighbors (cf. Fig. 8.4) due to a fluctuation. In these cases,  $\sigma \times (1 - \mu^{95\%CL})$  for the anomalous point is estimated as the average  $\sigma \times (1 - \mu^{95\%CL})$  of the four neighboring points. The errors on the individual values of  $\sigma \times (1 - \mu^{95\%CL})$  used in the estimate are propagated to the error on the average.

In the plots in Fig. 8.5, the expected limit (i.e. the contour derived from  $\sigma \times (1 - \mu_{\text{exp,scan}}^{95\%CL})$ ) is drawn in dark orange and the  $1\sigma$  experimental band around the expected limit (i.e. the shaded region between the contours derived from  $\sigma \times (1 - \mu_{\pm 1\sigma, \text{scan}}^{95\%CL})$ ) is drawn in light orange. The values of  $\mu_{\text{exp,scan}}^{95\%CL}$  and  $\mu_{\pm 1\sigma, \text{scan}}^{95\%CL}$  only reflect the experimental uncertainties given in Sec. 8.2.2.

The observed limits (derived from  $\sigma \times (1 - \mu_{\text{obs,scan}}^{95\%CL})$ ) and  $1\sigma$  theoretical error

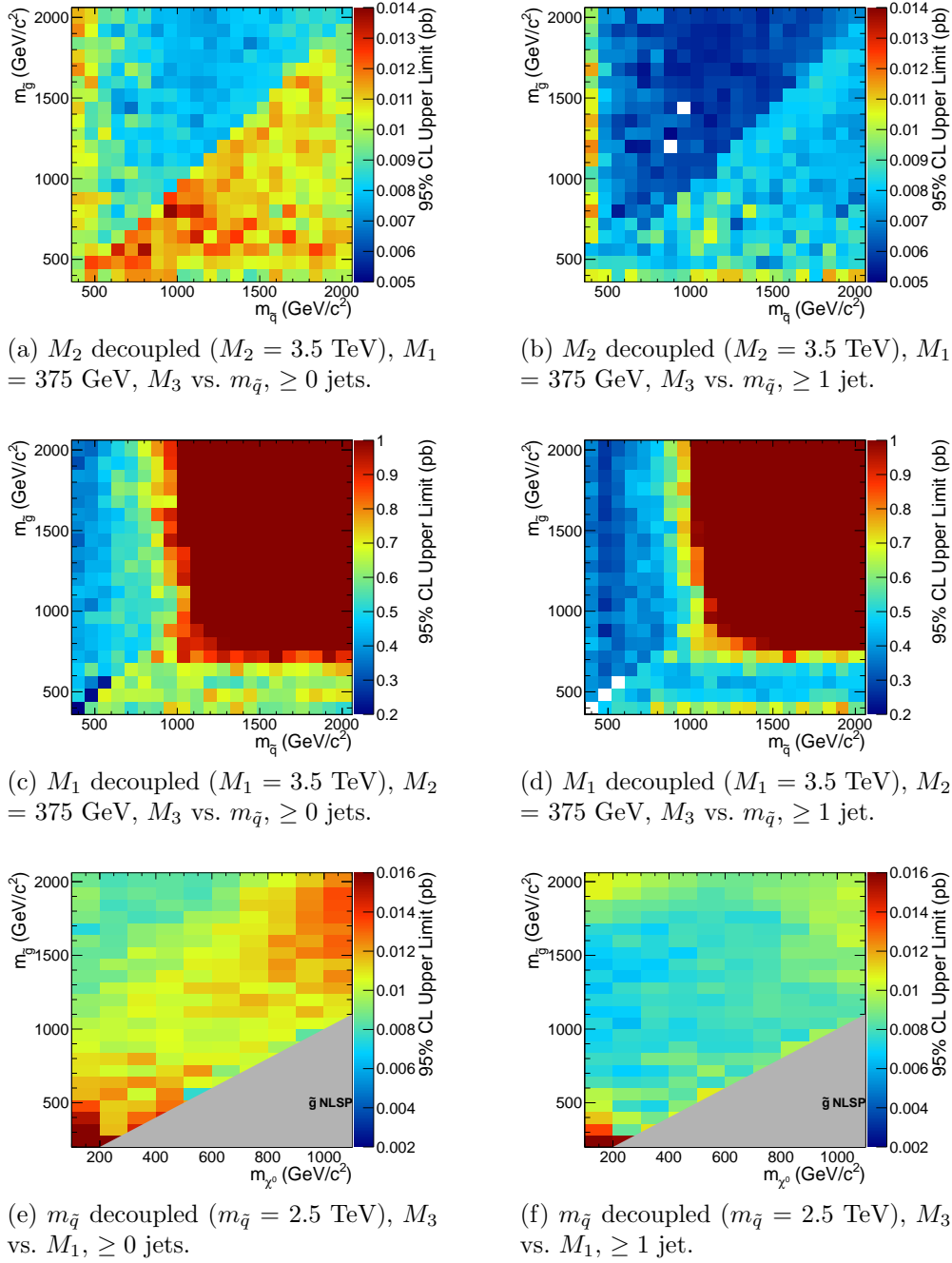


Figure 8.3: Cross section upper limits for the three different scenarios described in Sec. 8.1.

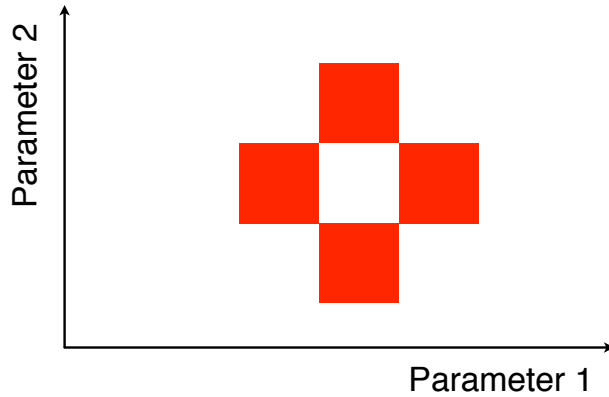


Figure 8.4: Diagram of the points (red squares) used in the estimation of an upper limit when a computational failure occurs (middle white square).

bands around the observed limits in Fig. 8.5 are drawn in blue. The contours that define this band are derived from  $\pm(\sigma_{\pm 1\sigma} - \sigma\mu_{\text{obs,scan}}^{95\% \text{CL}})$ , where  $\sigma_{\pm 1\sigma}$  is the nominal value of the predicted cross section  $\pm$  the one-standard-deviation theoretical error on the predicted cross section. In this way, the experimental and theoretical errors, the latter due to imperfect knowledge of the predicted cross section, are shown separately. Comparing with Fig. 8.1, one can easily see that the shapes of the exclusion curves are driven by the contours in the expected cross section plane. In all the plots, the observed limit is slightly higher than the expected limit, reflecting the fact that the background prediction is slightly higher than the observation.

The dominant theoretical uncertainties on the GMSB cross sections are due to:

- PDF uncertainty (4%-100% depending on model)
- Renormalization scale uncertainty (0.036%-25% depending on model)

The PDF4LHC [152–154] recommendations are used to calculate the effect of these uncertainties on the GMSB cross sections. The recommendations state that PDF sets

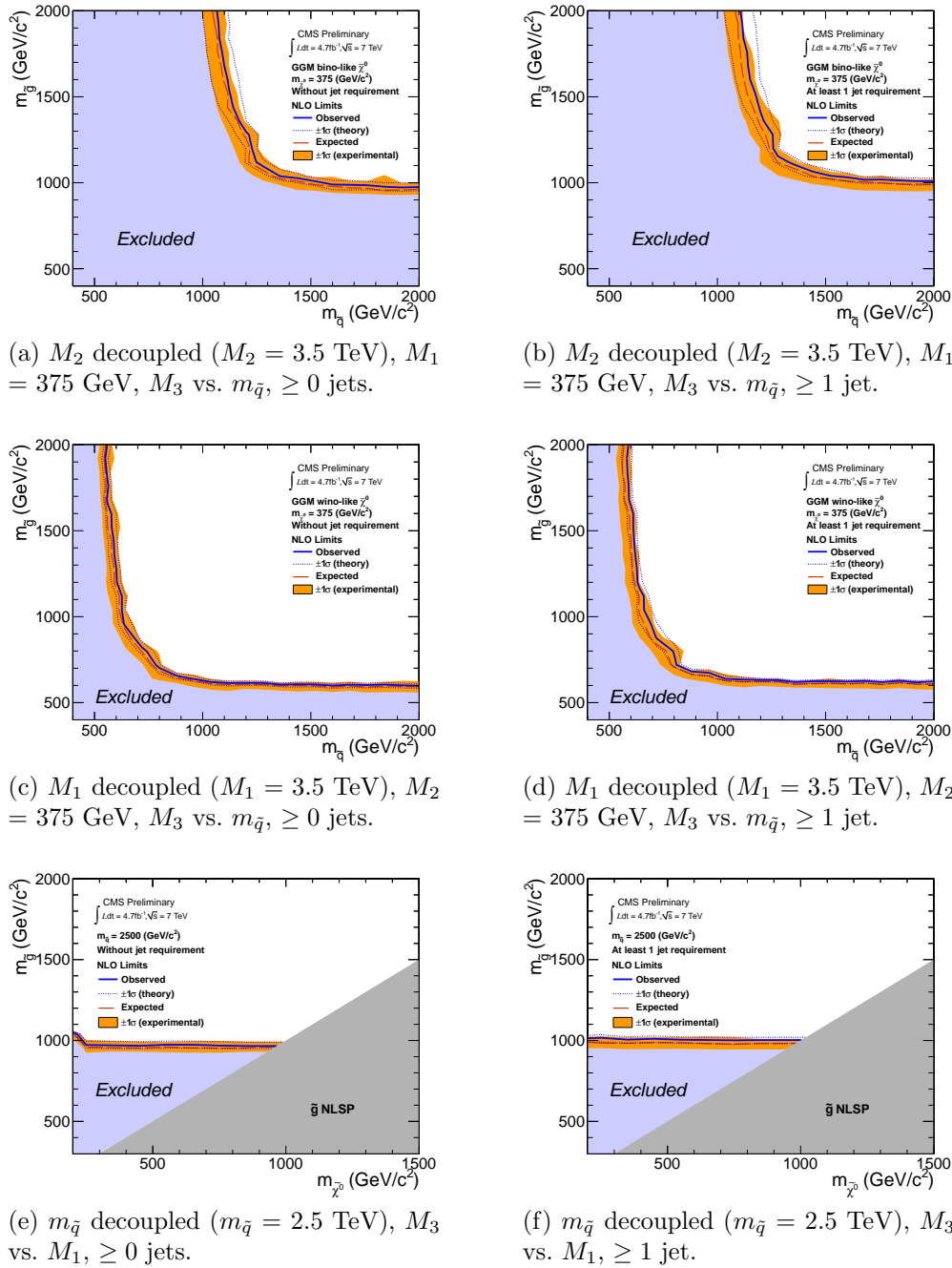


Figure 8.5: Exclusion contours for the three different scenarios described in Sec. 8.1.

from MSTW08 [155], CTEQ6.6 [156], and NNPDF2.0 [157] should be considered in the determination of the PDF uncertainties, because these three PDF sets include constraints from the Tevatron and from fixed target experiments, as well as from HERA [158], and are thus the most complete.

Each collaboration's PDF prediction comes from a global fit to experimental data with a certain number of free parameters. The best fit parameters come from minimizing the  $\chi^2$ ; increasing the  $\chi^2$  by one from its minimum can be written in terms of the  $N$ -dimensional Hessian error matrix [159] where  $N$  is the number of free parameters. To form the  $i^{\text{th}}$  pair of members of the PDF set, the PDF is evaluated once at the parameter values given by the  $i^{\text{th}}$  eigenvector of the Hessian matrix, and then again at the parameter values given by the negative of the  $i^{\text{th}}$  eigenvector. Each PDF set therefore contains  $2N$  members, corresponding to the positive and negative values of the  $N$  eigenvectors [160].

To calculate the PDF uncertainties for a given GMSB model, the leading order Pythia cross section is reweighted by a factor of the error PDF divided by the leading order PDF with which the model was generated. This is repeated for each error PDF in a given PDF set. The  $\pm 1\sigma$  deviations are proportional to the maximum difference between cross sections obtained this way. The actual equation for the  $\pm 1\sigma$  errors is Eq. (43) of ref. [160]. In the same way, the  $\pm 1\sigma$  errors are calculated for the CTEQ6.6, MSTW08, and NNPDF2.0 PDF sets. The total error is given by the half the difference between the largest  $+1\sigma$  deviation and the smallest  $-1\sigma$  deviation [152–154].

The uncertainties on the signal cross sections due to the choice of renormalization/factorization scale ( $\alpha_S(M_Z)$ ) are evaluated by calculating the PROSPINO next to leading order cross section once with  $\alpha_S(M_Z)$  halved, then once with  $\alpha_S(M_Z)$  doubled. The lower error on the cross section is taken as the absolute difference between the nominal and halved-scale values of the cross section, while the upper error is taken as the absolute difference between the nominal and doubled-scale values. The PDF

and  $\alpha_S$  uncertainties are added in quadrature to give the total PDF uncertainty.

Note that the quoted GMSB cross sections are evaluated at next to leading order using PROSPINO, but it is the leading order Pythia cross sections that are reweighted to the next to leading order MSTW08, CTEQ6.6, and NNPDF2.0 PDFs to get the error bands. In addition, since to a good approximation the GMSB production cross sections for the  $M_3$ - $m_{\tilde{q}}$  scans only depend on  $M_3$  and  $m_{\tilde{q}}$ , the same PDF errors per point are used for the  $\tilde{B}$ -like and  $\tilde{W}$ -like grids.

# Chapter 9

## Conclusion

The results of a search for evidence of new particle production via final states with 2 photons, large  $\cancel{E}_T$ , and  $\geq 0$  or  $\geq 1$  jet in  $pp$  collisions at  $\sqrt{s} = 7$  TeV have been presented. No deviation in the production rate from that predicted by the Standard Model has been found. The null results were used to constrain general models of gauge mediated supersymmetry breaking. In these types of models, gluinos and first- and second-generation squarks are restricted to masses above  $\sim 1$  TeV.

These bounds do not exclude supersymmetry. The gluinos and first- and second-generation squarks can be a little bit heavier (but not too much heavier than a few TeV) and still imply an elegant supersymmetric solution to the hierarchy problem. More importantly, the bounds on the first- and second-generation squarks say nothing about the stop squark, which is intimately connected to the Higgs mass. At one loop order in the supersymmetric Standard Model, the lightest Higgs mass is given by [161]

$$m_h^2 \lesssim m_Z^2 + \frac{3g^2 m_t^4}{8\pi^2 m_W^2} \left[ \ln \frac{M_S^2}{m_t^2} + \frac{X_t^2}{M_S^2} \left( 1 - \frac{X_t^2}{12M_S^2} \right) \right] \quad (9.1)$$

where  $g$  is the  $SU(2)_L$  coupling constant,  $M_S^2$  is the average of the two observable

stop squared masses, and  $X_t$  is a parameter that characterizes stop mixing. The Higgs mass is directly sensitive to the stop mass, for which the only current lower bound of 330 GeV [162] is much weaker than for the first- and second-generation squarks (and highly model dependent). The current hints of a Higgs with mass  $\sim 125$  GeV [22, 23] point to a stop mass below 2 TeV if SUSY is really a symmetry of nature, depending on model.

Future searches for GMSB could look for either direct pair production of stops decaying via top quarks to neutralinos that then decay to photons, or for stops produced in the decay of a heavier pair-produced particle like the gluino. Looking for a final state containing a top, antitop, and  $\geq 1$  photon may be advantageous because the expected SM background should be small.

Top quark reconstruction depends heavily on  $b$  jet identification. The same  $b$  tagging techniques needed to find stops could also be applied to a search for a Higgsino-like neutralino decaying primarily to  $b\bar{b}$ . If gaugino mixing were in a certain corner of parameter space, then photon +  $b\bar{b}$  events might provide a window onto GMSB.

There are a number of interesting possibilities for future GMSB searches in addition to those just outlined. SUSY searches will likely remain a fruitful avenue of investigation throughout the lifetime of the LHC.

# Appendix A

## Monte Carlo Samples

A number of MC samples are utilized in this analysis and referred to throughout the text. Below is a list of the MC samples used and an explanation of what the sample names mean.

### A.1 List of Samples

1. Drell-Yan + up to 2 hard jets:

```
/DYJetsToLL_TuneZ2_M-50_7TeV-madgraph-tauola/
Fall11-PU_S6_START42_V14B-v1/AODSIM
```

2. QCD enriched with  $B$  and  $D$  meson decays to electrons:

```
/QCD_Pt-20to30_BCToE_TuneZ2_7TeV-pythia6/
Fall11-PU_S6_START42_V14B-v1/AODSIM,
/QCD_Pt-30to80_BCToE_TuneZ2_7TeV-pythia6/
Fall11-PU_S6_START42_V14B-v1/AODSIM,
/QCD_Pt-80to170_BCToE_TuneZ2_7TeV-pythia6/
Fall11-PU_S6_START42_V14B-v1/AODSIM
```

3. Photon + jet doubly enriched with jets passing an EM filter:

`/GJet_Pt-20_doubleEMEnriched_TuneZ2_7TeV-pythia6/`

`Fall11-PU_S6_START42_V14B-v1/AODSIM`

4.  $W$  leptonic decays + up to 2 hard jets:

`/WJetsToLNu_TuneZ2_7TeV-madgraph-tauola/`

`Fall11-PU_S6_START42_V14B-v1/AODSIM`

5.  $t\bar{t}$  + up to 2 hard jets:

`/TTJets_TuneZ2_7TeV-madgraph-tauola/`

`Fall11-PU_S6_START42_V14B-v2/AODSIM`

## A.2 Explanation of Naming Conventions

- L: charged lepton
- B:  $B$  hadron
- C:  $D$ , or charmed, hadron
- E: electron or positron
- G: photon
- W:  $W$  boson
- Nu: neutrino
- T: top quark
- TuneZ2: Pythia tune incorporating 2010 LHC data with CTEQ6L1 [156] PDFs  
[163]
- M-50: Generated  $l^+l^-$  invariant mass threshold of 50 GeV
- 7TeV: Generated center-of-mass energy 7 TeV

- **pythia6**: Parton showering and hadronization simulated with Pythia v6.424 [144]
- **madgraph**: Hard interaction generated with MadGraph 5 [164]
- **tauola**:  $\tau$  decays generated with Tauola [165]
- **PU\_S6**: Generated with S6 pileup scenario, which has a mean between 6 and 7 interactions per crossing, and includes pileup from the neighboring bunch crossings according to a Poisson distribution with mean equal to the number of interactions in the in-time crossing [166]
- **START42\_V14B**: Reconstructed with best alignment and calibration constants and magnetic field conditions as of August 3, 2011
- **Pt\_XtoY**:  $X \leq \text{generated } \hat{p}_T < Y$
- **BCToE**: Only keeps events if they contain at least one electron with  $E_T > 10$  GeV in  $|\eta| < 2.5$  that came from a  $b$  or  $c$  quark
- **doubleEMEnriched**: Enriched in photons, electrons, electrons from  $b/c$  decay, and electromagnetic jets [167]
- **AODSIM**: Run through full CMS reconstruction algorithm based on a GEANT 4 [145] detector simulation; AOD data tier, including generator-level information

# Bibliography

- [1] URL <http://cms.web.cern.ch/news/cms-detector-design>.
- [2] S. L. Glashow, Nucl. Phys. **22**, 579 (1961), URL <http://www.sciencedirect.com/science/article/pii/0029558261904692>.
- [3] S. L. Glashow, J. Iliopoulos, and L. Maiani, Phys. Rev. D **2**, 1285 (1970), URL <http://link.aps.org/doi/10.1103/PhysRevD.2.1285>.
- [4] J. Goldstone, A. Salam, and S. Weinberg, Phys. Rev. **127**, 965 (1962), URL <http://link.aps.org/doi/10.1103/PhysRev.127.965>.
- [5] S. Weinberg, Phys. Rev. Lett. **19**, 1264 (1967), URL <http://link.aps.org/doi/10.1103/PhysRevLett.19.1264>.
- [6] A. Salam and J. Ward, Phys. Lett. **13**, 168 (1964), URL <http://www.sciencedirect.com/science/article/pii/0031916364907115>.
- [7] M. Gell-Mann, Phys. Lett. **8**, 214 (1964), URL <http://www.sciencedirect.com/science/article/pii/S0031916364920013>.
- [8] G. Zweig, in *Developments in the Quark Theory of Hadrons*, edited by D. B. Lichtenberg and S. P. Rosen (Hadronic Press, Nonantum, MA, 1980), pp. 22–101.
- [9] J. Drees, Int. J. Mod. Phys. A **17**, 3259 (2002), URL <http://www.worldscinet.com/ijmpa/17/1723/S0217751X02012727.html>.

- [10] P. Higgs, Phys. Lett. **12**, 132 (1964), URL <http://www.sciencedirect.com/science/article/pii/0031916364911369>.
- [11] P. W. Higgs, Phys. Rev. Lett. **13**, 508 (1964), URL <http://link.aps.org/doi/10.1103/PhysRevLett.13.508>.
- [12] P. W. Higgs, Phys. Rev. **145**, 1156 (1966), URL <http://link.aps.org/doi/10.1103/PhysRev.145.1156>.
- [13] I. Aitchison, *Supersymmetry in Particle Physics: An Elementary Introduction* (Cambridge Univ. Press, Cambridge, 2007).
- [14] C. Quigg, in *Flavor Physics for the Millennium: TASI 2000 : Boulder, Colorado, US, 2000*, edited by J. L. Rosner (World Scientific, Singapore, 2001), p. 3, URL <http://arxiv.org/abs/hep-ph/0204104>.
- [15] L. Álvarez Gaumé and J. Ellis, Nat. Phys. **7**, 2 (2011), URL <http://dx.doi.org/10.1038/nphys1874>.
- [16] G. Arnison et al. (UA1 Collaboration), Phys. Lett. B **122**, 103 (1983), URL <http://www.sciencedirect.com/science/article/pii/0370269383911772>.
- [17] G. Arnison et al. (UA1 Collaboration), Phys. Lett. B **126**, 398 (1983), URL <http://www.sciencedirect.com/science/article/pii/0370269383901880>.
- [18] J. F. Gunion, S. Dawson, H. E. Haber, and G. L. Kane, *The Higgs Hunter's Guide* (Westview, Boulder, CO, 1990).
- [19] K. Nakamura et al. (Particle Data Group), J. Phys. G **37**, 075021 (2010), URL <http://stacks.iop.org/0954-3899/37/i=7A/a=075021>.

- [20] S. P. Martin (2006), unpublished, arXiv:hep-ph/9709356, URL <http://arxiv.org/abs/hep-ph/9709356v6>.
- [21] G. Jungman, M. Kamionkowski, and K. Griest, Phys. Rept. **267**, 195 (1996), URL <http://www.sciencedirect.com/science/article/pii/0370157395000585>.
- [22] S. Chatrchyan et al. (CMS Collaboration), Phys. Lett. B **710**, 26 (2012), URL <http://www.sciencedirect.com/science/article/pii/S0370269312002055>.
- [23] G. Aad et al., Phys. Lett. B **710**, 49 (2012), URL <http://www.sciencedirect.com/science/article/pii/S0370269312001852>.
- [24] M. Dine and W. Fischler, Phys. Lett. B **110**, 227 (1982), URL <http://www.sciencedirect.com/science/article/pii/0370269382912412>.
- [25] C. R. Nappi and B. A. Ovrut, Phys. Lett. B **113**, 175 (1982), URL <http://www.sciencedirect.com/science/article/pii/037026938290418X>.
- [26] L. Alvarez-Gaumé, M. Claudson, and M. B. Wise, Nucl. Phys. B **207**, 96 (1982), URL <http://www.sciencedirect.com/science/article/pii/0550321382901389>.
- [27] M. Dine and A. E. Nelson, Phys. Rev. D **48**, 1277 (1993), URL <http://link.aps.org/doi/10.1103/PhysRevD.48.1277>.
- [28] M. Dine, A. E. Nelson, and Y. Shirman, Phys. Rev. D **51**, 1362 (1995), URL <http://link.aps.org/doi/10.1103/PhysRevD.51.1362>.
- [29] M. Dine, A. E. Nelson, Y. Nir, and Y. Shirman, Phys. Rev. D **53**, 2658 (1996), URL <http://link.aps.org/doi/10.1103/PhysRevD.53.2658>.

- [30] A. H. Chamseddine, R. Arnowitt, and P. Nath, Phys. Rev. Lett. **49**, 970 (1982), URL <http://link.aps.org/doi/10.1103/PhysRevLett.49.970>.
- [31] R. Barbieri, S. Ferrara, and C. Savoy, Phys. Lett. B **119**, 343 (1982), URL <http://www.sciencedirect.com/science/article/pii/0370269382906852>.
- [32] L. Ibáñez, Phys. Lett. B **118**, 73 (1982), URL <http://www.sciencedirect.com/science/article/pii/0370269382906049>.
- [33] L. Hall, J. Lykken, and S. Weinberg, Phys. Rev. D **27**, 2359 (1983), URL <http://link.aps.org/doi/10.1103/PhysRevD.27.2359>.
- [34] N. Ohta, Prog. Theor. Phys. **70**, 542 (1983), URL <http://ptp.ipap.jp/link?PTP/70/542/>.
- [35] J. Ellis, D. Nanopoulos, and K. Tamvakis, Phys. Lett. B **121**, 123 (1983), URL <http://www.sciencedirect.com/science/article/pii/0370269383909000>.
- [36] L. Alvarez-Gaumé, J. Polchinski, and M. B. Wise, Nucl. Phys. B **221**, 495 (1983), URL <http://www.sciencedirect.com/science/article/pii/0550321383905916>.
- [37] P. Meade, N. Seiberg, and D. Shih, Prog. Theor. Phys. Suppl. **177**, 143 (2009), URL <http://ptp.ipap.jp/link?PTPS/177/143/>.
- [38] G. Aad et al., Phys. Lett. B **710**, 519 (2012), URL <http://www.sciencedirect.com/science/article/pii/S0370269312001955>.
- [39] T. Aaltonen et al. (CDF Collaboration), Phys. Rev. Lett. **104**, 011801 (2010), URL <http://link.aps.org/doi/10.1103/PhysRevLett.104.011801>.
- [40] S. Chatrchyan et al. (CMS Collaboration) (2011), unpublished, CMS-PAS-SUS-11-009, URL <https://cdsweb.cern.ch/record/1377324>.

- [41] URL <http://en.wikipedia.org/wiki/Tevatron>.
- [42] E. Fernandez, W. T. Ford, N. Qi, A. L. Read, J. G. Smith, T. Camporesi, R. De Sangro, A. Marini, I. Peruzzi, M. Piccolo, et al., Phys. Rev. Lett. **54**, 1118 (1985), URL <http://link.aps.org/doi/10.1103/PhysRevLett.54.1118>.
- [43] E. W. Fernandez, W. T. Ford, N. Qi, A. L. Read, J. G. Smith, T. Camporesi, I. Peruzzi, M. Piccolo, R. B. Hurst, K. H. Lau, et al., Phys. Rev. D **35**, 374 (1987), URL <http://link.aps.org/doi/10.1103/PhysRevD.35.374>.
- [44] D. Decamp et al. (ALEPH Collaboration), Phys. Lett. B **237**, 291 (1990), URL <http://www.sciencedirect.com/science/article/pii/037026939091447J>.
- [45] F. Abe et al. (CDF Collaboration), Phys. Rev. Lett. **75**, 613 (1995), URL <http://link.aps.org/doi/10.1103/PhysRevLett.75.613>.
- [46] S. Abachi et al. (D0 Collaboration), Phys. Rev. Lett. **75**, 618 (1995), URL <http://link.aps.org/doi/10.1103/PhysRevLett.75.618>.
- [47] G. Alexander et al. (OPAL Collaboration), Phys. Lett. B **377**, 273 (1996), URL <http://www.sciencedirect.com/science/article/pii/0370269396005023>.
- [48] S. Aid et al. (H1 Collaboration), Z. Phys. C **71**, 211 (1996), 10.1007/BF02906978, URL <http://dx.doi.org/10.1007/BF02906978>.
- [49] S. Aid et al. (H1 Collaboration), Phys. Lett. B **380**, 461 (1996), URL <http://www.sciencedirect.com/science/article/pii/0370269396006405>.
- [50] B. Aubert et al. (BABAR Collaboration), Phys. Rev. Lett. **95**, 041802 (2005), URL <http://link.aps.org/doi/10.1103/PhysRevLett.95.041802>.

- [51] O. Buchmueller, R. Cavanaugh, A. De Roeck, M. J. Dolan, J. R. Ellis, H. Flacher, S. Heinemeyer, G. Isidori, D. Martinez Santos, K. A. Olive, et al., Report No. CERN-PH-TH-2011-220, CERN (2011), URL <https://cdsweb.cern.ch/record/1391061>.
- [52] URL [https://twiki.cern.ch/twiki/pub/CMSPublic/PhysicsResultsSUS/CMS\\_SUSY\\_2011Limits\\_tanb10.pdf](https://twiki.cern.ch/twiki/pub/CMSPublic/PhysicsResultsSUS/CMS_SUSY_2011Limits_tanb10.pdf).
- [53] B. Allanach, M. Battaglia, G. Blair, M. Carena, A. De Roeck, A. Dedes, A. Djouadi, D. Gerdes, N. Ghodbane, J. Gunion, et al., Eur. Phys. J. C **25**, 113 (2002), URL <http://dx.doi.org/10.1007/s10052-002-0949-3>.
- [54] G. Aad et al. (ATLAS Collaboration), J. Instr. **3**, S08003 (2008), URL <http://stacks.iop.org/1748-0221/3/i=08/a=S08003>.
- [55] A. Boyarsky, J. Lesgourgues, O. Ruchayskiy, and M. Viel, J. Cosmol. Astropart. Phys. **2009**, 012 (2009), URL <http://stacks.iop.org/1475-7516/2009/i=05/a=012>.
- [56] E. Komatsu, J. Dunkley, M. R. Nolta, C. L. Bennett, B. Gold, G. Hinshaw, N. Jarosik, D. Larson, M. Limon, L. Page, et al., Astrophys. J. Suppl. Ser. **180**, 330 (2009), URL <http://stacks.iop.org/0067-0049/180/i=2/a=330>.
- [57] C.-H. Chen and J. F. Gunion, Phys. Rev. D **58**, 075005 (1998), URL <http://link.aps.org/doi/10.1103/PhysRevD.58.075005>.
- [58] F. Staub, J. Niemeyer, and W. Porod, JHEP **2010**, 1 (2010), URL [http://dx.doi.org/10.1007/JHEP01\(2010\)058](http://dx.doi.org/10.1007/JHEP01(2010)058).
- [59] S. Chatrchyan et al. (CMS Collaboration) (2012), unpublished, CMS-PAS-SUS-12-001, URL <https://cdsweb.cern.ch/record/1436111>.

- [60] L. Evans and P. Bryant, J. Instr. **3**, S08001 (2008), URL <http://stacks.iop.org/1748-0221/3/i=08/a=S08001>.
- [61] URL <http://cms.web.cern.ch/news/summary-2011-p-p-running>.
- [62] URL <http://public.web.cern.ch/public/en/lhc/Facts-en.html>.
- [63] URL <http://cdsweb.cern.ch/record/833187>.
- [64] URL <http://www.rgbstock.com/photo/n7EsabW/Airplane>.
- [65] R. Flükiger, S. Y. Hariharan, R. Küntzler, H. L. Luo, F. Weiss, T. Wolf, and J. Q. Xu, in *SpringerMaterials - The Landolt-Börnstein Database: Nb-Ti*, edited by R. Flükiger and W. Klose (<http://www.springermaterials.com>, 2012), URL [http://www.springermaterials.com/docs/info/10423690\\_53.html](http://www.springermaterials.com/docs/info/10423690_53.html).
- [66] Y. Sun, F. Zimmermann, and R. Tomás, in *Proceedings of the 23<sup>rd</sup> Particle Accelerator Conference, Vancouver, 2009* (2009), URL <https://cdsweb.cern.ch/record/1235160>.
- [67] O. S. Brüning, P. Collier, P. Lebrun, S. Myers, R. Ostojic, J. Poole, and P. Proudlock, *LHC Design Report* (CERN, Geneva, 2004).
- [68] URL <http://cdsweb.cern.ch/record/841568/files/>.
- [69] P. Komorowski and D. Tommasini, IEEE Trans. Appl. Supercond. **10**, 166 (2000), URL <http://ieeexplore.ieee.org/xpl/articleDetails.jsp?arnumber=828202>.
- [70] URL <http://lhc-machine-outreach.web.cern.ch/lhc-machine-outreach/components/magnets.htm>.
- [71] S. Chatrchyan et al. (CMS Collaboration), J. Instr. **3**, S08004 (2008), URL <http://stacks.iop.org/1748-0221/3/i=08/a=S08004>.

- [72] G. L. Bayatian et al. (CMS Collaboration), *CMS Physics Technical Design Report Volume I: Detector Performance and Software*, Technical Design Report CMS (CERN, Geneva, 2006).
  
- [73] M. Ivova (2010), talk given at the Swiss Ph.D. School on Particle and Astroparticle Physics (CHIPP), Monte Verita', URL <https://indico.cern.ch/getFile.py/access?contribId=11&sessionId=14&resId=0&materialId=0&confId=80223>.
  
- [74] G. Bolla, D. Bortoletto, C. Rott, A. Roy, S. Kwan, C. Chien, H. Cho, B. Gobbi, R. Horisberger, and R. Kaufmann, Nucl. Instr. Meth. A **461**, 182 (2001), URL <http://www.sciencedirect.com/science/article/pii/S0168900200012018>.
  
- [75] URL [https://twiki.cern.ch/twiki/pub/CMSPublic/DPGResultsTRK/\\_imgf9e0ee48ebca770d7774454532b4b4ee.png](https://twiki.cern.ch/twiki/pub/CMSPublic/DPGResultsTRK/_imgf9e0ee48ebca770d7774454532b4b4ee.png).
  
- [76] URL [https://twiki.cern.ch/twiki/pub/CMSPublic/DPGResultsTRK/\\_img7569b7652b3f7c15030a11a4223e631c.png](https://twiki.cern.ch/twiki/pub/CMSPublic/DPGResultsTRK/_img7569b7652b3f7c15030a11a4223e631c.png).
  
- [77] URL [https://twiki.cern.ch/twiki/pub//CMSPublic/DPGResultsTRK/hv11\\_d1.png](https://twiki.cern.ch/twiki/pub//CMSPublic/DPGResultsTRK/hv11_d1.png).
  
- [78] URL [https://twiki.cern.ch/twiki/pub/CMSPublic/DPGResultsTRK/\\_imga571742cbcd3a14a9e2581ae95efa54c.gif](https://twiki.cern.ch/twiki/pub/CMSPublic/DPGResultsTRK/_imga571742cbcd3a14a9e2581ae95efa54c.gif).
  
- [79] URL <https://twiki.cern.ch/twiki/pub//CMSPublic/DPGResultsTRK/StripHitRes2.gif>.
  
- [80] URL [https://twiki.cern.ch/twiki/pub//CMSPublic/EcalDPGResults/history2\\_laser.png](https://twiki.cern.ch/twiki/pub//CMSPublic/EcalDPGResults/history2_laser.png).

- [81] G. Akopdzhianov, A. Inyakin, and P. Shuvalov, Nucl. Instr. Meth. **161**, 247 (1979), URL <http://www.sciencedirect.com/science/article/pii/0029554X79903914>.
- [82] J. Wood, work in progress at the University of Virginia high energy physics laboratory.
- [83] V. Khachatryan et al. (CMS Collaboration), Phys. Rev. Lett. **106**, 011801 (2011), URL <http://link.aps.org/doi/10.1103/PhysRevLett.106.011801>.
- [84] URL [https://twiki.cern.ch/twiki/pub//CMSPublic/EcalDPGResults/electronres\\_eb\\_inclusive.png](https://twiki.cern.ch/twiki/pub//CMSPublic/EcalDPGResults/electronres_eb_inclusive.png).
- [85] URL [https://twiki.cern.ch/twiki/pub//CMSPublic/EcalDPGResults/electronres\\_ee\\_inclusive.png](https://twiki.cern.ch/twiki/pub//CMSPublic/EcalDPGResults/electronres_ee_inclusive.png).
- [86] S. Chatrchyan et al. (CMS Collaboration) (2011), unpublished, CMS-PAS-EXO-11-067, URL <https://cdsweb.cern.ch/record/1394286>.
- [87] URL <https://twiki.cern.ch/twiki/pub//CMSPublic/EcalDPGResults/seed-time.EEEE.png>.
- [88] N. Akchurin and R. Wigmans, Rev. Sci. Instr. **74**, 2955 (2003), URL [http://rsi.aip.org/resource/1/rsinak/v74/i6/p2955\\_s1](http://rsi.aip.org/resource/1/rsinak/v74/i6/p2955_s1).
- [89] S. Chatrchyan et al. (CMS Collaboration) (2010), unpublished, CMS-DP-2010-025, URL <https://cdsweb.cern.ch/record/1364222>.
- [90] S. Chatrchyan et al. (CMS Collaboration), J. Instr. **5**, T03014 (2010), URL <http://stacks.iop.org/1748-0221/5/i=03/a=T03014>.
- [91] URL [https://twiki.cern.ch/twiki/pub//CMSPublic/PhysicsResultsMUO/dimuMass\\_2011Run\\_1fb\\_20July2011.pdf](https://twiki.cern.ch/twiki/pub//CMSPublic/PhysicsResultsMUO/dimuMass_2011Run_1fb_20July2011.pdf).

- [92] S. Chatrchyan et al., JHEP **2012**, 1 (2012), URL [http://dx.doi.org/10.1007/JHEP04\(2012\)033](http://dx.doi.org/10.1007/JHEP04(2012)033).
- [93] R. Alemany, C. Almeida, N. Almeida, M. Bercher, R. Benetta, V. Bexiga, J. Bourotte, P. Busson, N. Cardoso, M. Cerrutti, et al., IEEE Trans. Nucl. Sci. **52**, 1918 (2005), URL <http://ieeexplore.ieee.org/xpl/articleDetails.jsp?arnumber=1546528>.
- [94] W. Smith, P. Chumney, S. Dasu, F. D. Lodovico, M. Jaworski, J. Lackey, and P. Robl, in *Proceedings of the 7<sup>th</sup> Workshop on Electronics for LHC Experiments, Stockholm, 2001*, edited by C. Isabella (CERN, Geneva, 2001), pp. 238–242, URL <https://cdsweb.cern.ch/record/529417>.
- [95] R. Brun and F. Rademakers, Nucl. Instr. Meth. A **389**, 81 (1997), URL <http://www.sciencedirect.com/science/article/pii/S016890029700048X>.
- [96] J. Guteleber and L. Orsini, Clus. Comput. **5**, 55 (2002), URL <http://dx.doi.org/10.1023/A:1012744721976>.
- [97] D. Box, D. Ehnebuske, G. Kakivaya, A. Layman, N. Mendelsohn, H. Nielsen, S. Thatte, and D. Winer, Report No. W3C Note 08, W3C (2000), URL <http://www.w3.org/TR/2000/NOTE-SOAP-20000508/>.
- [98] R. Arcidiacono et al. (2005), talk given at the 10<sup>th</sup> ICAL-EPCS International Conference on Accelerator and Large Experiment Physics Control Systems, Geneva, URL [http://accelconf.web.cern.ch/accelconf/ica05/proceedings/pdf/o5\\_004.pdf](http://accelconf.web.cern.ch/accelconf/ica05/proceedings/pdf/o5_004.pdf).
- [99] C. Eck, J. Knobloch, L. Robertson, I. Bird, K. Bos, N. Brook, D. Dillmann, I. Fisk, D. Foster, B. Gibbard, et al., *LHC computing Grid: Technical Design Report. Version 1.06 (20 Jun 2005)*, Technical Design Report LCG (CERN, Geneva, 2005).

- [100] R. Brunelière, Nucl. Instr. Meth. A **572**, 33 (2007), URL <http://www.sciencedirect.com/science/article/pii/S0168900206019711>.
- [101] S. Chatrchyan et al. (CMS Collaboration), J. Instr. **5**, T03011 (2010), URL <http://stacks.iop.org/1748-0221/5/i=03/a=T03011>.
- [102] S. Chatrchyan et al. (CMS Collaboration) (2010), unpublished, CMS-NOTE-2010-012, URL <https://cdsweb.cern.ch/record/1278160>.
- [103] P. Meridiani and C. Seez, Report No. CMS IN-2011/002, CERN (2011), URL [http://cms.cern.ch/iCMS/jsp/openfile.jsp?type=IN&year=2011&files=IN2011\\_002.pdf](http://cms.cern.ch/iCMS/jsp/openfile.jsp?type=IN&year=2011&files=IN2011_002.pdf).
- [104] P. Adzic et al. (CMS Electromagnetic Calorimeter Group), Eur. Phys. J. C **44**, 1 (2006), URL <http://dx.doi.org/10.1140/epjcd/s2005-02-011-3>.
- [105] P. Adzic et al. (CMS Electromagnetic Calorimeter Group), J. Instr. **3**, P10007 (2008), URL <http://stacks.iop.org/1748-0221/3/i=10/a=P10007>.
- [106] M. Malberti, in *Nuclear Science Symposium Conference Record (NSS/MIC), 2009 IEEE* (2009), p. 2264, URL [http://ieeexplore.ieee.org/xpls/abs\\_all.jsp?arnumber=5402068](http://ieeexplore.ieee.org/xpls/abs_all.jsp?arnumber=5402068).
- [107] S. Chatrchyan et al. (CMS Collaboration), J. Instr. **5**, T03010 (2010), URL <http://stacks.iop.org/1748-0221/5/i=03/a=T03010>.
- [108] R. Paramatti, J. Phys.: Conf. Ser. **293**, 012045 (2011), URL <http://stacks.iop.org/1742-6596/293/i=1/a=012045>.
- [109] Y. Yang (2011), poster presented at the Achievement Awards session of CMS Week, CERN, Geneva, URL [http://www.hep.caltech.edu/cms/posters/PiOPoster\\_CMSWeekDec2011.pdf](http://www.hep.caltech.edu/cms/posters/PiOPoster_CMSWeekDec2011.pdf).

- [110] M. Anderson, A. Askew, A. Barfuss, D. Evans, F. Ferri, K. Kaadze, Y. Marvin, P. Meridiani, and C. Seez, Report No. CMS IN-2010/008, CERN (2010), URL [http://cms.cern.ch/iCMS/jsp/openfile.jsp?type=IN&year=2010&files=IN2010\\_008.pdf](http://cms.cern.ch/iCMS/jsp/openfile.jsp?type=IN&year=2010&files=IN2010_008.pdf).
- [111] A. David, M. Donega, M. Gataullin, et al. ( $H \rightarrow \gamma\gamma$  working group), Report No. CMS AN-2011/426, CERN (2011), URL [http://cms.cern.ch/iCMS/jsp/openfile.jsp?tp=draft&files=AN2011\\_426\\_v5.pdf](http://cms.cern.ch/iCMS/jsp/openfile.jsp?tp=draft&files=AN2011_426_v5.pdf).
- [112] URL <https://twiki.cern.ch/twiki/bin/view/CMS/ECALEnergyScaleCorrections>.
- [113] M. Cacciari, Report No. LPTHE-P06-04, LPTHE, Université P. et M. Curie (2006), URL <http://arxiv.org/abs/hep-ph/0607071>.
- [114] M. Cacciari, G. Salam, and G. Soyez, Report No. CERN-PH-TH-2011-297, CERN (2011), URL <https://cdsweb.cern.ch/record/1402449>.
- [115] V. Khachatryan et al. (CMS Collaboration), Phys. Rev. Lett. **106**, 082001 (2011), URL <http://link.aps.org/doi/10.1103/PhysRevLett.106.082001>.
- [116] A. Askew, B. Cox, D. Elvira, Y. Gershtein, M. Hildreth, D. Jang, Y.-F. Liu, D. Mason, D. Morse, U. Nauenberg, et al., Report No. CMS AN-2011/515, CERN (2011), URL [http://cms.cern.ch/iCMS/jsp/openfile.jsp?tp=draft&files=AN2011\\_515\\_v6.pdf](http://cms.cern.ch/iCMS/jsp/openfile.jsp?tp=draft&files=AN2011_515_v6.pdf).
- [117] W. Adam, R. Frühwirth, A. Strandlie, and T. Todorov, J. Phys. G **31**, N9 (2005), URL <http://stacks.iop.org/0954-3899/31/i=9/a=N01>.
- [118] S. Chatrchyan et al. (CMS Collaboration) (2009), unpublished, CMS-PAS-PFT-09-001, URL <https://cdsweb.cern.ch/record/1194487>.

- [119] S. Chatrchyan et al. (CMS Collaboration) (2010), unpublished, CMS-PAS-PFT-10-002, URL <https://cdsweb.cern.ch/record/1279341>.
- [120] S. Chatrchyan et al. (CMS collaboration), J. Instr. **6**, P11002 (2011), URL <http://stacks.iop.org/1748-0221/6/i=11/a=P11002>.
- [121] M. Cacciari, G. P. Salam, and G. Soyez, JHEP **2008**, 063 (2008), URL <http://stacks.iop.org/1126-6708/2008/i=04/a=063>.
- [122] G. Salam (2009), talk given at CERN Theory Institute: SM and BSM Physics at the LHC, CERN, Geneva, URL <https://indico.cern.ch/getFile.py/access?contribId=1&sessionId=9&resId=0&materialId=slides&confId=43022>.
- [123] C. W. Fabjan and R. Wigmans, Rep. Prog. Phys. **52**, 1519 (1989), URL <http://stacks.iop.org/0034-4885/52/i=12/a=002>.
- [124] URL <http://www-cdf.fnal.gov/physics/new/top/2004/jets/cdfpublic.html>.
- [125] S. Chatrchyan et al. (CMS collaboration), J. Instr. **6**, P09001 (2011), URL <http://stacks.iop.org/1748-0221/6/i=09/a=P09001>.
- [126] S. Chatrchyan et al. (CMS Collaboration) (2009), unpublished, CMS-PAS-JME-09-002, URL <https://cdsweb.cern.ch/record/1190234>.
- [127] F. Beaudette, D. Benedetti, P. Janot, and M. Pioppi, Report No. CMS AN-2010/034, CERN (2010), URL [http://cms.cern.ch/icMS/jsp/openfile.jsp?tp=draft&files=AN2010\\_034\\_v2.pdf](http://cms.cern.ch/icMS/jsp/openfile.jsp?tp=draft&files=AN2010_034_v2.pdf).
- [128] M. Konecki, in *Proceedings of the European Physical Society Europhysics Conference on High Energy Physics, EPS-HEP 2009, Krakow, Poland* (Proc. Sci., 2009), p. 131, URL <http://inspirehep.net/record/861487>.

- [129] T. Sjöstrand, S. Mrenna, and P. Skands, *Comput. Phys. Commun.* **178**, 852 (2008), URL <http://www.sciencedirect.com/science/article/pii/S0010465508000441>.
- [130] URL <https://twiki.cern.ch/twiki/bin/view/CMS/PVTMain>.
- [131] J. P. Chou, S. Eno, S. Kunori, S. Sharma, and J. Wang, Report No. IN-2010/006, CERN (2010), URL [http://cms.cern.ch/iCMS/jsp/openfile.jsp?type=IN&year=2010&files=IN2010\\_006.pdf](http://cms.cern.ch/iCMS/jsp/openfile.jsp?type=IN&year=2010&files=IN2010_006.pdf).
- [132] R. Korzekwa, F. Lehr, H. Krompholz, and M. Kristiansen, *IEEE Trans. Elec. Dev.* **38**, 745 (1991), URL <http://ieeexplore.ieee.org/xpl/articleDetails.jsp?arnumber=75200>.
- [133] Y. Chen (2011), talk given at a meeting of the CMS JetMET group, CERN, Geneva, URL <https://indico.cern.ch/getFile.py/access?contribId=1&resId=0&materialId=slides&confId=129896>.
- [134] W. Adam, B. Mangano, T. Speer, and T. Todorov, Report No. CMS-NOTE-2006-041, CERN, Geneva (2006), URL <https://cdsweb.cern.ch/record/934067>.
- [135] G. Daskalakis, D. Evans, C. Hill, J. Jackson, P. Vanlaer, J. Berryhill, J. Haupt, D. Futyan, C. Seez, C. Timlin, et al., Report No. CMS AN-2007/019, CERN (2007), URL [http://cms.cern.ch/iCMS/jsp/openfile.jsp?tp=draft&files=AN2007\\_019\\_v3.pdf](http://cms.cern.ch/iCMS/jsp/openfile.jsp?tp=draft&files=AN2007_019_v3.pdf).
- [136] F. James and M. Roos, *Comput. Phys. Commun.* **10**, 343 (1975), URL <http://www.sciencedirect.com/science/article/pii/0010465575900399>.
- [137] W. Verkerke and D. P. Kirkby, in *Proceedings of the Conference on Statistical Problems in Particle Physics, Astrophysics, and Cosmology: PHYSTAT 2005*,

- Oxford, England, United Kingdom*, edited by L. Lyons and M. K. Unel (Imperial Coll. Press, London, 2006), p. 186, URL <http://inspirehep.net/record/621398>.
- [138] J. E. Gaiser, Ph.D. thesis, Stanford University, 450 Serra Mall, Stanford, CA 94305 (1982), URL <http://www.slac.stanford.edu/cgi-wrap/getdoc/slac-r-255.pdf>.
- [139] A. Askew, S. Arora, Y. Gershtein, S. Thomas, G. Hanson, R. Stringer, W. Flanagan, B. Heyburn, U. Nauenberg, S. Zang, et al., Report No. CMS AN-2010/271, CERN (2010), URL [http://cms.cern.ch/iCMS/jsp/openfile.jsp?tp=draft&files=AN2010\\_271\\_v8.pdf](http://cms.cern.ch/iCMS/jsp/openfile.jsp?tp=draft&files=AN2010_271_v8.pdf).
- [140] URL <https://cmsweb.cern.ch/das/>.
- [141] S. Chatrchyan et al. (CMS Collaboration), Phys. Rev. Lett. **106**, 211802 (2011), URL <http://link.aps.org/doi/10.1103/PhysRevLett.106.211802>.
- [142] A. Djouadi, J.-L. Kneur, and G. Mourtaka (2005), unpublished, arXiv:hep-ph/0211331, URL <http://arxiv.org/abs/hep-ph/0211331>.
- [143] M. Mühlleitner, A. Djouadi, and Y. Mambrini, Comp. Phys. Commun. **168**, 46 (2005), URL <http://www.sciencedirect.com/science/article/pii/S0010465505000822>.
- [144] T. Sjöstrand, S. Mrenna, and P. Skands, JHEP **2006**, 026 (2006), URL <http://stacks.iop.org/1126-6708/2006/i=05/a=026>.
- [145] J. Allison, K. Amako, J. Apostolakis, H. Araujo, P. Dubois, M. Asai, G. Barrand, R. Capra, S. Chauvie, R. Chytracek, et al., IEEE Trans. Nucl. Sci. **53**, 270 (2006), URL <http://ieeexplore.ieee.org/xpl/articleDetails.jsp?arnumber=1610988>.

- [146] W. Beenakker, R. Hoepker, and M. Spira (1996), unpublished, arXiv:hep-ph/9611232, URL <http://arxiv.org/abs/hep-ph/9611232>.
- [147] G. Aad (ATLAS Collaboration), S. Chatrchyan (CMS Collaboration), and LHC Higgs Combination Group, Report No. CMS-NOTE-2011-005, CERN, Geneva (2011), URL <https://cdsweb.cern.ch/record/1379837>.
- [148] A. L. Read, in *Proceedings of the First Workshop on Confidence Limits, Geneva, 2000*, edited by L. Lyons, Y. Perrin, and F. James (CERN, Geneva, 2000), p. 81, URL <https://cdsweb.cern.ch/record/411537>.
- [149] G. Cowan, K. Cranmer, E. Gross, and O. Vitells, Eur. Phys. J. C **71**, 1 (2011), URL <http://dx.doi.org/10.1140/epjc/s10052-011-1554-0>.
- [150] J. Neyman and E. S. Pearson, Phil. Trans. R. Soc. London **231**, 289 (1933), URL <http://rsta.royalsocietypublishing.org/content/231/694-706/289.short>.
- [151] S. Chatrchyan et al. (CMS Collaboration) (2011), unpublished, CMS-PAS-EWK-11-001, URL <https://cdsweb.cern.ch/record/1376102>.
- [152] S. Alekhin et al. (PDF4LHC Working Group) (2011), unpublished, arXiv:1101.0536 [hep-ph], URL <http://arxiv.org/abs/1101.0536>.
- [153] M. Botje et al. (PDF4LHC Working Group) (2011), unpublished, arXiv:1101.0538 [hep-ph], URL <http://arxiv.org/abs/1101.0538>.
- [154] URL <http://www.hep.ucl.ac.uk/pdf4lhc/index.html>.
- [155] A. Martin, W. Stirling, R. Thorne, and G. Watt, Eur. Phys. J. C **63**, 189 (2009), URL <http://dx.doi.org/10.1140/epjc/s10052-009-1072-5>.

- [156] P. M. Nadolsky, H.-L. Lai, Q.-H. Cao, J. Huston, J. Pumplin, D. Stump, W.-K. Tung, and C.-P. Yuan, Phys. Rev. D **78**, 013004 (2008), URL <http://link.aps.org/doi/10.1103/PhysRevD.78.013004>.
- [157] R. D. Ball, L. D. Debbio, S. Forte, A. Guffanti, J. I. Latorre, J. Rojo, and M. Ubiali, Nucl. Phys. B **838**, 136 (2010), URL <http://www.sciencedirect.com/science/article/pii/S0550321310002853>.
- [158] A. Cooper-Sarkar (2012), unpublished, arXiv:1206.0894[hep-ph], URL <http://arxiv.org/abs/arXiv:1206.0894>.
- [159] D. Bourilkov, R. C. Group, and M. R. Whalley (2006), unpublished, arXiv:hep-ph/0605240, URL <http://arxiv.org/abs/hep-ph/0605240>.
- [160] J. M. Campbell, J. W. Huston, and W. J. Stirling, Rep. Prog. Phys. **70**, 89 (2007), URL <http://stacks.iop.org/0034-4885/70/i=1/a=R02>.
- [161] M. Carena, J. Conway, H. Haber, and J. Hobbs (2000), unpublished, arXiv:hep-ph/0010338, URL <http://arxiv.org/abs/hep-ph/0010338>.
- [162] G. Aad et al. (ATLAS Collaboration) (2012), unpublished, ATLAS-CONF-2012-036, URL <https://cdsweb.cern.ch/record/1432203>.
- [163] R. Field (2011), talk given at LHC Physics Centre at CERN Minimum Bias and Underlying Event Working Group Meeting, Geneva, URL <https://indico.cern.ch/getFile.py/access?contribId=11&sessionId=2&resId=1&materialId=slides&confId=140054>.
- [164] J. Alwall, M. Herquet, F. Maltoni, O. Mattelaer, and T. Stelzer, JHEP **2011**, 1 (2011), URL [http://dx.doi.org/10.1007/JHEP06\(2011\)128](http://dx.doi.org/10.1007/JHEP06(2011)128).
- [165] Z. Wąs, Nucl. Phys. B - Proc. Suppl. **98**, 96 (2001), URL <http://www.sciencedirect.com/science/article/pii/S0920563201012002>.

- [166] URL [http://cmslxr.fnal.gov/lxr/source/SimGeneral/MixingModule/python/mix\\_E7TeV\\_Fall2011\\_Reprocess\\_50ns\\_PoissonOOTPU\\_cfi.py](http://cmslxr.fnal.gov/lxr/source/SimGeneral/MixingModule/python/mix_E7TeV_Fall2011_Reprocess_50ns_PoissonOOTPU_cfi.py).
- [167] URL <http://cmslxr.fnal.gov/lxr/source/GeneratorInterface/GenFilters/src/doubleEMEnrichingFilterAlgo.cc>.